UNIVERSITY OF SOUTHAMPTON

Faculty of Physical Sciences and Engineering
School of Physics and Astronomy

The energy dependence of AGN variability as a means to probe the nature of accretion

by

Dominic Ian Ashton
MPhys (Hons)
ORCiD: 0000-0002-1021-0250

A thesis for the degree of
Doctor of Philosophy

December 2021

University of Southampton

Abstract

Faculty of Physical Sciences and Engineering
School of Physics and Astronomy

Doctor of Philosophy

The energy dependence of AGN variability as a means to probe the nature of accretion

by Dominic Ian Ashton

The study of X-ray variability in AGN allows us to probe the nature of accretion in highly curved space-time. This work sets out to study energy-resolved *XMM-Newton* observations of a large sample of AGN using Fourier analysis techniques, in order to search for X-ray quasi-periodic oscillations (QPOs) across as yet unexplored energy bands, and more broadly investigate the energy dependence of X-ray variability in AGN.

Robust detection of QPOs in AGN (i.e. repeat detections over multiple observations) have been limited to a single source to-date, with only tentative claims of single observation detections in several others. I develop a deep QPO search using the *XMM-Newton* archive to analyse the energy-resolved lightcurves of 38 bright AGN, and apply a conservative false alarm testing routine folding in the uncertainty of the modelled broad-band noise. I report statistically significant QPO candidates in 6 AGN (+1 tentative detection) from this initial study, including four cases of candidates at the same frequency across at least two observations, indicating they are highly unlikely to be spurious in nature. I additionally explore the impact of a number of effects which may act to bias the detection significance and scrutinise the validity of these detections.

I also explore the energy-dependence of the power spectrum for five AGN across the *XMM-Newton* bandpass and find a ubiquitous flattening of the power spectrum towards harder energies. I develop a theoretical framework to explore this behaviour, considering both propagation and reflection components, and investigate the nature of the radial emissivity of the accretion flow. Assuming a simple disc-like geometry, I extract the energy dependence of the emissivity, finding it to range from $\overset{\propto}{\sim} R^{-2}$ at energies around the soft excess to $\overset{\propto}{\sim} R^{-4}$ or steeper at harder energies. I attempt to correlate the gradient of the linear function used to parameterise the emissivity index against key AGN parameters but, as yet, the sample size is too small to confirm hints of a correlation with Eddington ratio.

Contents

List of Figures

List of Tables

Declaration of Authorship

I declare that this thesis and the work presented in it is my own and has been generated by me as the result of my own original research.

I confirm that:

1. This work was done wholly or mainly while in candidature for a research degree at this University;
2. Where any part of this thesis has previously been submitted for a degree or any other qualification at this University or any other institution, this has been clearly stated;
3. Where I have consulted the published work of others, this is always clearly attributed;
4. Where I have quoted from the work of others, the source is always given. With the exception of such quotations, this thesis is entirely my own work;
5. I have acknowledged all main sources of help;
6. Where the thesis is based on work done by myself jointly with others, I have made clear exactly what was done by others and what I have contributed myself;
7. Parts of this work have been published as:
   D. I. Ashton and M. J. Middleton. Searching for energy-resolved quasi-periodic oscillations in AGN. *MNRAS*, 501(4):5478–5499, March 2021a,
   Dominic I. Ashton and M. J. Middleton. Constraining Energy-dependent emissivity profiles of AGN inflows [Accepted, awaiting publication upon acceptance of revisions]. *MNRAS*, September 2021b

Signed:.. Date:..................

Acknowledgements

First and foremost, I wish to thank Matt Middleton for his supervision, in which he has shown tireless dedication to the pursuit of new, innovative research and the application of proper scientific method, from which I have learnt so much. I thank him for his unwavering commitment to my work throughout.

I extend my thanks to those in Office 4075, particularly James, Norman, Peter, John and Adam, all of whom have been resolute in their support and fantastic people to work alongside, whether in person or virtually, sharing the good times and a plentiful supply of coffee. I must also thank Miika for his wisdom and generosity, Phil for effectively being the big data/running brother I never had, and of course Seb for basically being the best life/running coach possible.

My time in Southampton has been made by Lordshill Road Runners and those associated with the club, which has served as a family away from home. There are too many individuals to thank, but to those coaches/run leaders and all those in Group F, it's been a pleasure to train and race alongside you, as well as lead the group and be involved on the committee. In particular, I have to thank those in the training group, each of whom have supported me above and beyond what anyone could expect, throughout the PhD and pandemic. Thank you Dave, Jonathan, Doggett, Dan and Chris. Part of me will always bleed the white, red and blue of LRR.

I extend my thanks to those friends beyond Southampton: to Tim, Streeter and G-Man, for all the adventures had over the years, and most of all to Lizzy, thank you for your support and being able to share all the ups and downs with you, as a team. Finally to my parents and sister, for supporting me on this journey from school to PhD study.

List of Abbreviations

ADAF	Advection Dominated Accretion Flow
AGN	Active Galactic Nucleus/Nuclei
AIC	Akaike Information Criterion
BH	Black Hole
BIC	Bayesian Information Criterion
BKNPLC	Broken power law + constant
BLR	Broad-line Region
CCD	Charge Coupled Device
CLT	Central Limit Theorem
DFT	Discrete Fourier Transform
EHT	*Event Horizon Telescope*
EM	Electromagnetic
EPIC	European Photon Imaging Camera
ESA	European Space Agency
EUV	Extreme Ultraviolet
EXOSAT	*European X-ray Observatory Satellite*
FFT	Fast-Fourier Transform
FRMS	Fractional Root-Mean Square
FWHM	Full Width Half Maximum
GMM	Gaussian Mixture Model
GR	General Relativity
GS	Global Significance
HFQPO	High-frequency Quasi-periodic Oscillation
IFFT	Inverse Fast-Fourier Transform
ISCO	Innermost Stable Circular Orbit
LFQPO	Low-frequency Quasi-periodic Oscillation
LHS	Left-hand Side
L-BFGS-B	Limited-memory Broyden-Fletcher-Goldfarb-Shanno
MC	Monte-Carlo
MCMC	Markov Chain Monte-Carlo
MHD	Magnetohydrodynamics
MOS	Metal Oxide Semi-conductor

MRI	Magneto-rotational Instability
NLR	Narrow-line Region
NLS1	Narrow-line Seyfert 1
OM	Optical Monitor
PLC	Power law + constant
pn	positive-negative junction
PSD	Power Spectral Distribution
QPE	Quasi-periodic Eruption
QPO	Quasi-periodic Oscillation
QSO	Quasi-stellar Object
RGS	Reflection Grating Spectrometer
RHS	Right-hand Side
RMS	Root-Mean Square
RPM	Relativistic Precession Model
RXTE	*Rossi X-ray Timing Explorer*
SAS	Science Analysis System
SED	Spectral Energy Distribution
SMBH	Super-massive Black Hole
TDE	Tidal Disruption Event
WA	Warm Absorber
UFO	Ultra-fast Outflow
UV	Ultraviolet
XMM	*X-ray Multi-Mirror Mission*
XRB	X-ray Binary

Chapter 1

Introduction to accretion processes in active galactic nuclei

1.1 Preface

Active galactic nuclei (AGN) have been a substantive topic of both observational and theoretical research in astrophysics for multiple decades, as they provide a unique insight into the extreme physical environments close to a black hole. Despite the progress made in this time however, our current understanding of many of the most important properties of AGN remains significantly limited, and a number of open questions remain on the subject. In this thesis I will detail the work undertaken to explore one such open topic concerning AGN phenomenology: that of high-energy variability in AGN, and the search for quasi-periodic oscillations (QPOs) in AGN X-ray time series.

I will begin by outlining our current state of understanding regarding AGN phenomenology and the accretion physics which underpins it. I will then introduce the Fourier analysis techniques which are central to the time analysis methodologies employed in studying AGN variability throughout this work. With this groundwork in place, the goal of this research is then to address several pertinent questions in the study of AGN, including, but not limited to:

- Are QPOs more readily present in AGN than previously thought, and can these be uncovered with a refined energy resolved search of archived *XMM-Newton* observations?
- What are the underlying characteristics of any detected QPOs; are these consistent between sources and how does this change our understanding of the phenomena in a broader context of accretion physics within AGN?

- What is the energy dependence of measured X-ray variability from AGN, and can this be married with a theoretical framework of the accretion flow which drives it?

1.2 AGN: A brief history

The evolution in the understanding of AGN began in the early 20$^{\text{th}}$ century, with observations of broad emission lines in galaxies made by Edward A. Fath and Edwin Hubble in 1908 and 1926 respectively (Carroll and Ostlie, 1996). Observations made by Carl K. Seyfert, in following decades, recorded a number of galaxies with both these emission lines and distinctly bright nuclear regions – these sources would later take the eponymous name of Seyferts (Seward and Charles, 2010). Although appearing with spectra similar to stellar counterparts (hence the name: Quasi-stellar objects – QSOs), both Schmidt (1963) and Greenstein (1963) identified sources – 3C 273 and 3C 48 respectively – to be at high redshifts, leading to the conclusion that these systems must not only be extragalactic, but also exist with extremely high intrinsic luminosities to be observed at their apparent magnitudes.

To generate the level of radiative power necessary for these objects requires an energetic process capable of producing the most luminous persistent objects ever observed – far exceeding what was capable by stellar nuclear fusion (Seward and Charles, 2010). The mechanism through which the necessary luminosities may be generated, in line with observations, was first proposed by Edwin Salpeter and Yakov Zeldovich in 1964 (Shields, 1999). In this process, known as accretion, material infalls via gravitational attraction onto a super-massive black hole (SMBH) – the compact object present at the centre of galaxies. Lynden-Bell (1969) further proposed that AGN existed in an 'active' state of ongoing accretion, in contrast to other galactic nuclei which were effectively 'dead', now existing in a quiescent state in which accretion is no longer sustained over long timescales.

With the development of new technology, radiative emission from these sources was observed across the broader electromagnetic spectrum, first beyond the optical waveband with the development of radio, and later with the advent of X-ray astronomy (Shields, 1999). The requirement to send X-ray detectors beyond the protective cloak of the Earth's atmosphere limited the first observations to rockets carrying counting instruments, which detected galactic sources of X-rays from the galactic centre, Scorpius constellation (Giacconi et al., 1962), the Crab Nebula (Bowyer et al., 1964) and later from AGN in 3C 273 and M 87 (Friedman and Byram, 1967). The first dedicated X-ray satellite, *Uhuru*, launched in 1970 and performed the first all sky survey across the energy range $2 - 20$ keV (Giacconi et al., 1971), detecting X-rays originating from active

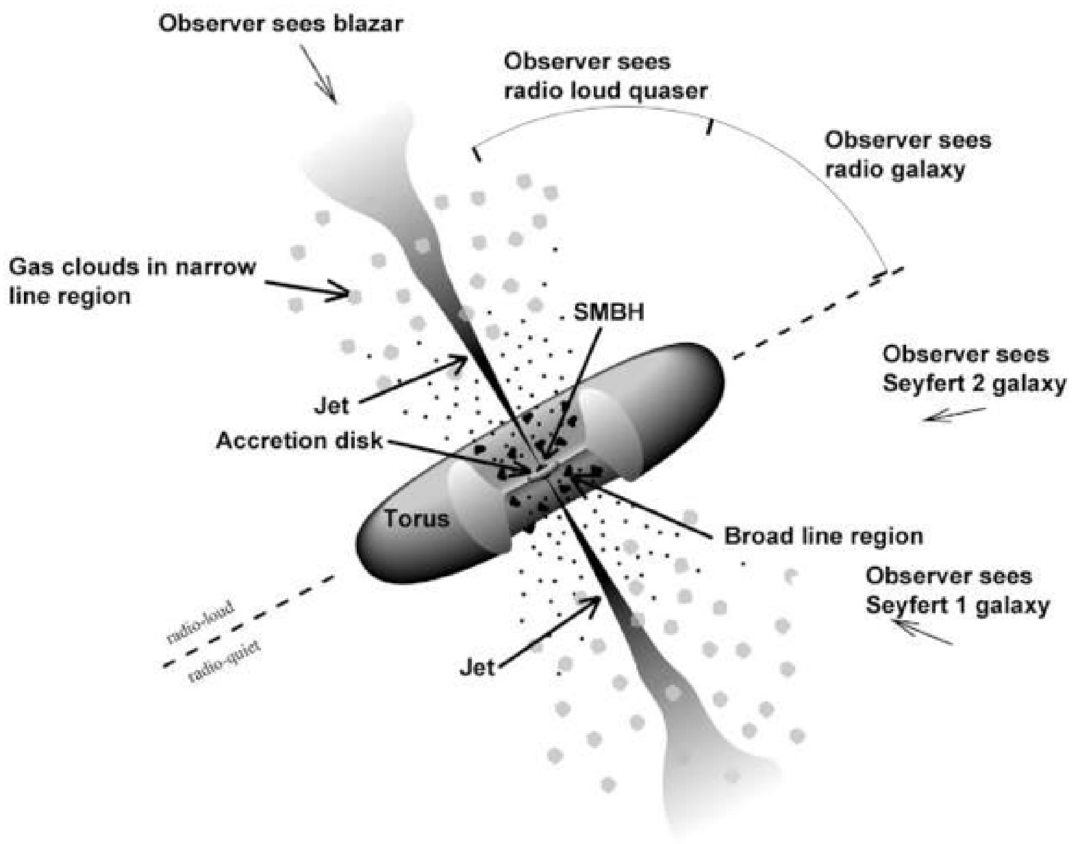

FIGURE 1.1: Illustration of a unified AGN model[1], with subclasses dependent on both viewing angle and observed radio emission.

Seyfert galaxies NGC 1275 and NGC 4151 (Gursky et al., 1971), and establishing the field of detailed AGN study with X-ray observatories.

Our present understanding of AGN X-ray astronomy connects the observational characteristics of AGN to the theoretical underpinnings of complex accretion flows in the inner nuclear regions (Shakura and Sunyaev, 1973; Marshall et al., 1981). X-ray astronomy thus gives a unique insight into the accretion physics ongoing in a strong gravity environment and associated high energy phenomena, including complex variability patterns observed in AGN (Lawrence et al., 1987). This chapter is therefore focused on outlining both the types of AGN and radiative processes which occur in these systems, to understand the nature of AGN variability in further detail.

1.3 AGN taxonomy

The wide-ranging diversity of AGN is built upon the observation, or non-observation, of several key features of any given source (e.g. radio-loud, radio-quiet, broad optical/UV lines etc. – see e.g. Antonucci 1993). The consequence is the formation of an

[1] https://fermi.gsfc.nasa.gov/science/eteu/agn/

effective 'zoology' of AGN, constructed from a protracted list of AGN subclasses which match each given criteria. Attempts to unify this zoology of AGN species into a simplified model are predominantly based on the viewing angle of the observer relative to the source (e.g. Antonucci 1993; Krolik 1999; Seward and Charles 2010).

Figure 1.1 illustrates the fundamental composition of an AGN in the unified model. Within the central region of the AGN lies the SMBH surrounded by an accretion disc of infalling gas, in a system which acts as the central engine of radiative electromagnetic (EM) emission. Jets of accelerated ionised material – launched outwards from this central region, where the base of the jet has been theorised to originate, see e.g. Blandford et al. 2019 – are also observed in some AGN.

Scaling out to a ∼few parsecs, the central region is enveloped by an expansive dusty 'torus' (although the geometry of this component is a subject of debate, see e.g. Hönig and Beckert 2007; Hönig 2019). The dusty torus absorbs emission from the inner region and re-radiates this predominantly in the infrared. AGN observed from an 'edge-on' viewing angle, i.e. along the line-of-sight through the torus, are principally obscured in the high energy X-ray waveband, as the inner regions are concealed. These sources are known as Compton thick AGN – see reviews: e.g. Matt 2002; Comastri 2004.

The broad-line region (BLR) exists in a geometry close to the accretion disc, and within the torus (see Figure 1.1). The BLR is understood to produce broad (FWHM $\sim$ 5000 km s^{-1}) optical/UV spectral lines (e.g. Balmer lines) observed in some AGN (Peterson, 2006). The nature of the BLR itself is a subject of debate, with 'cloud' models proposing a clumpy gas structure close to the accretion disc. The observation of smooth broad lines and lack of granular structure at high spectral resolution suggests that the BLR is extremely dense or part of a continuous flow of gas, not simply a discrete, unchanging cloud structure (Peterson, 2006; Czerny and Hryniewicz, 2011). The origin of the BLR may therefore be, in part, tied to dusty winds launched from the disc through magnetic or radiation pressure, creating a dynamic system of inflows and outflows (Czerny and Hryniewicz, 2011). Similarly, observed narrow (FWHM $\sim 200 - 500$ km s^{-1}) spectral lines (e.g. the [O_{III}] λ5007Å forbidden line) are ascribed to nebulous material in the narrow-line region (NLR), located at a greater extent from the accretion flow and BLR (see Figure 1.1), such that it is possible to spatially resolve the NLR in certain cases (Bennert et al., 2006; Groves, 2007).

In categorising AGN, a primary distinction between sources is that of observed radio emission, with 'radio-loud' AGN accounting for a small fraction (estimated at $\sim 10 - 15\%$, see e.g. Katgert et al. 1973; Fanti et al. 1977; Smith and Wright 1980) of the total AGN population. The distinction between 'radio-loud' and 'radio-quiet' AGN is made on the basis of the observed ratio of radio to optical flux, which is found to be close to unity in radio-quiet, and considerably higher in radio-loud sources (Kellermann et al., 1989). The origin of radio emission in AGN is associated with jets launched from the inner regions (Krolik, 1999), which in some cases can result in the formation of extended 'radio lobes' in a majority of radio-loud AGN, which have been resolved to hundreds of kiloparsecs out from the galactic centre (Antonucci, 1993) – but these are not strictly ubiquitous. The Fanaroff-Riley classification (Fanaroff and Riley, 1974) is used to categorise radio galaxies based on the radio luminosity of the local environments, with FR-I galaxies defined as brightest towards the central galaxy, with flux from the extended radio lobes rapidly diminishing with distance (i.e. edge-darkened), and FR-II galaxies being those that show most luminous emission from the radio lobes (i.e. edge-brightened).

A similar characterisation is made using optical/UV spectroscopic line profiles, which defines Type 1 AGN as those showing both broad line and narrow line features (i.e. BLR and NLR are both observable), whereas Type 2 AGN are those observed with only narrow lines (BLR is obscured) – as expected from low ('face on') to high ('edge on') inclinations to the source (Antonucci, 1993; Carroll and Ostlie, 1996). Type 0 AGN are those observed at the most extreme 'face on' viewing angle, i.e. when effectively observing down the jet, and are typically characterised by flat spectral emission (e.g. in flat-spectrum radio quasars) as well as extreme (relativistically boosted) emission extending into the gamma-ray waveband (see e.g. Chadwick et al. 1999, Brown 2013).

The term 'quasar' is now most frequently used to describe AGN at high redshifts (e.g. typically $z > 2$), whilst the aforementioned 'Seyferts' (both Type 1 and 2) is a term used to describe radio-quiet sources that exist at lower redshifts, i.e. in the more local universe. Seyferts are specifically of interest in this work as they are known to exhibit significant X-ray variability (e.g. Lawrence et al. 1987, Vaughan and Uttley 2005), in addition to being typically observed with higher apparent magnitude/signal-to-noise ratios, due in part to their relative proximity.

X-ray variability and high signal-to-noise ratios are both commonly apparent in a subtype of Seyfert 1 AGN called Narrow-line Seyfert 1s (NLS1s), which are observed with the narrowest (Balmer) broad-lines (FWHM $\lesssim$ 2000 km s^{-1}) amongst Seyfert 1s (Osterbrock, 1989; Goodrich, 1989), and a strong anticorrelation between the strengths of the [O_{III}] and [Fe_{II}] spectral lines (Boroson, 2002). NLS1s are typically observed to be highly variable in both the X-ray and optical regimes, and are believed to host low-mass SMBHs, exhibiting high accretion rates (Mathur, 2000; Fabian et al., 2002). The study of NLS1s (and AGN more generally) suffers from observational bias however, in that brighter sources (such as those with higher accretion rates) are more likely to be observed. Hence, although prime candidates in timing analyses due to their prominent X-ray variability, this subset of observed AGN may not represent a true random sample of the AGN population at large.

1.4 Black holes

SMBHs ($\sim 10^6 M_\odot - 10^{10} M_\odot$) are thought to be ubiquitous in the nuclei of galaxies, although the formation process is not well understood. Possible genesis pathways include the merger of multiple 'seed black holes' in a proto-galaxy, initially formed from massive stars (Rees, 1984) – which gravitationally collapse into stellar mass black holes (BHs) ($\sim 10 M_\odot$) following the exhaustion of their fuel used for internal nuclear fusion – and the direct collapse of gas clouds in galactic dark matter haloes, through dynamical instabilities (Begelman et al., 2006). The result, in principle, is a compact object with all its mass concentrated at an infinitesimally small point, or singularity, at its centre. The extreme gravity region around a black hole can be well described by Einstein's equations of General Relativity (GR), which can be used to illustrate the existence of an effective radius at which the curvature of space-time around a black hole is sufficient for light itself to be unable to escape: the event horizon (Schwarzschild, 1916; Kerr, 1963).

Although termed 'black holes' due to this absorption of light, and thus rendering them near-invisible in the EM spectrum (with theoretical black-body radiation from a black hole, known as Hawking radiation, being a negligible effect – see Hawking 1974, Hawking 1975), there are numerous methods capable of observing both BHs and SMBHs indirectly. In binary systems, these include measurements of the radial velocities (e.g. Corral-Santana et al. 2016) or astrometric measurements of the characteristic 'wobble' detectable in an orbiting companion star (e.g. with *GAIA* – Mashian and Loeb 2017), allowing for the mass of the compact object to be constrained and the presence of a black hole inferred. Measurements tracing stellar motion around the central mass of Sgr A* in the galactic centre also infer the presence of a gravitational attractor, as expected of a central SMBH (Eckart et al., 2002). Moreover, recent innovations have allowed for more direct methods of detecting black holes; the first in 2016 being the observation of the merger of a black hole binary pair (LIGO Scientific Collaboration and Virgo Collaboration, 2016), using *LIGO* to detect ripples of propagating space-time, known as gravitational waves. This heralded the dawn of gravitational wave astronomy; offering new insights into studying previously undetectable black hole interactions. The second result, published in 2019, is that of the now famous 'direct' observation of the black hole shadow within M87 using radio interferometry with *EHT* (Event Horizon Telescope) (see Event Horizon Telescope Collaboration 2019a, Event Horizon Telescope Collaboration 2019b).

In terms of mass accretion onto a black hole, both BHs and SMBHs can be observed in a state of active accretion, thus in principle undergoing the same physical processes related to accretion within an extreme gravity environment; a concept which forms the basis of the mass invariance principle in accretion physics. On a smaller scale, accretion is observed in X-ray binaries (XRBs), where material from a companion star accretes onto a compact object (typically a black hole, neutron star or white dwarf – Done et al. 2007a). The mass scaling principle then considers AGN to be 'scaled up' versions of black hole XRBs, with the same underlying physics acting over timescales which scale inversely with mass (McHardy et al., 2006). Demonstrating this scale invariance remains an important area of research into the nature of accretion physics.

Black holes on a fundamental level are remarkably simple systems, and following the 'no hair theorem' may be described entirely by the observable parameters of mass, spin and charge. As black holes on a macroscopic scale are electrically net neutral, charge is of no relevance, but their mass and spin impact the characteristics of the surrounding region (Middleton, 2016).

The spin of a black hole relates to the angular momentum, $\mathbf{J}$, of a black hole of mass M. In its dimensionless form, it is represented by:

$$a_* = \frac{|\mathbf{J}|c}{GM^2} \tag{1.1}$$

and is effectively maximal at $|a_*| = 0.998$ (Thorne, 1974), due to the increased capture cross section of photons with momentum aligned *opposite* to the BH spin, which then act as a physical buffer such that $|a_*|$ cannot reach unity (Bardeen et al., 1973). The accretion of material onto the black hole imparts a change of angular momentum, such that accretion in a prograde orbit with the black hole causes the black hole to 'spin-up', and offers a mechanism through which the effective maximal spin may be approached. By extension, the accretion of material in a retrograde orbit (such as the aforementioned opposite momentum aligned photons) causes the black hole to 'spin-down' (Volonteri et al., 2013).

A black hole of spin zero, $a_* = 0$, follows the Schwarzschild solution to the GR equations, where the innermost stable circular orbit (ISCO) of a massive particle in motion around the black hole exists at $6GM/c^2 = 6R_g$ (Schwarzschild, 1916). The Schwarzchild metric in GR becomes inadequate with non-zero spins, where instead the Kerr metric is employed (Kerr, 1963). In this solution of GR the radius of the ISCO is tied to the spin, through the equations (Bardeen et al., 1972):

$$r_{isco} = M\left[3 + Z_2 \pm \sqrt{(3 - Z_1)(3 + Z_1 + 2Z_2)}\,\right]^2 \tag{1.2}$$

for both prograde spins $(-)$, and retrograde spins $(+)$, where:

$$Z_1 = 1 + \sqrt[3]{1 - a/M}\left[\sqrt[3]{1 + a/M} + \sqrt[3]{1 - a/M}\right], \quad Z_2 = \sqrt{3a^2/M^2 + Z_1^2} \tag{1.3}$$

such that a 'maximally' prograde spinning black hole has the ISCO reduced towards $\sim 1.25R_g$, while a 'maximially' retrograde spinning black hole pushes the ISCO out towards $9R_g$. The location of the ISCO represents the idealised inner boundary for stably orbiting material around a black hole, and represents the effective inner boundary of the accretion disc, beyond which material spirals inwards towards, and over, the event horizon. The horizon is the radius of no return, and material at this point plunges into the depths of the gravitational well.

1.5 Accretion

The accretion of matter onto a SMBH produces the electromagnetic emission from AGN. Energy is liberated from a particle in the conversion of gravitational potential energy to other forms of energy (e.g. kinetic, thermal) as material passes through the gravitational potential surrounding the black hole. The total luminosity output from this process depends on the accretion rate $\dot{M}$ of material and accretion efficiency η:

$$L = \eta \dot{M} c^2 \tag{1.4}$$

For the case of spherical accretion, the theoretical limit to the accretion rate is defined as the point at which the gravitational pull on infalling material is balanced by the radiation pressure projected outwards from the black hole. In the case of pure hydrogen as the accreting material, the luminosity of this *Eddington limit* is defined numerically as:

$$L_{Edd} = \sim 1.3 \times 10^{38} \frac{M}{M_{\odot}} \text{erg s}^{-1} \tag{1.5}$$

The accretion rate in AGN may often be expressed in units of Eddington, using the ratio L_{bol}/L_{Edd}, with the bolometric luminosity, L_{bol}, defined as the output luminosity over all wavelengths. The assumptions made in computing the Eddington limit do not hold for a non-spherical accreting body of non-pure atomic hydrogen, and allows these limits to be bypassed in a physical accretion system. Should this ratio exceed unity, the source is considered to be in a *super-Eddington* accretion state.

In physical systems, material does not accrete spherically, but instead through an accretion disc, which is formed of material which coalesces along the orbital plane. Material can move through the accretion disc through the conservation of angular momentum, which allows for an inward flow of matter towards the black hole and subsequently down the gravitational potential well, given an equal amount of angular momentum is transferred out through the disc. The mechanism by which angular momentum is transferred is related to viscous dissipation throughout the fluid flow, but remains poorly understood (Pringle, 1981). Multi-scale turbulence acts as the effective viscosity in the disc, and on Kolmogorov microscales is manifested as random particle motions (e.g. see Kolmogorov 1941; Kolmogorov 1962), which convert the bulk motion of material into thermal energy on particle scales. The leading mechanism thought capable of producing the magnitude of viscosity required to dissipate sufficient angular momentum is that of the Magnetic-Rotational Instability (MRI) (see e.g. Balbus and Hawley 1991; Balbus and Hawley 1992). The MRI acts through the interaction of weak magnetic fields with ionised material within the fluid flow produces a sheer stress of sufficient magnitude to transfer angular momentum outwards through the disc and form a stable disc. These concepts are detailed further in a review by Blaes (2014).

1.5.1 Thin accretion discs

Shakura and Sunyaev (1973) first proposed the thin disc approximation, whereby an accretion disc is considered geometrically thin, optically thick, in a steady state (constant local accretion rate) and in thermal equilibrium. In this model the fluid viscosity, v, is driven by turbulence and is defined as:

$$v = \alpha c_s h \tag{1.6}$$

which relates the sound speed through the disc, c_s, to the scale height of the disc, h, and the dimensionless viscosity scaling parameter α, where $0 \leq \alpha < 1$. This disc approximation is equivalently known as an α-disc model. No universal value for α is determined, but is commonly considered to be $\alpha \sim 0.01 - 0.1$ (Frank et al., 2002). α effectively quantifies the turbulence acting on accreting material (i.e. through the MRI), and thus relates to the differential viscous torques acting on material throughout the disc. As these torques result in viscous dissipation and the loss of mechanical energy in the material, the magnitude of α is responsible for the amount of internal heating of the disc, as this mechanical energy is transferred into thermal energy on Kolomogorv scales (Frank et al., 2002).

In the simplest, non-relativistic case, the torque, τ_ϕ, acting on circular rings of gas (with area $2\pi R$), takes the form:

$$\tau_\phi(R) = 2\pi R v \Sigma R^2 \Omega' \tag{1.7}$$

for a kinematic viscosity, v, surface density $\Sigma = \rho h$, and angular velocity, Ω (Frank et al., 2002). The rate of mechanical energy loss is given by $\tau_\phi \Omega' dR$, (where Ω' is the rate of change of angular velocity) over a ring of width dR. Considering both faces of the disc, the energy loss per unit area, or flux, $f(R)$, is defined by:

$$f(R) = \frac{\tau_\phi \Omega'}{4\pi R} = \frac{1}{2} v \Sigma R^2 \Omega'^2 \tag{1.8}$$

For a conceptual solid body disc, undergoing rigid rotation, $\Omega' = 0$ and thus any differential torque vanishes, which results in zero flux from the disc. Instead considering a Keplerian disc, such that angular velocity $\Omega_K = \sqrt{\frac{GM}{R^3}}$, the flux then goes by:

$$f_K(R) = \frac{9}{8R^3} v GM\Sigma \tag{1.9}$$

Following the conservations of mass and angular momentum, as detailed in Section 5.3 of Frank et al. (2002), and assuming the torque reaches zero $(\Omega' = 0)$ at the inner edge of the disc, the form of $\nu\Sigma$ can be obtained:

$$\nu\Sigma = \frac{\dot{M}}{3\pi}\left[1 - \left(\frac{R_{isco}}{R}\right)^{1/2}\right] \tag{1.10}$$

and thus equations 1.9 and 1.10 combine to give the common form of flux from the disc:

$$f_K(R) = \frac{3GM\dot{M}}{8\pi R^3}\left[1 - \left(\frac{R_{isco}}{R}\right)^{1/2}\right] \tag{1.11}$$

which highlights two key results. The first being that the flux from the disc is dependent on radius, R, mass, M and mass accretion rate, $\dot{M}$, but crucially *not* viscosity, v. The observed flux does not require a detailed understanding of the viscosity then, to determine other properties of the accretion disc. Secondly, it shows that with these assumptions, the flux, $f(R) \propto R^{-3}$, for $R > R_{isco}$, and that the inner disc is responsible for relatively more flux emission than the outer disc.

The flux can then be used to determine the luminosity produced by the disc between radii R_1 and R_2:

$$L(R_1, R_2) = 2\int_{R_1}^{R_2} f(R) 2\pi R dR \tag{1.12}$$

Assuming the disc to be optically thick to thermal emission, the local emission from the disc should be described by a black-body spectrum, with effective temperature, T_{eff}. In this case, Stefan-Boltzmann's law applies, such that the flux directly relates to T_{eff} by:

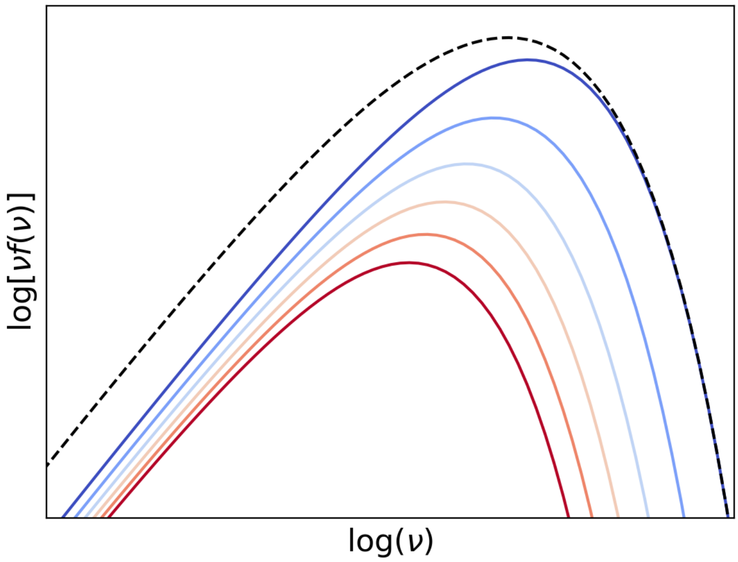

FIGURE 1.2: Multi-colour black-body disc spectrum formed of a superposition of individual black-body emission spectra, from individual annuli across the accretion disc. Increasing frequency corresponds to increasing temperature; closer to the black hole.

$$f(R) = \sigma T_{eff}^4 \tag{1.13}$$

which then yields the relation:

$$T^4 = \frac{3GM\dot{M}}{8\pi R^3 \sigma}\left[1 - \left(\frac{R_{isco}}{R}\right)^{1/2}\right] \tag{1.14}$$

and a $T \propto R^{-3/4}$ temperature-radius relationship across the disc. This demonstrates that the temperature increases closer to the black hole. As shown in Figure 1.2, the full (multi-colour) disc black-body spectrum is then formed from a superposition of black-body spectra, each corresponding to the effective temperature of a given local annulus of the disc (e.g. Mitsuda et al. 1984). As is evident, this emission increases in energy (emitting at a higher EM frequency, ν) closer to the black hole. Here, Wien's Law can then be applied to determine the peak wavelength, λ_{max} of the full black-body distribution (which is close to the temperature at the ISCO, T_{isco}):

$$\lambda_{max} = \frac{\sim 2.9 \times 10^{-3}\ \mathrm{K\ m}}{T_{isco}} \tag{1.15}$$

which corresponds to the UV waveband across an AGN disc. The reduced physical scale of an XRB disc decreases the peak thermal wavelength correspondingly, such that for an XRB it lies in the X-ray waveband.

The effective temperature assumes the photons are produced in the mid-plane of the disc, and does not take into account the interaction of these photons before emission from the surface of the disc. This final, emitted temperature is known as the colour temperature, T_{col}, and deviates from T_{eff} by a colour correction/spectral hardening factor, f_{col} (Mitsuda et al., 1984; Makishima et al., 1986), defined as:

$$T_{col} = f_{col} T_{eff} \tag{1.16}$$

f_{col} arises from opacity within the disc, both from electron scattering, κ_T and absorption, κ_{abs}. f_{col} can then be approximated by a ratio of the opacities, where $\kappa_{tot} = \kappa_T + \kappa_{abs}$ (Davis et al., 2006):

$$f_{col} = \left(\frac{\kappa_{tot}}{\kappa_{abs}}\right)^{1/4} \tag{1.17}$$

Adopting the colour temperature correction results in the spectral hardening of the multi-colour black-body spectrum (as in Figure 1.2), effectively shifting the black-body spectra to higher energies.

1.5.1.1 Accretion timescales

In the thin disc approximation, it is possible to determine the timescales over which physical processes occur (Frank et al., 2002). The dynamical timescale, t_{dyn}, is the time it takes for a point mass particle to complete an orbit of the disc, assuming Keplerian orbital dynamics:

$$t_{dyn} = 2\pi\sqrt{\frac{R^3}{GM}} \tag{1.18}$$

Considering now the radius in terms of R_g units, such that $R = rR_g = r\frac{GM}{c^2}$, it follows that the dynamical timescale scales linearly with mass:

$$t_{dyn} = \frac{2\pi r^{3/2}}{c^3} GM \;\rightarrow\; t_{dyn} \propto M \tag{1.19}$$

The viscous timescale, t_{vis} corresponds to the time it takes a particle to pass through the disc and fall into the black hole. It is related to the dynamical timescale by (Frank et al., 2002):

$$t_{vis} = \frac{R^2}{\alpha h^2} t_{dyn} \tag{1.20}$$

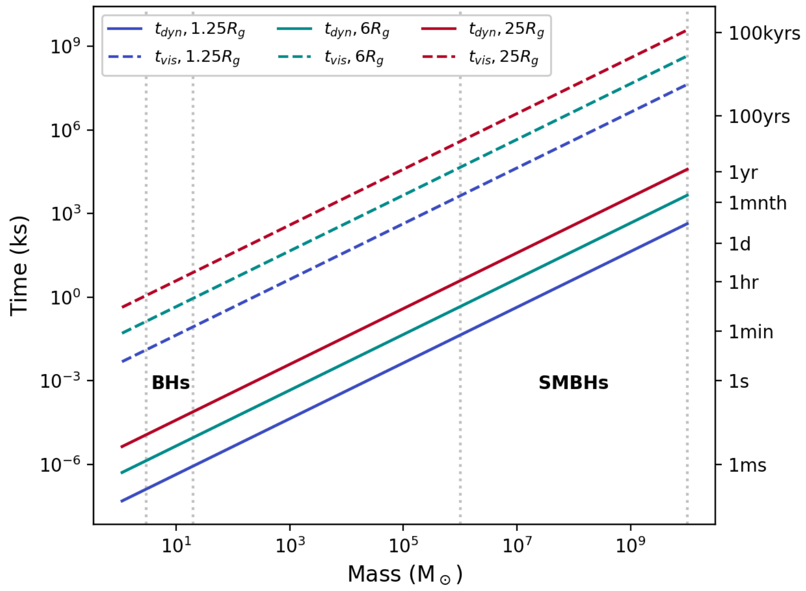

FIGURE 1.3: The linear mass scaling of dynamical and viscous accretion timescales for a thin disc, assuming $\alpha = 0.1$ and $h/R \sim 0.01$, at three radii of interest, 1) $1.25R_g$: the ISCO of a maximally spinning black hole, 2) $6R_g$: the ISCO of a zero spin black hole and 3) $25R_g$: an example of an outer radius. These timescales are calculated over a large range of possible black hole masses, with a highlighted approximate stellar BH mass range of $3 - 20M_\odot$ and SMBH mass range of $10^6 - 10^{10}M_\odot$.

and thus the viscous timescale at some disc annulus is longer in a disc with a low viscosity parameter α and small scale height h. For some disc with these parameters, the viscous timescale also increases with radial extent, R, across the disc.

Figure 1.3 demonstrates the linear scaling of both dynamical and viscous timescales with increasing SMBH mass, across a range of radii, in units of R_g. It is immediately evident that the viscous timescales are several orders of magnitude above the dynamical timescales, and that these timescales decrease with radius. For low mass SMBHs ($\sim 10^6 M_\odot$), dynamical timescales correspond to periods of $\sim$ hour, and viscous timescales correspond to periods $\sim$ months-years.

1.5.2 Thick discs

The true nature of AGN accretion discs does not fit neatly into this simple thin-disc framework. Building on the thin-disc prescription by Thorne (1974) and Page and Thorne (1974) in the context of GR, Fishbone and Moncrief (1976), Kozlowski et al. (1978) and Abramowicz et al. (1978) motivated disc models in which the accretion discs are required to have a finite thickness. This is motivated by both gas and radiation pressures generated within the disc, which act to 'puff' out the disc; increasing the scale height beyond the thin disc assumptions of Shakura and Sunyaev (1973). These pressures, and thus the scale height of the disc, are tied to both the accretion rate, $\dot{M}$,

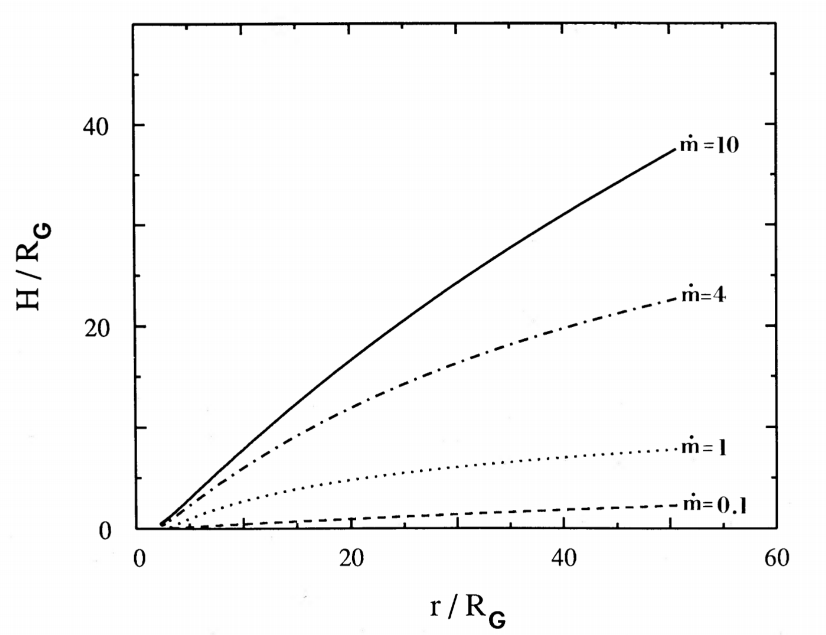

FIGURE 1.4: The accretion disc scale height, h/R_g across the radius of the disc, considering a range of accretion rates in terms of Eddington ratios, $\dot{M}$ and a fixed opacity. Original from Abramowicz et al. (1988).

and the opacity in the disc. The higher the opacity, the greater the abundance of radiation pressure within the disc, which increases with the number of bound-bound (absorbed photon; no ionisation) and bound-free (absorbed photon; ionisation) transitions – which arise from the abundance of UV radiation in the disc These effects act to divert the accretion disc away from 'razor-thin' ($h \sim 0$) disc models at $\dot{M} \gtrsim 0.1 - 1\dot{M}_{Edd}$, into what is generally considered a 'slim disc' model, with non-negligible scale height (Abramowicz et al., 1988; Jiang et al., 2016; Taylor and Reynolds, 2018a). Similarly it is argued that true 'thick discs' with scale height, $h \sim R$ exist at super-Eddington accretion rates, $\dot{M} \gtrsim \dot{M}_{Edd}$ (see e.g. Poutanen et al. 2007). Abramowicz et al. (1988) used the accretion disc equations in Paczynski and Bisnovatyi-Kogan (1981), to yield the positive correlation between accretion rate and scale height, for a fixed opacity, as shown in Figure 1.4.

A separate mechanism which can drive the scale height of the AGN disc is that of advection. Advection describes the the bulk transfer of energy through the fluid flow, when material in the disc is unable to radiate efficiently and thus cannot properly thermalise (Frank et al., 2002). As such, photons cannot easily escape the material and are swallowed by the black hole before they can be radiated (see Begelman 1978 who describes this with an effective 'trapping radius'). In extreme cases this process can form what is known as an advection dominated accretion flow (ADAF). ADAFs are thought to be able to form in both cases of very high accretion rates, where high density material, with high opacity, causes a reduced radiative efficiency in the flow as photons cannot escape, and also at low accretion rates, where low density hot material in the disc (i.e. a nebulous 'corona' of high energy electrons – see Section 1.6.1) cannot thermalise efficiently and this material is swallowed by the SMBH (Narayan et al., 1998). The radiative processes in ADAFs result in an 'inflated' accretion disc, unlike that of a Shakura and Sunyaev (1973) thin disc, which requires thermalisation across the accretion flow (e.g. see Narayan and Yi 1994; Narayan and Yi 1995; Narayan et al. 1998).

In the case of ADAFs, the nature of the radiative emissivity, $\epsilon(R)$, changes from the one derived from a thin disc, and both $\epsilon(R)$ and the emitted flux do not follow the R^{-3} dependence of equation 1.11. Narayan and Yi (1994) and Watarai and Fukue (1999) derived the radial dependence of the effective temperature to follow $T_{eff} \propto R^{-1/2}$ in an advection dominated disc. As laid out in Watarai et al. (2000a), by requiring hydrostatic equilibrium along the vertical plane of the disc gives $\Omega H \propto R^{-1}$, and combining with the radial relations in Kato et al. (1998), whereby $\Omega \propto R^{-3/2}$ which relates to the pressure, p and density ρ by $\Omega \propto \frac{p}{\rho} \propto R^{-3/2}$; $H \propto R$; $\rho \propto R^{-1/2}$, it then follows $T_{eff}^4 \propto p/H\rho \propto R^{-2}$. The emissivity in the advection dominated case then goes by $\epsilon(R) \propto R^{-2}$, and the effective temperature $T_{eff} \propto p/H\rho \propto R^{-1/2}$.

1.5.3 Outflows

Soft X-ray absorption in the line of sight of AGN was first detected by Halpern (1984), and this 'warm absorber' (WA) feature has subsequently been detected in $\sim$ 50% of Seyfert 1 galaxies in an study of *ASCA* spectra, modelling absorption edges of O VII, O VIII lines (Reynolds, 1997; George et al., 1998). WAs have since been observed to feature blue-shifted ($\sim 100 - 1000$ km s^{-1}), ionised narrow-absorption lines (Kaastra et al., 2000; Kaspi et al., 2000). This suggests they are outflows of material along the line of sight. A range of ionisation states have been observed in warm absorbers, particularly in iron (Sako et al., 2001; Reeves et al., 2004). Blustin et al. (2005) conclude the WAs are most likely an outflow from the dusty torus, with higher ionisation states perhaps corresponding to an origin closer to the accretion disc. The driver of these winds is not well constrained, with models including magneto-rotational models (Fukumura et al., 2010), thermally driven, X-ray heated models (Begelman et al., 1983) and radiation pressure models (Murray et al., 1995; Proga et al., 2000; Proga and Kallman, 2002).

In addition to observations of WAs are observations of broad emission lines in quasar atomic spectra (e.g. H I, O VI, N V, C IV, and Si IV) (Osterbrock, 1989; Blandford, 1990), suggesting Doppler broadening in gas moving at high velocity close to the accretion disc. Moreover, broad absorption lines in highly ionised gas (e.g. [N V], [C IV], and [Si IV]) (Proga et al., 2000) are observed to be blue-shifted from the galactic nucleus at velocities reaching $60,000$ km s^{-1} (Tombesi et al., 2013). The blue-shifting again suggests an outflow of material, but now at 'mildly' relativistic velocities with an mean observed mean velocity $\sim 0.1c$ Tombesi et al. (2013), and therefore these winds are termed as ultra-fast outflows (UFOs). Tombesi et al. (2011) constrained the origin of

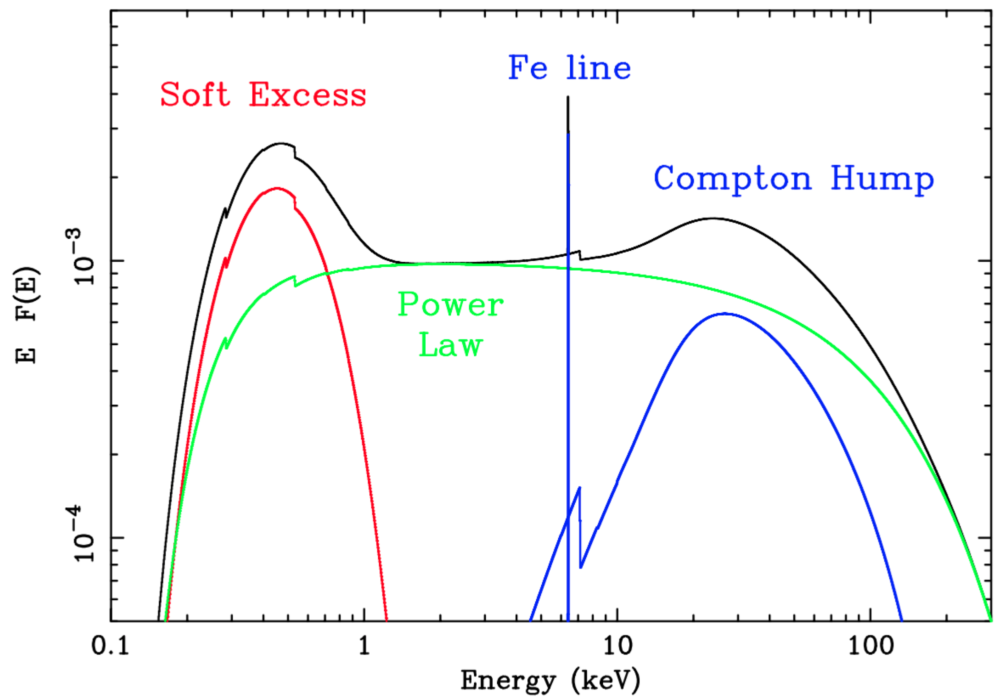

FIGURE 1.5: A generalised AGN spectral energy distribution in black, with highlighted soft excess (red), Comptonisation power law (green) and reflection (blue) components across $\sim 0.1 - 100$ keV. Original from Fabian (2006).

UFOs to sub-parsec scales from the SMBH and are thus argued to be compatible with outflows from the accretion disc itself (King and Pounds, 2003; Proga and Kallman, 2004; Sim et al., 2010). A powerful acceleration mechanism is required to produce the high velocities observed in UFOs. Tombesi et al. (2013) found a linear relation between outflow momentum and momentum of the radiation field, connecting the power of outflows to the accretion rate.

1.6 AGN X-ray spectra

The spectral energy distribution (SED) of an AGN describes its output luminosity as a function of energy. The broad X-ray energy spectrum (i.e. $\sim 0.1 - 100$ keV), as generalised in Figure 1.5, may be described by a combination of components, namely the power law (Compton continuum), reflection and soft excess. Here, Figure 1.5 is plotted in $EF(E)$ units.

An understanding of these components forms the basis for the X-ray spectral models discussed in later chapters, with models constructed using the XSPEC software package (Arnaud, 1996).

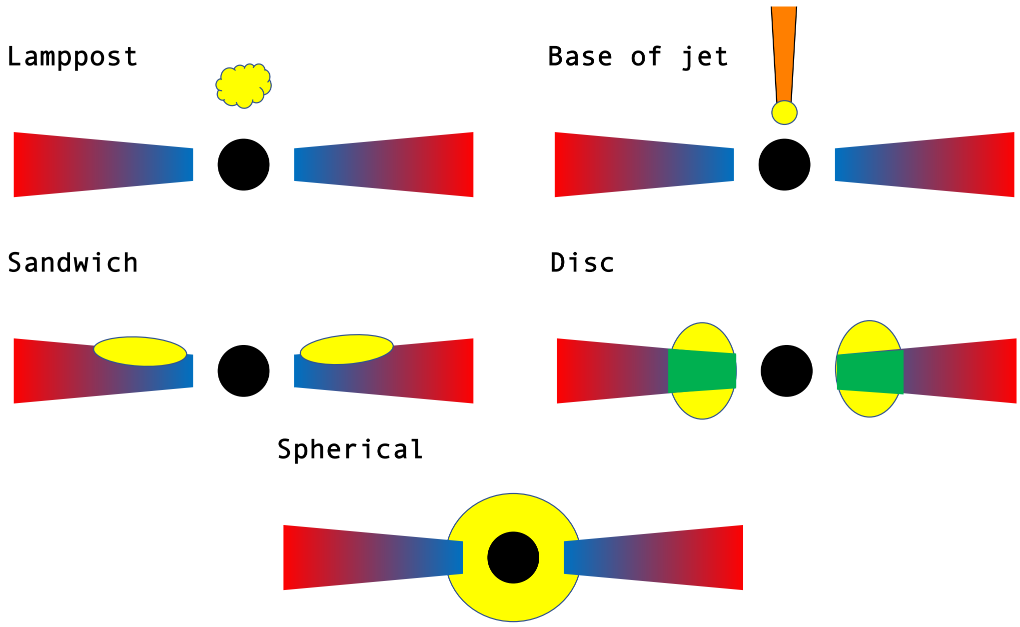

FIGURE 1.6: AGN coronal geometries (corona in yellow), including a point-source lamppost, base of jet, sandwich, inner-disc, and spherical, geometries.

1.6.1 The corona

X-rays are produced in AGN when lower energy photons radiated from the disc interact with and scatter off a population of high energy electrons, in a process of inverse Compton scattering (Sunyaev and Titarchuk, 1980). This electron population likely takes the form of a plasma corona somewhere close to the black hole, but the origin, structure and nature of this corona are fiercely debated topics.

1.6.1.1 Coronal geometries

Multiple coronal geometries have been proposed and investigated, with the primary candidates sketched out in Figure 1.6, and each considered here individually.

- Lamppost: To first order, the corona has been considered as a point source suspended at height h above the black hole – orthogonal to the accretion disc – in a geometry known as the 'lamppost' model (see e.g. Martocchia and Matt 1996; Reynolds and Begelman 1997; Taylor and Reynolds 2018a). The relative simplicity of this model is evidenced by recent studies (see e.g. Reis and Miller 2013; Fabian et al. 2015) which argue for a compact corona, close to the SMBH. Photons scattered isotropically from such a corona can either escape the accretion system, and be observed as intrinsic emission, or re-radiate the disc (which produces the reflection spectrum, see Section 1.6.2). For a corona sufficiently close to the black hole, the local strong-gravity environment would allow for light-bending of photon paths to focus the majority of the radiation emission onto the inner disc.

A complication of the lamppost model is the physical motivation underpinning the proposed geometry. Key to this is requiring a mechanism for producing the 'cloud' of electrons which form the corona, and an agency for keeping the corona approximately stationary, so close to the SMBH. It is commonly assumed this is possible through the action of magnetic fields, perhaps produced from a magnetic dipole close to the black hole, or suspended on the base of a jet (see Merloni and Fabian 2001; Fabian et al. 2015). This also applied extensions to this model including a double lamppost (two, distinct sources) system (Chainakun, 2019). Clearly, the true physical picture is likely complex beyond any simple model and perhaps non-identical between AGN.

- Base of Jet: Merloni and Fabian (2002) consider the corona in AGN being the base of a jet, which is launched close to the black hole. The launching mechanism is associated to magnetohydrodynamic (MHD) action, which can carry powerful, magnetic driven outflows from the disc. This mechanism and geometry is considered most applicable in low accretion rate systems, with the coronal power scaling inversely with radiation pressure from the disc, due to increased magnetic energy density and effective viscous stresses in high total pressure, high accretion rate environments (Merloni and Fabian, 2002).

- Sandwich: In contrast, Di Matteo et al. (1997) coined the term 'sandwich' corona, to illustrate a model where the hot corona is active in thin sheets of thermal electrons lying on-top of a cool, thin accretion disc, effectively 'sandwiching' the black hole between two coronal regions (see Figure 1.6). This followed from previous studies (see e.g. Haardt and Maraschi 1991; Haardt and Maraschi 1993; Hua and Titarchuk 1995) and has the thin corona supported by tenuous magnetic fields permeating through the accretion disc.

- Disc: Done and Kubota (2006) propose an inner-disc geometry, where a corona of constant opacity effectively forms part of the inner accretion disc, truncating the full disc (see Figure 1.6). Of the segmented disc, the cooler outer disc, at $R > R_{corona}$, emits as a colour-corrected black-body (Done et al., 2012), and the hot inner disc, at $R < R_{corona}$, emits via Compton upscattering of cool photons from the outer disc.

- Spherical: A spherical coronal geometry is a simple, commonly assumed model (see e.g. Raginski and Laor 2016; Fabian et al. 2017; García et al. 2019; Chainakun et al. 2019) in which the corona of uniform density and fixed temperature envelopes the black hole, with uniform radius and opacity. This satisfies the need for a compact corona close to the SMBH (Reis and Miller, 2013; Fabian et al., 2015) but again

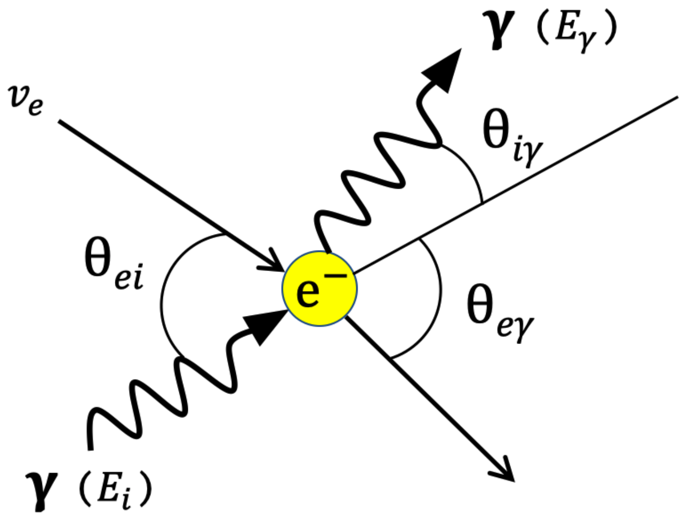

FIGURE 1.7: Basic Compton scattering schematic, showing the scattering of a photon off an electron with initial velocity, v_e. The energy of the scattered photon is then given by equation 1.21.

requires a mechanism, such as magnetic fields, to support this structure, similar to the lamppost model.

1.6.1.2 Compton scattering

For any given coronal geometry, the photon scattering from the electrons in the corona can be understood with the mathematics of Compton scattering (Compton, 1923). First, the corona is assumed to be at constant temperature, T, density, ρ, and optical depth, τ, with the electron population in thermal equilibrium – i.e. with velocities described by a Maxwellian distribution and a temperature defined as $\Theta = kT_e/m_e c^2$, with the electron temperature $kT_e \sim 100$ keV.

An incident photon – with energy E_i – scattering off an electron – with velocity v_e, and thus an Lorentz factor of $\gamma_L = (1 - \beta_L^2)^{-1/2}$, where $\beta = v_e/c$ – has an output energy, E_γ, defined by (Compton, 1923):

$$E_\gamma = \frac{E_i(1 - \beta_L \cos\theta_{ei})}{1 - \beta_L \cos\theta_{e\gamma} + (E_i/\gamma_L)(1 - \cos\theta_{i\gamma})} \tag{1.21}$$

where θ_{ei}, $\theta_{e\gamma}$, $\theta_{i\gamma}$ are the angles between electron/incident photon, electron/output photon and incident/output photon, respectively (as in Figure 1.7).

In the case of an isotropic distribution of both photons and thermal electrons, such that the mean electron velocity goes by $v_e \sim \sqrt{3kT/m_e}$, and thus $\beta^2 = 3\Theta$. The angle-averaged output photon energy is then given by (Rybicki and Lightman, 1979; Done, 2010):

$$E_\gamma \sim E_i(1 + 4\Theta + 16\Theta^2 + ...) \tag{1.22}$$

If the electrons are highly non-relativistic, $\Theta << 1$, and $E_\gamma \sim (1 + 4\Theta)E_i$. The probability of any photon scattering off an electron is set by the optical depth of the electron population, $\tau = nR\sigma_T$, where n is the electron density, R the path length and σ_T the Thompson cross-section. For optically thick coronae ($\tau >> 1$) the probability of scattering is ~ 1, whereas it follows an exponential for optically thin cases ($\tau << 1$), going by $e^{-\tau} \sim 1 - \tau$ (Rybicki and Lightman, 1979).

Multiple scatterings of the same photon act to produce a power law relationship with electron temperature, whereby a first scattering goes by $E_{\gamma,1} = E_i(1 + 4\Theta)$, a second $E_{\gamma,2} = E_{\gamma,1}(1 + 4\Theta) = E_i(1 + 4\Theta)^2$, etc. Extending this to n scatterings, the photon energy is then given by:

$$E_{\gamma,n} = E_i(1 + 4\Theta)^n \tag{1.23}$$

Where $E_{\gamma,n}$ has an upper limit of $\sim 3\Theta$ set by the thermal temperature of the electrons, such that energy cannot be gained indefinitely. As shown in Rybicki and Lightman (1979), equation 1.23 follows a power law, such that $E_{\gamma,n} \propto E_i^{-\alpha}$, where α is the power law index: $\alpha = \ln(\tau)/\ln(1 + 4\Theta)$. Importantly, the power law index is dependent on both optical depth and electron temperature. N.B. an alternative term used to describe the shape of the power law is the photon index, $\Gamma = \alpha + 1$ (Ishibashi and Courvoisier, 2010), where typically $1.5 \lesssim \Gamma \lesssim 2.5$ (Nandra and Pounds, 1994; Reeves and Turner, 2000; Piconcelli et al., 2005; Page et al., 2005).

This idealised form of the Comptonisation spectrum thus forms a power law (as seen in Figure 1.5), with intensity of scattered photons given by:

$$I(E_{\gamma,n}) = I(E_i) \left(\frac{E_{\gamma,n}}{E_i} \right)^{-\ln \tau / \ln(1+4\Theta)} \tag{1.24}$$

Above the upper energy limit of the thermal electron temperature the intensity of the photon population exponentially declines, which forms the exponential cutoff above the power law, as observed at high energies in the AGN spectrum (see Figure 1.5).

In the case of a relativistic population of electrons, where $\Theta \gtrsim 1$, the energy from a single scattering is $E_{\gamma,1} = E_i(1 + 4\Theta + 16\Theta^2)$, and similarly for n scatterings, $E_{\gamma,n} =$

$E_i(1 + 4\Theta + 16\Theta^2)^n$. The optical depth of this relativistic population cannot be determined with the (classical) Thompson cross-section, σ_T; the Klein-Nishina cross-section (see Klein and Nishina 1929) – dependent on input and output photon energies and scattering angle – must be used instead.

These theoretical constructs represent the idealised case of both non-relativistic and relativistic Compton scattering, both of which motivate an exponential cutoff power law to explain the Comptonisation spectral component. In reality, these approximations are inadequate in cases of non-thermal or a mixture of thermal and non-thermal electron populations, as well as low optical depths or high temperature electrons, as discussed further in Rybicki and Lightman (1979) and Done (2010).

1.6.2 Reflection

A proportion of the X-ray photons radiated from the corona are projected back onto the accretion disc, there being photo-absorbed and further heating the disc, or again scattered. This re-processed emission is described in full by the reflection spectrum. Multiple physical processes may occur in these interactions including further Compton scattering, fluorescence (the emission of EM radiation by excited atomic material) or de-excitation (e.g. Auger de-excitation, whereby an excited atom undergoes an L $\rightarrow$ K-shell transition, emitting a new photon which is absorbed by a bound electron, which is then ejected, leaving ionised material), as discussed in e.g. Guilbert and Rees 1988; George and Fabian 1991; Fabian et al. 2000.

The cosmic abundance and strong fluorescence yield of iron result in it featuring prominently in the reflection spectrum. X-ray radiation from the corona with sufficient energy (7.1 keV) can eject a K-shell (n = 1) electron from an iron atom/ion in the disc, before an L-shell (n = 2) electron transitions into the empty K-shell and releases a photon at $\sim$ 6.4 keV (Fabian et al., 2000). This is the origin of the ($\sim$ 6.4 keV) iron Kα line in reflection spectra , as well as the creation of the iron Kα edge (see Figure 1.5), present at 7.1 keV, where photons are readily absorbed. This emission occurs in only $\sim$ 34% of iron excitation cases however, with the aforementioned Auger de-excitation being the preferred transition (Fabian et al., 2000). By extension, additional emission lines are predicted in AGN reflection spectra, including the nickel Kα line at $\sim$ 7.5 keV, and the iron Kβ line at $\sim$ 7.06 keV (Fabian et al., 2000). Perhaps the best example of a unique emission line detection was that of the broad ($\sim$ 1 keV) iron L line in the prominent reflection spectra of 1H 0707-495 (Fabian et al., 2009).

The theorised 6.4 keV energy of the iron Kα line assumes neutral iron is present throughout the accretion disc; not taking into account the ionisation caused by coronal excitation (see e.g. Ross and Fabian 1993; Ross et al. 1999). With increased ionisation of iron, the electron ionisation energy increases, in turn biasing the Kα emission line and edge

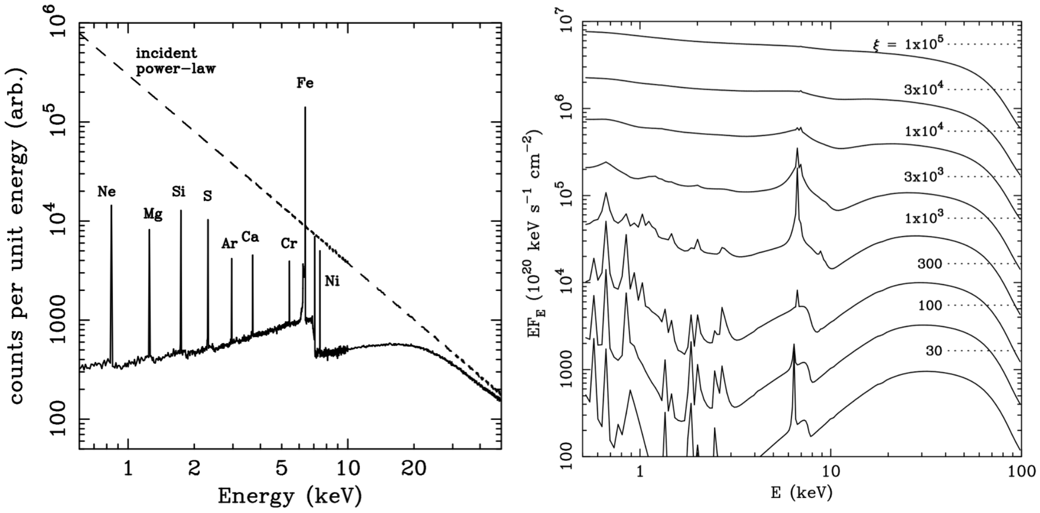

FIGURE 1.8: Left-hand panel: the expected emission line reflection features predicted from a power law ($\Gamma = 2$) illuminated disc, with iron (Fe) most prominent at $\sim$ 6.4 keV. Original from Reynolds (1996). Right-hand panel: the reflection spectrum in the case of a range of ionisation states, set by ξ. Original from Ross et al. (1999).

towards higher energies. Matt et al. (1993a); Matt et al. (1993b) and Matt et al. (1996) set out a framework considering elemental abundances and ionisation states of the accretion disc, with the latter set by parameter $\xi = L/nr^2$ where ionising luminosity L interacts with material of electron density, n, at distance, r (Tarter et al., 1969). Both elemental abundances and ionisation states are important components in determining the overall structure of the reflection spectrum. In these frameworks they consider the accretion disc as a slab of material at different values of the ionisation parameter, ξ, ranging from 'cold'/neutral material, up to a very highly ionised disc. Figure 1.8 highlights both the expected atomic line features predicted from a ($\Gamma = 2$) power law illuminated disc (left-hand panel), and the shape of the reflection spectrum in the case of a range of ionisation states (right-hand panel).

The rapid rotation of the accretion disc impacts the shape the iron line through the Doppler effect. Assuming a Keplerian rotating disc, the observed reflection spectrum sees not a single iron Kα line, but a composite of both red- and blue-shifted lines, associated with receding and approaching circular motion respectively. In a Newtonian gravity regime, this leads to the so-called 'double-horned' line profile (see Figure 1.9), with separation between peaks increasing in energy at radii approaching the black hole. This shape becomes smeared both by special and general relativistic effects. At radii close to the black hole, the material becomes mildly relativistic, such that relativistic beaming (longitudinal Doppler boosting) applies to blue-shifted emission, and de-boosting to red-shifted material (Fabian et al., 1989; Stella, 1990; Fabian et al., 2000). Additionally, the transverse Doppler shift predicted by special relativity applies, whereby material moving perpendicular to the line-of-sight is observed to be blue- or red-shifted as it

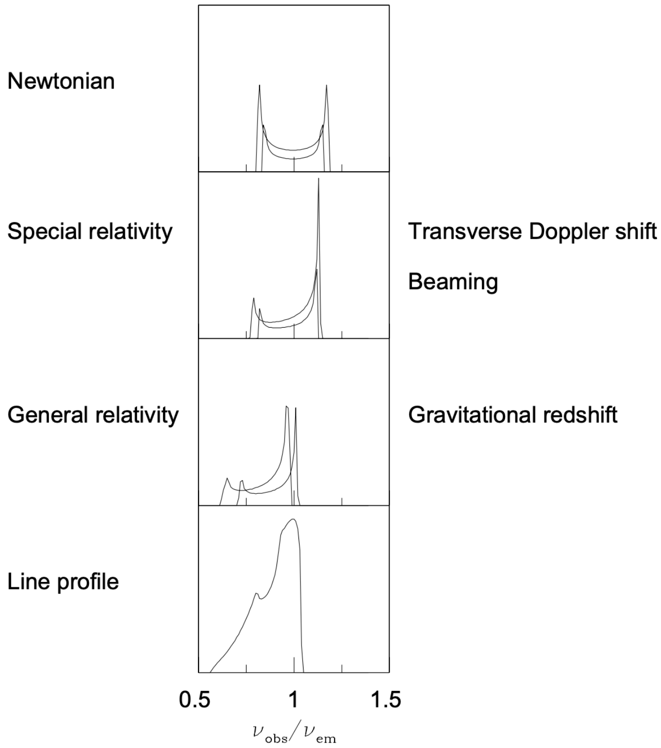

FIGURE 1.9: Relativistic line profiles from the standard Newtonian framework of a rotating disc, through the SR altered profile due to transverse Doppler shifts and relativistic boosting, to GR altered profiles from gravitational redshifts. The combined effects gives the observed line profile. Original from Fabian et al. (2000).

approaches/recedes from the direct line-of-sight in the laboratory rest-frame (Figure 1.9). This effect acts to reduce the observed line profile energies (Fabian et al., 2000). An overall reduction in line energy also occurs due to general relativistic red-shift, in the strong gravity regime around a black hole (Fabian et al., 2000). The resulting line profiles (Figure 1.9), with associated 'red/blue wings' can be used as proxies to determine both the black hole spin and position of the inner edge (from the red wing) and source inclination (from the blue wing) – see Laor 1991.

Above the iron Kα edge ($\sim$ 10 keV) extends the Compton hump, which forms from a balance of the down-scattering of high energy photons – emitted from the corona at electron temperature $\sim$ 100 keV – and the absorption of softer photons by iron with high photoelectric opacity (García et al., 2020). These effects curtail the flux towards both $\sim$ 10 keV and 100 keV, with the balance of these effects resulting in a spectral peak at $\sim 20 - 50$ keV, i.e. the Compton hump. For more detail see e.g. Matt et al. 1991; Petrucci et al. 2001; Kara et al. 2015).

Modelling the complex structure of the reflection spectrum is possible with several specifically designed models in XSPEC [2,3]. The ideal model must incorporate both the

[2] https://heasarc.gsfc.nasa.gov/xanadu/xspec/manual/Models.html
[3] https://heasarc.gsfc.nasa.gov/xanadu/xspec/newmodels.html

reprocessed line emission, and the relativistic nature of the accretion disc which distorts it, as well as the relative iron abundance and ionisation states of the disc. The model RELXILL (see Dauser et al. 2014; García et al. 2014; Dauser et al. 2016) is designed specifically to model relativistic, partly-ionised, reflection spectra, by combining the ray-tracing, line emission models from RELLINE (Dauser et al., 2010, 2013) and the XILLVER reflection framework (García and Kallman, 2010; García et al., 2011, 2013). RELXILL is thus an advanced model used for understanding relativistic reflection.

1.6.3 Soft excess

A spectral component almost ubiquitously observed in bright AGN, and especially NLS1s, is that of the 'soft excess'. It is the term used to encapsulate the broad, featureless, peak in flux observed below the Comptonised power law, at energies lower than 2 keV and peaking at $\sim$ 0.5 keV (see Figure 1.5) (Arnaud et al., 1985; Gierliński and Done, 2004; Done et al., 2007b). The soft excess also appears to show remarkably consistent temperatures at these energies across multiple AGN, when modelled by a thermal component (Czerny et al., 2003; Crummy et al., 2006b), and is too hot to be described by disc black-body radiation.

The origin of the soft excess is the cause of much debate in AGN spectral studies (see e.g. Gierliński and Done 2004; Crummy et al. 2006b; Sobolewska and Done 2007; Middleton et al. 2007), and differs from both Comptonisation and reflection components in having no ubiquitous XRB counterpart (see Middleton and Done 2010 for a discussion on the potential soft excess characteristics in the high Eddington XRB, GRS 1915+105). Three leading candidates to explain the soft excess are absorption, reflection and intrinsic flows, which are introduced individually here and are illustrated in Figure 1.10. It is important to note that while the origin of the soft excess remains an open question, the solution quite probably lies in not a single origin, but through a *combination* of multiple factors.

1.6.3.1 Absorption

The universality of the soft excess shape (Walter and Fink, 1993; Czerny et al., 2003) motivated Gierliński and Done (2004) to propose an origin in relativistically smeared absorption, with atomic features masked by the rotation of the accretion disc or changing velocity along the line-of-sight. The absorbing material has been motivated to be an optically thin, outflowing wind (Murray and Chiang, 1997) and ejected at sufficient velocity to smear absorption features in the spectrum (Done, 2007) (see Figure 1.10). Radiatively driven disc winds are expected in high accretion rate AGN (Proga et al., 1998), consistent with NLS1s in which the soft excess is most prominent.

Assuming this geometry allowed Gierliński and Done (2004) to model the spectrum of NLS1 PG 1211+143 with a single Comptonised continuum and propose the presence of [O_{VII}], [O_{VIII}] absorption lines within the spectrum. Chevallier et al. (2006) found absorption models capable of accounting for some strong soft excesses found in NLS1s, in which comparable reflection models could not. Limitations to these models include the need for 'fine-tuning' of the ionisation state in the absorber however, to describe a predicted spectral trough at 1 keV, which is otherwise unconstrained. Sobolewska and Done (2007) similarly showed an absorption model can successfully explain the observed strong soft excess in 1H 0707-495, albeit not uniquely, with reflection models of the soft excess statistically comparable. In this case, an absorption model was favoured as the relative strength of observed soft excess components in NLS1 could be well modelled with a variable column density parameter of the outflow, while not requiring any specific source geometry, as the outflow may be launched in any direction. A 'fine-tuned' ionisation state is required however, to allow oxygen to be partially ionised.

Middleton et al. (2007) also argued for an absorption model to explain the soft excess observed in the high accretion rate PG Quasars, but with the limitation of requiring a outflow velocity $\geq 0.4c$ to create the smooth soft excess features observed in their sample. Proga and Kallman (2004) constrain the terminal velocity for radiatively driven disc winds at $\sim 0.2c$, thus requiring the predicted outflows in Middleton et al. (2007) to instead be a magnetically driven (jet) outflow, to reach these relativistic velocities. The extreme nature of such outflows is a limiting factor for extending this model to all AGN with a prominent soft excess.

1.6.3.2 Reflection

The reflection model for the soft excess is based on the reprocessed emission of photons from partially ionised, optically thick and out of the line-of-sight material (Done, 2007). This mechanism is possible through anisotropic illumination of the accretion disc, which requires strong light-bending of coronal emission in order to magnify the inner reflective component and suppress the direct continuum emission (Fabian et al., 2004; Crummy et al., 2006b; Done and Nayakshin, 2007) – see Figure 1.10. Moreover, the presence of short spectral lags ($\lesssim$ 500s) suggests the height of the corona above the black hole must be very small in strong gravity environments (see e.g. Alston et al. 2014a; Kara et al. 2017; García et al. 2019). The effective smearing of the soft excess is then accounted for by the dynamics of material in the inner disc, within an extreme Kerr (high spin) spacetime (Done, 2007).

Czerny and Zycki (1994) used an ionised reflection model to describe *ROSAT* AGN data and found the soft excess could originate from a high reflection fraction. The unfortunate degeneracy of modelling X-ray spectra resulted in both absorption and reflection models being capable of reproducing soft excesses to similar statistical significance to in several cases (see e.g. Chevallier et al. 2006; Sobolewska and Done 2007). Chevallier et al. (2006) however reported reflection models capable of reproducing weak soft excess components only, under the condition that the corona is not obscured, i.e. that the required anisotropic illumination of the disc was not sufficient to describe the large soft excesses seen in some NLS1s (e.g. PG quasars). This conclusion was partially at odds with Crummy et al. (2006b), who used the Ross and Fabian (2005) disc reflection model to successfully reproduce the soft excess in their sample (including for PG quasars) and reproduced spectral features typically considered to be warm absorption edges, but importantly considering geometries where the corona is visible. Done and Nayakshin (2007) investigated hydrostatic (as opposed to constant density) disc models, as first proposed by Crummy et al. (2006b), and found these models unable to produce the observed soft excess. Moreover, constant density models required further 'fine-tuning' of parameters to describe the observed component. These extreme conditions led Done and Nayakshin (2007) to conclude that reflection is less likely to be the primary means of producing the soft excess in AGN, at least in direct comparison to absorption models.

1.6.3.3 Intrinsic disc emission

A further mechanism to describe the soft excess invokes Compton upscattered, soft X-ray photons from a warm accretion disc. Middleton et al. (2009) applied such a model to describe the large soft excess observed in NLS1, RE J1034+396, in part due to the lack of variability at these energies, comparable to the findings in Jin et al. (2009a) and newer results from recent observations of AGN in Jin et al. (2021). Done et al. (2012) later postulated that the soft excess might originate from intrinsic emission from the accretion disc, in AGN exhibiting high accretion rates, such that the black-body disc spectrum extends beyond the extreme ultra-violet and into the soft X-rays. This alone does not reproduce observed soft excesses however. Done et al. (2012) rectify this by proposing the presence of Compton upscattered photons from the optically thick, warm inner disc. The geometry proposed by Done et al. (2012) segments the disc between an inner, warm, Comptonising disc, and an outer disc which radiates a cooler black-body spectrum, the photons from which provide the seeds for Comptonisation (see Figure 1.10). These combined components are capable of reproducing the observed soft excess in highly accreting NLS1s, such as RE J1034+396. It is likely however, that the warm inner Comptonising disc is a feature of those AGN with high accretion rates, so cannot be extended universally.

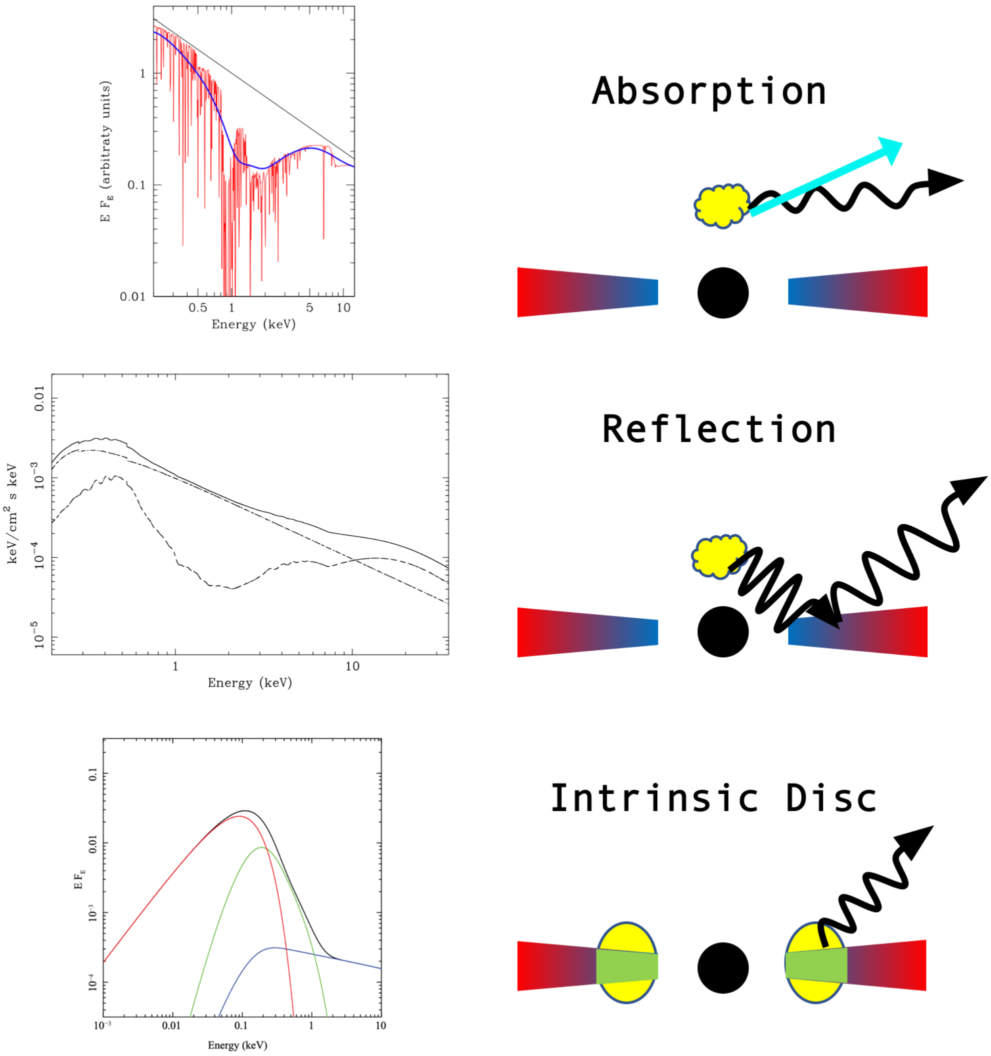

FIGURE 1.10: Soft excess spectral models and associated model sketches for the three primary mechanisms used to explain the soft excess in AGN. 1) Absorption: Smoothed absorption features of a spectrum of AGN, PG 1211+143 (original from Gierliński and Done 2004), and schematic showing continuum emission passing through an optically thin, high velocity wind/jet along the line of sight. 2) Reflection: High reflection fraction (dashed line) at soft energies $<$ 1 keV used to model a spectrum of AGN, PG 1202+281 (original from Crummy et al. 2006b), and schematic showing anisotropic illumination of the inner disc through gravitational 'light bending' in an extreme Kerr metric environment. Reprocessed emission observed as soft X-rays. 3) Intrinsic Disc emission: model spectrum showing contributions from both outer disc blackbody (green) and inner disc Compton upscattering (red), forming the soft excess at energies below the power law (blue) – original from Done et al. 2012 – and the colour matched schematic which shows these defined regions in the disc.

Chapter 2

AGN variability and timing analysis

Time series data in X-ray astronomy describe features of an astronomical source, as it changes with time. In the study of AGN X-ray variability, these data may correspond to the variation of the measured X-ray count rate, represented as a lightcurve. This chapter is dedicated to the study of AGN variability, first through an introduction to astronomical time series, before describing the necessary Fourier toolkit for studying data in the Fourier domain, which will then be used to conduct a search for quasi-periodic signals in aperiodic broad-band noise.

2.1 X-ray lightcurves

A key characteristic of AGN is the inherent, stochastic nature of X-ray emission (Lawrence et al., 1987; McHardy, 1989). This variability is commonly termed as 'noise', with any individual observation itself being only a single realisation of the underlying stochastic process, itself intrinsic to the accretion flow of the AGN.

An X-ray lightcurve, $x(t)$, consisting of N bins of size dt (total duration $T = Ndt$), has associated uncertainties $\sigma(t)$. Summary statistics for this time series include the mean count rate, $\bar{x}$, and a total variance, $\sigma^2_{tot} = \frac{1}{N-1}\sum_{i=1}^{N}(x_i - \bar{x})^2$, where the absolute rms amplitude of the full lightcurve is simply given by $\sigma_{rms} = \sqrt{\sigma^2_{tot}}$. In any given observation, a mean square variance, $\overline{\sigma^2}_{err}$, is introduced by Poisson counting statistics, and is known as white, or simply Poisson-noise (see Gehrels 1986). The variance attributable to the intrinsic noise profile in an AGN may then be represented by the excess variance, $\sigma^2_{xs} = \sigma^2_{tot} - \overline{\sigma^2}_{err}$ (Nandra et al., 1997; Edelson et al., 2002; Vaughan et al., 2003a). The excess variance observed in AGN is importantly *not* Poisson, instead being described by a more complex noise process, generated directly within the accretion flow.

The fractional root-mean square (rms) amplitude of the excess variance, F_{var} (Edelson et al., 1990; Rodríguez-Pascual et al., 1997; Vaughan et al., 2003a) is given by:

$$F_{var} = \sqrt{\frac{\sigma_{xs}^2}{\bar{x}^2}} \tag{2.1}$$

and represents a statistic through which the excess variance may be evaluated, relative to the mean count rate, which allows comparison between different sources. This value may be used to study the energy dependent nature of the excess variability in a fractional rms spectrum, in which F_{var} is measured in energy-binned lightcurves.

2.1.1 Stationarity

The concept of stationarity in AGN is based on the statistical properties of a variability process remaining unchanged over time (Vaughan et al., 2003a). Given that any observation is only a single realisation of an underlying stochastic process, the mean count rate and excess variance are liable to change, at random, between independent observations. The concept of *weak non-stationary* arises when the mean of a variability process is inherently 'unknowable', as the variance diverges (Press and Rybicki, 1997). AGN variability processes are expected to meet the criteria of weakly non-stationary processes (see Press and Rybicki 1997) and the assumption is made that the expectation values of the statistics describing the process remain time independent (Bendat and Piersol, 1986). This assumption allows for observations to be treated as independent realisations of the same noise generating process in an AGN, and stationarity to be generally assumed in timing analyses.

2.2 The foundations of Fourier analysis

In order to study AGN variability in greater detail, we are often motivated to represent time series data not in the *time domain*, but instead as a set of frequencies in the *frequency/Fourier domain*. For this we may utilise a field of mathematics named after French mathematician, Joseph Fourier, whose work on heat flow using Fourier series in the 19$^{\text{th}}$ century spawned the broad mathematical field of Fourier Analysis (Fourier, 1822).

2.2.1 The Fourier transform

For some time series data $x(t_i)$, with N bins of size dt (total duration $T = Ndt$), the Fourier Transform may be used to describe the signal as a summation of sinusoids, with angular frequencies, ω_j – defined across frequency terms j, whereby $\omega_j = 2\pi j/T$. In the most general, complex form, the Fourier Transform may be written as:

$$\mathcal{F}[x(t_i)] = \int_{-\infty}^{\infty} x(t_i)e^{-i\omega_j t_i}dt \tag{2.2}$$

For application to real world time series, the Discrete Fourier Transform (DFT) is used to deconvolve the signal into a discrete sum of sinusoids (Press et al., 1996). The DFT, $X(\nu_j)$ (hereafter X_j) of a time series is computed using the expression:

$$X(\nu_j) = \sum_{i=1}^{N} x(t_i)e^{-2i\pi\nu_j t_i} \tag{2.3}$$

across Fourier frequencies, $\nu_j = \frac{\omega_j}{2\pi} = \frac{2\pi j}{2\pi T} = \frac{j}{T}$, where j is an integer in the range $\frac{-N}{2} \leq j \leq \frac{N}{2}$.

In practice the Fast-Fourier-Transform (FFT) is employed in order to improve computational efficiency of this calculation, which is maximised in the case of a time series, $x(t)$, to be of length 2^n (Cooley and Tukey, 1965), where $n > 0$ and an integer. Modern FFTs are capable of processing time series not of length 2^n, although these calculations are less computationally efficient.

Importantly, Fourier methods here depend on the assumption of regularly sampled data. Aliasing can be neglected only for contiguous data or very high sampling rates.

2.2.1.1 Inverse Fourier transform

The inverse Fourier Transform arises as the mathematical inverse to the Fourier Transform (equation 2.2). It allows for the transformation from Fourier space, $X(\nu_j)$, back to the time domain, $x_i(t)$. In the discrete form, this is defined as:

$$x_i(t) = \mathcal{F}^{-1}[X(\nu_j)] = \sum_{i=1}^{N} X(\nu_j)e^{2i\pi\nu_j t_i} \tag{2.4}$$

In order to compute this efficiently, the Inverse-Fast-Fourier-Transform (IFFT) algorithm is used. This method then allows for the approximate reproduction of a time series, derived directly from an observed or simulated power spectrum (Cooley and Tukey, 1965). The true input time series cannot be reproduced however, as all phase information (see equation 2.2) is lost in the production of the power spectrum.

2.2.2 The power spectrum

The power spectrum is obtained directly from the FFT. The notion of *power* as a variable in Fourier Analysis may be obtained through invoking Parseval's Theorem (van der Klis, 1988):

$$\sum_{i=0}^{N-1} |x_i|^2 = \frac{1}{N} \sum_{j=-\frac{N}{2}}^{\frac{N}{2}-1} X_j^* X_j = \frac{1}{N} \sum_{j=-\frac{N}{2}}^{\frac{N}{2}-1} |X_j|^2 \tag{2.5}$$

which relates the (complex) Fourier amplitudes, X_j, to the statistical variance of the time series, $\mathrm{Var}(x_i) = \frac{1}{N-1}\sum_i (x_i - \bar{x})^2 = \sum_i x_i^2 - \frac{1}{N}(\sum_i x_i)^2 = \frac{1}{N}\sum_j X_j^2 - \frac{1}{N}X_0^2$, through Parseval's theorem, such that $\mathrm{Var}(x_i) = \frac{1}{N}\sum_{j=-\frac{N}{2}}^{\frac{N}{2}-1} |X_j|^2$, where $j \neq 0$ (van der Klis, 1988).

The concept of Fourier power, P_j, is then defined directly from the above, such that:

$$P_j = A_{\mathrm{norm}} X_j^* X_j = A_{\mathrm{norm}} |X_j|^2 \tag{2.6}$$

Which includes an arbitrary normalisation term, A_{norm}. From this, it is clear that the power corresponds to the *magnitude of variance* in the time series data across a set of discrete Fourier frequencies. In other words, for a given frequency of interest within the time series, a higher power corresponds to a greater measured variance of the data at this frequency.

The power spectrum is constructed using positive frequency terms, j, from equation 2.6. The concept of negative frequencies arises from the cyclical nature of angular frequencies, ω_j, and are calculated as part of equation 2.5. However, equation 2.3 shows the the equivalence between any Fourier amplitude and its complex conjugate at equivalent negative frequency, $X_j = X_{-j}^*$. From this equivalence relation, equation 2.6 demonstrates that Fourier powers P_j exhibit a mirror symmetry, such that $P_j = P_{-j}$ about a null frequency term, $|X_0|^2$ – which itself represents the mean count rate (van der Klis, 1988). In the physical application of astronomical power spectra it is therefore possible to discard all negative frequencies without loss of information (Uttley et al., 2014b).

The power spectrum is thus defined, for physical Fourier frequencies, ν_j as:

$$P(\nu_j) = A_{\mathrm{norm}} |X_j|^2 \tag{2.7}$$

where $j = (1, 2, ..., \frac{N}{2})$ (Vaughan et al., 2003a). The range of positive frequencies in the power spectrum is limited due to the cyclical nature of angular frequencies, ω_j (see equation 2.2), reaching a sampling limit at $N/2$.

Recalling that the angular frequencies of equation 2.2 may be expressed equivalently as $\nu_j = \frac{j}{T}$, the lowest Fourier frequency is then $\nu_1 = \frac{1}{T}$. The lowest Fourier frequency is also the frequency resolution, i.e. the width of the Fourier bin, $\delta\nu = \frac{1}{T}$. Thus, the sampling frequency is dependent only on the length of the time series, which motivates the use of long astronomical observations, in order to obtain high frequency resolution.

Each subsequent frequency increases by a factor $\frac{1}{T} = \frac{1}{Ndt}$, up to the maximum Fourier frequency, known as the Nyquist frequency, of value equal to $\nu_{\frac{N}{2}} = \frac{N}{2T} = \frac{1}{2dt}$ and Fourier amplitude $X_{j=\frac{N}{2}}$ (van der Klis, 1988). The periodogram ordinate at the Nyquist frequency does not follow the same statistics that underpin the rest of the power spectrum (as discussed in Section 2.2.3), and must be treated accordingly.

The power spectrum in this form, i.e. *unaveraged*, is called the *periodogram*. As above, the periodogram spans the full range of Fourier frequencies, $\nu_1 - \nu_{\frac{N}{2}}$, and offers the maximum number of Fourier frequencies which may be investigated within a given time series.

2.2.2.1 The power spectral distribution

The *averaged* periodogram is (generally) a consistent estimator of the underlying power spectrum (see Section 2.4 for where other effects may limit this), and is known as the power spectral distribution (PSD). The averaged powers of the PSD, $\bar{P}(\nu_j)$, are obtained from the following arithmetic averaging process:

$$\bar{P}(\nu_j) = \frac{1}{KM} \sum_{n=i}^{i+K-1} \sum_{m=1}^{M} P_{n,m} \tag{2.8}$$

when averaged over M segments and over K frequencies per segment (with each, new, frequency bin, ν_j, containing frequencies in the range ν_i to ν_{i+K-1}) (Uttley et al., 2014a). This is equivalent to the segmentation of a time series into M segments, before obtaining a periodogram for each, in which the original Fourier frequencies are re-binned into K new frequencies. The powers at each re-binned frequency are then averaged across all the available segments.

This re-binning reduces the frequency range of the PSD as the effective length of the time series is reduced. The number of bins in the *averaged* time series takes the value $m = \frac{N}{KM}$, with the number in the PSD reduced from $N/2$ to $m/2$ bins. The new, lowest frequency is given by $\nu_1 = \frac{1}{mdt}$ but the maximal, Nyquist frequency remains the same as in the periodogram: $\nu_{\frac{m}{2}} = \frac{m/2}{mT} = \frac{1}{2dt}$.

Given a sufficiently high number of averages (e.g. > 50) the uncertainty on the power spectral noise may be given by the standard error on the powers, where $\sigma_{\bar{P}_j}$ is the standard deviation of the averaged powers, $\bar{P}_j$, as in equation 2.8 (Uttley et al., 2014b):

$$\sigma_{P_j} = \frac{\sigma_{\bar{P}_j}}{\sqrt{KM}} \tag{2.9}$$

In the case of a low number of averages (e.g. < 50), the error instead can take the form (Uttley et al., 2014b):

$$\sigma_{P_j} = \frac{\bar{P}_j}{\sqrt{KM}} \tag{2.10}$$

such that in the case of the periodogram, the error on the power is equivalent to the power itself. N.B. the HEASARC tool `POWSPEC` uses equation 2.9 in its error bar evaluation when the number of averages, $KM > 5$ and equation 2.10 otherwise.

Figure 2.1 shows an example of a simulated astronomical time series (using the method in Timmer and Koenig 1995), with associated periodogram and 8-segment averaged PSD, both with errors. A PSD provides a trade-off between reduced uncertainty in the powers and a reduction in precision in frequency bin width, and a reduced frequency range. As such, a PSD is preferred in cases with long observations, and where the longest variability timescales, as well as frequency precision, are not of paramount importance.

2.2.2.2 Normalisations

Within X-ray astronomy there are a few commonly used definitions for A_{norm} (Vaughan et al., 2003a), which are briefly listed here:

- $A_{\mathbf{rms}^2} = \frac{2dt}{m\bar{x}^2}$ yields the power in fractional rms^2 units. When the power spectrum is then integrated, the area provides the fractional variance, in units $(\sigma_{tot}/\bar{x})^2$ Hz^{-1}
- $A_{\mathbf{Leahy}} = \frac{2dt}{m\bar{x}}$ is the normalisation for Leahy power, which is set such that the expected Poisson noise level is equal to 2 (see Section 2.3.2)
- $A_{\mathbf{abs}} = \frac{2dt}{m}$ yields the power in rms^2 units, which when integrated across frequency gives the absolute variance, in units σ_{tot}^2 Hz^{-1}

Unless stated otherwise, the A_{rms^2} normalisation is used from this point forwards, as is commonplace in most published works on timing analyses of AGN.

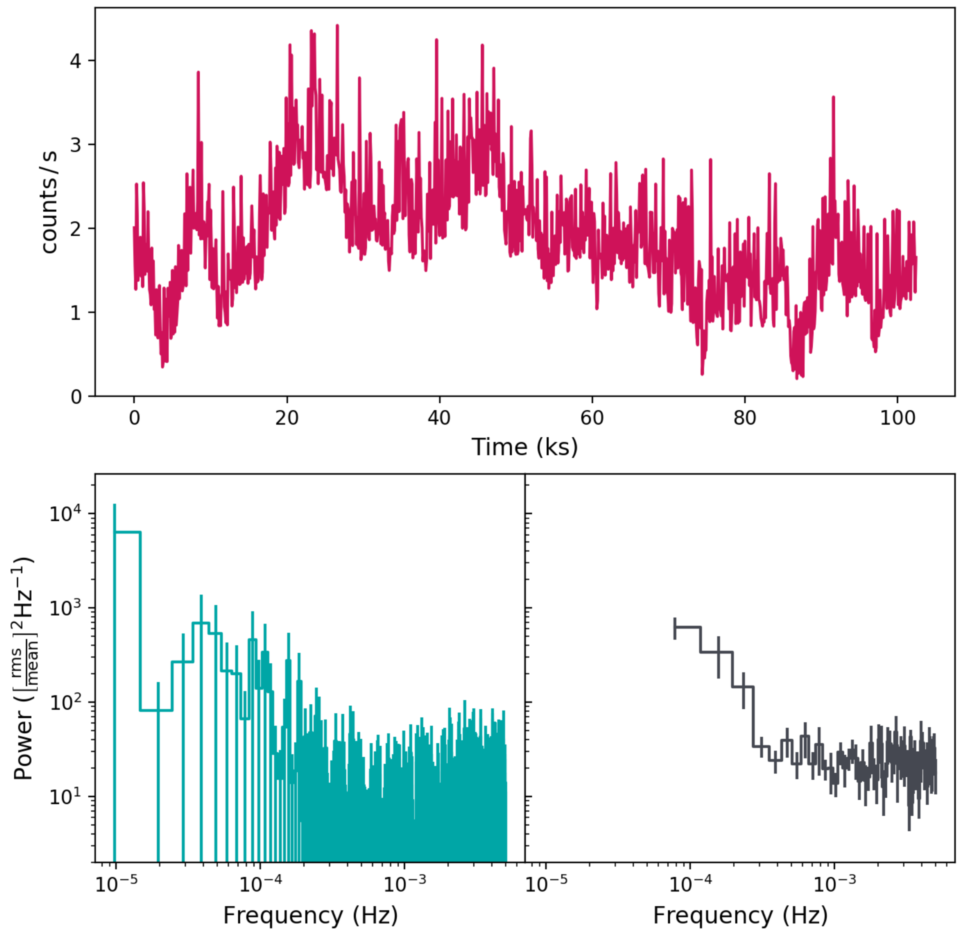

FIGURE 2.1: Top: Simulated time series, with 1024 time bins, with an arbitrary width of 100s. Bottom left: periodogram, with errors, of this time series. Bottom right: PSD of this time series, using 8 averages – with corresponding Gaussian errors – and shown across the same frequency range as the periodogram.

2.2.3 Power spectral statistics

The observed periodogram, $P_j(\nu)$, may be considered as a combination of real and imaginary (Gaussian) components, such that, $P_j(\nu) = \mathrm{Re}_j^2 + \mathrm{Im}_j^2$, and results in $P_j(\nu)$ being describes by a χ_2^2 distribution (Jenkins and Watts, 1968; van der Klis, 1988; Timmer and Koenig, 1995), with two degrees of freedom. This applies to all frequencies except the Nyquist, where $P_{Nyq}(\nu) = \mathrm{Re}_{Nyq}^2$ such that the Nyquist value then follows a χ_1^2 distribution with a single degree of freedom. The observed periodogram (discounting the Nyquist) is therefore a statistical realisation of the (true) intrinsic AGN power spectrum, $\mathcal{P}_j(\nu)$, modulated by a χ_2^2 distribution (Jenkins and Watts, 1968; Vaughan et al., 2003a):

$$P(\nu) = \mathcal{P}(\nu)\chi_2^2/2 \tag{2.11}$$

The probability density function of a χ_k^2 distribution (k degrees of freedom) is described by (Barlow, 1999):

$$f(x;k) = \frac{1}{2^{k/2}\Gamma(k/2)} x^{k/2-1} e^{-x/2} \tag{2.12}$$

where $x \geq 0$. The expectation value, $E(x)$, of this probability distribution is given by k – the number of degrees of freedom – and the variance, $\mathrm{Var}(x)$, by $2k$ (Barlow, 1999). For a χ_2^2 distribution, this yields $E(x) = 2$ and $\mathrm{Var}(x) = 4$. Importantly, this highlights the strong non-Gaussian nature of the periodogram. The highly skewed nature of the χ_2^2 distribution leads to large scatter in any single, observed periodogram relative to the intrinsic power spectrum (Vaughan et al., 2003a).

The effect of averaging over the χ_2^2 distribution is for the distribution of powers to increasingly tend it towards a a Gaussian distribution (van der Klis, 1988). This is the result of the standard Central Limit Theorem (CLT), whereby summing a number of independent, random events drawn from a distribution will cause the sampled distribution to tend towards a Gaussian with an increasing number of averages (Hughes and Hase, 2010). This applies to the distribution of powers in a PSD. However, due to the periodogram χ_2^2 distribution having a highly skewed nature, a high number of averages (> 50) is required for the distribution to tend towards being quasi-Gaussian (Uttley et al., 2014b). An example of this is depicted in Figure 2.2, whereby the distribution of powers at a single frequency is shown for both a periodogram and for PSDs fromed from M = 2, 16 and 128 segments respectively.

2.3 Flavours of power spectral noise

Understanding the properties and shape of the frequency-dependent noise is fundamental to subsequently modelling the observed variability of the AGN.

2.3.1 Red noise

Intrinsic variability generated within the accretion flow of the AGN can take several, complex forms. In the simplest case it may be described as 'red noise'. In Fourier space, red noise is observed as power variability steeply increasing towards low frequencies, in a relationship which is commonly described by a power law, with a non-zero index, β:

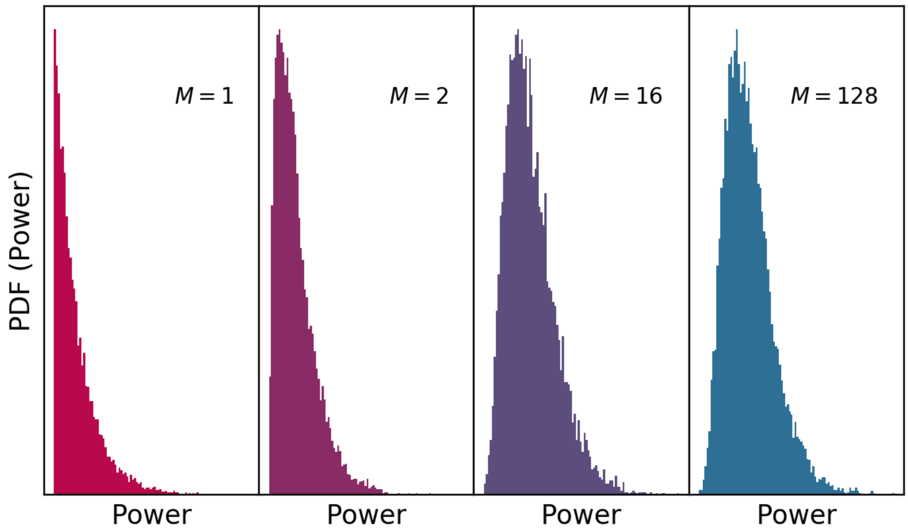

FIGURE 2.2: Probability distribution functions of simulated powers at a single, arbitrary, frequency – for a simulated lightcurve of length 4096 bins. Far left: the periodogram case, which follows a χ^2_2 distribution. Other panels: the PSD case, for $M = 2$, $M = 16$ and $M = 128$ averages, which increasingly tend towards a Gaussian distribution with an increasing number of averages, through the CLT.

$$P_{red}(\nu_j) \propto \nu_j^{-\beta} \tag{2.13}$$

although in some cases the *technical* definition of red noise – also called Brownian noise – is the specific case where $\beta = 2$. More generally, such a distribution is often used to describe the characteristic shape of AGN power spectra, with values of β typically found to lie between 0.5 and 2.5 (Green et al., 1993; Lawrence and Papadakis, 1993; Uttley et al., 2002; Markowitz et al., 2003; Vaughan and Fabian, 2003).

Importantly, red noise is *not statistically independent* between neighbouring frequencies, such that the power measured in a given frequency bin is not independent of a power in a different frequency bin – in contrast to pure Poisson noise, which is instead statistically independent across all frequencies.

The observed structure of an AGN spectrum is one which follows a power law of index $\beta \sim 2$ (although this is found to be highly energy dependent in practice – e.g. McHardy et al. 2005; Vaughan et al. 2011; Jin et al. 2020; Chapter 6), back to the location of a high-frequency break, below which the power as a function of frequency flattens towards an index of $\beta \sim 1$ – a shape that is comparable to the high-frequency break seen in XRBs (Edelson and Nandra, 1999; Uttley et al., 2002; Markowitz et al., 2003; McHardy et al., 2006; González-Martín and Vaughan, 2012). The nature of this break, including its location and possible energy dependence remain an open area of study. In some observations, the high frequency break may not be observed at all. Current, individual observations of AGN are of insufficient length to probe timescales corresponding to the low-frequency break in XRBs, and would instead require a concatenation of many observations taken over the timescale of many months - years.

2.3.2 White noise

Counting statistics are Poisson in nature, and commonly referred to as 'white noise'. This noise is described by a flat power law and takes the approximate form of:

$$P_{white}(\nu_j) \propto \nu_j^0 \tag{2.14}$$

Poisson noise is a mainstay of low-count astronomical studies (Gehrels, 1986), and is not intrinsic to the AGN itself (Vaughan et al., 2003a). The probability density function of a Poisson distribution is described by:

$$f(k;\lambda) = \frac{\lambda^k e^{-\lambda}}{k!} \tag{2.15}$$

where k is the number of occurrences and $k \geq 0$. The expectation value, $E(k)$, of this probability distribution is given by λ which is exactly equivalent to the variance.

Considering equation 2.14 it is evident that white noise in the power spectrum is projected as stochastic noise about a constant value of power. Common practice is to approximate the white noise as a constant, C, following Vaughan et al. (2003a):

$$C = \frac{2dt}{\bar{x}^2}\overline{\sigma^2}_{err} \tag{2.16}$$

Figure 2.3 shows the shape of both red ($\beta = 2$, $\beta = 1$) and white noise profiles in time and frequency domains.

2.3.3 Real power spectra

In reality, AGN power spectra consist of a combination of both red and white noise. Given sufficient signal-to-noise, the red noise component dominates above the white noise at low frequencies. The 'white noise floor', is the threshold in power at which point the red noise component falls below the white noise, as approximated by the constant, C, in equation 2.14. At frequencies above this point, the intrinsic AGN variability is white noise dominated.

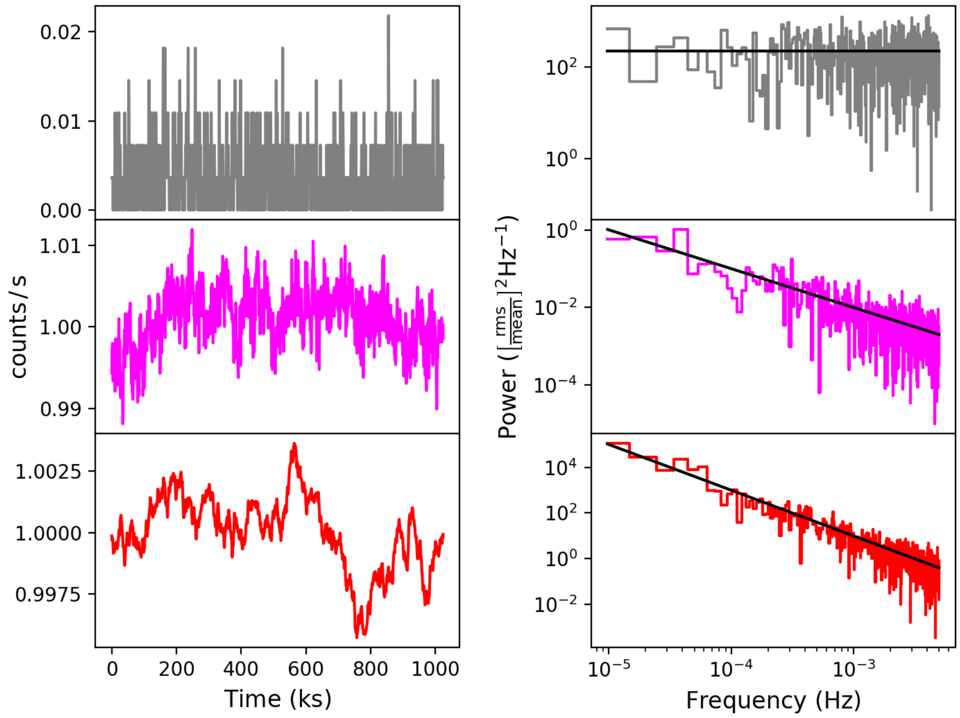

FIGURE 2.3: Simulated noise profiles, as lightcurves – with $\bar{x} = 1$ and equivalent fractional variance – in the time domain (LHS) and power spectra (in fractional rms^2) in the Fourier domain (RHS), simulated around a defined power spectral index, β, in black. From top to bottom: 1) White/Poisson noise, $\beta = 0$; 2) Red noise where $\beta = 1$ (sometimes called 'pink noise'); 3) Red noise where $\beta = 2$ ('true red'/Brownian noise).

To maximise power spectral data quality requires the red noise to dominate over the white noise. To minimise the level of white noise requires as high a signal-to-noise ratio as possible in the data (i.e. a high count rate). Additionally, as the red noise powers scales inversely with frequency, longer observations, or unaveraged power spectra, allow for lower frequencies to be observed, with a relatively higher red noise component compared to the underlying white noise. Together this motivates analysis of bright AGN with long observations.

2.4 Red noise leak

The power spectrum in real observations is subject to the additional effect of red noise leak, which arises from the unavoidable windowing of an X-ray lightcurve (see e.g. Deeter and Boynton 1982; van der Klis 1988; Vaughan et al. 2003a). The finite timeframe of an observation effectively creates a window over a conceptual, infinitely long, time series. The result is that power on timescales longer than the observation effectively transfers (or 'leaks') power from these unobserved lower frequencies onto the observed bandpass, in turn biasing the observed power spectrum away from the *intrinsic* AGN power spectrum.

Mathematically, red noise leak may be described by a transfer function acting on the intrinsic power spectrum, which results in the modified, observed power spectrum. First, consider both an intrinsic time series $x(t)$ and an observed time series $y(t)$, which are related by a function $\psi(t)$, such that:

$$y(t) = \int_{-\infty}^{\infty} \psi(t-\tau)x(t)d\tau = \psi(t) \cdot x(t) \tag{2.17}$$

The power spectra of which can be obtained in the Fourier domain. Through the convolution theorem, the multiplication of the impulse response function $\psi(t)$ and time series $x(t)$, may then be expressed as a convolution of a transfer function $\Psi(\nu)$ and a Fourier amplitude, $X(\nu)$:

$$Y(\nu) = \mathcal{F}[\psi(t) \cdot x(t)] \equiv \Psi(\nu) \circledast X(\nu) \tag{2.18}$$

Given an observation exists with a defined start and end time, the impulse response, $\psi(t)$ may be represented by a 'top hat' function of width a, centred on $t = b$. As such, $\psi = \frac{1}{a}$ within $-a/2 + b \leq t \leq a/2 + b$, and 0 elsewhere. Applying the Fourier transform to a 'top hat' function yields a sinc function, such that the squared modulus of the transfer function, $|\Psi(\nu)|^2 \propto \mathrm{sinc}^2$ – which in this specific case is known as the Fèjer kernel. The observed power spectrum then takes the form:

$$P_{obs}(\nu) = |\Psi(\nu)|^2 \circledast P_{int}(\nu) = a^2\,\mathrm{sinc}^2(a\nu)P_{int}(\nu) \tag{2.19}$$

The shape of the Fèjer kernel biases the the observed power spectrum towards the a power law of index $\beta = -2$. This effect is most dominant in the case of steep power spectra (of index steeper than $\beta = -2$) as the red noise spectrum implies a large amount of power exists at lower frequencies beyond the observed bandpass. The observed power spectrum is then a biased form of the *true* power spectrum which describes the variability process. This effect is exacerbated for short observation windows, but typically considered negligible for relatively flat power spectra (where $\beta < 1.5$) (Vaughan et al., 2003b). Figure 2.4 highlights the 'ringing' effect of the Fèjer kernel, in which harmonics across frequency space act to reduce power from the intrinsic power spectrum, appearing as dips in the observed power spectrum. In a real observation however, this effect is somewhat offset by the presence of white noise and random stochasticity in the intrinsic power spectrum.

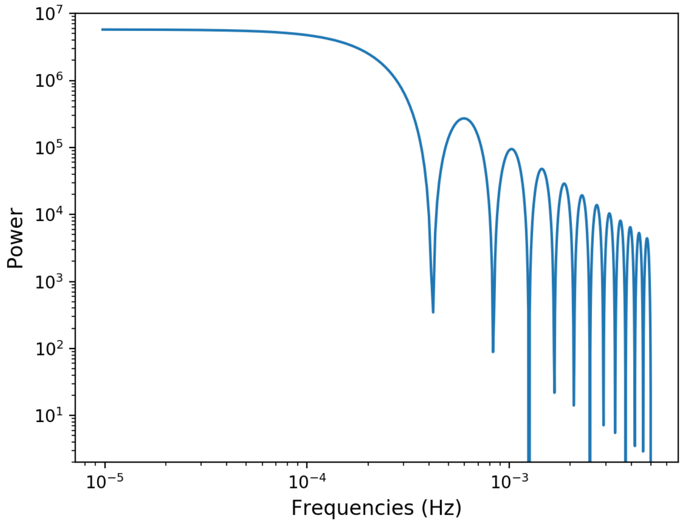

FIGURE 2.4: Fèjer kernal, for a 100 ks observation window, with 'ringing' effects produced where the sinc^2 function approaches zero.

2.5 The origin of AGN variability

X-ray variability is a prominent feature across a significant proportion of observed AGN (Lawrence et al., 1987) and gives an insight into the accretion flow and the coronal regions close to the black hole. Due to the concept of mass invariance in accretion physics, the variability in AGN is commonly seen as analogous to that observed in XRBs, but on considerably longer timescales (see Figure 1.3, and e.g. McHardy et al. 2006).

The origin of intrinsic X-ray variability in both AGN and XRBs is thought to be tied to inward propagation of random turbulence fluctuations of material passing through the accretion disc (Lyubarskii 1997; Kotov et al. 2001; Arévalo and Uttley 2006) – as shown in a basic schematic in Figure 2.5. In the context of X-ray variability, a causal connection between disc and corona must exist, such that the effect of propagation can be considered to be acting equivalently within the corona. The framework for this is dependent on coronal geometry (see Section 1.6.1) and is considered further in Chapter 6.

Through the propagation process, lower frequency fluctuations (at larger radii) actively modulate variability at higher frequencies (at smaller radii), as these fluctuations propagate through the accretion disc. This modulation is a multiplicative process, and is set out mathematically by Lyubarskii (1997), in which each annulus in the disc produces independent turbulent fluctuations, which then lead to local changes in accretion rate described by $\dot{m}(r,t)$. The variability power at each radius peaks at the local viscous frequency, $\nu_{visc} = \frac{r^{-3/2}}{2\pi}\alpha(\frac{h}{R})^2$ (Kato et al., 1998), where higher frequency variability results from fluctuations produced at smaller radii, r, in the disc (where r here is in units

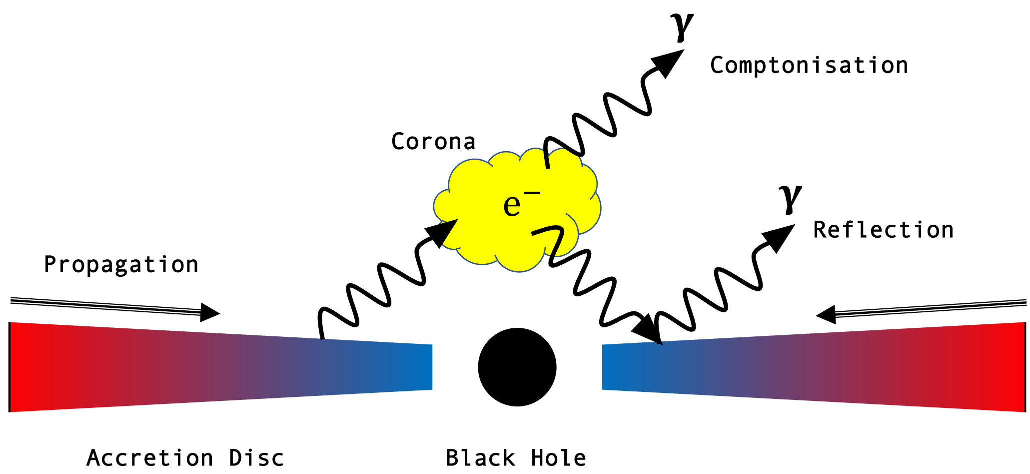

FIGURE 2.5: Basic schematic of a thin accretion disc, with material inwardly propagating towards the central black hole and increasing in temperature, as given by equation 1.14. Variability produced in the disc from the propagation of turbulence fluctuation is imprinted on photons which undergo inverse Compton scattering in the corona. A HFQPO in this schematic could take the form of some orbiting plasma 'hotspot' (Ingram and Motta, 2014), the corona/jet precessing in some quasi-periodic way (Ma et al., 2021) or as part of a standing wave 'breathing mode' (Blaes et al., 2006b) in the disc or near the corona – or indeed some other alternative or combination of multiple effects.

of gravitational radius, such that ν_{visc} is in terms of c/R_g). At any radius, the new accretion rate, $\dot{M}(r_i, t)$, is set by the local accretion rate, $\dot{M}_o(r, t)$ and local fluctuations, $\dot{m}(r_j, t)$, through the multiplicative process:

$$\dot{M}(r_i, t) = \dot{M}_o(r, t) \prod_{j=0}^{i} [1 + \dot{m}(r_j, t)] \tag{2.20}$$

which sets the new value of $\dot{M}_o(r, t)$, at each iterative radial annulus. Variability thus propagates through the disc, with higher frequencies modulated by low frequency variability at outer radii. Importantly, the amplitude of the fluctuations scales with accretion rate (Arévalo and Uttley, 2006). Thus, the amount of radiated flux scales linearly with variability (i.e. rms amplitude), and this directly explains the linear rms-flux relation typically observed across both XRBs and AGN (Uttley and McHardy, 2001). Figure 2.6 illustrates this relationship observed in an observation of XRB Cygnus X-1, across two independent frequency ranges,consistent with propagation through an outer section of the disc ($0.125 - 1$ Hz) into an inner section ($2 - 20$ Hz).

The nature of the propagating fluctuations also sets the shape of the broad-band noise. As the radial position of the propagating fluctuations through the disc is tied to the viscous frequency (Lyubarskii, 1997; Kato et al., 1998; Arévalo and Uttley, 2006), this sets an upper frequency limit for the broad-band noise at the location of the inner edge

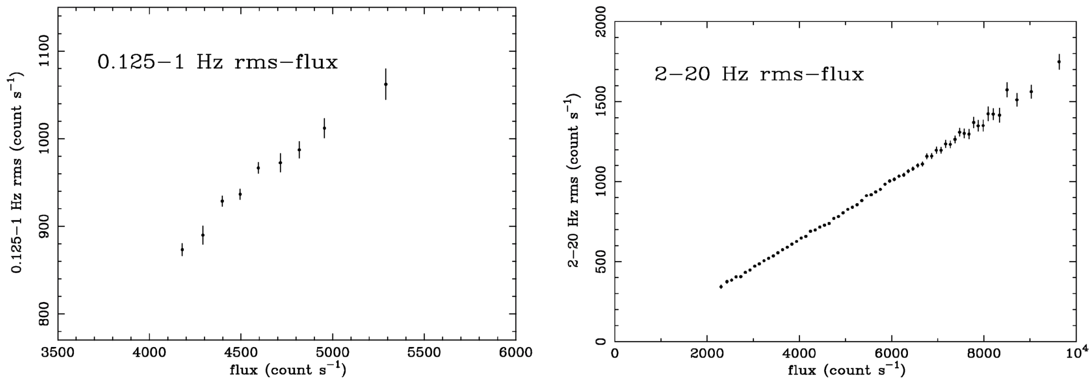

FIGURE 2.6: Linear rms-flux relationships in the same observation of Cygnus X-1, in the energy band $2-13$ keV, and over two frequency ranges, $0.125-1$ Hz and $2-20$ Hz. Original from Uttley et al. (2005).

of the accretion disc – i.e. R_{in}, the ISCO. At any other radii, frequencies above the local viscous frequency are rapidly dampened out by both viscous and differential rotation effects (Churazov et al., 2001; Ingram, 2016), i.e. acting as a low pass filter. The general form of the dampening factor may be described mathematically by $e^{-k_0 t}$, where $k_0 = 1/\tau$, with τ the decay timescale. The Fourier transform of this is given by:

$$\mathcal{F}[e^{-k_0 t}] = \frac{1}{\pi}\frac{k_0}{\nu^2 + k_0^2} \tag{2.21}$$

which is equivalent to a zero-centred Lorentzian.

The broad-band noise in AGN can therefore be understood as the combination of many Lorentzians, across the range of possible viscous frequencies. The presence of low and high-frequency power spectral breaks in AGN, then must be described by some change or dilution in the low pass filter in the propagation fluctuations model. The final break comes at the position of the inner edge, beyond which higher frequencies cannot be generated as material is swallowed by the black hole.

The propagating fluctuations model is also capable of explaining the lognormal flux distribution which is typically observed in AGN. Due to the multiplicative modulation of fluctuations in equation 2.20, a time series, $x(t)$ – which obeys the linear rms-flux relationship over all time-scales – may equivalently be considered as a multiplicative model of sines (Uttley et al., 2005), across frequencies ν_i, with phases ψ_i and with amplitude A_i:

$$x(t) = \prod_{i=1}^{\infty}[1 + A_i \sin{(2\pi\nu_i t + \psi_i)}] \tag{2.22}$$

Taking the logarithm of this time series, and using the multiplication rules of logarithms, it is then possible to represent the above equation as a linear function in log-space, where $a_i = A_i \sin(2\pi\nu_i t + \psi_i)$:

$$\log[x(t)] = \sum_{i=1}^{\infty} \log[1 + a_i(t)] \tag{2.23}$$

Importantly, the a_i terms are *independent* of one another, due to the uncorrelated phases, ψ_i, between the sinusoids. The CLT then approximates the distribution of $\log[x(t)]$ to be Gaussian, if assuming stationarity in the time series. By extension, if $\log[x(t)]$ is Gaussian-like, $x(t)$ is described by a lognormal distribution, which then explains the lognormal flux distribution of X-ray time series (Gaskell, 2004; Uttley et al., 2005).

Both the linear rms-flux and lognormal flux distributions have been considered a universal trait of accreting sources, including AGN and XRBs. Deviation from these models have been reported by Alston et al. (2019) however, who found a non-linear rms-flux relationship – rms $\propto$ flux$^{2/3}$ – and non-lognormal flux distribution in the AGN, IRAS 13224-3809. This suggests either an additional factor is acting to modify these underlying distributions or that the accretion flow is inherently non-stationary (Alston et al., 2019).

2.6 Energy dependence of the AGN power spectrum

A deeper study of X-ray variability is possible using energy resolved lightcurves to probe the energy-dependent shape of the power spectrum. This was first investigated in a $\sim$ 30 day *RXTE* observation of NGC 7469, in which Nandra and Papadakis (2001) reported a flattening of the power spectrum, from $\beta = 1.55$ in the $2 - 10$ keV energy band to $\beta = 1.12$ in the $10 - 15$ keV band. Both Vaughan et al. (2003b) and McHardy et al. (2005) found similar results in MCG-6-30-15, with the former using *XMM-Newton* and reporting a change in power spectral index from $\beta = 2.55$ across $0.2 - 0.7$ keV, to $\beta = 2.30$ across $0.7 - 2.0$ keV and $\beta = 2.10$ in the $2.0 - 10.0$ keV energy band, as shown in Figure 2.7. McHardy et al. (2004) showed the flattening of the power spectrum in NGC 4051 in two energy bands, with Vaughan et al. (2011) doing so over three energy bands using a series of concatenated observations (totalling $\sim$ 570 ks). Most recently, Jin et al. (2020) found the power spectrum in RE J1034+396 flattened with increasing energy, from $\beta = 1.29$ for $0.3 - 1.0$ keV, to $\beta = 0.71$ for $1.3 - 4.0$ keV and $\beta = 0.37$ in the $2.0 - 10.0$ keV energy band.

The power spectral index values, β, are not necessarily identical between AGN, but the energy dependent nature of the AGN power spectral shape is remarkably consistent across multiple observations of multiple AGN, flattening with increasing energy

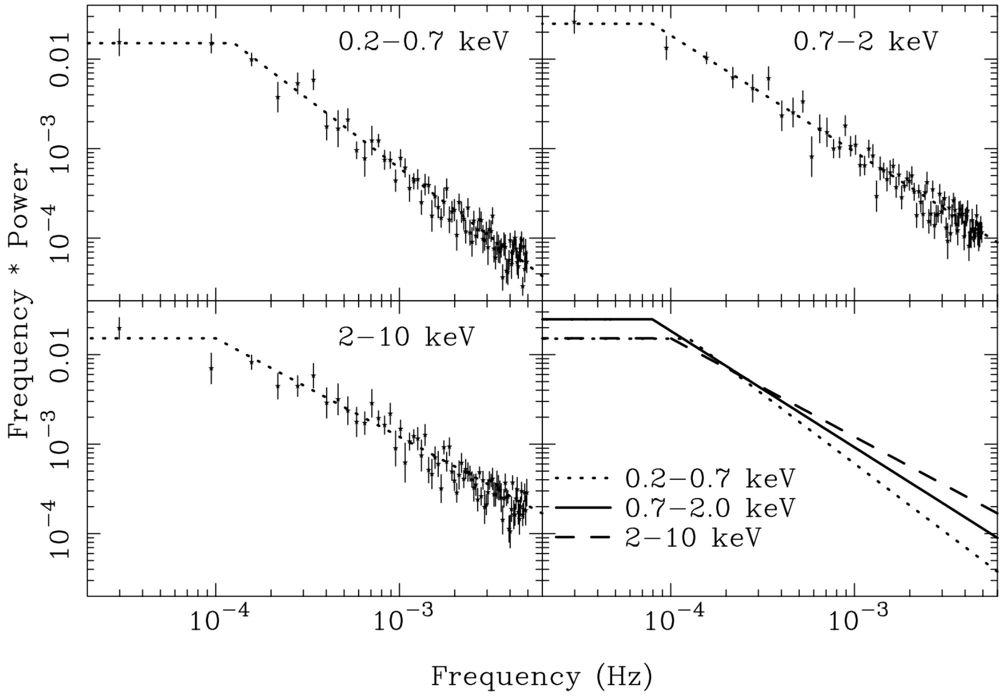

FIGURE 2.7: Energy resolved PSDs, in bands: 0.2 − 0.7 keV, 0.7 − 2.0 keV, 2.0 − 10.0 keV from an observation of MCG–6-30-15, (plotted in $\nu P(\nu)$ vs ν units). The slope of the power spectra (above the high frequency break) is found to flatten with increasing energy, similar to observations of other AGN. Original from Vaughan et al. (2003b)

in each case. The cause for this remains as yet undetermined, but has been suggested to be the result of propagating fluctuations through the disc, at low energies, then interacting with the corona at high energies, with additional variability from the corona enhancing power at high frequencies (Gardner and Done, 2014; Jin et al., 2020), and is investigated further in Chapter 6.

2.7 Quasi-periodic oscillations

Aperiodic variability dominates the X-ray broad-band noise of observed AGN and XRBs. Stable, periodic (or more accurately, quasi-periodic) signals were first detected within the broad-band noise of XRBs (Motch et al., 1983), and are known as quasi-periodic oscillations (QPOs). The fact that these phenomena are observed to be *quasi*-periodic suggests the signal consists not simply of a single stable frequency, but instead of a range of dynamical frequencies – in turn implying that a QPO has some complex radial structure across the accretion flow. X-ray QPOs then offer a unique, diagnostic test of accretion in strong gravity due to the frequencies across which they have been observed.

XRB QPOs are typically categorised as either low-frequency QPOs (LFQPOs) – which are commonly observed at $\sim 0.01 - 1$ Hz – and high-frequency QPOs (HFQPOs) – which are broadly found at $\sim 10 - 100+$ Hz (Remillard and McClintock 2006, Ingram and Motta 2020). Multiple theoretical frameworks have been proposed to explain this phenomenology, both through wave modes through the accretion flow (Tagger and Pellat, 1999; Titarchuk and Osherovich, 1999; Wagoner et al., 2001) and through precession induced by relativistic effects in the presence of strong gravity (Stella and Vietri, 1998; Abramowicz and Kluźniak, 2001; Fragile et al., 2005; Ingram and Motta, 2014). The Relativistic Precession Model (RPM) (Stella and Vietri, 1998; Stella et al., 1999) invokes three non-equal frequencies of precession which a particle experiences in the accretion flow, and connects these modes of precession to the production of QPOs. As described in Ingram and Motta (2014), a particle orbiting at radius r around a mass M in a Kerr spacetime (spin a_*) and perturbed from the equatorial plane, experiences orbital precession (ν_ϕ), periastron precession (precession of the elliptical semi-major axis, ν_{per}) and nodal precession (ν_{nod}) frequencies, which are given by:

$$\nu_\phi = \pm \frac{\zeta}{M} \frac{1}{r^{3/2} \pm a_*} \tag{2.24}$$

where $\zeta = \frac{c^3}{2\pi G M_\odot}$ and r in units of R_g and mass in units of $M_\odot$.

$$\nu_{per} = \nu_\phi \left[1 - \sqrt{1 - \frac{6}{r} + \frac{8a_*}{r^{3/2}} - \frac{3a_*^2}{r^2}} \right] \tag{2.25}$$

$$\nu_{nod} = \nu_\phi \left[1 - \sqrt{1 \mp \frac{4a_*}{r^{3/2}} + \frac{3a_*^2}{r^2}} \right] \tag{2.26}$$

where the top sign refers to prograde orbits and the bottom sign, retrograde. The nodal mode of oscillation occurs as a result of the Lense-Thirring effect (Thirring, 1918), in which the frame-dragging of space-time in a region of strong gravity causes the precession of the orbital spin axis around the spin axis of the central mass (Ingram and Motta, 2014). The Lense-Thirring effect is thought to be the mechanism by which LFQPOs are produced (Stella and Vietri, 1998), and are a relatively commonly observed phenomena in XRBs – as further characterised and summarised by Ingram and Motta (2020). Recent work by Ma et al. (2021) makes an alternative proposition that the LFQPO in XRB MAXI J1820+070 is the result of the precession of the jet, with an energy range exceeding 200 keV, and is a QPO mechanism which will likely be the focus of future investigations.

By comparison to LFQPOs, HFQPOs are far more rarely observed (Ingram and Motta, 2020). They were first observed in GRS 1915+105 (Morgan et al., 1997) at a characteristic

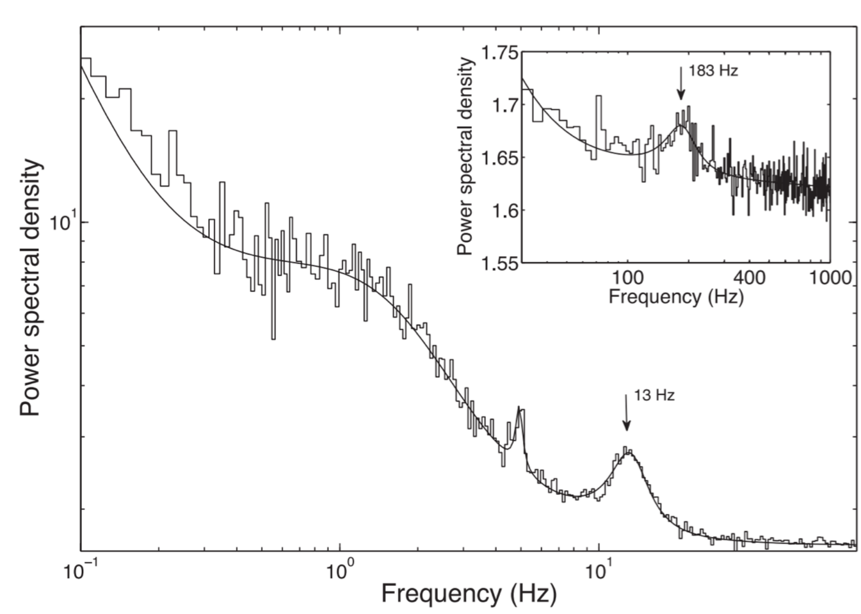

FIGURE 2.8: PSD of XRB XTE J1550-564, with modelled broad-band noise and two LFQPO features at $\sim$ 5 and $\sim$ 13 Hz. The sub-panel highlights a HFQPO at $\sim$ 183 Hz, which is detectable, but less significant above the broad-band noise compared to the LFQPOs. Original from Motta et al. (2014)

$\sim$ 67 Hz, and later at higher frequencies in XRBs such as GRO J1655-40 and XTE J1550-564 etc (Remillard and McClintock, 2006), in which the QPO appears linked to a high accretion rate. HFQPOs have been observed as two distinct frequencies in XRBs, which typically appear in a 3 : 2 resonance with each other. Figure 2.8 highlights an example of a trio of observed QPO features in the PSD of XRB XTE J1550-564 (Motta et al., 2014); two LFQPOs close to $\sim$ 10 Hz and a HFQPO at $\sim$ 183 Hz.

The RPM explains the lower frequency HFQPOs as being produced by periastron precession (equation 2.25) and the highest frequency HFQPOs as the orbit of thermal instabilities or 'hotspots' in a Keplerian orbit (equation 2.24 – Ingram and Motta 2014). In principle therefore, a (theoretical) simultaneous observation of both a LFQPO and HFQPO (3 : 2 resonance) pair allows for equations 2.24, 2.25 and 2.26 to be solved for the key macroscopic, physical properties of mass, radius and the spin magnitude, $|a_*|$, as the solution is degenerate about (prograde/retrograde) spin (Ingram and Motta, 2014).

To first-order, the RPM offers a unique potential to study the properties of the accretion system; it does however have notable limitations. Firstly, on an observational front, the simultaneous observation of these types of QPOs is extremely rare in XRBs (Ingram and Motta, 2014), suggesting that other factors negate the magnitude of these RPM effects. Secondly, the framework for RPM is based on considering a single particle in motion through an accretion flow, whereas a more realistic model must account for the relativistic fluid flow. An alternative mechanism by which HFQPOs may be created has been presented by Blaes et al. (2006b), in which the concept of oscillatory modes, including 'breathing modes' across the accretion disc are invoked. In this framework, pressure gradients across the accretion flow allow for the standing waves to form, with oscillation modes responsible for the production of stable coherent features in the flow which may be observed as QPOs. Interestingly, this methodology has been able to naturally reproduce the observed 3 : 2 resonance between HFQPO pairs.

The concept of mass invariance in accretion flows has then subsequently motivated the search for QPOs in AGN, with their detection a major objective in the field of AGN variability studies for decades (see e.g. Papadakis and Lawrence 1995, Vaughan and Uttley 2005, González-Martín and Vaughan 2012), but one that remains acutely challenging (see e.g. Vaughan et al. 2016). The basis of the search for AGN QPOs is directly tied to the assumption of mass scale invariance in accretion physics, which considers the frequencies across the broad-band noise to scale inversely with the mass of the system, $\nu \propto 1/M_{BH}$ – e.g. Lawrence et al. 1987; Uttley et al. 2002; Vaughan et al. 2003a; McHardy et al. 2004, 2006; Middleton and Done 2010 – such that the expected frequency of an AGN QPO is lower in comparison to its XRB counterpart by a factor equal to the mass ratio between the two (see Figure 1.3). As an example, considering an XRB with BH mass, $M_{BH} \sim 10M_{\odot}$ and AGN with SMBH mass $M_{SMBH} \sim 10^6 M_{\odot}$, an XRB LFQPO observed at a frequency of ~ 0.1 Hz would correspond to a AGN LFQPO at a frequency of $\sim 10^{-7}$ Hz; a period of several months. Considering instead an XRB HFQPO at ~ 100 Hz, the analogous AGN HFQPO would lie at $\sim 10^{-4}$ Hz; a period of several hours. Considering the huge timescales required to observe multiple periods of LFQPOs, this work is limited to searching for HFQPO analogues only.

The value in the detection and study of AGN QPOs is multifaceted. The high luminosity of AGN and the theoretical timescale of an AGN QPO leads to the conclusion that more photons per phase bin are expected to be observed in an AGN QPO, in comparison to any XRB HFQPO (Uttley, 2008), motivating the search for and study of AGN QPOs above those XRB HFQPO counterparts. As a simple calculation, consider an AGN with a mass $\sim 10^6 M_{\odot}$, at a distance of $D_{AGN} \sim 10$ Mpc, and an XRB, with a mass $\sim 10M_{\odot}$, at a distance of $D_{XRB} \sim 1$ kpc. Consider both to be at the Eddington limit and emitting isotropically. The ratio of observed flux per second between AGN and XRB is then given by $L_{AGN}D^2_{XRB}/L_{XRB}D^2_{AGN} \approx 10^{-3}$. If an expected AGN HFQPO frequency is $\sim 10^{-4}$ Hz, and an XRB HFQPO frequency ~ 100 Hz, the AGN HFQPO period is $10^6\times$ longer, and thus would yield an expected $\sim 10^{-3} \times 10^6 \approx 10^3$ times as many photons per QPO phase bin over its XRB analogue.

AGN QPOs therefore allow for a more detailed analysis of both the broad-band noise and QPO structure for an AGN, relative to an XRB. AGN QPO detection and study then offers both an opportunity to test QPO models as well as the concept of mass scale invariance. An example of the former utilises the high signal to noise per phase bin to test whether precession or orbital motion close to the SMBH provide the QPO mechanism.

2.7.1 AGN QPOs: A brief history

The search for AGN QPOs has a long and chequered history, which serves as a lesson in rigorous statistical detection of quasi-periodic signals within sources exhibiting complex broad-band noise (Vaughan and Uttley, 2006; Vaughan et al., 2016). The capability to search for X-ray QPOs was made possible with the advent of X-ray observatories advancing from *EXOSAT* (Taylor et al., 1981) through *RXTE* (see Rothschild et al. 1998; Jahoda et al. 2006) and *XMM-Newton* (see Jansen et al. 2001) – which remains active to the present day. All of these missions featured timing resolution of sufficient precision to allow for detailed study of AGN X-ray variability, including the search for X-ray QPOs (Vaughan and Uttley, 2006).

Early claims of QPO detection were later deemed inaccurate due to not properly accounting for the true *red noise* nature of the underlying broad-band noise observed in AGN. An important property of a red noise time series is the capacity to generate quasi-periodic noise artefacts at random, which are inherently indistinguishable from any intrinsic quasi-periodic signal. As such, proper statistical hypothesis testing is required to determine the nature of the signal. By instead assuming an inappropriate null hypothesis comparing a candidate signal against a purely Poisson noise, several studies (e.g. Halpern and Marshall 1996; Iwasawa et al. 1998; Lee et al. 2000; Boller et al. 2001; Pfefferkorn et al. 2001) reported quasi-periodic features with grossly inflated statistical significance (Vaughan, 2005; Vaughan and Uttley, 2006; Vaughan et al., 2016) across a number of AGN observations. This problem with periodicity detection has also been highlighted in the search for SMBH binary systems (see e.g. Graham et al. 2015a; Graham et al. 2015b; Vaughan et al. 2016). Similarly inflated statistical significances can be reached if not accounting for the full number of *free trials* in any study. For example, searching for a QPO in a single observation but across a broad range of frequencies then must account for the number of frequencies examined, each of which represents a free trial (and in each case a chance for a spurious event to occur in). In order to conduct a robust statistical test of QPO candidates therefore requires a null hypothesis based on well understood broad-band variability and accounting for the full number of free trials. This is the fundamental basis of the methodology presented in Chapter 3.

It is worth noting that the search for AGN QPOs is itself not limited to the X-ray band, with reported detections being made across the EM spectrum, including in the radio (e.g. Zhang and Wang 2021), optical (Smith et al., 2018), and gamma-ray wavebands (e.g. Zhou et al. 2018; Gupta et al. 2019). The physical significance of these reported detections is intriguing, but currently the connection to X-ray QPOs through theoretical frameworks is still in its infancy. In addition to this, there are a subset of (non-X-ray) AGN QPO claims at timescales corresponding to LFQPO analogues (e.g. King et al. 2013; Smith et al. 2018), which consider data from concatenated observations and report QPO timescales of $\sim$ 100s days. At these timescales it is possible to observe low frequency breaks (e.g. Ryan et al. 2019), but discerning the statistical significance of a QPO is challenging, due both to the small number of QPO periods which are observed, and the poorly understood nature of the low frequency break (and thus the broad-band noise). Finally, there have also been reported detection of QPOs appearing after tidal-disruption events (TDEs) (Reis et al., 2012; Pasham et al., 2019), whereby an orbiting or passing star/object is torn apart by the gravity of the central SMBH in a (quiescent) galaxy, and the resultant X-ray emission is detected to show a quasi-periodic feature. These events are likely similar to quasi-periodic eruptions (QPEs) detected in low mass SMBHs, whereby a $\sim$ 9hr quasi-periodic X-ray burst was detected in GSN 069 (Miniutti et al., 2019), before decaying over 54 days of observations. These events are both interesting and offer a new route to investigate X-ray variability produced in AGN, but are somewhat limited in scope due to their inherently transient nature. The X-ray emission fades once the bulk of the material is consumed, and repeated observations are not easily possible. Both LFQPOs and TDE QPOs/QPEs are areas of study has the potential to develop further in future, and may be investigated in the X-ray bandpass with all-sky monitors, such as *MAXI* and *eROSITA*.

An encompassing trend of (almost) all AGN QPOs is the difficulty in observing the most convincing case of QPO detection, in which independent observations report the quasi-periodic phenomena at identical/near-identical frequencies, each over many cycles. This standard has eluded almost all studies to date (Vaughan and Uttley, 2005), and is only reasonably achievable if considering HFQPO analogues.

2.7.2 The RE J1034+396 QPO

The first highly significant X-ray AGN QPO, which proved the exception amongst studies at the time, was found in the NLS1 AGN, RE J1034+396, with a reported $> 5\sigma$ detection found in a selected segment of the *XMM-Newton* lightcurve (Figure 2.9 – Gierliński et al. 2008), with further detections of the same QPO in some, but not all, subsequent observations – including in five of eight observations in Alston et al. (2014b) and most recently again in the newest *XMM-Newton* observation (Jin et al., 2020). The X-ray QPO in RE J1034+396 is thus considered the first, statistically robust, detection of an AGN QPO. The QPO remains present in observations over ten years after the first detection (Jin et al., 2020), and therefore suggests some long-term stability to the mechanism creating this feature.

Figure 2.9 shows the $\sim$ 80 ks X-ray lightcurve, obtained from *XMM-Newton* over an energy range of $0.3 - 10$ keV in the initial QPO detection study (Gierliński et al., 2008). The power spectrum corresponding to this lightcurve is shown in the upper panel of Figure 2.10, with the QPO corresponding to the unmistakable peak in variability power at $\sim 2 \times 10^{-4}$ Hz. The approach to determining the statistical significance of the QPO

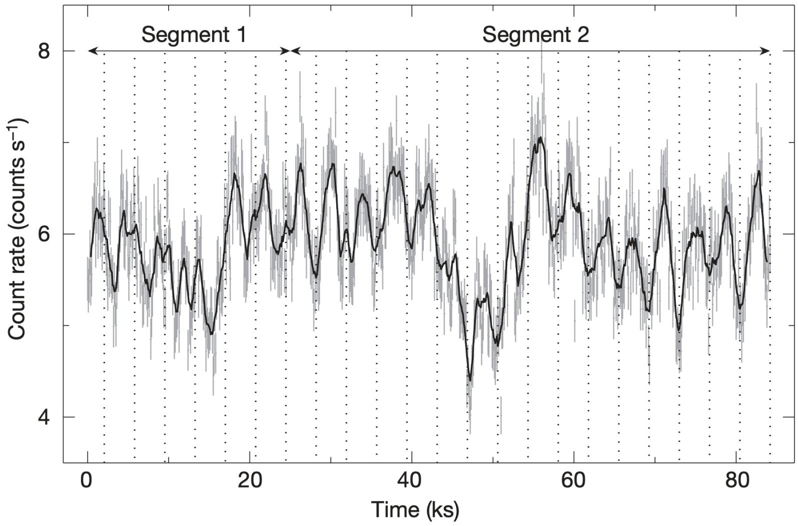

FIGURE 2.9: *XMM-Newton* lightcurve of first detected AGN QPO, in RE J1034+396 over energy range 0.3 − 10 keV. The study focused on 'Segment 2' of the lightcurve, where the periodic feature was found to me coherent. Original from Gierliński et al. (2008).

in RE J1034+396 reported by Gierliński et al. (2008) differs from aforementioned studies by testing an appropriate null hypothesis, based on the modelling the red noise component of the broad-band noise in the power spectrum. 3σ and 99.99% contours are plotted in Figure 2.10, demonstrating the high statistical significance of this QPO feature, which is claimed to be found at $> 5\sigma$. The lower panel of Figure 2.10 plots the residuals of the observed power, $P(\nu)$, over the modelled power, $\mathcal{P}(\nu)$, through the relation $\frac{2P(\nu)}{\mathcal{P}(\nu)}$, and highlights again the statistically significant deviation of variability power in the QPO frequency bin.

It is important to highlight that the study by Gierliński et al. (2008) is not the most conservative of studies, with the $> 5\sigma$ value slightly inflated by the non-blind selection of a section of the lightcurve where the signal is most coherent. This *a priori* data selection biases the result as to inflate the statistical significance of the QPO. Importantly, the full number of trials, representing the number of frequencies in the power spectrum which were investigated, was accounted for. A subsequent study using Bayesian inference by Vaughan (2010) re-evaluate this feature as a $> 3\sigma$ (where 3σ is considered the 'gold-standard' benchmark for a significant detection in a single observation – Vaughan 2005).

In the context of finding further AGN QPOs, the natural question to ask is what makes RE J1034+396 unique? As is typical of many NLS1s, RE J1034+396 appears to host a low-mass SMBH, accreting at or close to the Eddington limit (Boroson, 2002). In addition, spectroscopic study of RE J1034+396 has shown a prominent soft excess is present

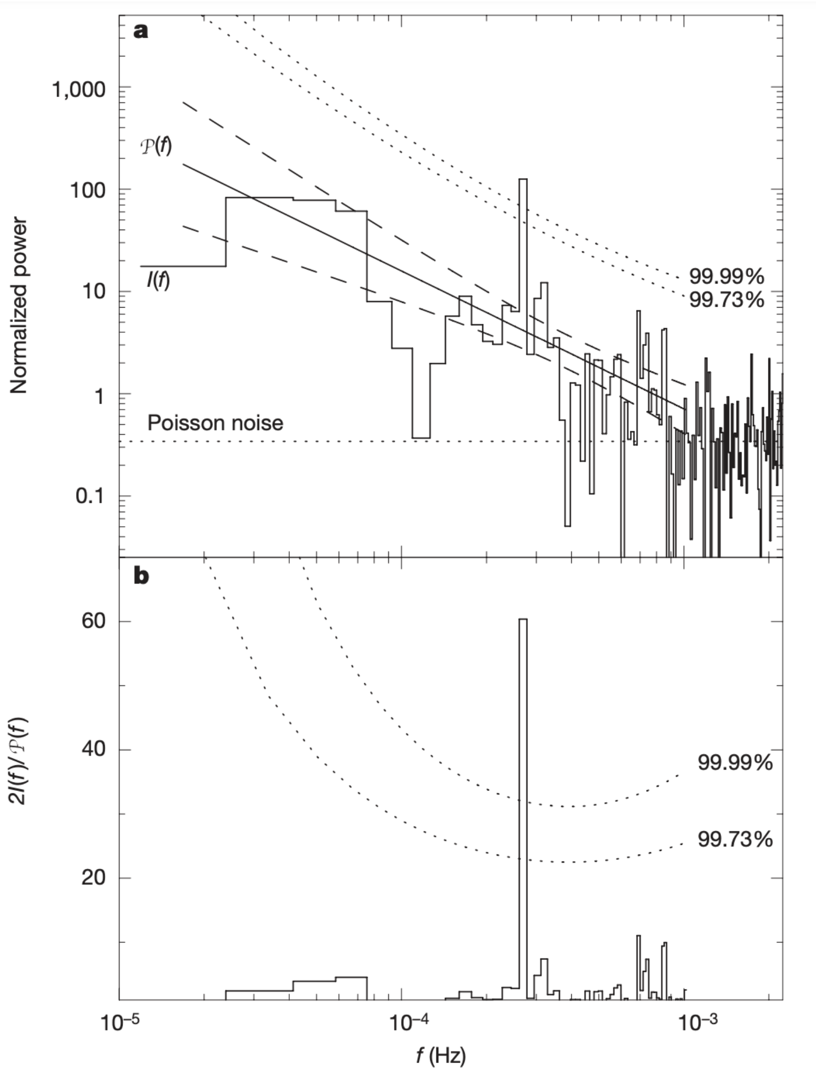

FIGURE 2.10: Upper panel **(a)**: Power spectrum of first detected AGN QPO, in RE J1034+396, with best-fitting power law model $\mathcal{P}(\nu)$ and $(3\sigma, 99.99\%)$ confidence contours. Lower panel **(b)**: Measure of $\frac{2P(\nu)}{\mathcal{P}(\nu)}$ residual of powers above the modelled broad-band noise, where in the figure frequency is denoted by f, not ν, and observed power by $I(f)$, not $P(\nu)$ as in this work. Original from Gierliński et al. (2008).

below 2 keV (Middleton et al., 2009; Jin et al., 2021), which connects to extreme ultraviolet (EUV) emission from the accretion disc (Puchnarewicz et al., 1995; Middleton et al., 2007; Zoghbi and Fabian, 2011).

The presence of a strong soft excess may also act to suppress variability when observing a broad energy bandpass, as in cases where spectral components overlap, variability from one or more components (e.g. the power law continuum, with emission at harder energies) may become damped and effectively swamped by the soft excess. Considering the excess fractional variance, $(\sigma_{xs}/\bar{x})^2$, of an observation as a function of both a soft excess component – with variance σ^2_{sxs} and mean $\bar{x}_{sxs}$ – and a second component, with overlaps in energy with intrinsic variance σ^2_{obs}, mean $\bar{x}_{obs}$ – it follows that this can be represented in the form:

$$\left(\frac{\sigma_{xs}}{\bar{x}}\right)^2 = \frac{\sigma_{\rm obs}^2 + \sigma_{\rm sxs}^2}{(\bar{x}_{\rm obs} + \bar{x}_{\rm sxs})^2} \tag{2.27}$$

Given that the variability of the soft excess component is negligible ($\sigma_{sxs}^2 \sim 0$) (Middleton et al., 2009; Jin et al., 2009b), a system with a high soft excess count rate (high $\overline{x}_{sxs}$) would act to suppress the overall fractional variance at these energies.

The prominent QPO, high Eddington accretion rate and strong soft excess component in RE J1034+396 has led to a search for an XRB counterpart, as an examination of mass scale invariance in accretion physics. Middleton and Done (2010) found a potential analogue in the well-studied XRB GRS 1915+105; with its characteristic $\sim$ 67 Hz HFQPO detected only in the soft-intermediate state (Middleton and Done, 2010; Middleton et al., 2011; Jin et al., 2021). Moreover, Middleton and Done (2010) highlight evidence showing both sources being close to in excess of Eddington, the observed QPO frequencies satisfying a linear mass scaling and similar energy spectra being dominated by the disc and a warm, optically thick, corona; in all hinting at a link in the underlying physical processes between the sources.

The discovery of a bona-fide AGN QPO in RE J1034+396 changed the landscape of AGN QPO studies, providing an effective laboratory to probe the nature of quasi-periodic variability over timescales of $\sim$hours and to subsequently make comparisons to QPOs in XRB systems.

2.7.3 QPO energy dependence

The first examination of the energy dependence of the QPO was by Middleton et al. (2009) who found the rapid variability from RE J1034+396 was most likely from the tail of the Comptonised power law (i.e. a 'hot disc dominated' spectrum), above the constant soft excess, and these spectral characteristics were found to be similar to the low temperature Comptonised disc in GRS 1915+105 by Middleton and Done (2010), prompting the connection between AGN and XRB in this case. Furthermore, Middleton et al. (2009) investigated the energy dependence of the fractional rms at the QPO frequency, finding this peaked at $\sim$ 2 keV and more generally that the variability measured at the QPO frequency could be energy dependent.

Alston et al. (2014b) then used an energy dependent PSD to locate the QPO in eight *XMM-Newton* observations of RE J1034+396, across defined 'soft' $(0.3 - 0.8$ keV); 'hard' $(1.0 - 4.0$ keV$)$ and 'total' $(0.2 - 10.0$ keV$)$ energy bands. They report the significant detection of the QPO in the hard band of five observations, with only a single detection in the soft band – from the original observation studied by Gierliński et al. (2008). Jin et al. (2020) later explored a new observation of RE J1034+396 across three energy bands, $0.3 - 1.0$ keV, $1.0 - 4.0$ keV and $2.0 - 10.0$ keV, in which they again detect the

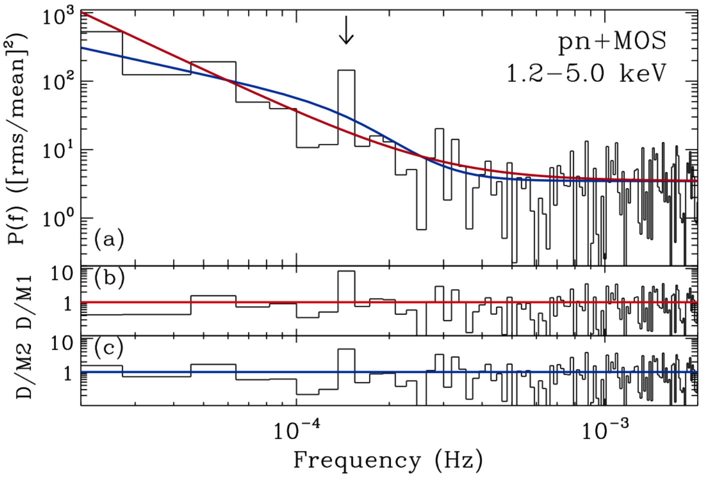

FIGURE 2.11: Upper panel **(a)** Power spectrum of an *XMM-Newton* observation of MS 2254.9–3712 in the $1.2 - 5.0$ keV energy band, with a highlighted $\sim 3.2\sigma$ detection of a QPO candidate at a frequency of $\sim 1.5 \times 10^{-4}$ Hz. Lower panels **(b)**/**(c)** show residuals to both power law and bending power law models, respectively, used to describe the broad-band noise. Original from Alston et al. (2015)

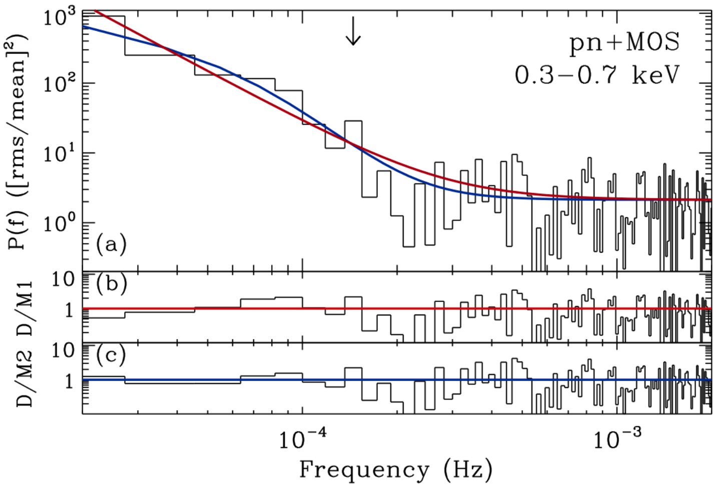

FIGURE 2.12: Upper panel **(a)** Power spectrum of an *XMM-Newton* observation of MS 2254.9–3712 in the $0.3 - 0.7$ keV energy band, with a highlighted non-significant detection of a QPO candidate at a frequency of $\sim 1.5 \times 10^{-4}$ Hz. Lower panels **(b)**/**(c)** show residuals to both power law and bending power law models, respectively, used to describe the broad-band noise. Original from Alston et al. (2015)

QPO to high significance, with no energy dependence in QPO frequency, but with an energy dependence in the rms variability, which increases from 4% in the $0.3 - 1.0$ keV band, to 12% in the $1.0 - 4.0$ keV band (similar to Middleton et al. 2009).

Alston et al. (2015) investigated the NLS1 MS 2254.9–3712, using an energy resolved approach in a single ~ 70 ks observation made with *XMM-Newton*, over four energy bands, $0.3 - 0.7$ keV, $0.7 - 1.2$ keV, $1.2 - 5.0$ keV and $5.0 - 10.0$ keV. The detection of a QPO to $\sim 3.3\sigma$ significance at a frequency of $\sim 1.5 \times 10^{-4}$ Hz in the $1.2 - 5.0$ keV band *only*, is considered the second statistically significant detection of an AGN QPO. Figure 2.11 shows the peak in the power spectrum associated with this feature, relative to two best-fitting power law and bending power law models which describe the broad-band noise. The QPO feature is then shown to be reduced to a statistically *non-significant* level in Figure 2.12, in the $0.3 - 0.7$ keV energy band. Moreover, the absolute rms at the QPO frequency was found to be greatest in the $1.2 - 5.0$ keV band (6%), larger than values measured in the $0.3 - 0.7$ keV band (3%) and $0.7 - 1.2$ keV band (4%), further underlying the energy dependence of the QPO in MS 2254.9–3712.

With a comparable QPO frequency to the one found in RE J1034+396 (Gierliński et al., 2008; Alston et al., 2014b), a similar energy dependence in the statistical strength of the QPO towards harder energies (as reported by Alston et al. (2014b), although not found in a later observation by Jin et al. 2020) and similar energy dependence of measured rms at the QPO frequency (higher towards harder energies), the MS 2254.9–3712 QPO has been seen as comparable to the QPO in RE J1034+396. Moreover, the evidence that MS 2254.9–3712 is a super-Eddington accretor (Wang, 2003) suggests this QPO may be related to HFQPOs in XRBs, similar to RE J1034+396.

The primary drawback in comparing the reported QPO in MS 2254.9–3712 to that in RE J1034+396 is the limitation of a single significant detection. Independent re-detection in a new observation would allow for it to be considered bona-fide.

2.7.4 QPO searches

González-Martín and Vaughan (2012) carried out a deep QPO search of 209 *XMM-Newton* observations of 104 AGN, including of 61 Type 1 AGN and 15 NLS1s, searching across three energy bands: a 'soft' $0.2 - 2.0$ keV, 'hard' $2.0 - 10.0$ keV and a 'total' $0.2 - 10.0$ keV energy band. The key result was the non-detection of QPOs in all bands, with the exception of the re-confirmation of the QPO in RE J1034+396. This has left the field with a population of AGN QPOs limited to RE J1034+396, in addition to the more tentative case of MS 2254.9–3712, as well as the aforementioned questionable claims.

With the relative ubiquity of QPOs in XRBs (although the population of XRB HFQPOs is considerably smaller – Remillard and McClintock 2006) the concept of mass scale invariance predicts that X-ray QPOs in AGN should be of approximate prevalence (Vaughan and Uttley, 2005; Uttley, 2008). Due to the long timescales required to investigate LFQPO analogues in AGN however, the search for AGN QPOs is predominately limited to those rarer HFQPO analogues. The number of detected XRB HFQPOs is low, but higher than the number detected in AGN. This then leads to one of two conclusions, either an (unknown) number of AGN QPOs remain undetected, or, that AGN QPOs are inherently extremely rare phenomena and the QPOs detected in RE

J1034+396 and MS 2254.9–3712 represent exceptional cases, which would prove a substantial finding in itself and motivate further analysis of the idiosyncrasies of the QPO state.

The motivation for finding AGN QPOs has been well documented for many years (e.g. Vaughan and Uttley 2005; Vaughan 2005; Middleton and Done 2010; Middleton et al. 2011; Alston et al. 2014b; Vaughan et al. 2016), as both a test of the nature of the inner accretion flow and in testing the relationship of AGN accretion to that observed in XRBs. The potential for detection of a QPO in specific energy bands has been shown in exploratory analysis (Alston et al., 2014b, 2015), but only on coarse scales, i.e. $2-4$ energy bands over the *XMM-Newton* bandpass. Given the interesting result in MS 2254.9–3712 of a QPO being present in only a single energy band, it remains possible that QPOs in AGN remain undetected in narrower, harder, energy bands corresponding to components in the X-ray spectrum producing the QPO.

Chapter 3

A statistical framework for locating energy-resolved QPOs in AGN

In this chapter I will present a comprehensive analytical procedure to process archival observations of bright AGN using *XMM-Newton*, in the search for QPO candidates. I will first outline the instrumentation used and the AGN sample selected to investigate, before then outlining and discussing the statistical framework which underpins the QPO candidate search.

3.1 Instrumentation

The study of X-ray variability in AGN has been possible with numerous observatories over the past four decades, with data from *EXOSAT* (Taylor et al., 1981), *RXTE* (Rothschild et al., 1998), *XMM-Newton* (Jansen et al., 2001), *Swift* (Burrows et al., 2005), and *NuSTAR* (Collaboration, 2013). Amongst these, the X-ray Multi-Mirror Mission, *XMM-Newton*, has proven a workhorse for AGN timing studies across the $0.3 - 10$ keV energy band and serves as the primary source of data for this research.

3.1.1 XMM-Newton

Launched in 1999, *XMM-Newton* is the primary X-ray observatory for the European Space Agency (ESA). It occupies a $\sim$ 48 hour elliptical orbit, allowing for an upper limit of $\sim$ 40 hour long continuous observations. The satellite carries both an optical/UV telescope, the Optical Monitor (OM), and a trio of X-ray focusing mirror modules, each with a CCD detector known collectively as the European Photon Imaging Cameras (EPIC). EPIC is partitioned into a set of two Metal Oxide Semi-conductor CCD arrays (MOS-1, MOS-2; Turner et al. 2001) and a p-n junction semiconductor CCD array

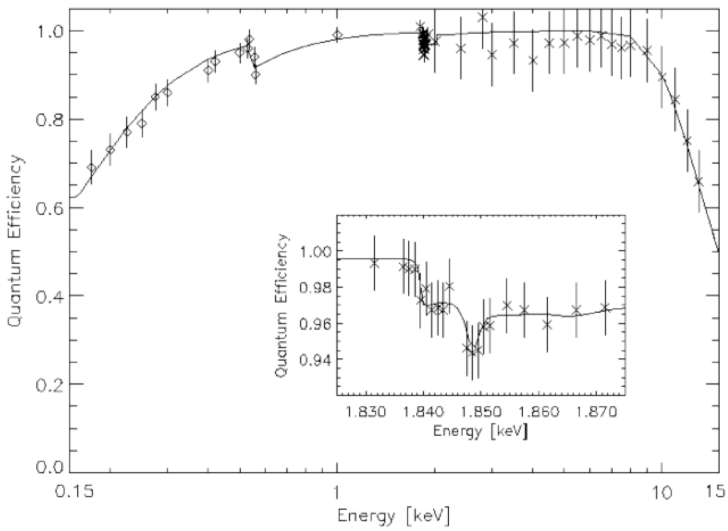

FIGURE 3.1: Energy dependence of the quantum efficiency of the EPIC-pn instrument aboard *XMM-Newton*, which declines below $\sim$ 0.4 keV and above $\sim$ 8 keV. The inset shows the 'X-ray absorption fine structure' close to the silicon K edge at $\sim$ 1.838 keV (Strüder et al., 2001). Original from Strüder et al. (2001).

(pn; Strüder et al. 2001). In addition, the MOS modules house the Reflection Grating Spectrometers (RGS-1, RGS-2; den Herder et al. 2001), used for high resolution X-ray spectroscopy.

EPIC offers a theoretical energy range of $0.1 - 15$ keV, but due to quantum efficiency (e.g. Figure 3.1) and effective area (e.g. Figure 3.2), this is effectively limited to a useful energy range of $0.2/0.3 - 10$ keV. The pn detector is typically favoured over the MOS detectors due to higher effective area over $0.2/0.3 - 10$ keV, but all cameras may be used in unison. The CCDs effectively act as individual photon counters, recording the time, energy and location of each photon as it reaches the detector. The large effective area and fast read-out time of each detector allows *XMM-Newton* to excel in studies of X-ray variability, in addition to being capable of imaging sources, which detectors such as *RXTE* were not capable of. In cases of particularly bright sources however, the observation may be at risk of pile-up, which occurs when the count rate is so high that multiple soft photons incident on the detector are misassigned as a single, hard photon event.

The continued use of *XMM-Newton* over two decades of operation has allowed for a comprehensive catalogue of AGN observations to be developed; a resource which is utilised throughout this work. Observational data files may be downloaded from the XAMIN[1] database, and processed using the *XMM-Newton* Science Analysis System (SAS)[2].

[1]https://heasarc.gsfc.nasa.gov/xamin/
[2]https://www.cosmos.esa.int/web/xmm-newton/sas-threads

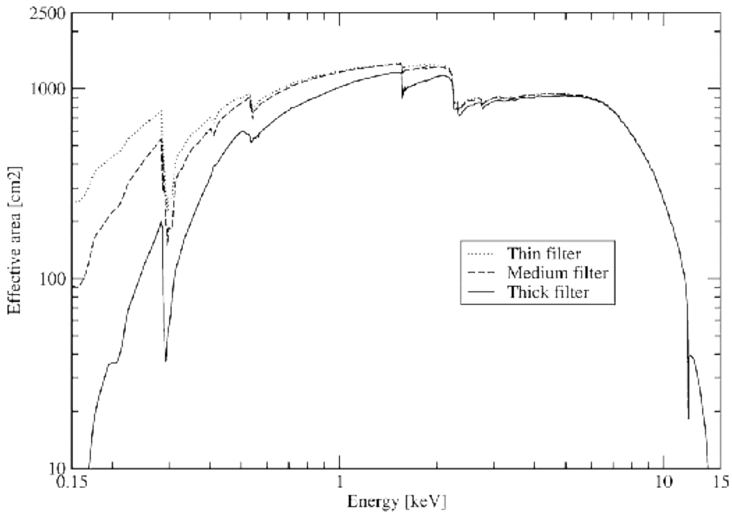

FIGURE 3.2: Energy dependence on the effective area (cm^2) of the EPIC-pn instrument aboard *XMM-Newton*, simulated using three different filters which act to reduce exposure to non-X-ray photons and protect the CCDs from soft protons in orbit. In all cases, the effective area is most prominent in the $1-2$ keV energy range, while diminished below 0.3 and above 10 keV. Original from[3].

3.2 Observations

3.2.1 AGN sample

The AGN sample is constructed primarily from the Palomar Green QSO (PGQSO) catalogue used by Crummy et al. (2006a) and Middleton et al. (2007) as these are extremely bright sources and have been well-studied by *XMM-Newton*; this provides high signal-to-noise ratio data and the possibility of long (up to 130 ks) unbroken observations. In addition to this sample, the AGN 1H 0707-495, MS 22549-3712, NGC 4151, PHL 1092 are included, and data from the most recent campaign on IRAS 13224-3809 (see Alston et al. 2019, 2020 for details). The total sample consists of 22 NLS1s and 16 Type-1 Seyferts (38 AGN total), as defined by Veron-Cetty and Veron (2010). Across these AGN, there are 200 observations in total which are included in this study. Of particular interest are the Narrow Line Seyfert 1 AGN, which include the widely-accepted case of X-ray QPOs in RE J1034+396 (Gierliński et al., 2008) as well as the reported case in MS 2254.9-3712 (Alston et al., 2015).

3.2.2 Data reduction

For each AGN in this sample, all observations in the *XMM-Newton* public HEASARC archive[4] up to September 2019 were extracted (see Appendix A). Data for this analysis

[3] `https://xmm-tools.cosmos.esa.int/external/xmm_user_support/documentation/uhb/epicfilters.html`

[4] `https://heasarc.gsfc.nasa.gov/`

were limited to the EPIC-pn detector, as the pn has a higher throughput than the MOS detectors leading to a lower Poisson noise contribution. A circular aperture source region of 40″ radius was centred on each AGN, with a background source region (also a circular aperture of 40″ radius) positioned on the same CCD, but away from the source and chip read-out direction. Following standard procedure, only single/double pixel events (with `PATTERN<=4`) were selected. Using the standard *XMM-Newton* data reduction pipeline[5] , the source and background light curves were extracted, using `EVSELECT` in *SAS* v*17.0.0*. These lightcurves are of a 100s binsize and utilised a sliding energy window across the nominal $0.3-10$ keV range of the instrument. This window is split into 50 approximately linear energy bins, allowing 1225 energy combinations to be studied (e.g. $0.3-0.5$ keV, $0.3-0.7$ keV etc.). `EPICLCCORR` was then used to subtract the background and apply the necessary corrections (e.g. vignetting, bad pixels, good-timing-intervals etc.[6]) to the lightcurves. Whilst detector pile-up is present in some of the observations, the redistribution of counts from soft to hard energies (where the count rate is typically much lower) is not expected to lead to false QPO detections as non-QPO counts act to dilute the signal's presence. Pile-up could, however, result in QPO candidates being located in energy bands in which they are not intrinsically the strongest.

For each observation, the high-energy ($10-12$ keV), full-field background lightcurve was extracted with a binsize of 10s in order to identify soft-proton events which could contaminate the source lightcurve. A cut-off is applied such that any flares at 5σ (where σ is the standard deviation in the $10-12$ keV lightcurve) or more above the stable (non-flaring) count rate level are removed – this is achieved through sigma-clipping outlier rejection above a flat background model which is fitted to this $10-12$ keV lightcurve. This process can introduce gaps into the lightcurves, which, if left unmodified, have the potential to introduce spurious peaks in power (introducing inaccuracies into both broad-band noise modelling and any subsequent QPO detections). Whilst there is no standard method to correct for gaps, previous approaches include linearly interpolating between short missing segments of data (e.g. <200s), with count-rate variations accounted for by drawing from a Poisson distribution (González-Martín and Vaughan, 2012; Alston et al., 2015). This method has the caveat of introducing a non-red noise background component to the light curve, which cannot replicate the component which has been removed, and thus is best applied sparingly (e.g. the interpolation used by Alston et al. 2015 is typically applied to $<0.5\%$ of the duration of the lightcurve). In this analysis, the most conservative approach is taken in considering only the longest continuous segment between flares (see Figure 3.3). This avoids all interpolation assumptions, but has the limitation of reducing the amount of data available for analysis.

[5] https://www.cosmos.esa.int/web/xmm-newton/sas-thread-timing
[6] https://heasarc.gsfc.nasa.gov/docs/xmm/sas/help/epiclccorr/node3.html

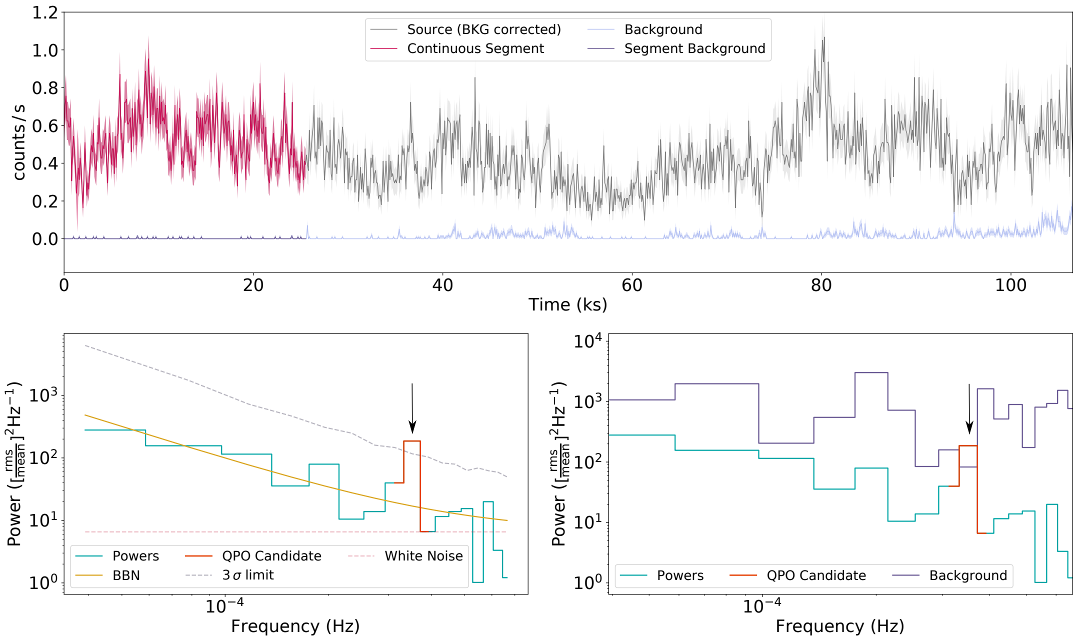

FIGURE 3.3: Top: the entire *XMM-Newton* EPIC-pn light curve for NGC 4051, OBS ID: 0109141401 over an energy range: $4.0 - 6.4$ keV, with the longest continuous (flareless) segment highlighted. Bottom left: periodogram of the background subtracted, flareless segment, with best fitting PLC model, simulated 3σ line and QPO candidate highlighted. Bottom right: a direct comparison between the source and background periodogram, highlighting the lack of a corresponding peak of power in the background at the QPO candidate frequency.

However, many of the longest continuous segments in the sample are of sufficient duration to probe down to $\leq 10^{-4}$ Hz, below the frequencies of previously detected AGN QPOs (Gierliński et al., 2008; Alston et al., 2015).

The data reduction process (i.e. through EPICLCCORR) requires the creation of the background source lightcurve; the periodogram of which is inspected to ensure that any potential QPO is associated only with the AGN itself. An example of this is shown in Figure 3.3, where the absence of a feature in the background confirms this example QPO candidate originates in the AGN, in this case, in NGC 4051 (see Section 3.3.3.1 for how the QPO candidate in this example is explicitly defined).

3.3 Periodogram analysis and QPO search

A robust statistical framework in which to search for QPOs in broad-band noise is vital (see Vaughan and Uttley 2005), and the approach presented here is based on that of Vaughan (2005). Periodograms are produced for each energy-resolved lightcurve (with lightcurves reduced to 2^n bins where n is an integer) by applying a fast-Fourier transform (FFT) and a fractional-rms normalisation (Vaughan et al., 2003a). As explained in Section 2.3.3, using the periodogram (rather than the PSD) allows the number of

Fourier frequencies to be maximised, improving parameter constraints when modelling, whilst also allowing for QPO searches down to the lowest possible frequencies in the lightcurve.

3.3.1 Maximum likelihood statistics

Modelling the periodogram requires appropriate use of statistical methods. Standard regression techniques such as ordinary least-squares or χ^2 regression are biased by the assumed Gaussian nature of the data which they are applied to. As such, if not using a highly averaged form of the PSD, an alternative method which is not biased by the non-Gaussian nature of the periodogram is required. Anderson et al. (1990), Stella et al. (1994) and Vaughan (2005) all implement a form of the Whittle likelihood statistic (Whittle, 1953) for such a case, derived from the probability density function of periodogram ordinates (Duvall and Harvey, 1986), where:

$$p(I_j) = \frac{e^{-I_j/\mathcal{P}_j}}{\mathcal{P}_j} \tag{3.1}$$

for observed powers, I_j, the expectation value of the periodogram, $\mathcal{P}_j$ – equivalent to the 'true' underlying distribution assumed by a frequentist framework – and frequencies j (where $j = 1,\ 2,\ ...\ n-1$, due to the Nyquist being distributed differently).

Given a model, $P_j(\theta_k)$, with parameters $\theta_k = (\theta_1 ... \theta_{\mathrm{M}})$ to represent these data, the joint probability density gives the form of the likelihood, $\mathcal{L}$, here over a frequency range $j = (1 \rightarrow n-1)$:

$$\mathcal{L} = \prod_{j=1}^{n-1} p(I_j) = \prod_{j=1}^{n-1} \frac{e^{-I_j/P_j}}{P_j} \tag{3.2}$$

where the likelihood then represents the conditional probability relating observed powers to model parameters, $p(I_j|\theta_k)$. The likelihood represents a distribution with its peak (maximum likelihood) described by model parameters, $\hat{\theta}_k$.

Taking the logarithm of equation 3.2, gives:

$$\ln \mathcal{L} = \sum_{j=1}^{n-1} \left[-\frac{I_j}{P_j} - \ln[P_j] \right] \tag{3.3}$$

Defining the negative log-likelihood as $S = -2 \ln \mathcal{L}$, it then takes the form:

$$S = 2\sum_{j=1}^{n-1}\left\{\ln[P_{\rm j}] + \frac{I_{\rm j}}{P_{\rm j}}\right\} \tag{3.4}$$

with minimising S being equivalent to maximising the likelihood.

3.3.2 Broadband noise models

Similar to the work by González-Martín and Vaughan (2012), the above maximum likelihood statistic is used to fit the sample periodograms, with two selected models.

The first (PLC) is a power law plus constant model:

$$P(\nu) = N_0 \nu^{\beta} + C \tag{3.5}$$

and consists of three free parameters: β, the power spectral index, N_0, the normalisation and C, a constant to account for Poisson noise. This is the simplest common model for fitting red noise power spectra.

The second model (BKNPLC) takes the form of a broken power law, with break frequency, ν_b:

$$P_1(\nu) = N_1 \nu^{\beta_1} + C \quad \text{for } \nu \leq \nu_{\rm b}$$
$$P_2(\nu) = N_2 \nu^{\beta_2} + C \quad \text{for } \nu > \nu_{\rm b} \tag{3.6}$$

At frequencies at, or below the break ($\nu \leq \nu_{\rm b}$) the model assumes a power spectral index β_1 and normalisation N_1, whilst at frequencies above the break ($\nu > \nu_{\rm b}$), a power spectral index β_2. The normalisation above the break, N_2, is calculated directly from the previous parameters. In using both models, the constant (C) is fixed to the expected level of the white noise following the method as in equation 2.16.

The broken power law model is motivated by the presence of high-frequency breaks, detected in several AGN (Papadakis et al., 2002; Markowitz et al., 2003; McHardy et al., 2006; González-Martín and Vaughan, 2012). It has analogues such as the bending power law model (see e.g. McHardy et al. 2004; González-Martín and Vaughan 2012; Alston et al. 2019) which similarly search for a 'flattening' of the power spectrum at low frequencies, but here the BKNPLC model is implemented to search for a 'sharp break' occurring at the break frequency, $\nu_{\rm b}$. Although breaks in AGN power spectra are readily observed, a power spectral break may not be found in some cases, leading to a PLC model being statistically preferred. Reasons may include the physical absence of a break feature, but also an insufficient frequency range (in the investigated periodogram) to probe the break, often such that those observed frequencies are above the break. This likelihood is increased given the multiple, individual observations investigated here, as opposed to studies which utilise a single, concatenated lightcurve.

3.3.3 Analysis procedure

The PLC model is first applied to each periodogram, using the maximum likelihood statistics (equation 3.4) inbuilt into a limited memory Broyden-Fletcher-Goldfarb-Shanno (L-BFGS-B) minimisation algorithm (see Fletcher 1987), with bounds set at (-10, 10) for β and $(0, \infty)$ for the normalisation, N_0. A preliminary fit is performed with this minimisation routine to obtain the maximum likelihood parameters $(\hat{\beta}, \hat{N_0})$ which are successful in minimising the negative log likelihood, S.

Following the procedure of Vaughan (2005), a *frequency cut* is made where the Poisson noise begins to dominate in this preliminary PLC model (defined where $C > P_j$), such that all frequencies above this are ignored. This cutoff procedure ensures the model fit is not dominated by white noise, which can hinder the selection of a statistically preferred model. It does create the caveat that information at frequencies above the white noise threshold is lost, such that any QPO candidate located at such frequencies will not be considered; this is considered an unlikely scenario however, as the red noise is sufficiently diminished at these frequencies.

In practice, a minimum number of Fourier frequencies are required in the remaining periodogram to ensure a sufficient number of degrees of freedom to constrain the underlying noise with simple models. There is no agreed upon minimum number, so this value is arbitrary, but as a very general rule of thumb it is advisable to have approximately five data points per degree of freedom. In this analysis, the lower limit is set to be 13 Fourier bins, below which the periodogram is considered white noise dominated and is disregarded. Note, any energy-resolved lightcurve where the fitting returns a positive β is also rejected at this stage, given this only occurs in the case of poor data quality or white noise dominated data.

3.3.3.1 Defining the null hypothesis

The analysis procedure defines a QPO candidate to be a peak of power above the modelled (white noise cutoff) broad-band noise. For both simplicity and conservatism, a candidate is defined to exist within a single Fourier frequency bin. A single QPO candidate is determined for each periodogram at this stage, following the method in Vaughan (2005) whereby for each frequency, the ratio $R = 2I_\mathrm{j}/P_\mathrm{j}$ is calculated (comparing the observed powers I_j and model powers, P_j). The frequency, j, in which R_j is maximised, is then defined as the QPO candidate frequency, ν_Q, with power, P_Q, at this ratio R_Q.

In order to determine the statistical significance of any outlier (here, the QPO candidate), a null hypothesis must be defined; in this case, the null hypothesis is that the observed QPO candidate power, P_Q, is due to an inherently random, statistical fluctuation of the underlying red noise, itself intrinsic to the AGN. Following Vaughan (2005), this Fourier bin is removed from the periodogram (leaving ≥ 12 bins as per the predefined restrictions above) and the broad-band noise refit up to the previously defined white noise cutoff frequency, at first with a PLC model (and subsequently with a BKN-PLC model, see Section 3.3.3.2), in order to obtain the best description of the underlying continuum (the impact of fixing the position of the white noise cutoff is discussed in Section 5.3.1).

The applied methodology to refit the periodogram utilises a bootstrap-with-replacement L-BFGS-B minimisation algorithm, using maximum likelihood statistics (equation 3.4), over $10,000$ iterations. Over the $10,000$ bootstrap iterations, a minimum of 5% are required to fulfil the minimisation success criteria as predefined by the SCIPY L-BFGS-B minimisation algorithm[7](in practice, this number is typically $> 95\%$), which also includes returning a negative value of β. The successfully minimised bootstrapped parameters are grouped into a histogram, with 100 bins, with the maximum likelihood set of PLC parameters, $(\hat{\beta}, \hat{N}_0)$, given by the median of this distribution. The 68% confidence limits are constrained using the $[16, 84]$ percentiles, to constrain the variation about $(\hat{\beta}, \hat{N}_0)$. This minimised PLC model now describes the broad-band noise minus the QPO candidate.

This bootstrap-with-replacement method has several advantages over a single fitting iteration, in that it minimises the biasing effect of any individual bins on the overall model fit, and inherently samples the parameter space, returning a discrete sample of parameters from this probabilistic distribution. The former point is important given the QPO candidate search focuses on a single Fourier frequency, and any excess power in adjacent bins have the potential to bias the fitting process towards a flatter power law index, β, and higher normalisation, N_0, in extreme cases. The latter point is used directly to obtain the uncertainty on the minimised PLC model, which is illustrated in Figure 3.5.

3.3.3.2 Power law vs broken power law

Given sufficient data quality, AGN power spectra spanning a large frequency range may be better described by a broken power law (Uttley et al., 2002; McHardy et al.,

[7] https://docs.scipy.org/doc/scipy/reference/optimize.minimize-lbfgsb.html#optimize-minimize-lbfgsb

2007; González-Martín and Vaughan, 2012). For the BKNPLC fitting process, the L-BFGS-B minimisation algorithm was again used, with bounds of (-10, 0), (-10, 0), (0, ∞) for parameters β_1, β_2 and N_1 respectively, over a set of possible break frequencies: $\nu_{\mathrm{b,j}}$ – spanning the white noise cutoff frequency range $\nu_1 \rightarrow \nu_{n-1}$ (n here is the number of Fourier bins in the white noise cutoff periodogram) and with a resolution twice that of the Fourier frequencies. As before, it is required that β_1 and β_2 take only physically relevant, negative values, otherwise the BKNPLC model is rejected. Additionally, any maximum likelihood model fit where $\beta_2 > \beta_1$ is also rejected. Importantly, this again is a fully frequentist procedure, which sets no priors or weighting towards any set of break frequencies, or any other parameter. This test is designed to be simply driven by the shape of the broad-band noise, without using *a-priori* knowledge from previous observations of high-frequency breaks. Ultimately this is a trade-off between a more computationally intensive Bayesian approach with priors based on a very limited sample of well studied (energy resolved) AGN high-frequency breaks, and a more computationally efficient, 'agnostic', frequentist search for breaks.

Given the best-fitting BKNPLC and PLC models for a periodogram, a test is needed to discern the statistically preferred model. One method involves use of the likelihood ratio test between two nested models (the more complex model reverts to the simple model in a specific case), where $R = -2\ln[\mathcal{L}_1/\mathcal{L}_2] = S_1 - S_2$, which is then distributed as a χ^2_ν variable (Vaughan, 2005). A more general approach, which does not require nested models) is to use an information criterion test, such as the Aikike Information Criterion (AIC) (Akaike, 1974) or the Bayesian Information Criterion (BIC) (Liddle, 2007). Both tests act to penalise the addition of free parameters, measured against the negative log-likelihood. Here, the BIC test is used as the penalisation term scales with the natural log of the number of frequency bins, then guarding against over-fitting in the case of a periodogram observed over a large frequency bandpass (the AIC sets only a scalar penalisation term).

In order to perform a consistent BIC test, the number of frequency bins are kept the same between PLC and BKNPLC models. The BIC is defined as:

$$BIC = S + k\ln(m) \tag{3.7}$$

with negative log-likelihood, S, number of model parameters, k and number of data points, m (the number of data points in the periodogram). The BIC value is minimised for the most statistically preferred model, i.e. it allows for the identification of which model, PLC or BKNPLC, best describes the observed data (the impact of noise entering from outside of the bandpass is explored in Section 5.3.2).

Across the sample of non-white noise dominated observations (i.e. those with sufficient data points to be processed through this analysis), the results show the BKNPLC model

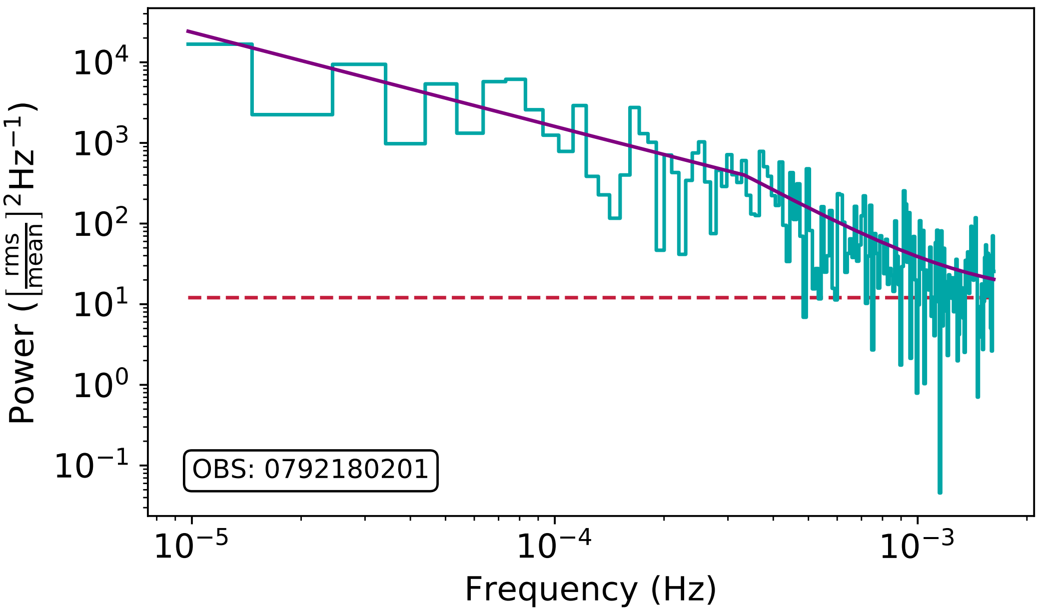

FIGURE 3.4: An example case of IRAS 13224-3809, OBSID:0792180201, where the periodogram is preferentially fitted with a BKNPLC (in purple) over a PLC model, following the BIC criteria set out in equation 3.7. The plot also shows the level of underlying white noise in red.

is preferred in $\sim$ 10% of cases. This sample includes the re-identification of break features in observations first reported in González-Martín and Vaughan (2012), in a study that, by comparison, found 16% of AGN PSDs in their sample to be best described by a bending power law, and, as with this analysis, the majority instead by a simple power law. An example of this methodology fitting a BKNPLC model is shown in Figure 3.4.

It is worth noting that the nature (e.g. the position and energy-dependence) of the break is not well constrained across a large sample of AGN. Indeed, in some cases, e.g. RE J1034+396 as in Gierliński et al. (2008), a power law is sufficient to describe the broad-band noise over the full *XMM-Newton* bandpass, down to $\sim 10^{-5}$ Hz. Caution must be taken however, to ensure that neither QPO candidate nor the broad-band noise model are compromised by the presence of the break even after maximum likelihood fitting and model selection through the BIC test – biases which are considered further in Section 3.3.4. For simplicity, the primary focus of the subsequent analysis is on the remaining datasets best described with a PLC model.

3.3.3.3 Uncertainty on the best-fitting PLC model

A common approach amongst previous AGN periodogram studies is to consider the maximum likelihood broad-band noise (e.g. PLC) model in isolation, free from any underlying uncertainty. To have a more complete grasp of the null hypothesis however, the uncertainty on the maximum likelihood parameters which describe the broad-band noise model must be considered. For a generic M-dimensional model, the relationship between parameters would be expected to form an M-dimensional paraboloid, which Vaughan (2005) demonstrates takes the form of a highly covariant ellipse between $(\beta, \log[N_0])$ parameters in the 2-dimensional, PLC, case.

Following the approach of Vaughan (2005), $\Delta S = -2\Delta \ln[\mathcal{L}]$ values may be used to map confidence contours across parameter space, analogous to the $\Delta\chi^2$ statistic. The 1σ parameter limits are defined following χ^2_ν where in this case, ν is the number of model parameters (such that a 1σ deviation for a 2-dimensional model occurs at $\Delta S = 2.3$), and may be determined from mapping the ΔS space. Given these confidence limits, it is then possible to determine the terms of the covariance matrix (Coe, 2009) describing the M-dimensional Gaussian distribution, which can then be used as the basis for subsequent Monte Carlo simulations.

A direct approach to modelling the parameter space is to use a numerical grid; this allows the 1σ parameter limits to be accurately determined, but is computationally intensive and also dependent on the data quality (which sets the scale of the initial grid). Semi-analytical methods assuming a Gaussian symmetry in the parameter space were also tested and found to provide reasonable limiting values, however, such symmetry may not hold universally (i.e. in the case where the sampled parameter space is not perfectly Gaussian, nor symmetric). A third approach is to utilise the bootstrap method (Section 3.3.3.1) which *automatically* constructs a discretised distribution of model parameters, centred on the best fitting values. This discrete distribution represents a probabilistic sampling of parameter space, which may then be described by a continuous function (defined by an $M \times M$ covariance matrix). One effective method of modelling this discretised bootstrap dataset is through the application of a Gaussian-mixture-model (GMM), unsupervised machine learning approach, which identifies and describes the data as a continuous model. The GMM uses a single Gaussian, or sum of Gaussian distributions, with inbuilt maximum likelihood statistics in its fitting process, using an internally defined covariance matrix. The GMM algorithm implemented in this work is available from the SCIKIT-LEARN library (Pedregosa et al., 2011).

The BIC test is again utilised to determine the number of independent Gaussians needed in the GMM to best describe a given boostrapped dataset. For every iteration of GMM, an additional Gaussian distribution is included, up to a maximum of 10 iterations. The BIC penalises the added complexity of additional model parameters and the BIC value is minimised in the case where the likelihood is sufficiently high for a sufficiently low number of model parameters, through equation 3.7. Using this, the GMM successfully models the bootstrap dataset with a combination of Gaussian distributions, and allows for an efficient and effective modelling of ΔS parameter space. Parameters may then be

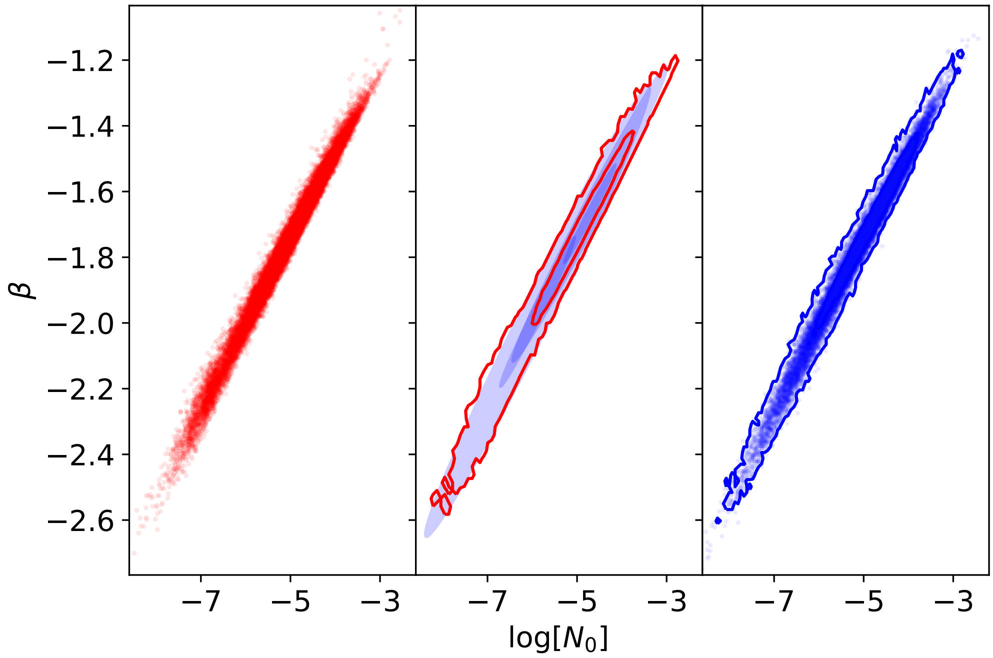

FIGURE 3.5: Plots showing the modelling of PLC parameter space applied to the broad-band noise, used to define the null hypothesis and constrain the QPO candidate significance. Left: discretised bootstrap distribution of PLC parameter space. Middle: a two-stage (i.e. two overlapped Gaussians) GMM model (blue), with bootstrap $\sim 68.3\%$ and $\sim 99.7\%$ probability density contours. Right: individual GMM parameter draws, with highlighted $\sim 68.3\%$ and $\sim 99.7\%$ probability density contours (i.e such that $\sim 99.7\%$ of parameters drawn directly from the GMM lie within the outer contour).

drawn directly from this GMM distribution. Figure 3.5 outlines this procedure, showing an example of a discrete bootstrap sample (left hand panel), which is modelled by the GMM using two overlapping Gaussian distributions, which are shown to match well to the discrete sample (middle panel) which then allows for the random drawing of $10,000$ samples from this continuous distribution, which replicate the expected highly covariant elliptical shape of parameter space (right hand panel).

This approach to modelling uncertainty on the broad-band noise model is effective and efficient, but by no means the only option. A commonly used, alternative approach is through the use of a Markov-chain Monte Carlo (MCMC) methods. An MCMC is a dependent sampling method for exploring and describing the posterior probability distribution in Bayesian statistics (see e.g. Lambert 2018). As in Vaughan (2010), an MCMC may be applied to model the broad-band noise and associated error through credible intervals defined through this method. The computational intensity of MCMC methods do not suit the scale of this analysis however, given a maximum of $245,000$ lightcurves/periodograms (1225 energy binned lightcurves for each of the 200 observations in this sample) under investigation. As such, the bootstrap-GMM approach presented here is considered a viable and effective frequentist alternative.

3.3.3.4 QPO candidate significance testing

To evaluate the statistical significance of QPO candidates identified in the energy-resolved periodograms the analysis performs Monte Carlo simulations of red noise power spectra through the method described in Timmer and Koenig (1995). In this procedure, a red noise time series is simulated, for some chosen index, β, through a random walk. For each iteration of the walk, two numbers are drawn at random from a Gaussian distribution ($\mu = 0, \sigma = 1$) and are used to form the real and imaginary components (R_{Re}, R_{Im}) of the simulated power, P_{TK}. In order to obtain powers normalised to N_0, the term $B_{norm} = \sqrt{N_0/2}$ is introduced into the calculation. Altogether this takes form:

$$\begin{aligned} P_{Re}(\nu_j) &= B_{norm} R_{Re} \nu_j^{-\beta/2} \\ P_{Im}(\nu_j) &= B_{norm} R_{Im} \nu_j^{-\beta/2} \end{aligned} \tag{3.8}$$

and thus simulated powers by:

$$P_{TK}(\nu_j) = P_{Re}(\nu_j)^2 + P_{Im}(\nu_j)^2 \tag{3.9}$$

which across the defined frequency range corresponds to a red noise time series with power spectral index, β and normalisation N_0. As this method is used on power spectra below the white noise cutoff, white noise may be introduced as a constant, from 2.14, such that $P_{TK+C}(\nu_j) = P_{TK}(\nu_j) + C$.

By invoking the inverse Fourier Transform, the procedure described above naturally allows the production of simulated red noise lightcurves directly from the powers obtained in equation 3.9. In this case, white noise can be added onto the purely red noise time series through an additional term drawn at random from a Poisson distribution for each bin of the light curve, and only requires knowledge of the mean count rate of the lightcurve. These simulation methods were used to produce Figure 2.3. It should be noted that these simulated lightcurves do not automatically follow a lognormal flux distribution (Uttley et al., 2005), and highlights an important caveat of this method.

For each QPO candidate at this stage, a total of 10,000 fake periodograms are simulated through the Timmer and Koenig (1995) procedure, with input (β, N_0) parameters drawn at random from the GMM distribution, in order to account for the intrinsic uncertainty on the maximum likelihood broad band noise fit. Each simulated dataset was treated in an identical manner to the real data, first by fitting each fake periodogram using a maximum likelihood minimisation routine (using a PLC model only), before identifying the largest oulier (i.e. QPO candidate) in each, removing it and refitting the underlying continuum as before. Importantly, the refitted PLC model at this stage will not be equivalent to the initial, input PLC model due to the inherent randomness of the simulation procedure.

If the fitting routine was unsuccessful (as there is a very low but finite chance that the fitting algorithm cannot successfully minimise), a new fake dataset was drawn, and this is repeated if necessary to ensure the number of modelled simulation is equal to $10,000$.

In each successful case, the ratio $R_{\mathrm{TK,j}} = \frac{2I_{\mathrm{TK,j}}}{P_{\mathrm{TK,j}}}$ was evaluated across all frequencies (where, as before, $I_{\mathrm{TK,j}}$ indicates the 'observed'/simulated power, and $P_{\mathrm{TK,j}}$ the best-fitting model power, at the same frequency). A search for a 'false detection' is then undertaken, where a false detection occurs when $R_{\mathrm{TK,j}} > R_{\mathrm{Q}}$, where $R_{\mathrm{TK,j}}$ can be an outlier *at any frequency* (thereby treating each frequency as an independent free trial).

Across N simulations, M number of datasets are found with such 'false detections' and the *global significance*, GS, of the QPO candidate is defined through:

$$GS = 1 - \frac{M}{N} \tag{3.10}$$

To exceed a 3σ significance, it is required that $GS > 0.9973$ (equivalent to $M < 27$, given $N = 10,000$). A global significance of 0.9973 thus represents the case where under these conditions, a QPO candidate can expect to be replicated by chance with a frequency of 27 times out of $10,000$. It is important to note that any such candidate identified in isolation must still be treated with caution until additional evidence is obtained (e.g. the persistence of the signal across multiple observations and at similar frequencies – Alston et al. 2014b – or other characteristic behaviour which distinguishes it from the broad-band noise). Caution is also taken in the case of any detections at the white noise cutoff, for at these frequencies, the relative fraction of Poisson noise (which is assumed to be constant rather than providing any additional stochastic variability) increases relative to the simulated red noise. Although only frequencies below the white noise cutoff are investigated, the position of this threshold itself has uncertainty (as explored in Section 5.3.1) and those frequencies at the cutoff are those most likely to be biased by white noise.

In a similar fashion to the global significance calculation, 3σ confidence limits on observed powers from these Monte Carlo simulations can be obtained following the method of Vaughan (2005). The $(1 - \epsilon_1)100\%$ confidence limit at one frequency (e.g. $\epsilon_1 = 0.0027 \rightarrow 99.73\%$ confidence) can be expanded to include all n' frequencies of the periodogram as free trials, through the relation (Vaughan, 2005):

$$\epsilon_{n'} = 1 - (1 - \epsilon_1)^{n'} \tag{3.11}$$

which arises due to the multiplicative nature of performing for the same $(1 - \epsilon_1)$ test, over each of the n' frequencies. These confidence limits are calculated directly from the simulated periodograms, selecting the $\epsilon_{n'}$ percentile power simulated at each frequency. These values are used for illustrative purposes, being plotted onto periodograms to highlight the confidence contours of interest (e.g. Figure 3.3).

Whilst each frequency is considered an independent free trial, this does not extend similarly to each energy bin across an observation, as some level of correlation is expected between bands (as evidenced in AGN rms spectra – see e.g. Middleton et al. 2011). Finally, the most statistically rigorous approach would be to take each AGN observation itself to be an independent free trial. However, as the conditions required to produce a QPO are not well known, nor for how long they persist, *at this stage* a more heuristic approach is taken whereby the number of free trials is considered to be the total number of frequency bins investigated in the (white noise removed) periodogram. The impact of instead considering all AGN observations as free trials is considered separately in Section 5.2.

A working summary of this analysis is visualised in Figure 3.6, which details each key step, across the three main stages of data processing, the analysis pipeline and the Monte Carlo power spectrum simulations.

3.3.4 Further QPO candidate significance tests

Even in the case of a QPO candidate located with a high global significance value after Monte Carlo testing, it is plausible that, regardless of the fact a PLC model may be statistically preferred in a given case, the BIC test may exclude a BKNPLC model due to a low number of frequency bins below any putative break (i.e. if the break is not well sampled). Any unaccounted-for break in the broad-band noise has the potential to produce spurious peaks of power (which may be erroneously identified as QPO candidates, or bias the modelled broad-band noise which is used to determine the statistical significance of the QPO candidate). Thus an extra two tests are instigated in all cases of interest ($GS \geq 3\sigma$) to better judge the validity of the QPO candidate located using a PLC model.

1. In only those energy bands where a QPO candidate is located to $\geq 3\sigma$, the entire frequency bandpass is refit (minus the *a priori* known QPO candidate frequency bin, but including the previously discarded white noise) with a BKNPLC model. The index above and below the break (β_1, β_2) and the break frequency $\nu_{\rm b}$ are allowed to be free, while the break is bounded to be $\leq \nu_{\rm Q}$. The requirement for $\nu_{\rm b} \leq \nu_{\rm Q}$ is motivated by observations of black hole binaries (notably GRS 1915+105), where the HFQPOs (as the expected analogues to AGN QPOs at these

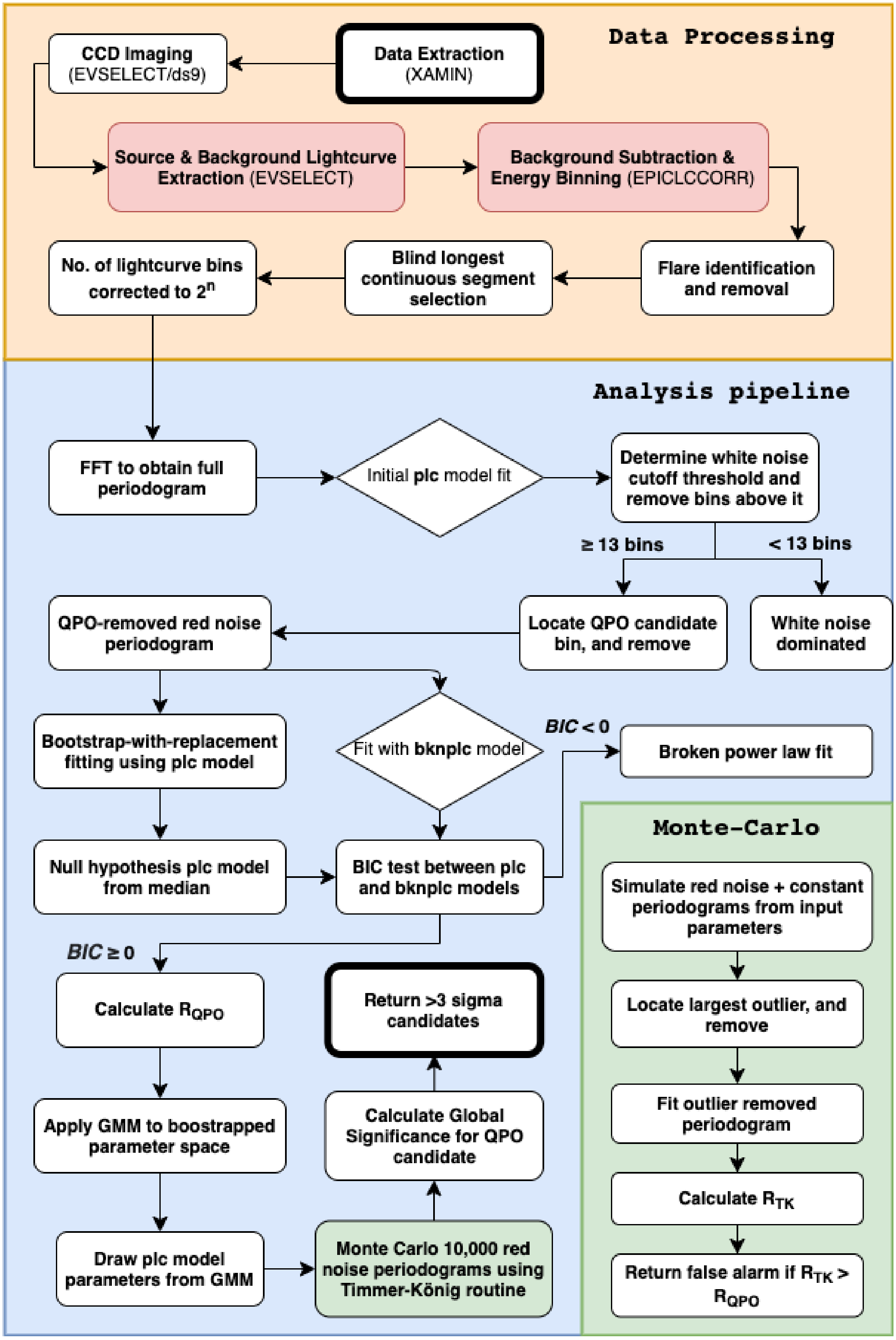

FIGURE 3.6: Flow chart summarising the key steps taken in this analysis. The procedure is broken into three main stages: the **data processing**, which includes use of the *XMM-Newton SAS* tools (steps in red) to prepare the lightcurve; the **analysis pipeline** which is a fully automated, parallelised PYTHON package used to search for QPO candidates using the statistical techniques detailed above – including Timmer and Koenig (1995) red noise **Monte Carlo** simulations.

frequencies, Middleton and Done 2010) occur above the high frequency break in the PSD (Morgan et al., 1997).

A new white noise cutoff frequency is established, which can differ from that found in the PLC fitting (see Section 5.3.1), and the best fitting model is found ($\nu_{\rm b}$ β_1, β_2 and N_0). Monte Carlo simulations are then performed assuming this revised best-fitting model for the broad-band noise and a new GS value for the QPO candidate is obtained. This is termed the 'free-index test'.

2. In only those energy bands where a QPO candidate is located to $\geq 3\sigma$, the entire frequency bandpass is refit once again with a BKNPLC model, but now with a fixed lower index, β_1 set to -1.1, following the assumption made in Alston et al. (2019). This is done to investigate whether $\beta_1 = -1.1$ can be a good assumption and lowers of number of free parameters from 4 to 3. Again, the break frequency must lie at, or below, the QPO candidate frequency $\nu_{\rm b} \leq \nu_{\rm Q}$. As before, the revised best-fitting model is then used for Monte Carlo simulations, returning a new GS value for the QPO candidate. This is termed the 'fixed-index test'.

3.4 Chapter summary

In this chapter I have outlined the use of *XMM-Newton* to search for QPOs in AGN, and selected a sample of 200 archived observations from a total of 38 bright, variable AGN, in an effort to maximise the data quality for investigations. Motivated by the potential energy dependent nature of AGN QPOs, a sliding energy window was implemented such that, for each observation, a total of 1225 energy bins are investigated, from 0.3 to 10 keV. The lightcurves are processed using standard *XMM-Newton SAS* tools, with highly significant ($> 5\sigma$) high energy flare events identified and removed. I chose a conservative approach of (blindly) selecting the longest continuous segment of the observation for analysis.

A standard Fourier analysis is applied to the lightcurve, and the periodogram used in favour of the PSD to maximise frequency range. The white noise threshold is determined and from this only the red noise dominated section of the periodogram analysed. The QPO candidate is determined to be the greatest outlier in power in a single bin above the broad-band noise assuming an initial PLC model. The null hypothesis is based on this outlier, here called a QPO candidate, being a statistical fluke and is tested using Monte Carlo simulations of red noise power spectra using the routine described in Timmer and Koenig (1995).

Both PLC and BKNPLC models are fitted to each (non-white noise dominated) periodogram using maximum likelihood statistics, in a search for breaks. For those which are best modelled by a PLC model (according to a BIC test), the significance of the QPO candidate is tested with the aforementioned Monte Carlo simulation, while accounting for uncertainty on the PLC model by using both a bootstrap-with-replacement and GMM methods. Those QPO candidates with a global significance of $\geq 3\sigma$ are deemed QPO candidates of interest and are the subject of the following chapter.

Chapter 4

Multiple detections of energy-resolved QPOs in AGN

In this chapter I utilise the statistical framework developed in Chapter 3 to search for QPOs in energy-resolved *XMM-Newton* lightcurves of AGN. I detail the results of these findings, highlighting each statistically significant set of candidates in detail, conduct a series of further tests on each, and investigate the characteristics of these features, including frequency and energy dependence.

4.1 Results

From a total of 200 observations across a sample of 38 AGN, an initial 21 QPO candidates are reported at a $\geq 3\sigma$ global significance level, with 3 candidates at a borderline 3σ level (i.e. a candidate with $GS \sim 0.9973$, such that the uncertainty on each Monte Carlo run is sufficient for this candidate to be on the border of the 3σ threshold) – altogether from 7 AGN. Within these results, the well-reported QPO in RE J1034+396 is re-detected in 4 observations, leaving up to 20 additional detections across a further 6 AGN. These initial results, based on the procedure detailed in Chapter 3, are shown in Table 4.1, which details the energy band in which the detection significance is maximised, the candidate frequency (and its error), the fractional rms at this frequency (found by integrating the QPO candidate's power and removing the Poisson noise) and the 'quality factor' $Q = \nu/\Delta\nu$. In addition, the table lists the duration of the studied (flare removed) lightcurve – i.e. the longest continuous segment – and the reported SMBH mass for each AGN. For each of these initial results of interest, the additional tests listed in Chapter 3 are performed, with each AGN considered in turn.

An immediate result of importance is the non-detection of a QPO in all available observations of MS 2254.9-3712, likely due to the restriction of using only continuous

Obs ID	Duration (ks)	Peak Significance	Peak Energy (keV)	QPO candidate Frequency (Hz)	Frequency Error (Hz)	FRMS Value	Q
RE J1034+396, $M_{\rm BH} \sim 6.17$ [a]							
0506440101	28.94	1.0000	0.7 - 1.0	2.34×10^{-4}	3.91×10^{-5}	0.071	5.98
0655310201	41.60	1.0000	1.2 - 2.4	2.34×10^{-4}	3.91×10^{-5}	0.123	5.98
0675440101	23.92	1.0000	0.7 - 3.4	2.34×10^{-4}	7.81×10^{-5}	0.097	3.00
0675440201	28.82	1.0000	0.9 - 6.2	2.73×10^{-4}	3.91×10^{-5}	0.112	5.98
IRAS 13224-3809, $M_{\rm BH} \sim 6.00$ [b]							
† 0780561301	125.29	0.9991	6.0 - 10.0	7.81×10^{-5}	9.77×10^{-6}	0.201	8.00
0780561301	125.29	0.9980	2.2 - 6.4	2.83×10^{-4}	9.77×10^{-6}	0.121	29.0
† 0780561401	82.92	1.0000	4.0 - 5.8	7.81×10^{-5}	1.95×10^{-5}	0.279	4.00
0780561401	82.92	0.9997	3.2 - 9.8	4.69×10^{-4}	1.95×10^{-5}	0.136	24.1
0780561701	113.20	0.9995	3.2 - 3.8	9.77×10^{-5}	9.77×10^{-6}	0.209	10.0
* 0792180201	128.63	0.9979	4.0 - 5.6	1.66×10^{-4}	9.77×10^{-6}	0.294	17.0
† 0792180301	53.26	0.9994	4.8 - 9.6	9.77×10^{-5}	1.95×10^{-5}	0.304	5.01
0792180501	93.83	0.9992	0.9 - 1.6	1.02×10^{-3}	1.95×10^{-5}	0.059	52.3
0792180601	105.02	0.9984	6.6 - 8.6	9.77×10^{-5}	9.77×10^{-6}	0.246	10.0
1H 0707-495, $M_{\rm BH} \sim 6.3$ [c]							
0653510301	95.19	0.9984	4.8 - 6.2	1.95×10^{-4}	1.95×10^{-5}	0.255	10.0
0653510501	94.72	0.9997	4.0 - 5.4	1.95×10^{-4}	1.95×10^{-5}	0.225	10.0
* 0653510601	105.85	0.9975	5.6 - 8.2	1.27×10^{-4}	9.77×10^{-6}	0.224	13.0
PG 1244+026, $M_{\rm BH} \sim 6.24$ [d]							
0675320101	71.81	0.9993	3.0 - 5.8	2.15×10^{-4}	1.95×10^{-5}	0.074	11.0
NGC 4051, $M_{\rm BH} \sim 6.24$ [e]							
0109141401	25.77	0.9997	5.0 - 6.0	3.52×10^{-4}	3.91×10^{-5}	0.095	9.00
0606321801	39.83	0.9998	3.4 - 4.0	1.56×10^{-4}	3.91×10^{-5}	0.180	3.99
ARK 564, $M_{\rm BH} \sim 6.41$ [f]							
† 0006810101	4.95	1.0000	3.0 - 5.4	1.88×10^{-3}	3.13×10^{-4}	0.134	6.00
0670130501	17.18	0.9987	2.0 - 3.8	8.59×10^{-4}	7.81×10^{-5}	0.073	11.0
0670130701	44.71	1.0000	2.6 - 2.8	2.73×10^{-4}	3.91×10^{-5}	0.163	6.98
0670130801	51.65	0.9998	3.0 - 3.4	2.54×10^{-4}	1.95×10^{-5}	0.072	13.0
MRK 766, $M_{\rm BH} \sim 6.63$ [g]							
*† 0304030301	38.35	0.9976	3.0 - 4.6	4.69×10^{-4}	3.91×10^{-5}	0.055	12.0

TABLE 4.1: 3σ QPO candidate summary. The columns indicate: (1) Observation ID, (2): The duration of the studied, longest continuous flareless lightcurve segment, (3): the highest value of global significance obtained in a single energy bin, with the corresponding p-value being $(1 - GS)$, such that a $GS = 1.0000$ gives a p-value < 0.0001, given 10,000 simulations were performed in each case (4): the energy range of this bin, (5): the Fourier frequency of the QPO candidate detected at $\geq 3\sigma$, (6): the Fourier frequency bin width, (7): the (peak significance) fractional rms (FRMS) value at the QPO candidate Fourier frequency, (8): the QPO candidate quality factor ($Q = \frac{\nu}{\Delta\nu}$). * Note that IRAS 13224-3809, OBSID:0792180201, 1H 0707-495 OBSID: 0653510601 and MRK 766, OBSID:0304030301 are considered borderline 3σ results with ambiguous detections assuming a PLC model. † highlighted observations are those which are not validated by those further tests outlined in Section 3.3.4. All SMBH masses are provided in the form: $\log_{10}(\frac{M}{M_\odot})$ The estimated SMBH masses are obtained from: [a] Done et al. (2012), [b] Alston et al. (2019), [c] Done and Jin (2016), [d] Gierliński and Done (2004), [e] Denney et al. (2010), [f] Wang and Lu (2001), [g] Giacché et al. (2014).

(flare removed) data, which yields a 27.8ks observation for analysis, in comparison to the 63ks combined EPIC-pn/EPIC-MOS segment defined in Alston et al. (2015) where gaps were removed via interpolation.

4.1.1 RE J1034+396

4.1.1.1 Initial PLC search

To test the procedure for locating QPO candidates, eight observations of RE J1034+396 were examined, and the results compared to those in Alston et al. (2014b), noting once again that the lack of interpolation in the approach here can act to restrict the frequency range of the periodograms.

The previously reported QPO is detected to a $> 3\sigma$ confidence in four observations, all at a frequency of $2 - 3 \times 10^{-4}$ Hz – see Figure 4.1. Notably, the energy band in which the global significance is maximised (i.e. the maximum significance energy band) extends down to 0.7 keV and reflects the presence of the QPO in the soft X-ray component (see Middleton et al. 2011). For comparison, Alston et al. (2014b) detect a QPO in five of the eight observations, including the four where a significant candidate is found. The disparity arises from OBSID:0655310101, in which the flare-less segment has a duration of only 28.2ks, from which the QPO candidate is reported only at a $> 2\sigma$ level. Also of note is the renewed detection of the QPO (again at the same frequency) in the new 2018 observation of RE J1034+396 (see Jin et al. 2020, Jin et al. 2021) – the data from which were not public at the time of this analysis.

Figure 4.2, presents energy-resolved significance heat-maps for all $\geq 3\sigma$ candidates detailed in Table 4.1. It visualises the global significance values *at the specific QPO candidate frequency* in all other energy bands, in the case of a best fitting PLC model – energy bands where a BKNPLC model is statistically preferred or where the periodogram is

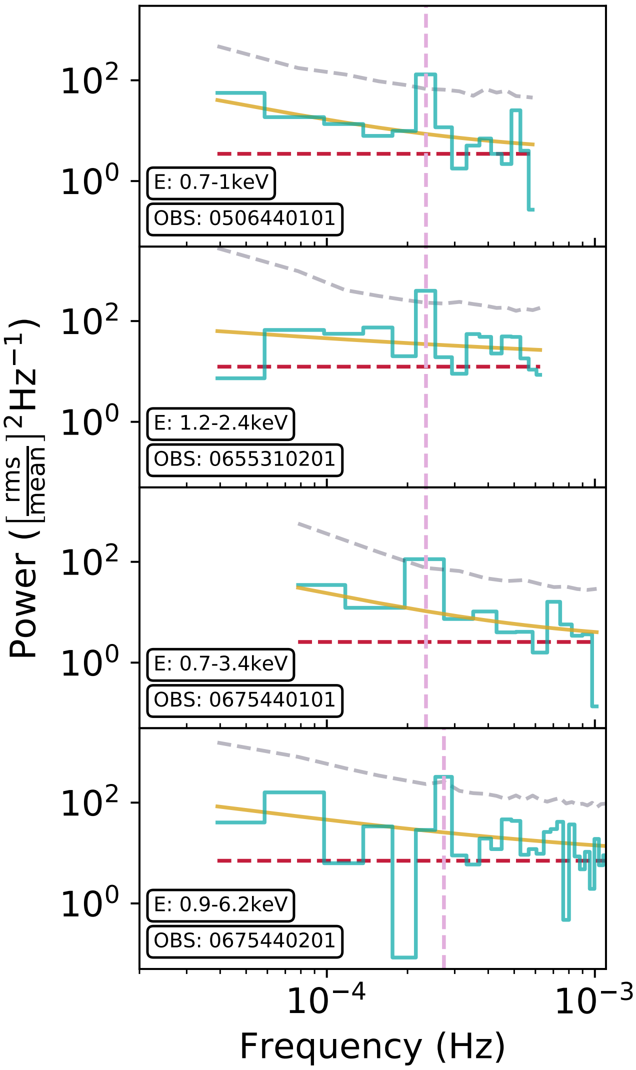

FIGURE 4.1: The highest significance ($\geq 3\sigma$) energy-resolved QPO candidates detected in RE J1034+396, using the PLC model, with the corresponding frequency bin highlighted as a vertical dashed line. The consistency of the QPO frequency across each observation has historically set RE J1034+396 apart, as it is highly improbable to create false peaks in power across multiple observations at the same frequency. Following the same format of Figure 3.3, the observed periodogram is shown in blue, the PLC model in gold, white noise level in red, 3σ confidence level in dashed silver and QPO candidate frequency in dashed pink. This format is used throughout this chapter.

white noise dominated are greyed out. Note, the significances presented in Figure 4.2 are purely blind (i.e. the full number of independent trials is still taken into account, although the results are for a specific frequency *a priori*).

4.1.1.2 Further tests

As the QPO in RE J1034+396 is well established and thoroughly investigated in the literature (e.g. Vaughan 2010), the application of additional tests was forgone in this instance.

Frequency-restricted search: Given the detection of multiple $\geq 3\sigma$ QPO candidates at consistent frequencies (i.e. $\sim 2.34 \times 10^{-4}$ Hz), the reasonable assumption of *a-priori* knowledge of the QPO frequency in RE J1034+396 is made, and a frequency-restricted search conducted across all observations where a $\geq 3\sigma$ QPO candidate was not detected. This revised search re-defines the QPO candidate to be in the bin at the *a-priori* frequency (or the closest Fourier frequency bin to this). The procedure is repeated and the global significance of this new candidate it reported. In effect, this revised p-value test *lowers* the effective threshold for detection, as it reduces the number of free trials from the full frequency range, to a single Fourier bin of interest. However, this frequency-restricted search does not locate any additional QPO candidates at $\geq 3\sigma$.

4.1.2 IRAS 13224-3809

IRAS 13224-3809 is one of the most variable NLS1 AGN (Boller et al., 1997; Dewangan et al., 2002; Fabian et al., 2013; Alston et al., 2019) and has been the focus of a recent 1.5 Ms study with *XMM Newton*, yielding high quality data from individual orbits (see Alston et al. 2019, Alston et al. 2020). 16 available observations were studied, and in 6 of these QPO candidates are detected at $\geq 3\sigma$, with one additional observation with a borderline 3σ detection.

4.1.2.1 Initial PLC search

Three observations are found to have consistent QPO candidate frequencies at 9.77×10^{-5} Hz (OBSIDs:0780561701, 0792180301 and 0792180601) with an extremely high fractional rms ($> 20\%$) – see Figure 4.3 and Table 4.1. In addition to these, a borderline 3σ QPO candidate with a frequency of 1.66×10^{-4} Hz found in OBSID:0792180201; although the significance fluctuates around 3σ, it sits close to the frequency of QPO candidates detected in other observations and is therefore of interest.

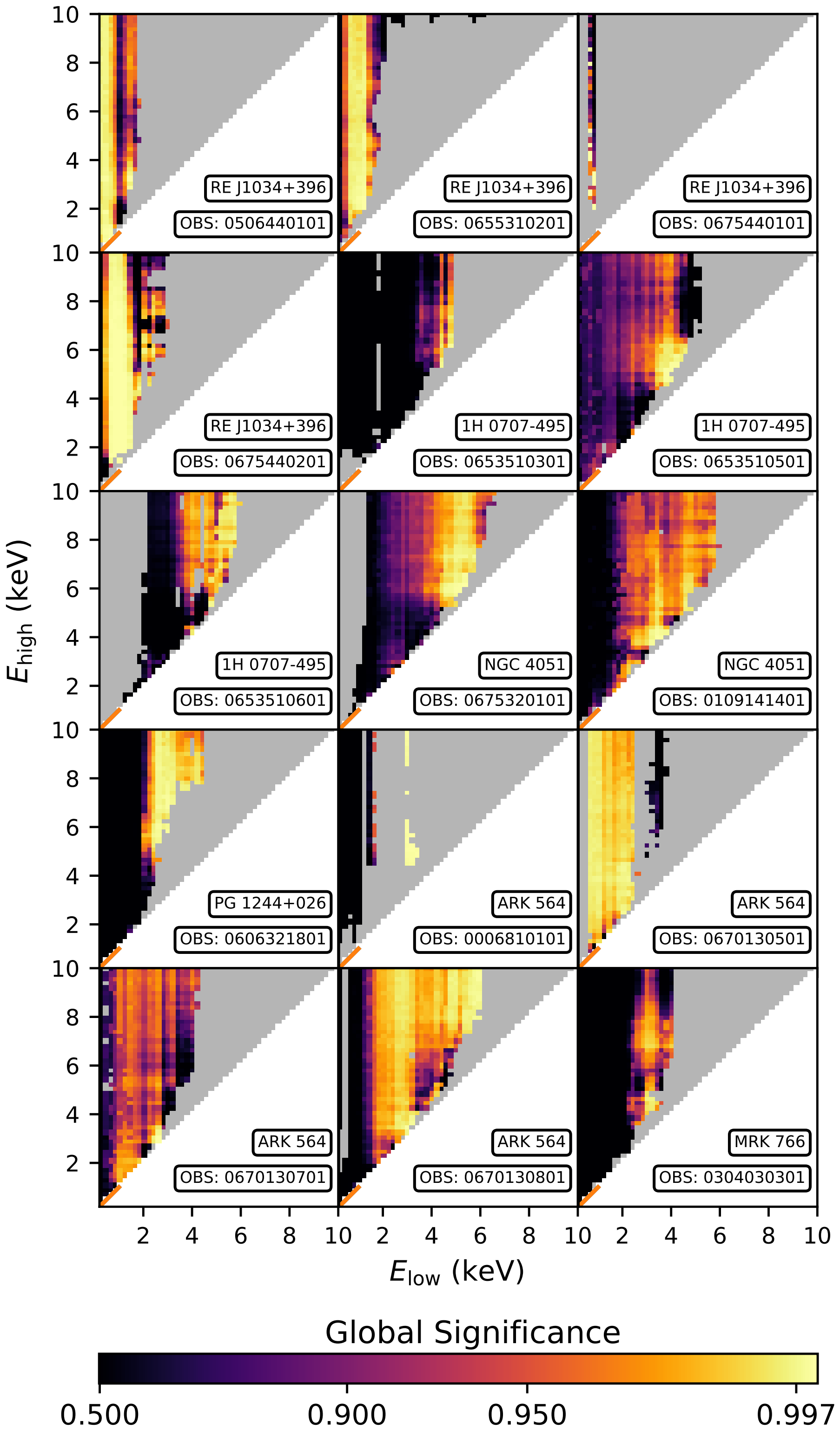

FIGURE 4.2: Energy-resolved significance heatmaps displaying the measured global significance of QPO candidates (excluding IRAS 13224-3809, for which see Figure 4.4) using the PLC model, at the frequency of the highest significance blind detection in an energy bin defined as $E_{low} \rightarrow E_{high}$. The grey areas, including 'gaps' in the heatmaps, indicate energy bands which do not fit the PLC criteria set out in Chapter 3 – including both white noise dominated observations and BKNPLC model preferred fits.

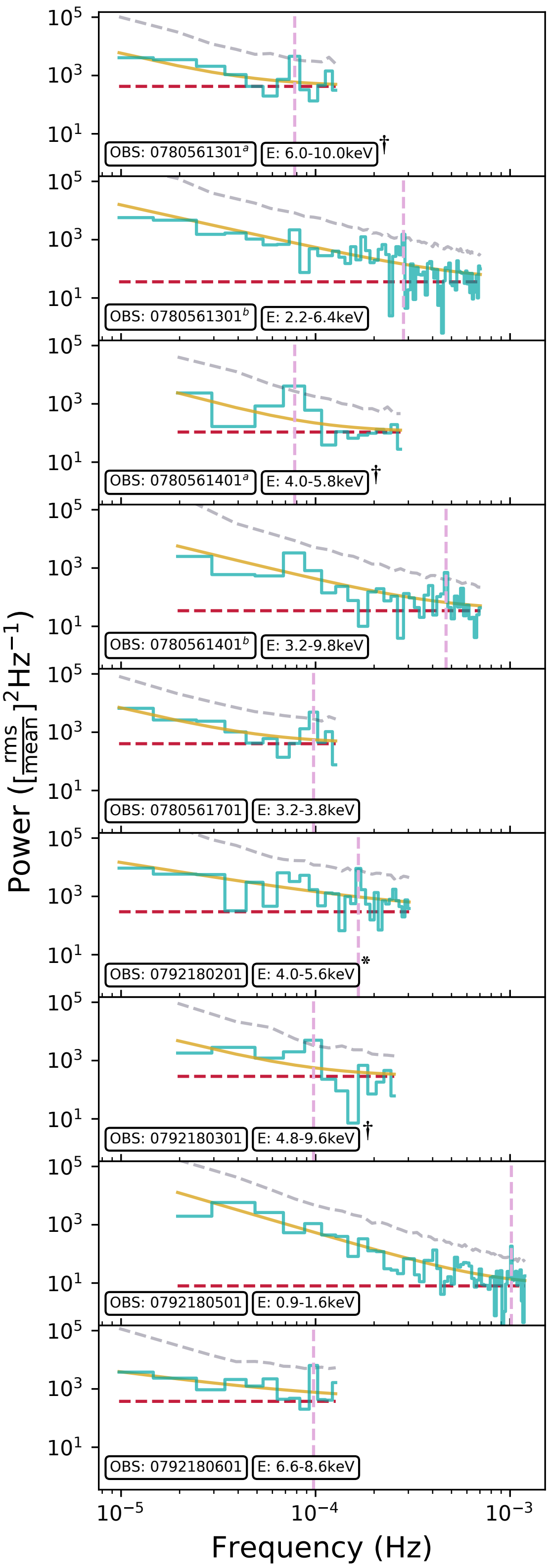

FIGURE 4.3: The highest significance ($\geq 3\sigma$) QPO candidates found in IRAS 13224-3809 using the PLC model, with the corresponding frequency bin highlighted. Of note is the consistency of frequencies across multiple observations, with the clear exception of OBSID:0792180501. See Table 4.1 for supplementary information. Borderline 3σ results (*) and those not validated by further tests († – see Section 3.3.4) are shown.

A $> 3\sigma$ QPO candidate is also detected at 7.81×10^{-5} Hz in two observations (OBSID:0780561301 and 0780561401). These two observations provide a potentially intriguing result in that they contain $> 3\sigma$ QPO candidates at *two* different frequencies, dependent on the energy band selected, both of which are presented in Table 4.1. In OBSID:0780561301, the higher frequency QPO candidate is found at 2.83×10^{-4} Hz, whilst in OBSID:0780561401 it is found at 4.69×10^{-4} Hz. If assuming these candidates to be harmonically related to the 7.81×10^{-5} Hz feature then these correspond to 7:2 and 6:1 resonances respectively. Figure 4.4 displays the energy dependence of the global significance of these QPO candidates; the energies at which they become statistically significant at $\geq 3\sigma$, are almost entirely confined to hard energies > 3 keV. The notable exception to the energy-dependence is that of OBSID:0792180501, which appears to show several features that are unique amongst the wider sample.

The QPO candidate in OBSID:0792180501 is found at a still higher frequency of 1.02×10^{-3} Hz, as shown in Figure 4.5. This QPO candidate is almost unique amongst these detections (the other example being found in ARK 564), as it lies at a frequency higher than the Poisson noise cutoff for the vast majority of investigated observations across the entire sample, but is detectable due to prominence of red noise power above the white noise: due both to the high count rates and high variability of IRAS 13224-3809. This, in combination with the extensive length of the observation at $\sim$ 105 ks (which sets the width of the natural Fourier frequency bin, $\Delta\nu$), this QPO candidate has the largest Q value of any of these detections ($Q > 50$). The energy band in which the significance of this QPO candidate is maximised also differs from those of the lower frequency QPO candidates, being found at softer energies (specifically $0.9 - 1.6$ keV, see Figure 4.4) without significant detections above 2 keV (although at these higher energies, the data quality becomes insufficient to study such high frequencies as the Poisson noise increases and brings this white noise cutoff to a lower frequency than the QPO candidate). It is of interest to note that those QPO candidates detected at lower frequencies do not appear in this observation.

4.1.2.2 Further tests

The two additional tests outlined in Section 3.3.4 are implemented here and the results described on an observation-by-observation basis.

Free-index test:

- OBSID:0780561301. The duel QPO candidate detection in OBSID:0780561301 is an important case to be studied with a forced break, as it is possible a break feature in one energy band is being erroneously identified as a QPO. Applying a BKNPLC model under these conditions finds the break to be energy dependent. A break

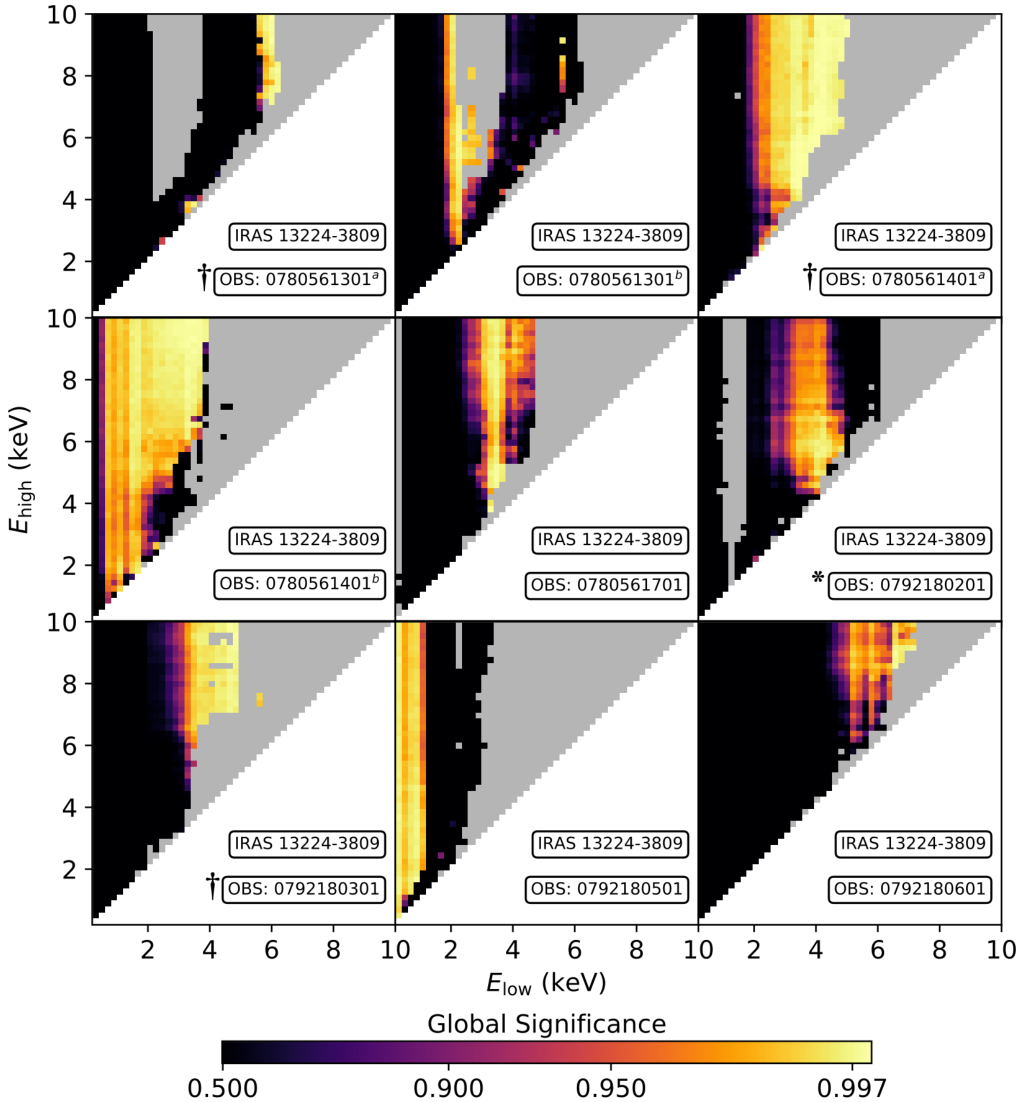

FIGURE 4.4: Energy-resolved significance heatmaps displaying the measured global significance of the QPO candidates in IRAS 13224-3809, using the PLC model, at the frequency of the highest significance blind detection (see Table 4.1), in an energy bin defined as $E_{low} \rightarrow E_{high}$. The grey areas, including 'gaps' in the heatmaps, indicate energy bands which do not fit the PLC criteria set out in Section 3.3.4 – including both white noise dominated observations and BKNPLC model preferred fits.

at $\sim 2 \times 10^{-4}$ Hz is found at energies $\sim 2-6$ keV. In this case a sudden drop in power is observed above the higher frequency QPO candidate at 2.83×10^{-4} Hz, as shown in the lower panel of Figure 4.6. This sudden drop in power may not be best described by a high-frequency break, as the trend in power at higher frequencies than this point is relatively flat, such that the change in index (i.e. $\beta_2 - \beta_1$) is considerable (> 1). This is similar to the findings of González-Martín and Vaughan (2012) when modelling the PSD of MS 22549-3712, in which they report a poorly constrained fit using a bending power law with an extremely steep index above the break, but no QPO. Assuming a free BKNPLC model (instead of a PLC model) does not lower the significance of the higher frequency candidate QPO in

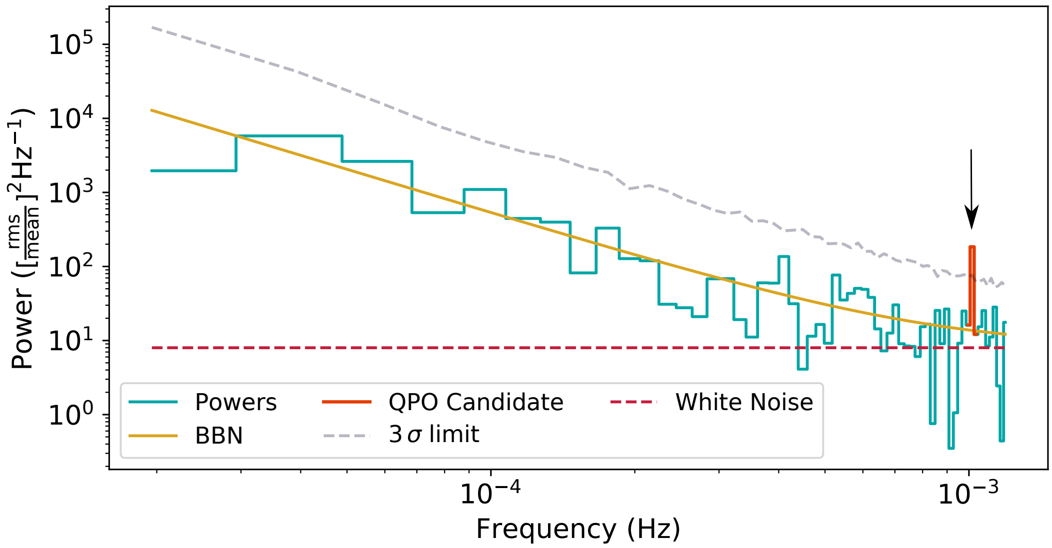

FIGURE 4.5: The highest significance QPO candidate (in the $0.9 - 1.6$ keV band) found using the PLC model, in OBSID:0792180501 of IRAS 13224-3809. This standout candidate is observed with $Q > 50$ and is one of only two QPO candidate examples found at $> 1 \times 10^{-3}$ Hz. See Table 4.1 for supplementary information.

this observation (remaining $> 3\sigma$), and hence it remains of interest.

In the case of energies > 6 keV, a break is found at the lower frequencies of $\sim 2 \times 10^{-5}$ Hz or $\sim 6 \times 10^{-5}$ Hz (depending on the exact energy range), and in doing so, the significance of the QPO candidate at 7.81×10^{-5} Hz drops to below 3σ, in either case – as shown in the upper panel of Figure 4.6, where the BKNPLC model is plotted. By including a break in this way, the white noise cutoff is brought to lower frequencies, as compared to the maximum likelihood PLC model fit, and restricts the number of frequency bins in the periodogram. As a result, multiple energy bands which contained $\geq 3\sigma$ QPO candidates using the PLC model, are subsequently deemed white noise dominated in this test – i.e. with < 13 Fourier bins below the cutoff. This finding lends itself to the conclusion that the 7.81×10^{-5} Hz QPO candidate (upper panel of Figure 4.6) being unlikely to be genuine († in Table 4.1). It is also worth noting that this feature also appears at lower energies (lower panel of Figure 4.6), but with a lower global significance value. The difficulty in detecting the break feature at $\sim 2 \times 10^{-5}$ Hz is likely because it is covered by only a $2 - 3$ bins, such that the applied BIC test finds a simpler PLC model statistically preferable.

- OBSID:0780561401. Similarly to the previous observation, the possible significant detection of two, separate, QPO candidates in OBSID:0780561401 is intriguing, but is investigated in case of mis-identification of a break as a QPO candidate. After enforcing a BKNPLC model, a break is identified at 7.81×10^{-5} Hz, and the higher-frequency QPO candidate, at 4.69×10^{-4} Hz, is found to lie consistently

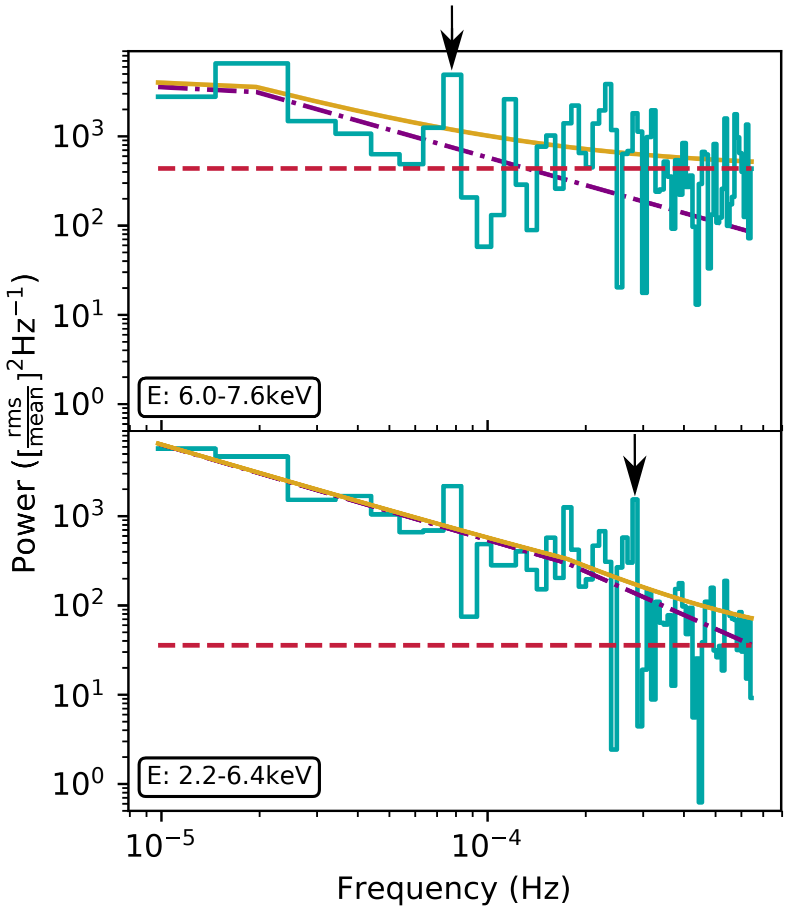

FIGURE 4.6: Energy resolved periodograms of IRAS 13224-3809 OBSID:0780561301, fitted with BKNPLC models following test (i). Top: periodogram in the $6.0 - 7.6$ keV band, with the QPO candidate highlighted at 7.81×10^{-5} Hz. Fitting with this model causes the QPO candidate to drop to a 2σ significance. Bottom: periodogram in the $2.2 - 6.4$ keV band, with the QPO candidate highlighted at 2.83×10^{-4} Hz, which remains $> 3\sigma$ before a steep drop in power at higher frequencies. Note: this frequency lies within the white noise in the higher energy band periodogram (top panel).

above the 3σ threshold when below the white noise cutoff, as in upper panel of Figure 4.7. For energy ranges above 3.2 keV however, the white noise cutoff moves to frequencies below 4.69×10^{-4} Hz and the QPO candidate is no longer within the range of frequencies considered. This represents a case where the position of the white noise can make the significance of the candidate more difficult to reliably constrain.

The lower frequency QPO candidate at 7.81×10^{-5} Hz shows an interesting case where fitting with a BKNPLC model results in no clear break feature. As a result, the QPO candidate is found with a very high significance through either a PLC or an enforced BKNPLC model. However, as is clear from Figure 4.7, this QPO candidate investigated in the energy range $3.2 - 4.6$ keV (bottom panel) is itself identified as the location of the break feature across the broader energy range of

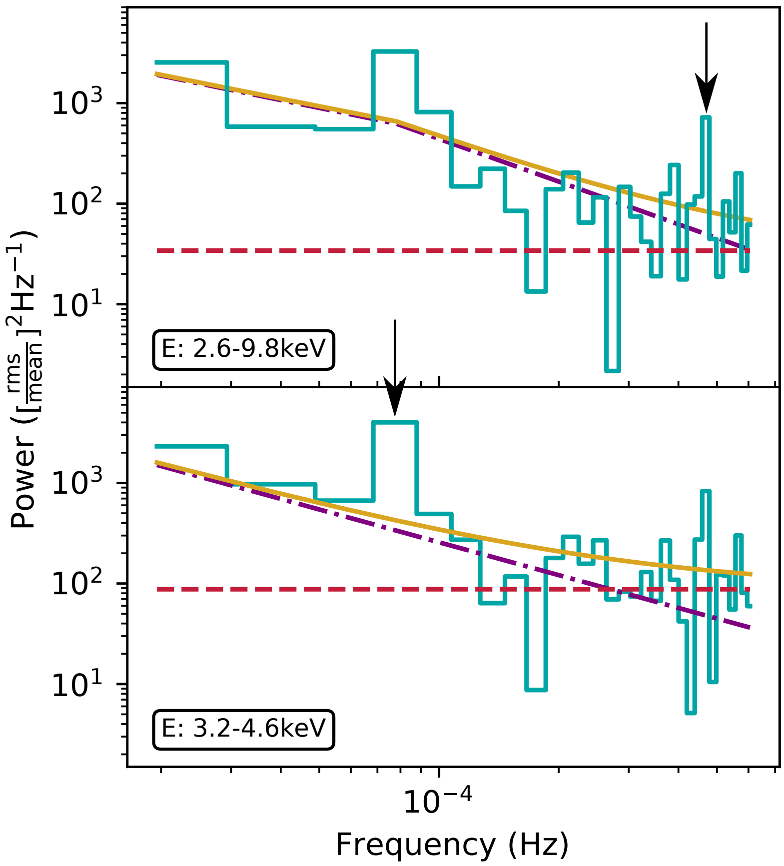

FIGURE 4.7: Energy resolved periodograms of IRAS 13224-3809 OBSID:0780561401, fitted with BKNPLC models following test (i). Top: periodogram in the $2.6 - 9.8$ keV band, with the QPO candidate highlighted at 4.69×10^{-4} Hz, found at a $> 3\sigma$ significance using a BKNPLC model, with the break located at 7.81×10^{-5} Hz. Bottom: periodogram in the $3.2 - 4.6$ keV band; the QPO candidate is now found at the position of the break (contrast with the top panel) at 7.81×10^{-5} Hz. In this energy band, a break does not well describe the data and, following test (i), the QPO candidate at 7.81×10^{-5} Hz is found to reach a $> 3\sigma$ significance. Note: the QPO candidate at 4.69×10^{-4} Hz is beyond the white noise cutoff in this energy band (contrast with the top panel).

$\sim 2 - 10$ keV – as it the case for when the higher-frequency QPO candidate is investigated (top panel). Moreover, the higher frequency QPO candidate (4.69×10^{-4} Hz) is beyond the white noise threshold in the $3.2 - 4.6$ keV energy band, such that it is not investigated.

Altogether, it may be reasonably assumed that the lower frequency QPO candidate is more likely to be an artefact of the high-frequency break, the shape of which is clearly energy dependent and difficult to constrain, and it is highlighted as a case that requires further investigation († in Table 4.1). The higher frequency QPO candidate remains of interest as it does not appear to correspond to a break feature (although it is close to the white noise and above the cutoff in some energy bands).

- OBSID:0780561701. A weak break (i.e. a value of β_1/β_2 close to unity) is found at $\sim 2 \times 10^{-5}$ Hz and at energies > 3 keV, which has no impact on the significance of the QPO candidate at 9.77×10^{-5} Hz.

- OBSID:0792180201. The original PLC model found this QPO candidate at a borderline 3σ detection. Applying this enforced BKNCPLC test leads to a break being found at $\sim 8 \times 10^{-5}$ Hz. However, the QPO candidate at 1.66×10^{-4} Hz becomes *more* significant when using this model as the null hypothesis.

- OBSID:0792180301. The QPO candidate at 9.77×10^{-5} Hz drops to $< 3\sigma$ significance with the introduction of a break at $\sim 4 \times 10^{-5}$ Hz, located before a steep drop in power at frequencies above the QPO candidate. Neither the PLC or BKNPLC models are found to provide a good description of the broad-band noise, but in assuming a BKNPLC model, the significance of the candidate drops and the white noise cutoff is brought to sufficiently low frequencies for the data to be white noise dominated. Due to poor constraints on the broad-band noise, this candidate is labelled as an unreliable result († in Table 4.1).

- OBSID:0792180501. A weak break is found around $\sim 4 \times 10^{-5}$ Hz, but the QPO candidate at 1.02×10^{-3} Hz remains unchanged in significance.

- OBSID:0792180601. Including a break does not lower the significance of the QPO candidate at 9.77×10^{-5} Hz, but the enforced BKNPLC model does reduce the number of frequencies below the white noise cutoff, although still above the imposed restriction of 13 bins.

Fixed-index test:

All of the results with a fixed β_1 agree with the reported findings from the free-index test, (as expected given $\beta_1 = -1.1$ was found previously in the case of IRAS 13224-3809 Alston et al. 2019) although this assumed shape below the break does not always provide a good description of the broad-band noise, when considering different energy bands. Importantly, the assumption of $\beta_1 = -1.1$ by Alston et al. (2019) is made when not considering the same energy resolution as is implemented in this analysis.

Frequency-restricted search: As with RE J1034+396, the detection of multiple $\geq 3\sigma$ QPO candidates at consistent frequencies, allows the assumption of *a-priori* knowledge for possible QPO candidates at frequencies of 7.81×10^{-5} Hz and 9.77×10^{-5} Hz (or the closest Fourier frequency). Searching at an *a-priori* frequency of 9.77×10^{-5} Hz, a frequency-restricted $\geq 3\sigma$ QPO candidate is found at energy ranges > 3 keV in OBSID:0673580401, which matches similarly significant detections at this frequency in OBSIDs: 0780561701, 0792180301 and 0792180601. Note, this observation does not show any $\geq 3\sigma$ global significance features, so does not appear in Table 4.1.

Searching at an *a-priori* frequency of 7.81×10^{-5} Hz, a single frequency-restricted $\geq 3\sigma$ QPO candidate is found in the narrow energy range $2.8 - 3$ keV in OBSID:0792180201, although this similarly could be the edge of the break possibly detected in OBSID:0780561301 and OBSID:0780561401.

In light of the possible harmonic features observed in OBSIDs:0780561301 and 0780561401, a similar search for QPO candidates was undertaken at frequencies of 2.83×10^{-4} Hz and 4.69×10^{-4} Hz respectively. At a frequency of 2.83×10^{-4} Hz, frequency-restricted $\geq 3\sigma$ candidates are found in OBSIDs: 0673580101 and 0780561601, both in the $3 - 6$ keV range, comparable to the QPO candidate in OBSID:0780561301. At a frequency of 4.69×10^{-4} Hz, frequency-restricted $\geq 3\sigma$ candidates are found in OBSID:0673580101 in the $2 - 8$ keV range, and in OBSID:0780560101, at energies around 2 keV. In these cases, it is important to remember that the claims are made based on a reduced number of free trials.

4.1.3 1H 0707-495

1H 0707-495 has been studied extensively by *XMM-Newton* with a total observing time in excess of 1 Ms (e.g. Kara et al. 2013).

4.1.3.1 Initial PLC search

As shown in Figure 4.8, $\geq 3\sigma$ QPO candidates are detected in three observations (including one borderline detection), from a total of 11. The QPO candidates are measured with a high fractional rms ($> 20\%$) and across a narrow frequency range of $1 - 2 \times 10^{-4}$ Hz.

The $\geq 3\sigma$ QPO candidates in OBSID:0653510301 and 0653510501 both lie at the exact same frequency, 1.95×10^{-4} Hz. OBSID:0653510601 represents a borderline $\sim 3\sigma$ QPO candidate, and in this case, the QPO candidate frequency lies close to or even at the white noise cutoff in some energy bins. In this observation, the candidate is observed at a frequency of 1.27×10^{-4} Hz, offset by only 0.68×10^{-4} Hz. All three QPO candidates are measured with almost identical fractional-rms fractions of 22.5% (for OBSID:0653510301, 0653510501) and 22.4% (for OBSID:0653510601), suggesting the strength of the QPO remains broadly consistent across the examined broad-band noise in each observation.

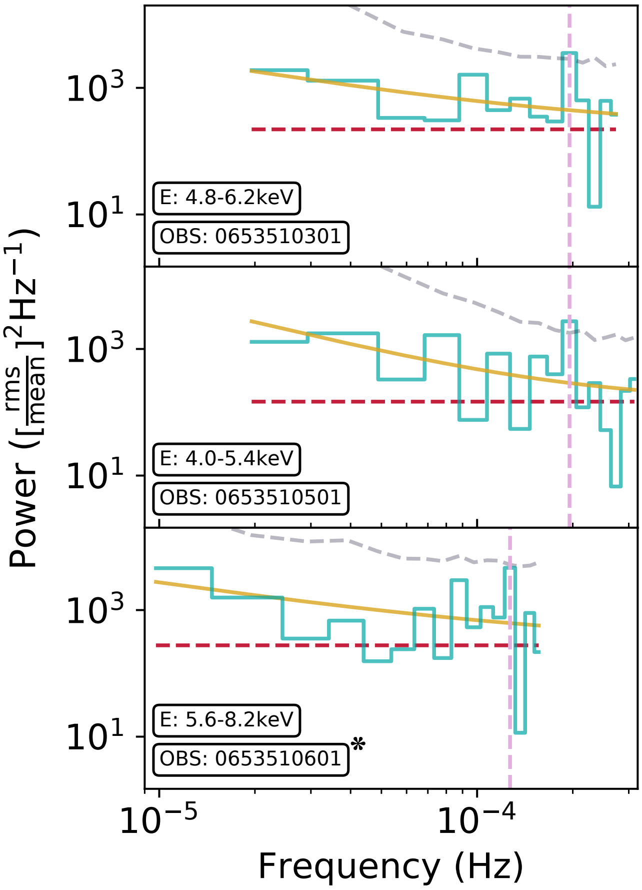

FIGURE 4.8: The highest significance ($\geq 3\sigma$) QPO candidates detected in 1H 0707-495 using the PLC model, with the corresponding frequency bin highlighted. As with RE J1034+396 and IRAS 13224-3809, the consistency of the QPO candidate frequency across multiple observations is important. The borderline 3σ result is highlighted (*).

The peak QPO candidate significance in OBSID:0653510301 and 0653510501 are both found in the $\sim 4-6$ keV range, with no $\geq 3\sigma$ energy bands extending below 3.8 keV, whilst only borderline 3σ features in OBSID:0653510601 are found in the $\sim 4-8$ keV energy range. For this latter observation, there are only two $\geq 3\sigma$ energy bands (where the QPO candidate is found at frequencies below the PLC white noise cutoff) but $> 2\sigma$ significance detection clusters around similar energies ($\sim 4-6$ keV) to the observations OBSID:0653510301 and OBSID:0653510501. The extent of the significance variation is highlighted in Figure 4.2, which shows the remarkable consistency of the QPO detection significance as a function of energy across these three observations. Also of note is that the fractional-rms of the QPO candidates in 1H 0707-495 is similar to that found in IRAS 13224-3809.

4.1.3.2 Further tests

Free-index test:

- OBSID:0653510301. Assuming a BKNPLC model with free parameters, a small break is found at $\sim 1 \times 10^{-4}$ Hz. The biggest impact is the shift of the white noise cutoff; in the $4.4 - 5.4$ keV energy range the QPO candidate remains above the 3σ threshold but at the limit of the broad-band noise becoming white noise dominated. Moving to harder energy bands, (namely $4.8 - 6.2$ keV), the QPO candidate sits at the location of the white noise cutoff but its significance remains $> 3\sigma$.
- OBSID:0653510501. In the $3.8 - 5.4$ keV band, a break is fitted at $\sim 8 \times 10^{-5}$ Hz, whilst at $4.2 - 5.8$ keV, the break is instead preferred at $\sim 3 \times 10^{-5}$ Hz. In both cases, the QPO candidate at 1.95×10^{-4} Hz remains $\geq 3\sigma$. As with the previous observation, there are also energy bands in which the white noise cutoff is moved to within 13 bins. This is typically seen in narrower energy bands (e.g. $3.8 - 4.8$ keV and $4.2 - 5.4$ keV), as the number of counts is restricted and increases the Poisson noise level. In these cases, the QPO candidate remains $\geq 3\sigma$ but is now closer to the white noise cutoff.
- OBSID:0653510601. A borderline detection with a PLC model; when assuming a BKNPLC model a tentative break is found close to the the QPO candidate frequency at $\sim 1 \times 10^{-4}$ Hz. For this observation, there are only two $\geq 3\sigma$ energy bands, where the QPO candidate is found at frequencies below the PLC white noise cutoff. For the peak significance band ($5.6 - 8.2$ keV), the QPO candidate remains $\geq 3\sigma$, whilst in the $4.8 - 5.4$ keV band, the QPO candidate falls below 3σ due to the presence of the break.

Fixed-index test:

- OBSID:0653510301. Similar to the free-index case above, the QPO candidate remains significant above the broad band noise, but with a white noise cutoff located at a lower frequency, which in some energy bins leads to the periodogram being white noise dominated.
- OBSID:0653510501. Due to the forced upper index $\beta_1 = -1.1$ providing a poor description of the power spectrum of 1H 0707-495 at low frequencies, breaks are found in only a limited number of energy bands. Notably, the $\geq 3\sigma$ detection remains in the peak significance energy band ($4.0 - 5.4$ keV), but in others the index above the break is forced to be so steep to compensate, that the position of the white noise is moved such that these cases become white noise dominated.

- OBSID:0653510601. Similar to OBSID:0653510301, the detection in the peak significance energy band ($5.6 - 8.2$ keV), remains above the 3σ threshold, but the periodogram is at the limit of being white noise dominated, and in several energy bins where the detection significance is lower ($\sim 2\sigma$), the candidate is now found just beyond the white noise cutoff.

Frequency-restricted search: The detection of statistically significant QPO candidates at the same, or approximately the same, frequency in independent observations provides sufficient motivation for a frequency restricted search. The search across the other observations of 1H 0707-495 without blind detections uses the modal QPO candidate frequency of 1.95×10^{-4} Hz. Three additional candidates are detected at frequency-restricted p-value of $> 3\sigma$ in OBSID:0148010301, 0506200501 and 0511580101. In each case, a peak in power is found at the closest frequency bin to 1.95×10^{-4} Hz, similar to OBSID:0653510301, 0653510501 and 0653510601 where the blind $> 3\sigma$ QPO candidate is found, but with a smaller peak in power above the broad-band noise (in all cases, it remains the most prominent peak detected and is well modelled with a PLC model). In OBSID:0506200501 the $> 3\sigma$ frequency restricted p-value observations occur predominately over an energy range of $4 - 9$ keV, comparable to those aforementioned QPO candidates, while both OBSID:0148010301 and OBSID:0511580101 are only over a small number of softer energies, $\sim 2.4 - 3$ keV. At those harder energy ranges, these observations are found to be white noise dominated.

Previous claims: There are previous claims of significant QPO detections in 1H 0707-495, both concerning a single observation, OBSID:0511580401. Both Pan et al. (2016) and Zhang et al. (2018) report a QPO at 2.6×10^{-4} Hz in the full $0.2 - 10$ keV *XMM-Newton* energy range, via a Fourier and a non-Fourier wavelet analysis (see Scargle 1997 for an introduction to wavelet methods) respectively. A 3σ result is not recovered at this frequency in this analysis, where instead a 2σ feature at energies > 2.2 keV is found. Note, the blind selection criteria implemented here means a 88.9 ks flare-subtracted segment is studied for this observation, whereas Pan et al. (2016) opt instead to focus on the first ~ 55 ks, in a non-blind selection. Their selection process maximises their QPO claim significance, whilst considering the full observation reduces it to 90%, well below the 3σ detection threshold.

4.1.4 PG 1244+026

PG 1244+026 is highly variable, well studied NLS1 which has been the focus of numerous previous studies (Crummy et al., 2006b; Jin et al., 2013; Kara et al., 2013).

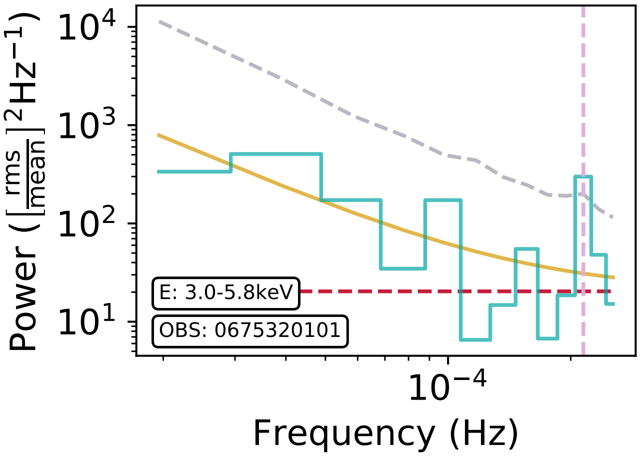

FIGURE 4.9: The highest significance ($\geq 3\sigma$) QPO candidate detected in a single observation of PG 1244+026 using the PLC model, with the corresponding frequency highlighted.

4.1.4.1 Initial PLC search

From a total of 7 *XMM-Newton* observations of the NLS1 PG 1244+026, only a single $\geq 3\sigma$ QPO candidate is detected, itself within the 71 ks longest continuous segment of OBSID:0675320101. This QPO candidate is found at a frequency of 2.15×10^{-4} Hz (see Figure 4.9), similar to the frequencies of those found in RE J1034+396, IRAS 13224-3809 (in some cases) and 1H 0707-495. The $\geq 3\sigma$ detections are largely restricted to energies above ~ 3 keV, as shown in Figure 4.2, similar to IRAS 13224-3809 and 1H 0707-495. This differentiates it from all QPO candidates in RE J1034+396 and the singular candidate in IRAS 13224-3809 (OBSID:0792180501) however, which also show $\geq 3\sigma$ detections at softer energies (< 2 keV).

4.1.4.2 Further tests

Free-index test:

- OBSID:0675320101. In all cases where the QPO candidate is determined to be $\geq 3\sigma$, a tentative break is found at $\sim 4 \times 10^{-5}$ Hz. The QPO candidate remains highly significant in the $\sim 2.0 - 7.0$ keV energy range, with reduced significance towards higher energies, e.g. $\sim 2.0 - 9.0$ keV. It is possible this break would be more easily modelled given a longer observation where lower frequencies could be sampled. In multiple energy bands, the QPO candidate is found to fall above the white noise cutoff and/or the number of frequencies is reduced such that the periodogram would be considered white noise dominated by the criteria set out in this analysis.

Fixed-index test:

- OBSID:0675320101. The periodogram can be well described with a fixed lower index, $\beta_1 = -1.1$ and the results from this test match those as above.

Frequency-restricted search: The frequency-restricted analysis was conducted across all observations of PG 1244+026, setting an *a-priori* QPO candidate frequency of 2.15×10^{-4} Hz. A single frequency-restricted $\geq 3\sigma$ candidate was found in OBSID:0744440301, strongest in the $2.0 - 7.8$ keV band, similar to the blind global significance test in OBSID:0675320101.

4.1.5 NGC 4051

As with the cases of IRAS 13224-3809 and 1H 0707-495, NGC 4051 is one of best-studied, highly variable NLS1s known (e.g. Breedt et al. 2010; Vaughan et al. 2011).

4.1.5.1 Initial PLC search

Across 17 *XMM-Newton* observations, two $\geq 3\sigma$ significance QPO candidates are detected. These two candidates are found at frequencies of 3.52×10^{-4} Hz and 1.56×10^{-4} Hz respectively. The former is shown as an example in Figure 3.3, and both candidates are compared directly in Figure 4.10. Notably, the QPO candidates in these observations are significant to $\geq 3\sigma$ in energy ranges of $4.6 - 7.6$ keV and $3.2 - 5.4$ keV respectively (as shown in Figure 4.2). Hence, there exists a difference in both frequency and energy bands in which the QPO candidates are found at $> 3\sigma$ significance.

4.1.5.2 Further tests

Free-index test:

- OBSID:0109141401. A tentative break at $\sim 1 \times 10^{-4}$ Hz is identified across most energy bands, and in each case the QPO candidate remains $\geq 3\sigma$. In a few energy bands – namely narrower bands such as $5.0 - 6.0$ keV and $5.2 - 6.2$ keV – the observations now class as white noise dominated. It is possible that the

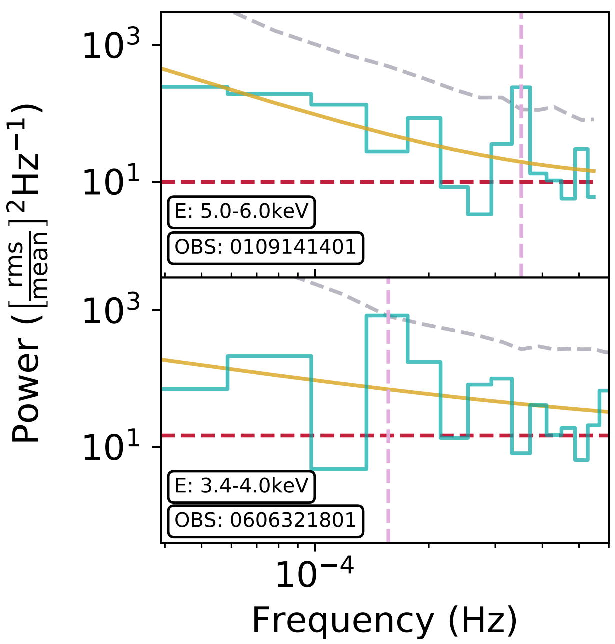

FIGURE 4.10: The highest significance ($\geq 3\sigma$) QPO candidates detected in NGC 4051 using the PLC model, with the corresponding frequency bin highlighted.

break occurs around the lowest frequencies observed this observation, such that it would be more easily determined given a longer observation. Figure 4.10 illustrates the QPO candidate being found at a frequency clearly higher than any putative break, such that ($> 3\sigma$) significance is not diminished if assuming a null hypothesis based on a BKNPLC model.

- OBSID:0606321801. A break is found consistently at $\sim 1 \times 10^{-4}$ Hz, across all energy bands, close to the QPO candidate at 1.56×10^{-4} Hz. The relative flatness of the index has led to identification of a QPO candidate when using the PLC model (as following the null hypothesis, removes the candidate bin from fitting), but describing the broad band noise with a break, lowers the candidate significance to a borderline 3σ detection.

Fixed-index test:

- OBSID:0109141401. Based on the previous test, the power spectrum of this observation can be well described with a lower index of -1.1. Freezing the index below the break therefore leads to results almost identical to the prior test: returning a QPO candidate well above the 3σ threshold for those energy bins not deemed to be white noise dominated.
- OBSID:0606321801. Unlike OBSID:0109141401, the power spectrum is *not* well described with a lower index of -1.1, and the magnitude of the break is reduced

near the QPO candidate frequency. In this case, the excess of power around the break is sufficient for the QPO candidate to remain detected at $> 3\sigma$ – highlighting the importance of model selection.

Frequency-restricted search: With two QPO candidate frequencies, it is difficult to motivate a single *a-priori* frequency for a search across those observations without blind detections. Searching at the two frequencies reported in Table 4.1, yields no supporting evidence of a feature at 1.56×10^{-4} Hz, but interestingly there is a single frequency-restricted $\geq 3\sigma$ candidate at 3.52×10^{-4} Hz in OBSID:0606320301, strongest at $3.6 - 5.0$ keV, similar to the case of OBSID:0109141401.

Previous claims: NGC 4051 has been the subject of multiple X-ray variability studies over several decades, with Papadakis and Lawrence (1995) reporting a broad QPO-like feature in *EXOSAT* data at a frequency of $\sim 4 \times 10^{-4}$Hz, which appears stronger in their low-energy band $(0.05 - 2)$ keV, than their medium-energy band $(2 - 10)$ keV. It should be noted that their methodology does not include the simulation of red noise following Timmer and Koenig (1995), but does consider fitting with complex models. They find a PLC + GAUSSIAN model provides a good description of the underlying power spectrum and QPO-like feature at low energies, with a highly significant improvement over a PLC model. Of note is the QPO candidate detected in OBSID:0109141401 lies at a similar frequency (3.52×10^{-4} Hz), but is significant at harder energies within their medium-energy band (see Figure 4.2).

Green et al. (1999) studied two, $0.1 - 2$ keV *ROSAT* observations of NGC 4051 and suggest the possible presence of a QPO-like feature at frequencies $>\sim 10^{-3}$ Hz. However, this is above the white noise limit for the observations studied here. Lastly, Vaughan et al. (2011) conducted a variability analysis of NGC 4051 using a series of *XMM-Newton* observations (with a total of ~ 570 ks), across the full energy range of $0.2 - 10$ keV, and across a frequency range of $\sim 1 \times 10^{-4} - \sim 1 \times 10^{-2}$ Hz. In which, they report no evidence of QPOs, although they do note that their analysis at harder energies $(2 - 10$ keV) provided tentative evidence for a possible feature at $\sim 4 \times 10^{-3}$ Hz, again beyond the frequency limit of this analysis. The key difference here is the high energy resolution of the lightcurves studied in this analysis, which allows for statistically significant features to be uncovered at narrower energy ranges. If considering the $0.3 - 10$ keV or $2 - 10$ keV energy bands only, this analysis would not detect any QPO features, in agreement with Vaughan et al. (2011).

4.1.6 ARK 564

ARK 564 is another well-studied NLS1, both on short (e.g. Kara et al. 2017) and long (e.g. McHardy et al. 2006) timescales, providing deeper insights into the complex nature of the broad-band noise, which is discussed further in Chapter 5.

4.1.6.1 Initial PLC search

QPO candidates are reported in 4 out of 11 *XMM-Newton* observations studied in this analysis. The nature of these candidates appears less stable than in the other AGN in the sample, and Figure 4.11 demonstrates the apparent movement of the QPO candidate towards lower frequencies with time (observations ordered chronologically).

The first observation in which a $\geq 3\sigma$ candidate is reported is OBSID:0006810101, and at a frequency of 1.88×10^{-3} Hz, is similar to the higher frequency QPO candidate located in IRAS 13224-3809, at a frequency of 1.02×10^{-3} Hz. The longest segment in this observation is uncharacteristically short, at only 4.95 ks, but with a period of $\sim$ 532s, a borderline acceptable quality factor of $Q \approx 6$ is obtained. The periodogram itself consists of the minimum required number of Fourier bins below the white noise to be able to well constrain the broad-band noise, making the model most at risk of bias from individual bins.

In OBSID:0670130501, a QPO candidate is detected at a frequency of 8.59×10^{-4} Hz, prior to the observations of OBSID:0670130701 and OBSID:0670130801 in which QPO candidates are found at 2.73×10^{-4} Hz and 2.54×10^{-4} Hz respectively – essentially equivalent given the error on the Fourier binning (see Table 4.1). The energy ranges in which these four QPO candidates are detected are largely consistent ($2 - 3$ keV), as shown in Figure 4.2.

4.1.6.2 Further tests

Free-index test:

- OBSID:0006810101. In requiring a break to occur at or below the QPO candidate frequency, this approach finds every energy bin of interest in this observation to be considerably restricted in the number of available frequency bins below the white noise cutoff. As a result, the significance of the QPO candidate cannot be discerned following the pre-defined criteria, and this is indicated by † in Table 4.1.

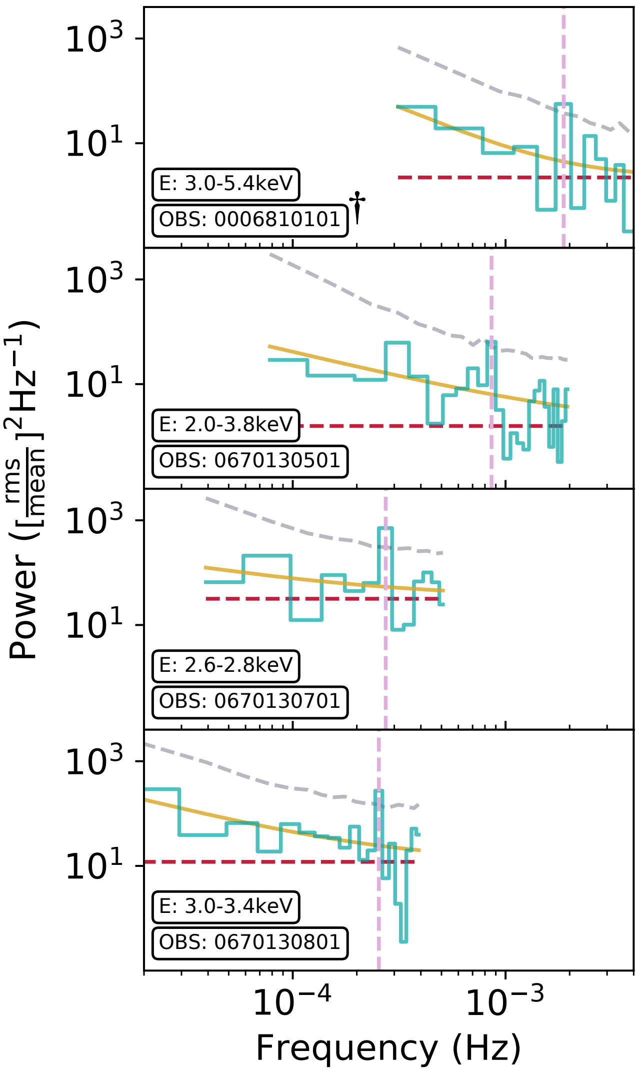

FIGURE 4.11: The highest significance ($\geq 3\sigma$) QPO candidates detected in ARK 564 using the PLC model, with the corresponding frequency bin highlighted. Of note is the apparent shift of the candidate to lower frequencies across each observation (and with time), where it appears to stabilise. Those which are not validated by further tests are highlighted († – see Section 3.3.4).

- OBSID:0670130501. A break is detected at a frequency of $\sim 3 \times 10^{-4}$ Hz above 2 keV, and instead at $\sim 5 \times 10^{-4}$ Hz when including energies below 2 keV. In the case of the former, the QPO candidate, at 8.59×10^{-4} Hz, is found to increase in significance as it lies above the break. In those energy bands where the break is located at 5×10^{-4} Hz, the significance of the QPO candidate is reduced, but remains around 3σ.

- OBSID:0670130701. The break is found to reside at a frequency of $\sim 8 \times 10^{-5}$ Hz in the $2.4 - 3$ keV energy range, and moves to $\sim 1 \times 10^{-4}$ Hz for $2.6 - 3.0$ keV and $\sim 2 \times 10^{-4}$ Hz for $2.6 - 3.2$ keV. The QPO candidate remains $> 3\sigma$, but decreases in significance with increasing energy and a higher break frequency. The peak significance band ($2.6 - 2.8$ keV) now classes as white noise dominated as the BKNPLC invokes a cutoff at a lower frequency.

- OBSID:0670130801. This observation contains the strongest QPO candidate located in ARK 564. Once again, the break is highly energy dependent: a break is found at $\sim 1 \times 10^{-4}$ Hz in the $3.0 - 4.0$ keV energy range, but this moves to $\sim 6 \times 10^{-5}$ Hz for $5.0 - 10.0$ keV, before the power spectrum flattens for energy bands > 6 keV and no break is detected. In each case, the QPO candidate is found above the 3σ threshold, although the significance lessens in energy bands > 6 keV.

Fixed-index test:

- OBSID:0006810101. All energy bands are classified as white noise dominated assuming this model.
- OBSID:0670130501. A lower index of -1.1 does not provide a good description for the break at any energy. This model typically locates the break at 6×10^{-4} Hz and reduces the QPO candidate significance, although not below the 3σ threshold.
- OBSID:0670130701. Once again, a lower index of -1.1 does not allow for a good description of the periodogram, but the QPO candidate remains above the 3σ threshold.
- OBSID:0670130801. As with the other observations, the periodograms are not well described with a lower index of -1.1, and most QPO candidates remain above the 3σ threshold, with the exception of energy bands > 5.6 keV, in which the candidates lie at the white noise cutoff frequency.

Frequency-restricted search: The observed variation in QPO candidate frequency means there exists minimal *a-priori* knowledge of a stable frequency for deeper searches, and therefore this step is excluded for ARK 564.

Previous claims: McHardy et al. (2007) reported an excess of power in the $2.0 - 8.8$ keV band in OBSID:0206400101 at $\sim 2 \times 10^{-4}$ Hz, but only at a 90% significance. This frequency is similar to two of the QPO candidates reported here in OBSID:0670130701 and OBSID:0670130801. The analysis presented here does not reproduce the feature found by McHardy et al. (2007), arguably because the longest continuous segment of this $\sim$ 101 ks observation is only $\sim$ 21 ks (due to numerous flaring effects), severely limiting the available frequency range.

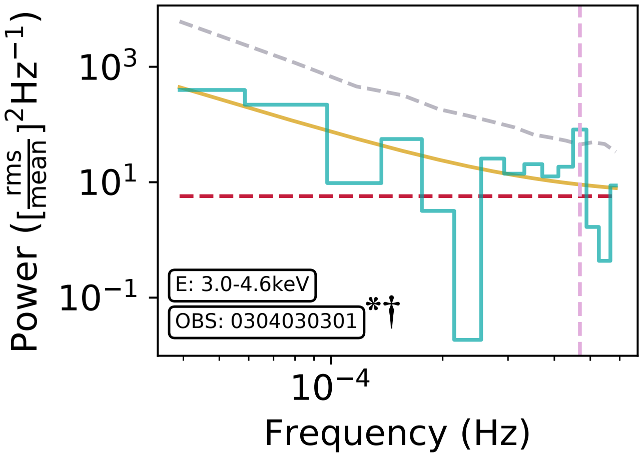

FIGURE 4.12: The highest significance – borderline – QPO candidate detected in the single observation of MRK 766 using the PLC model, with corresponding frequency bin highlighted. This observation is highlighted as being both a borderline 3σ detection, and a case which is not validated by further tests (*, † respectively – see Section 3.3.4).

4.1.7 MRK 766

MRK 766 is again well-studied (e.g. see Markowitz et al. 2007), with 9 archival *XMM-Newton* observations which were studied in this analysis.

4.1.7.1 Initial PLC search

A single QPO candidate at $\gtrsim 3\sigma$ is located, present at this borderline detection significance in a single energy bin, $3.0 - 4.6$ keV, and shown in Figure 4.12. Figure 4.2 demonstrates how the QPO candidate significance is found at a $> 2\sigma$ threshold in surrounding energy bins. At a frequency of 4.69×10^{-4} Hz, the QPO candidate frequency is similar to that of the other candidates located in the sample.

As the significance tests presented here are based on an underlying stochastic background, it is quite possible an observed outlier of power (above the modelled broadband noise) may appear to lie very close to 3σ (peaking above or dipping below this threshold under repeated tests). In the analysis of MRK 766, this occurs for this lone candidate. The borderline 3σ detection, coupled with a lack of supporting evidence from other observations (cf. IRAS 13224-3809 and 1H 0707-495 where there appear to be QPO candidates, at the same frequency, and similar energy ranges, observed across multiple, independent, observations) means this candidate detection is treated sceptically. It is reported here however for comparison.

4.1.7.2 Further tests

Free-index test:

- OBSID:0304030301. A break is found at $\sim 1 \times 10^{-4}$ Hz and white noise cutoff at $\sim 5 \times 10^{-4}$ Hz, which heavily restricts the number of frequency bins such that the periodogram is defined as white noise dominated.

Fixed-index test:

- OBSID:0304030301. With a frozen lower index of -1.1, identical results to test (i) are obtained.

Frequency-restricted search:

In order to search for supporting evidence for this singular candidate, a frequency restricted search was conducted at the frequency of 4.69×10^{-4} Hz. Searching across all other available observations, a restricted-frequency $> 3\sigma$ candidate is located in OBSID:0096020101, where it appears strongest in the $0.7 - 1.2$ keV band; notably at a lower energy range than in OBSID:0304030301.

Previous claims: There are previous claims of a strongly significant QPO in a single observation of MRK 766 (OBSID:0304030601) identified through a non-Fourier wavelet method (Zhang et al., 2017). However, this analysis does not find a significant feature at their reported frequency of 1.55×10^{-4} Hz.

4.1.8 Non-detections

In total, this study initially finds $\gtrsim 3\sigma$ candidates in 22 of 200 total observations (N.B. 2 observations of IRAS 13224-3809 find two distinct QPO candidates in different energy bands), which are then focus of further scrutiny. Another key result of this work however is the *non-detection* of QPOs to a $\gtrsim 3\sigma$ significance in 178 (or 89%) of observations. The potential reasons for non-detection of QPOs are multi-faceted. Within the studied sample, some AGN are of below average brightness, resulting in an observation with a lower signal-to-noise ratio and a relatively higher fraction of white noise, which may obscure much of the broadband noise, and subsequently result in the observation being deemed white noise dominated. Moreover, some observations are considerably shorter than those in which QPOs are detected (see Appendix A) and may be insufficient in length for the power spectrum to be reliably modelled (due to insufficient bins) or a QPO detected (as it lies outside the frequency bandpass).

The non-detection of QPOs is also likely a result of the inherent rarity, or at least difficulty in detection, of QPO phenomena. In the context of XRBs, HFQPOs are uncommon phenomena, often detected with a low fractional rms and typically only in certain spectral states. If this behaviour is extended to AGN, it would follow that QPOs may not be detected as they are of insufficient rms to be detected above the broadband noise, but also may be absent if the AGN exists in some spectral state analogous to XRBs which do not show QPO features. Indeed, a high proportion of those observations in the study were well described by a PLC model and showed no statistically significant QPO features, as would be expected under the above assumption. In order to detect more AGN QPOs therefore may require not just longer, high quality observations, but also an increased number to identify those AGN which exist in a preferential state for QPO detection. Future work may identify a link (spectral state, or otherwise) between those AGN in this study showing potential QPO phenomena, and those which do not.

4.2 Chapter summary

In this chapter I have presented the main results from the framework described in Chapter 3, in which 21 QPO candidates at $> 3\sigma$ were detected from the initial investigation, of which 4 are re-located QPOs in RE J1034+396. In addition, 3 borderline 3σ candidates are reported. Of note were detections of QPO features at the same/similar frequencies across independent observations in IRAS 13324-3809, 1H 0707-495 and ARK 564. This was not the case for NGC 4051, PG 1244+026 or MRK 766. The high energy resolution of this search uncovers the energy bands in which the QPO candidate frequencies are of highest significance and outside of RE J1034+396, these are shown to be almost universally at harder energies, above 2 or 3 keV. One exception is the highest frequency QPO candidate in the entire sample, IRAS 13324-3809 OBSID:0792180501, where it is detectable at soft energies only. This case is interesting due to the high coherence of the QPO ($Q > 50$) and the high frequency ($> 1 \times 10^{-3}$ Hz), setting it apart from the rest of the sample.

A key part of this work is understanding of the limitations of the approach. Further testing for the presence of undetected breaks in statistically preferred PLC models highlighted possible deviations from $> 3\sigma$ detection in 5 out of 20 new QPO candidates. These results are taken forward into the next chapter which further investigates additional sources of bias and uncertainty and draws some conclusions on how to interpret these initially promising findings in greater detail.

Chapter 5

Complexity in modelling broad-band noise and QPO detection

In this chapter I conclude the energy resolved search for QPOs in AGN by examining the biases introduced in the analysis procedure laid out in Chapter 3, and the limitations on the results which were detailed in Chapter 4. After which, I will discuss whether the investigated QPO candidates should be considered new detections of AGN QPOs, the key characteristics which they show and finally the implications of this research in the broader context of AGN X-ray timing analysis.

5.1 Effect of low count rates

The combination of exploring narrow bands and a falling instrumental response to high energies means that the effect of low count rates on the shape of the periodogram must be considered. Specifically, source count rates can approach the background count rate at high energies, even for the most luminous AGN. Due to the stochastic (Poisson) nature of the background, in the case of very low source count rates, the background-subtracted lightcurve may contain bins with unphysical, negative count rates. Across the full sample of $\sim 245,000$ energy resolved lightcurves, one or more negative bins were found in $\sim 30\%$ of cases. However, as shown in Figure 5.1, the vast majority of such lightcurves contain only a very small fraction of negative bins overall. For those cases where negative bins are present, the mean proportion of negative bins is $\sim 3\%$ of the lightcurve, with the 90th percentile at 7%.

The impact of negative count rates may be explored by simulating multiple sets of red noise lightcurves (using a PLC model and the Timmer and Koenig 1995 method

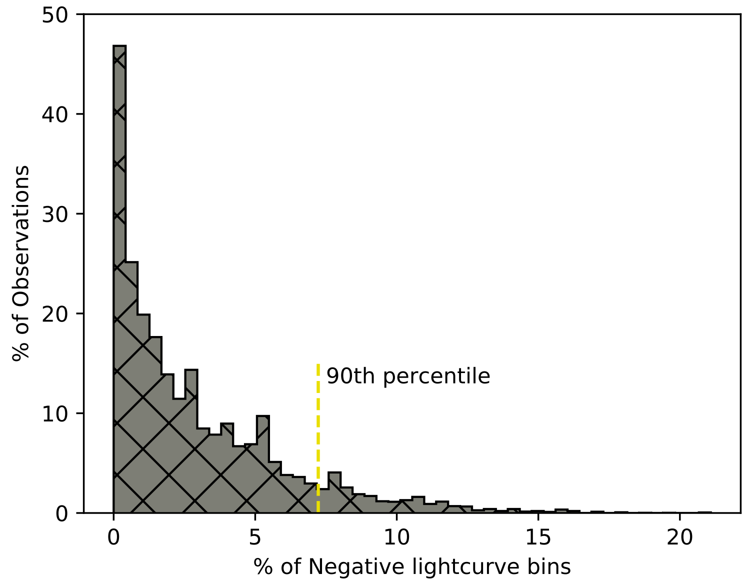

FIGURE 5.1: Histogram showing the percentage of negative count rate bins in the energy-resolved lightcurves with a minimum of a single negative bin ($\sim$ 30% of sample) and with periodograms determined to be above the white noise dominated threshold ($\geq$ 13 frequency bins at frequencies below the cut-off). It is found that most lightcurves have $<$ 1% negative bins, with the 90th percentile at $\sim$ 7%.

outlined in Chapter 3), each with a different fraction of negative count rates, achieved by changing the mean count rate of the background. The bias introduced from such negative count rate bins can then be directly inferred from the difference between the input index and that determined from fitting the resulting periodogram ($\Delta\beta = \beta_{\rm in} - \beta_{\rm out}$).

To perform the simulations, a set of best fitting PLC model parameters were selected: from IRAS 13224-3809, OBSID:0792180501 ($\beta = -1.95, \ln N_0 = -5.09$), and ARK 564 OBSID:0670130801 ($\beta = -0.99, \ln N_0 = -2.59$), as both have PLC models which well describe the data and respective indices close to -2 and -1 respectively, thereby allowing PLC parameter dependence to be investigated. Poisson noise was then added to the simulated red noise lightcurves based on the corresponding mean source count rate and a second *Poisson noise* lightcurve was added onto the first lightcurve, in order to simulate X-ray background in the detector (the mean count rate of the background being known in each case from the background lightcurve created through `EVSELECT`). Following an identical procedure to a real observation, this background was then subtracted using a new Poisson distributed lightcurve. This process then yields, in effect, a simulated, background-subtracted lightcurve, the periodogram of which is modelled following the method already described in Chapter 3.

The simulation described above is repeated $10,000$ times in total (across a range of increasing background count rates, from $0\% - 100\%$ the white noise level), with the

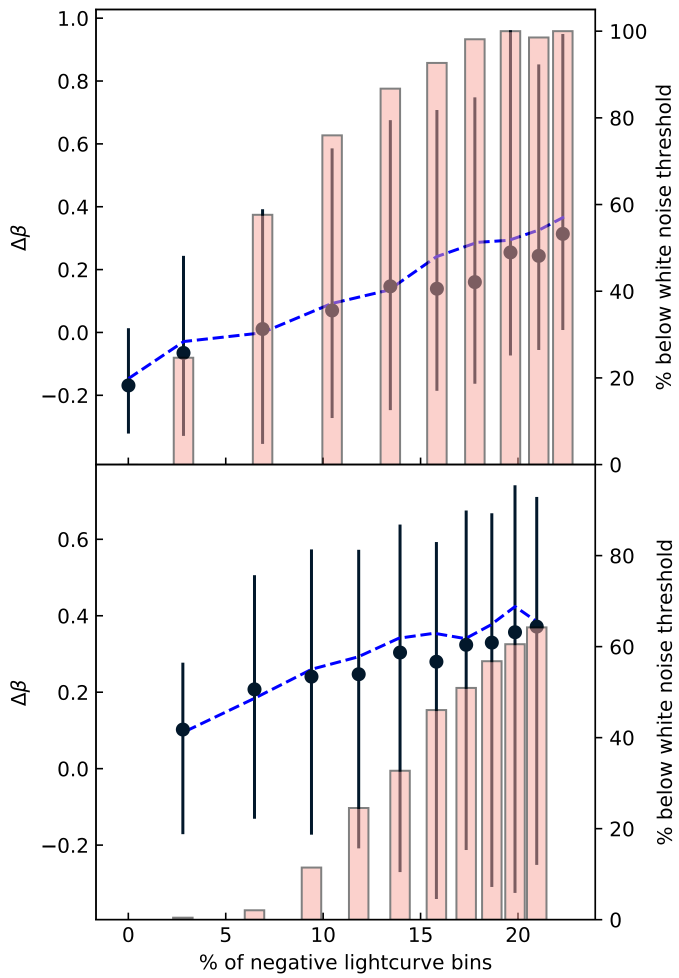

FIGURE 5.2: The impact on the inferred power spectral index, $\Delta\beta$, as a function of the percentage of negative bins found in a simulated Poisson-noise subtracted, red noise lightcurve (with 68% confidence intervals plotted). The blue dashed line shows the observed trend when these negatives are instead replaced with zeros. The pink bars correspond to the proportion of lightcurves where the periodogram would be rejected by the pre-defined requirement to have 13 or more Fourier bins at frequencies below where the white noise starts to dominate. Top panel: example case where PLC index $\beta \sim -1$, Bottom panel: example case where PLC index $\beta \sim -2$.

results shown in Figure 5.2. This figure indicates that for the vast majority of the actual lightcurves containing negative bins (7% at the 90th quantile level), their presence introduces a bias error on the index of $\Delta\beta < 0.2$, which lies comfortably within the expected 68.3% confidence intervals of β values using a PLC model – as shown in the case of Figure 3.5. This effect is slightly more pronounced in cases of steeper indices, towards $\beta \sim -2$, but even at the limit of the % of negative bins observed in the real data ($\sim$ 15%), this effect may be considered negligible compared to the uncertainty from fitting with a PLC model itself.

For both example PLC models, the number of simulated cases deemed to be white noise dominated (where the number of Fourier bins below the white noise cut off is < 13)

increases with the % of negative bins. This is especially true in simulated cases with a flatter index, $\beta \sim -1$, where this proportion becomes very high, at $> 70\%$ of cases when considering 10% negative bins. The application of this strict white noise cutoff therefore acts to reduce the bias from this effect, as those periodograms which are most affected are those where the number of bins is < 13. In the remaining sample periodograms there is only a very small proportion of negative bins, which introduce only a small source of secondary error unlikely to impact the results of the QPO search.

An alternative method of replacing all negative bins with zeros is also explored (see Figure 5.2), which results in a slightly increased level of uncertainty in the index, relative to the case of keeping negative bins as above. In both cases, $\Delta\beta$ increasing linearly with the fraction of negative bins in the time series. This approach clearly does not act to reduce the impact on the measured index, $\Delta\beta$, as the introduction of a non-stochastic count rate (of zeros) does not reflect the nature of the stochastic source and background. No statistical benefit is gained from this method, and this corrective procedure is not implemented.

5.2 Observations as free trials

The significance values quoted in Chapter 4 for each QPO candidate rely on the assumption that each observation is considered in isolation and only the number of free trials is limited to only the Fourier frequency bins considered, in any given observation. The motivation here for not treating each observation as being a free trial stems from the distinct possibility that certain spectral states, perhaps connected to the accretion rate, seem to be necessary for QPOs to appear (e.g. Alston et al. 2014b). A more stringent QPO candidate significance can instead be obtained by assuming each observation (200 in total) to be a free trial – regardless of data quality. This is a procedure which takes the most conservative perspective, but then fully accounts for the 'look elsewhere' effect, which is the expectation to observe statistically unlikely events given a sufficient number of observations, e.g. a 2σ event is expected to occur by chance approximately 1 in every 20 realisations of a random process.

In the case of those QPO candidates present at a single frequency in a single observation, such as PG 1244+026 and NGC 4051, the revised significance values fall to $< 3\sigma$. In the case of NGC 4051 OBSID:0109141401, this is reduced to the $\sim 2\sigma$ level, while PG 1244+026 OBSID:0675320101 falls to $< 2\sigma$. However it is important to stress that such decreases are likely to overestimate the impact, as treating each observation as a free trial assumes the data quality to be equivalent in all observations.

For those AGN with QPO candidate detections at the *same frequency* across multiple observations, the more stringent 'look elsewhere' effect is set against the conditional probability of detecting a QPO candidate at the same frequency in independent observations. This multiplicative probability calculation factors in $N = 200$ total observations (as a conservative estimate), the p-value (p_{Q_i}) derived from the global significance values of each QPO observation in a given AGN only at the same frequency (as in Table 4.1), with each subsequent detection (i.e. p_{Q_i} where $i \geq 2$) weighted by the number of frequency free trials (n_i) in each observation. Together this takes the form:

$$p_{value} = N \times (1 - p_{Q_1}) \prod_{i=1}^{C} \frac{1 - p_{Q_i}}{n_i} \tag{5.1}$$

for C number of observations where a QPO candidate is found at identical frequencies. Using this equation leads to the QPO candidate in 1H 0707-495 being found at $> 6\sigma$ significance, while the IRAS 13223-3809 QPO candidate at a frequency of 9.77×10^{-5} Hz may similarly be found at $> 6\sigma$ – although this drops to $> 4\sigma$ if excluding the detection in OBSID:0792180301, where the broad-band noise is not well constrained. In the cases of ARK 564 and RE J1034+396, the global significance values for some candidates of interest reach $GS = 1.0000$, whereby the precision limit for $10,000$ MC simulations is reached. If instead considering these individual global significance values to be similar to those observed in 1H 0707-495, the $2.54 - 2.73 \times 10^{-4}$ Hz QPO candidate in ARK 564 is found to be $> 4\sigma$, whilst RE J1034+396 reaches the $> 7\sigma$ level, due to exhibiting four observations all at equivalent frequencies (and remains the QPO detected to highest confidence in the AGN sample). These confidence values in themselves are additionally conservative as they consider only $> 3\sigma$ global significance values in Table 4.1, with no supplementary evidence from observations with lower significance candidates at the same frequencies.

5.3 Additional uncertainty in the broad-band noise

The analysis presented thus far has utilised only relatively simple models for the broad-band noise as these are typically a good description in the frequency range that is being studied (e.g. González-Martín and Vaughan 2012). However, there is the potential for further underlying complexity in the broad-band noise and power leakage which can affect the significance claims of a QPO candidate, and are considered here.

5.3.1 The impact of the white noise cutoff

Determining the frequency at which the underlying white noise within the observation becomes dominant over the intrinsic red noise is subject to inherent uncertainty in any fitting of the broad-band noise. In the procedure of defining the null hypothesis (Chapter 3) – the QPO candidate is removed from the periodogram and the broad-band noise is re-fitted (see Vaughan 2005), but the white noise cutoff frequency is left *unchanged* from the fit where the QPO candidate is included. Defining this frequency is a complex issue as the periodogram is by definition only one realisation of the underlying power spectrum. This is represented by the uncertainty in the underlying PLC model fit (see Figure 3.5), such that a different draw from the covariant matrix of model parameters may determine a different cutoff. As such this threshold is, in reality, best represented by a probabilistic distribution. When a single cutoff frequency is chosen in this analysis, it is done so with the caveat of not directly sampling from this distribution.

Re-fitting the broad-band noise with the QPO candidate removed tends to bring the white noise cutoff to a lower frequency. The result is that bins at high frequency may then be outside the investigated range of interest. Due to requiring a minimum of 13 Fourier bins (which includes the QPO candidate bin – although this frequency is ignored when the null hypothesis is defined) for fitting purposes, this can have the knock-on effect of removing energy bands from the results of this study. The combination of these two effects can remove QPO candidates either because they now fall into the white noise dominated region or because there are too few bins in the periodogram to reliably fit the underlying noise.

As an investigation of these effects, the white noise cutoff frequency was set from the PLC model applied to the data *without* the QPO candidate, rather than it being set by the fit with the outlier included. It is found that $\sim$ 39% of the $> 3\sigma$ energy bands are now white noise dominated (with < 13 frequencies in the periodogram, or < 12 bins when excluding the QPO candidate bin), a change driven by the removal of those narrow energy bands with relatively low count rates and so large amounts of white noise, which were close to being white noise dominated in the original analysis. Despite the loss of numerous energy bands, the majority of the reported $> 3\sigma$ QPO candidates remain (albeit constrained across fewer energy bands), with the few exceptions being: IRAS 13224-3809 OBSIDs: 0780561301 ($\nu = 7.81 \times 10^{-5}$ Hz only), 0792180301, 0792180601; 1H 0707-495 OBSID:0653510301, ARK 564 OBSID:0006810101, MRK 766 OBSID:0304030301, and perhaps most notably: RE J1034+396 OBSID:0675440101 (as well as almost all energy bins of OBSID:0655310201). It should be noted that a number of these observations were already borderline/close to the white noise threshold, so this result is as expected.

Whilst setting the white noise cutoff to the lower of the two frequencies is a more conservative approach, it also has the potential to remove real signals, as is evident for the case of RE J1034+396 (see Figure 5.3). In a similar fashion, the QPO candidate of 1H 0707-495 in OBSID:0653510301, is discarded by this more stringent approach but is still observed in OBSID:0653510501 *at the same frequency*, and so the choice of white noise cutoff can lead to the discarding of data which contain high probability detections at frequencies higher than the set threshold.

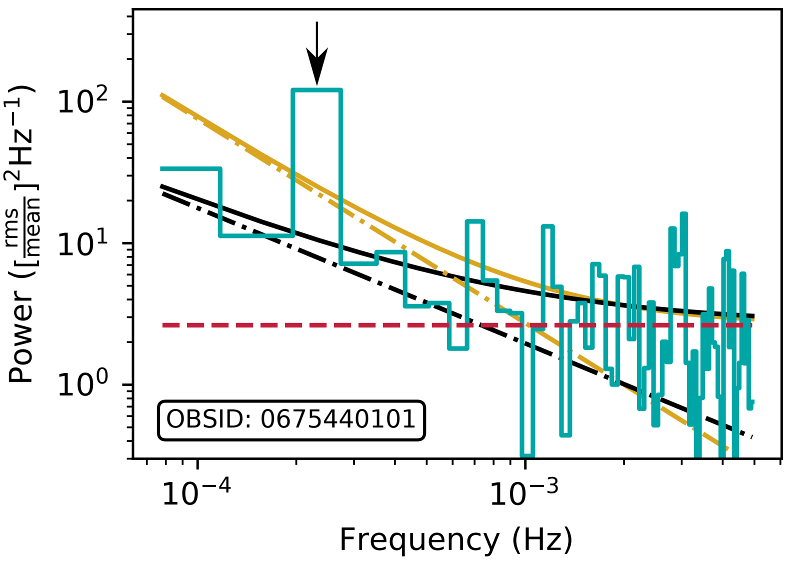

FIGURE 5.3: Example of the impact of the white noise cutoff selection via the two outlined approaches, for the established QPO in RE J1034+396, OBSID: 0675440101 (within the most significant energy band, see Table 4.1). Displayed are two PLC model fits, one (gold) including the QPO candidate bin, and the other (black) without the QPO candidate bin. The respective white noise cutoff frequencies in each case are determined to be the point where the underlying PLC model (dot-dashed) intersects the constant white noise level. As shown here, excluding the QPO candidate in the model fit results in the frequency of the white noise cutoff being lowered on average by $\sim 2 - 3$ bins. As demonstrated in this example, there is a risk of reducing the number of bins in the periodogram to below the minimum requirement set for modelling the broad-band noise – which would lead to the exclusion of this established and accepted QPO.

Alternatives to handling the uncertainty in the white noise cutoff include modelling the entire power spectrum, including all frequency bins dominated by the white noise. The limitation of this approach is that the quality of the fit can become dominated by the region dominated by white noise bins. This effect influences the BIC test, which implements a penalisation term for additional parameters, in addition to scaling by $\ln(m)$ for m bins in the fitted periodogram (see equation 3.7). The risk exists of favouring a simpler model (e.g. PLC) over a more complex one (e.g. BKNPLC), in a scenario of fitting some red noise data but now with white noise bins now included in the fitting, as would result in an increased maximum likelihood, but solely from the trivial fitting of white noise. This does not obtain insightful information about the AGN power spectrum. The BIC test may be preferred to the AIC test in this case for scaling with the number of data, but the caveats of fitting a predominantly white noise power spectrum remain.

5.3.2 The effect of windowing/red noise leak

As any individual observation spans only a relatively small frequency range compared to the full extent of the underlying power spectrum (see e.g. Uttley et al. 2002; McHardy et al. 2006), some amount of power leakage (i.e. red noise leak) is expected from longer timescales down into the observed band (see e.g. González-Martín and Vaughan 2012). In Fourier space, this is equivalent to convolving the Fourier transform of the window function (the Fejér kernel) with the underlying power spectrum (van der Klis, 1988). As a result, the intrinsic broad-band noise may not be well represented by that which is measured in the sample periodograms – measurements which underpin the null hypothesis test of all QPO candidates.

The impact of power leakage is explored on those periodograms in which there are found to be (all initially) significant QPO candidate detections (see Table 4.1), by simulating a lightcurve based on an underlying power law with an index of -2, following Timmer and Koenig (1995), but extending back to 10^{-5} Hz, i.e. down to lower frequencies than are typically observed in most cases, and then an effective window function is applied equivalent to the length of non-flared observation. To obtain an appropriate normalisation for the input power law, very long simulated lightcurves (far longer than the real data) are created from a power law with an index of -2 and trial normalisation. From each of these lightcurves a random segment of the same length as the real data is selected (representing a real, finite observation of the effectively infinite time series), the periodogram is generated and compared directly to the *observed* periodogram. This is done iteratively over a wide range of normalisation terms, stepping through each in log-space. The set of lightcurves whose median value minimises the negative log-likelihood between fake periodograms and observed periodogram indicate the normalisation of the *intrinsic* power spectrum – still assuming an index of -2. This process then simulates the windowing effect and determines the most probable (maximum likelihood) shape of the input power spectrum.

Using the best-fitting normalisation, $10,000$ long, fake lightcuves are simulated, the same window selection applied, periodograms obtained, and a search for false outliers conducted following the same process as the analysis pipeline for the observed data. In doing this, the standard analysis procedure is replicated for a case best approximating the true, intrinsic AGN power spectrum. As a test of the impact on the measured significance of the $> 3\sigma$ QPO candidates, this procedure is conducted on only the most significant energy-resolved QPO candidates, including borderline cases (as listed in Table 4.1). It is important to note that this is a somewhat extreme test, as it is likely that a break to to flatter indices occurs in most AGN before such low frequencies are reached (see e.g. McHardy et al. 2007) or that the power spectrum itself is flatter (i.e. $\beta > -2$), especially as the energy bands extend to higher energies (see e.g. Jin et al. 2020; Chapter 6), which is of importance as this is where the observed QPO candidates are mostly located. Figure 5.4 presents an example of this test for the impact of windowing as applied to NGC 4051 (OBSID:0109141401), where the intrinsic noise needed to create the observed noise is plotted onto the periodogram.

In applying the above test it is found that 8 out of the 24 candidates remain above the revised 3σ threshold. These include RE J1034+396 (OBSIDs: 0506440101 and 0675440201), IRAS 13224-3809 (OBSIDs: 0780561401 and 0792180501), NGC 4051 (OBSID: 0109141401) and ARK 564 (OBSIDs: 0006810101, 0670130701 and 0670130801). The remainder lie above a $\sim$ 98% threshold, i.e. an upper 2σ level. This is a clear indication that under extreme conditions it is possible for red noise leak to have an impact on QPO detection. It is also important to consider other factors before downgrading the significance of these candidates, such as those cases (e.g. RE J1034+396) where QPO candidate frequencies are observed to remain similar across multiple observations, which itself is hard to reproduce through fake signals generated by an underlying stochastic process.

The effect of red noise leak is most pronounced when dealing with short observations and steeper power spectra ($\beta \sim -2$) – the index assumed in the test above. In a number of cases, where the lightcurve is long ($\sim$ 100 ks) and/or the measured index flatter (e.g. 1H 0707-495 QPO periodograms are observed with $\beta \sim -1$), this effect is effectively suppressed.

5.3.3 Complex broad-band noise models

A natural extension to a test using a PLC or BKNPLC model is one in which the underlying noise is described by a series of Lorentzians (e.g. McHardy et al. 2007). This concept is physically motivated by propagating fluctuations through the accretion disc, where variability (at the viscous frequency) is produced locally at every radius, and the flow acts as a low pass filter to dampen out higher frequencies through both viscous and differential rotation effects (e.g. Churazov et al. 2001; Ingram et al. 2016; Chapter 2), such that variability is coupled between a broad range of timescales in the accretion flow (Uttley et al., 2017). McHardy et al. (2007) propose a double Lorentzian model to describe the underlying broad-band noise of ARK 564, and here the statistical impact that such a model might have on QPO significance is investigated – assuming the model can be applied to other AGN in the sample.

A set of fake periodograms are simulated down to a frequency of 10^{-5} Hz, using a Monte Carlo routine that assumes the power is generated from the Lorentzian model parameters used to describe the high energy power spectral data of ARK 564 (without white noise) in McHardy et al. (2007). For each simulated periodogram in turn, the R values, $R_j = 2I_j/P_j$ (see Chapter 3) are determined and a fit made with a PLC model (minus white noise) to obtain the best-fitting parameter values for the index and normalisation. Using these PLC parameters, a new set of fake periodograms is simulated,

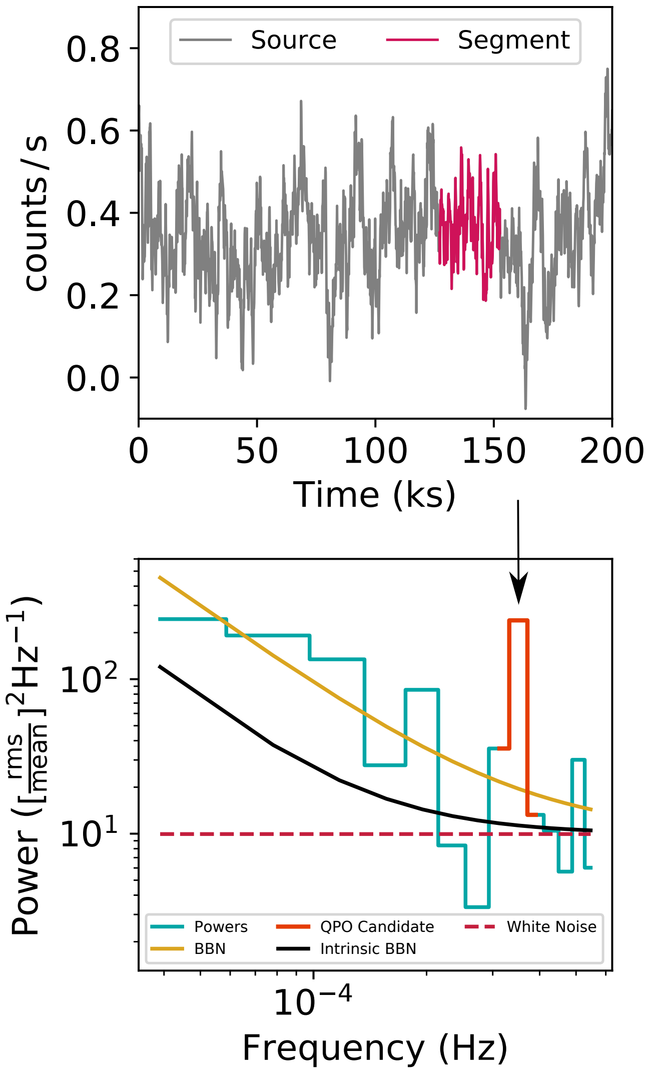

FIGURE 5.4: Top: example of a simulated light curve for NGC 4051 (OBS ID:0109141401), with a highlighted, randomly selected segment of length equal to the longest observed continuous segment of the real data. Bottom: observed periodogram (QPO highlighted), with best fitting PLC model and the intrinsic, pre-windowed PLC model.

assuming a PLC model. After 100,000 simulations, the distributions of powers across both the periodograms simulation from the Lorentzian model, and PLC model, are used to calculate the free-trial-corrected 3σ contours obtained across the broad-band noise at each frequency (see equation 3.11; Vaughan 2005).

Figure 5.5 compares the two sets of contours (determined from Lorenztian model inputs and PLC model inputs respectively) on top of two sets of simulated data (from each model). It is clear that, over much of the frequency range, the significance is in fact *under-estimated* when a PLC model is used as an approximation. The significance

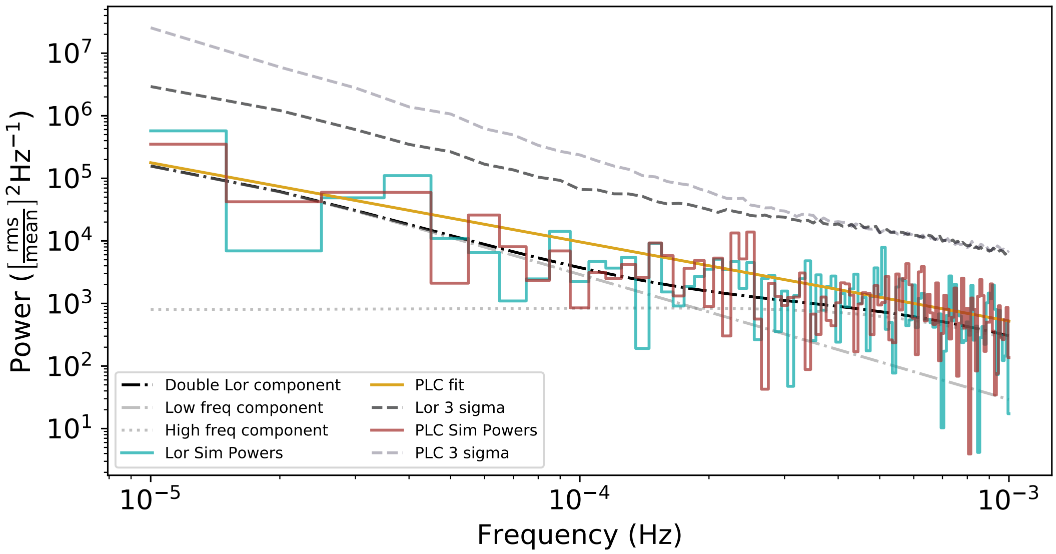

FIGURE 5.5: Simulated power spectra from $10^{-5} - 10^{-3}$ Hz, generated from the high energy, double Lorentzian model for ARK 564 (McHardy et al., 2007) and a PLC model fitted to the data generated from this. The model choice has a notable impact on the 3σ significance contours (Vaughan, 2005). In this case, should a PLC model be assumed, but a double Lorentzian model instead account for a more realistic description of the broad-band noise, then the resulting QPO candidate significances may be underestimated at low frequencies.

contours become more comparable as the higher frequency Lorentzian starts to dominate the broad-band noise however.

Should a multiple Lorentzian model be a more appropriate description of the underlying noise for all of the observations at high energies, then the impact on the QPO candidate significance is expected to be relatively minor. However, given the lack of constraints on the nature and energy-dependence of any Lorentzians underlying these data, it is clear that this remains an open question. A point worth reiterating is that accurately modelling the shape of the noise is vital for any robust significance claims (see Vaughan et al. 2016 for more discussion on this topic).

5.4 On the significance of QPO candidates

To-date, the presence of AGN X-ray QPOs across multiple observations has been limited to several significant detections in the NLS1 AGN, RE J1034+396 (Gierliński et al., 2008), with a single claim in MS 2254.9-3712 (Alston et al., 2015), a number of tentative claims in other NLS1s, and signals in tidal disruption events (TDEs, see Pasham et al. 2019). Following the methodology laid out in this work, an initial 21 QPO candidates are detected at $> 3\sigma$ (and 3 borderline 3σ) across 7 AGN. Subject to further tests, a total of 16 are considered unaffected by remodelling with a BKNPLC model. If considering the most conservative test in the impact of red noise leak, this number drops to 8.

5.4.1 Multiple independent detections

The reported results include the re-detection of the QPO in RE J1034+396 which was used to corroborate this approach, as well as in bright, highly variable, well studied NLS1s: IRAS 13224-3809, 1H 0707-495 and ARK 564, which have had QPO claims before, albeit quoted at different frequencies to those that are reported here. In addition, this search provides details of the energy dependence of the reported significance and the repeat occurrence of these signals across multiple observations. This last point is important: in several cases (notably 1H 0707-495 and IRAS 13224-3809) the QPO candidates appear at the same or very similar frequencies across multiple observations (see Table 4.1). The nature of the stochastic broad-band noise is such that for two or more independent realisations to show statistically significant QPO features at the *same frequency*, is to greatly increase the likelihood that they are genuine – see the conditional probabilities in Section 5.2, where significance levels in excess of 6σ are obtained for QPO candidates in 1H 0707-495, IRAS 13224-3809 and, as expected, RE J1034+396. It should also be noted that in most cases, the quality factor and rms of the signal is large ($Q > 10$ and FRMS $\gtrsim$ 10%, see Table 4.1) in keeping with the characteristics of the established QPO in RE J1034+396 (Middleton et al., 2011; Alston et al., 2014b; Jin et al., 2020).

Repeat detections have not been made for all reported QPO candidates. Notably, significant candidates in NGC 4051 and PG 1244+026 are seen in only a single observation, with minimal evidence of a comparable feature in other observations when performing a non-blind (frequency-restricted) test in NGC 4051 (at 3.56×10^{-4} Hz), and in PG 1244+026 (at 2.15×10^{-4} Hz). Although individually promising cases – much like the MS 2254.9-3712 QPO claimed by Alston et al. (2015) – the probability that these are bona-fide QPOs is reduced by the 'look elsewhere effect'. The case of MRK 766 is found to be both borderline 3σ in only a single energy bin, with minimal supportive evidence in a frequency restricted search and with an loss of the QPO if assuming a BKNPLC model. Altogether, the case of MRK 766 is considered an unlikely candidate and hereafter is not considered further.

5.4.2 Constraining the high-frequency break

A possible limitation in the approach taken to estimating the significance of QPO candidates, is rooted in the data-led maximum likelihood search for a break in the power spectrum, which does not incorporate any prior expectations for its position (e.g. McHardy et al. 2007; González-Martín and Vaughan 2012). As such, in incidences where the high frequency break is not well sampled (i.e. only appears across a minimal number of bins) or if the shape of the broad-band noise is not consistent with a BKNPLC model more generally, then the break may not be identified. This issue is exacerbated due to the fact observations are studied individually and independently of one another (i.e. they are not concatenated, which would extend the frequency range and better sample the high-frequency break).

To ensure the presence of an undetected break does not bias the calculated QPO candidate significance, the rigorous test of *forcing* a break into the periodogram (see Section 3.3.4) is implemented, and the occasional change in QPO candidate significance then underlines the need for caution when claiming the presence of a QPO, even when the PLC broad-band noise model is statistically preferred. In future, and with data which extend to lower frequencies (i.e. from longer observations/segments), more stringent tests will be possible. Naturally, a Bayesian methodology with informative priors motivating the expected nature of the break may appear at first to be a preferred approach to detecting the break, but it is important to note that the present lack of a well-constrained probability distribution describing the position and particularly the *energy dependence* of the break detracts from such an approach. The energy resolved nature of the search performed here may sample the break over energy ranges in which the nature of the break is not well understood (even if previously observed in a given AGN, in a broader energy bandpass).

Given the situation of poorly motivated priors and somewhat limited data, the analysis relies upon its frequentist approach, although Bayesian inference may allow for a more accurate assessment of the presence of breaks in future, given further energy dependent studies of AGN.

5.4.3 Key characteristics of QPO candidates

Given the above caveats and warnings over the uncertainty in the broad-band noise, the following section discusses the QPO candidates this analysis has identified and the possible unifying features in the sample.

5.4.3.1 Mass accretion rate

RE J1034+396 is well known for having a strong soft excess (Puchnarewicz and Soria, 2002; Casebeer et al., 2006; Middleton et al., 2007, 2009), likely a result of extremely high accretion rates, which has led to comparisons being made between its QPO and the $\sim$ 67 Hz HFQPO observed in GRS 1915+105 when accreting at high Eddington fractions (Morgan et al. 1997; Ueda et al. 2009; Middleton and Done 2010; Jin et al. 2020). More generally, HFQPOs are only seen in BHBs in their very high state (see

Remillard and McClintock 2006), when the mass accretion rates can reach significant fractions of their Eddington limit (see e.g. Nowak 1995). It is therefore reasonable to postulate that the HFQPO mechanism is intrinsically tied to these high mass accretion rates (Blaes et al., 2006a).

Of the AGN sample containing QPO candidates, RE J1034+396, IRAS 13224-3809, PG 1244+026, 1H 0707-495 and ARK 564 have all been reported accreting at close to their Eddington limits (Done and Jin, 2016; Alston et al., 2020; Kara et al., 2017; Done et al., 2012) as is also the case for MS 2254.9-3712 (Alston et al., 2015).

Indeed, NGC 4051 may be the only exception, accreting at $\sim$ 0.1 Eddington (Peterson et al., 2000; Alston et al., 2013a). Whilst the uncertainty involved in mass accretion rate determination means it is not possible to be entirely certain of the true nature of these sources, there could well be a link between the high accretion rates in these AGN (as well as in TDEs) and the QPO candidates discovered.

Naturally, high accretion rates (and therefore high luminosities) could result in some level of selection bias – the ability to detect a QPO relies on high signal-to-noise ratio data and so an observer may be more likely to detect signals in predominantly bright, high accretion rate AGN. A test for this bias is not easily achievable due to the uncertainty on both the SMBH mass measurements and accretion rate estimates. It remains quite possible however, that QPOs in AGN are far more commonplace than previously thought, but the present difficulty in obtaining the required data quality to probe a sufficient frequency range, biases this study towards intrinsically bright, or sufficiently local AGN. In future, new, high-throughput instruments such as *STROBE-X* and *Athena* will be able to probe many more AGN with a high signal to noise ratio, as well as extend searches for QPOs to higher frequencies.

5.4.3.2 Energy dependence

The energy bands in which significant QPO candidates have been found vary between sources, but remain largely consistent between observations of the same source and, with the exception of RE J1034+396, the detections are most significant in bands above 2 keV. This was also found by Alston et al. (2015) in their investigation of MS 2254.9-3712, where the QPO is detected at $2-5$ keV and provides evidence that the hard energy components (i.e. the coronal emission and reflection) of the AGN energy spectrum may be central to QPO production. The exception of RE J1034+396 is interesting, as Jin et al. (2020) argued for the QPO in this source to be driven by the soft excess component, in observed changes in the soft excess (i.e. different spectral states) appear to change the nature of the QPO, including the result where the QPO is absent in two observations in which the soft excess is strongest. This conclusion aligns with one made by Alston et al. (2014b), in which they speculate the soft component may impact the QPO state, given their report of the QPO being detected in five hard energy bands ($1.0 - 4.0$ keV) and only once in the soft band ($0.3 - 0.8$ keV). Alternatively, Alston et al. (2014b) propose the energy dependence of the QPO significance in RE J1034+396 could indeed relate to the hard energy components, a conclusion reached in Middleton et al. (2011). Neither conclusion need be at odds with the detection of the RE J1034+396 QPO in soft bands only in this analysis however, as Figure 4.2 shows, the energy bands typically > 2 keV become white noise dominated. This is in part due to the soft excess in RE J1034+396 which dominates the counts in the observations, such that at harder energies the excess power in the periodogram is diminished sufficiently such that it tends to become white noise dominated.

In the other investigated AGN, beyond RE J1034+396, the lack of QPO detection in the soft band, $\lesssim 2$ keV, may support the notion of AGN QPOs being associated with the Compton power law spectral component, in energy bands $\gtrsim 2$ keV. The case of IRAS 13224-3809 OBSID:0792180501, where the QPO candidate is clearly significant in the soft band (see both Figure 4.4 and 4.5) is the stand-out exception, and future studies will likely be able to investigate the spectral state of this observation to uncover if it has a different physical origin to those other QPO candidates in IRAS 13224-3809.

The energy-dependence of the statistical significance of these QPO candidates also indicates a reason as to why previous studies (e.g. González-Martín and Vaughan 2012) have not detected them, as they do not appear in the typically studied full bandpass $0.3 - 10$ keV, nor in generic soft, $0.3 - 2$ keV, or hard, $2 - 10$ keV bands, as also investigated by González-Martín and Vaughan (2012). This, in turn, suggests the nature of QPOs are physically tied to specific components of the SED, with variability intrinsic to the QPO most prominent in specific energy bands. In broader energy bands however, there is the possibility this QPO variability can become effectively ‘washed out’ by noise from other components (e.g. the soft excess in RE J1034+396), such that the QPO variability is not observed to be statistically significant. Moreover, the analysis explores the energy dependent shape of the underlying broad-band noise in the power spectrum, making it easier to locate QPOs in certain energy bands.

5.4.3.3 QPO frequency

The QPO frequency is naturally an important parameter in understanding the accretion flow (e.g. as a result of motion of the flow or characteristic timescale of an instability). The prior knowledge of AGN QPO frequencies in this regard was somewhat limited to the $\sim 2.5 \times 10^{-4}$ Hz detection in RE J1034+396 (Gierliński et al., 2008) and the $\sim 1.5 \times 10^{-4}$ Hz detection in MS 2254.9-3712 (Alston et al., 2015). In this analysis, QPO candidates are detected with very similar frequencies to these in both 1H 0707-495 and PG 1244+026, whilst NGC 4051 and IRAS 13224-3809 show greater variation in frequency between different observations, but still with some candidates around $\sim 1 \times 10^{-4}$ Hz.

The physical relevance of these frequencies will tie closely to the QPO genesis mechanism, which is as of yet not well determined. It is certainly of interest that the majority of candidates appear to cluster around the $\sim 1 - 3 \times 10^{-4}$ Hz range. Care must be taken before reading too much into this however, for the sample size remains small (although greatly improved) and an observational bias exists given that the vast majority of AGN periodograms in this sample (and more widely) investigate (at most) a $\sim 1 \times 10^{-6} - 1 \times 10^{-2}$ Hz frequency range. The majority of the observations in this sample are constrained between $\sim 1 \times 10^{-5} - 1 \times 10^{-3}$ Hz, limited at low frequencies by the length of observation and at high frequencies by the data quality (i.e. the Poisson noise level).

IRAS 13224-3809 is of particular interest for both the number of $\geq 3\sigma$ candidates and the consistency of their frequencies, with many close to $\sim 1 \times 10^{-4}$ Hz. The presence of *possible* harmonic features or, as reasoned in Section 3.3.4), probable (energy-dependent) break features is also unique amongst these observations, although this may simply be a consequence of being able to probe to lower frequencies due to the the longer observations available for this source (in part due to the recent 1.5 Ms study with *XMM-Newton*). Beyond the detection of QPO candidates at the same frequency, perhaps the most interesting QPO detection is the case of OBSID:0792180501 at 1.02×10^{-3} Hz, where it is observed at frequencies typically above the white noise threshold in most observations (see Figure 4.3). It is possible that this is not a unique occurrence, but a test for repeat detections is not possible in most of IRAS 13224-3809 (and other AGN more broadly) due to the Poisson noise level, which is only low enough for frequencies $> 1 \times 10^{-3}$ Hz to be observed for energy bands with high count rates. Although it is tempting to draw parallels with the speculated higher frequency QPO candidate detected in ARK 564 (1.88×10^{-3} Hz), the cases are considerably different, with the ARK 564 candidate detected only in a very short segment and where an additional test of a BKNPLC model found the periodogram white noise dominated. These candidates provide clear motivation for proving high, non-white noise-dominated frequencies (especially at higher energies) – an effort which may reveal many more QPO candidates in future.

ARK 564 is rather unusual amongst the AGN sample, with a QPO candidate frequency decreasing with time, before an apparent stabilisation around $\sim 2 \times 10^{-4}$ Hz, where a candidate is observed at the same frequency in subsequent observations. The apparent motion of the QPO candidate is difficult to discern as the frequency range and white noise cutoff similarly evolve across observations. It may however be the result of the physical process creating a genuine QPO changing with time, potentially settling, as suggested in the case of RE J1034+396 (Gierliński et al., 2008). As noted earlier, these results assume a simplified description of the underlying broad-band noise and, for ARK 564 specifically, previous modelling has identified the presence of breaks and Lorentzians (e.g. Papadakis et al. 2002; McHardy et al. 2007), which in one observation occurs close to the QPO candidate frequency (OBSID:0006810101). However, as evidenced via simulations, it is unlikely that modelling the broad-band noise with Lorentzians could lead to an overestimate of QPO significance.

Should these AGN QPO candidates be analogous to those observed HFQPOs in BHBs (Middleton and Done, 2010), then a simple inverse-mass relation might be expected for the QPO frequency, assuming that the mechanism producing HFQPOs also scales inversely with mass. Unfortunately, the SMBHs in the sample are of comparable mass (see Table 4.1), and the present uncertainty in the mass measuring techniques renders any correlation to be dominated by uncertainty, so investigating any linear relationship between QPO frequency and black hole mass (across AGN and XRBs) – as had been attempted previously, e.g. Smith et al. 2018 – is dominated by this uncertainty.

5.4.4 New AGN QPOs?

The search for X-ray QPOs in AGN has been an ongoing challenge within the field for a number of decades (Vaughan and Uttley, 2005) with multiple studies claiming QPO detections (e.g. Vaughan and Uttley 2005). To-date, only two AGN (non-TDEs) have signals which have been widely accepted as genuine (Gierliński et al., 2008; Alston et al., 2015), with RE J1034+396 the exceptional (i.e. bona-fide) case with repeated detections over many independent observations (Alston et al., 2014b; Jin et al., 2020). This work builds upon the broad AGN search conducted by González-Martín and Vaughan (2012) by performing a highly energy-resolved search to locate significant ($\geq 3\sigma$) QPO candidates across a small subset of bright AGN. Of those candidates located, the majority lie in harder energy bands, and some with repeat detections across several observations.

An important strand of this work is to develop an comprehensive understanding of the limitations of these statistically significant claims and robustly test the nature of models applied to the broad-band noise, in order to develop a realistic view of the complex nature of AGN variability. After conducting numerous tests in an attempt to investigate the true nature of these QPO candidates, there remain a number of highly significant features appearing at the same or similar frequencies across multiple (independent) observations, which diminishes the likelihood that they are spurious. As this study finds no evidence that these are in fact related to a high-frequency break or other component of the broad-band noise, it appears likely that the multiple QPO detections in 1H 0707-495 (at $1.27 - 1.95 \times 10^{-4}$ Hz), IRAS 13324-3809 (at 9.77×10^{-5} Hz) and ARK 564 (at $2.54 - 2.73 \times 10^{-4}$ Hz) are physically real QPO phenomena. This is arguably the most important discovery since the initial reporting of the first confirmed QPO in RE J1034+396, for it gives the first examples of AGN with a robust QPO signal in more than one AGN. In doing so, it more than doubles the sample size of known AGN QPOs and opens up the opportunity to both explore these phenomena further and study energy resolved power spectra of future observations for re-appearances of these features.

In addition to the above, it appears highly probable that the higher frequency QPO in IRAS 13224-3809 (at 1.02×10^{-3} Hz) is genuine. With a high coherence value, where $Q > 50$, this feature appears over many cycles, at high significance, in an observation that is over 100 ks in length (and is not preferentially selected or segmented). Unfortunately, it is not trivial to search for this QPO in other observations, which may not reach above 1×10^{-3} Hz. This candidate will likely be a key target for future observations of IRAS 13224-3809, in a search for re-detection. Beyond these AGN, the candidate in PG 1244+026 appears similar to other candidates in the sample if comparing its frequency (at 2.15×10^{-4} Hz), energy dependence of its significance and the shape of the broad-band noise. This is similarly the case for NGC 4051 (at 3.52×10^{-4} Hz). These factors alone typically warrant publication, even for a single observation, but considering the 'look elsewhere effect', it is best to be cautious and instead conclude that these are interesting cases which warrant further searches in future observations.

In all, the detection of those robust AGN QPO candidates not only expands the known sample size of such signals, but opens up the possibility of exploring the QPO formation mechanism in new, remarkable detail and implies that new missions (e.g. *Athena* and *STROBE-X*) will more regularly detect such features.

5.5 Chapter summary

In this chapter I have explored many effects which add additional complexity to both modelling the broad-band noise and subsequently testing the significance of QPO candidates. The effect of low count rates was investigated, finding that for a highly energy-resolved approach, a number of negative count rate bins in a lightcurve is expected, but a subsequent analysis finds the effect on the shape of the broad-band noise is typically negligible and within the range of error from the maximum likelihood fit. In addition, the impact of determining the white noise threshold was investigated, finding that this could negate QPO candidate detections, but not suppress those already reported. An investigation into the impact of red noise leak finds that this effect would reduce the significance of these candidates, some to below 3σ, but the assumptions made here represent the most extreme test for QPOs, which do not necessarily hold up in practice. More complex broad-band noise models were investigated, such as a double Lorentzian model, which found that assuming such a model would actually *increase* the significance of the reported QPO candidates at some frequencies.

The significance of each candidate was also re-evaluated, factoring in both the 'look elsewhere effect' if considering all observations as free trials, alongside the conditional probabilities of multiple detections in some cases. This led to significances in each case of RE J1034+396 ($> 7\sigma$), IRAS 13224-3809 ($> 6\sigma$), 1H 0707-495 ($> 6\sigma$) and ARK 564 ($> 4\sigma$). Those in PG 1244+026, NGC 4051 and MRK 766 fall in significance to $< 3\sigma$ however.

A summary of the QPO candidate characteristics found the majority lie at frequencies $\sim 1 - 3 \times 10^{-4}$ Hz, with some lower and higher frequency exceptions. The majority are also found to only become significant above ~ 2 keV, with only a few exceptions such as in RE J1034+396 and IRAS 13224-3809 OBSID:0792180501. In almost all cases, the coherence is fairly high, $Q \gtrsim 6$ with notable FRMS values in 1H 0707-495 and IRAS 13224-3809 in particular, highlighting the prominence of the reported detections. In all, it was concluded that there are highly realistic QPO features present in IRAS 13224-3809, 1H 0707-495 and ARK 564, with possible additions to this group in PG 1244+026 and NGC 4051 – which expands the known AGN QPO sample from one or two AGN (depending on set criteria), to at least double that.

Chapter 6

Constraining energy-dependent emissivity profiles of AGN inflows

In this chapter I explore the energy dependent nature of the shape of the periodograms of the full AGN sample studied in this work. I will investigate and present how the power spectral index changes with energy across (independent) energy bands of multiple AGN, and develop and implement a theoretical framework which derives the expected shape of the periodogram when incorporating the effect of propagating fluctuations in the accretion flow, while also considering the impact of reflection. This framework is based on a low pass filter and energy dependent emissivities. I then investigate whether there exists a relationship between the macroscopic properties of the sample SMBHs and the emissivity profiles.

6.1 Exploring the energy dependence of AGN variability

Studying the variability of AGN on short ($<$ Ms timescales) provides the observer with the means to probe the otherwise unresolvable geometry of the inner accretion flow (Fabian et al., 2009; Wilkins and Fabian, 2013; Kara et al., 2019; Alston et al., 2020); search for quasi-periodic oscillations (QPOs) resulting from plasma dynamics or instabilities (Gierliński et al., 2008; Middleton and Done, 2010; Alston et al., 2014b), and explore scaling relations to access the SMBH mass (e.g. Papadakis 2004; McHardy et al. 2006). Where data quality permits, the energy-dependence of the variability can provide even greater insight via, e.g. energy-lag spectra (Kara et al., 2019), deeper QPO searches (Ashton and Middleton 2021a; Chapters 3, 4, 5), rms and covariance spectra (Middleton et al., 2009, 2011; Uttley et al., 2014a).

The energy-dependent shape of the broad-band noise forming the power spectrum (periodogram or PSD) is thought to be a result of propagation of fluctuations (Lyubarskii

1997; Churazov et al. 2001; Ingram and Done 2011; Turner and Reynolds 2021), the sampling of different spatial scales, differing emissivities (Arévalo and Uttley, 2006), and the different processes dominating various energy bands (e.g. the soft excess versus bands in which the intrinsic coronal emission dominates). Studies of the energy-dependent shape of the power spectrum have been rather limited, partly due to the requirement for high signal-to-noise data and long observations (to probe down to low frequencies and accurately constrain the shape of the power spectrum). When studies have been performed, they are usually restricted to a single AGN of interest, e.g. NGC 7469 (in three energy bands: Nandra and Papadakis 2001), MCG-6-30-15 (in three energy bands: Vaughan et al. 2003b; McHardy et al. 2005), NGC 4051 (in two energy bands: McHardy et al. 2004, and in three energy bands using concatenated observations totalling $\sim$ 570 ks: Vaughan et al. 2011), and most recently in RE J1034+396 (in three energy bands: Jin et al. 2020). In all these previously published cases, the trend has been that the index of the power law describing the power spectrum becomes flatter with increasing energy (i.e. there is relatively more variability power at higher energies across the observed frequencies).

6.1.1 AGN sample and data reduction

The work of Chapter 3, in which 200 observations from 38 AGN were analysed across a sliding energy window of 1225 total energy bands, returns a catalogue of energy-resolved power spectra which forms the basis of this detailed study of the energy-dependent shape of the broad-band noise. The data processing is equivalent to what is described in Chapter 3 (see Figure 3.6), in which the lightcurves considered are flare-subtracted, and truncated to 2^n bins to perform a FFT to then obtain the periodogram in fractional-rms units (Vaughan et al., 2003a) (preferred over the PSD to maximise frequency range). As before, to ensure sufficient bins in the periodogram for modelling, a minimum of $\geq$ 13 frequency bins with power at frequencies below where the white noise starts to dominate are required, with the white noise threshold itself determined as in Chapter 3. Similar to González-Martín and Vaughan (2012) and as in Chapter 3, each periodogram is modelled with maximum likelihood statistics and tested with both PLC and BKNPLC models, where $\sim$ 10% of the total sample of power spectra (which match the data-quality criteria), are preferentially modelled with a broken power law using a BIC test (Liddle, 2007). This included the re-identification of break features in observations first reported in González-Martín and Vaughan (2012). To remove the impact of the break on the shape of the periodogram, these cases are excluded from the subsequent analysis. An example of this PLC model fitting methodology is shown in Figure 6.1.

From Chapter 4, 7 AGN in this sample of 38 were identified to show statistically significant QPO-like features in their power spectra, when the broad-band noise was found

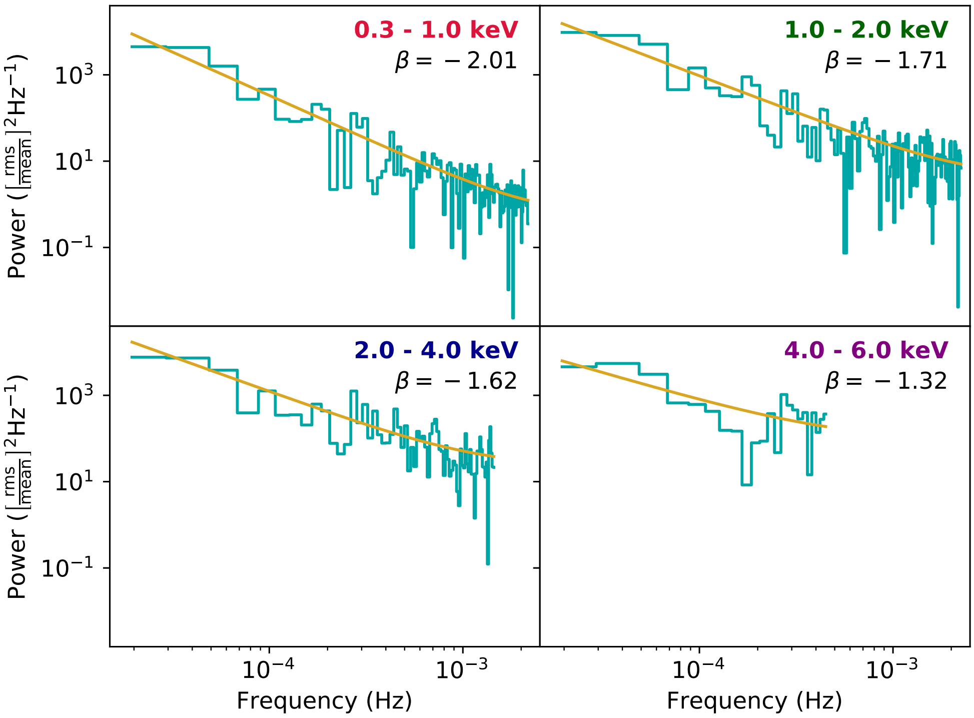

FIGURE 6.1: Example energy-binned (E_1, E_2, E_3 and E_4) periodograms of IRAS 13224-3809 OBSID:0780561601, each fitted using a maximum likelihood PLC model, with best-fitting β values illustrated.

to be best described by a PLC model. Therefore, the additional precaution is taken of identifying the Fourier bin corresponding to the most prominent outlier in power above the maximum likelihood PLC model, removing it, and refitting using a bootstrap-with-replacement methodology, as in Chapter 3. This approach minimises the bias from an individual, outlier bin on the shape of the power spectrum.

6.1.2 Energy dependent power spectra

The energy-dependent shape of the best-fitting PLC model is investigated for each AGN, in turn. As the data quality is insufficient to examine the energy dependence of the power spectrum at the highest resolution of the sliding energy window, the maximum likelihood PLC model parameters are obtained in five larger energy bins: $E_1 = 0.3 - 1.0$ keV, $E_2 = 1.0 - 2.0$ keV, $E_3 = 2.0 - 4.0$ keV, $E_4 = 4.0 - 6.0$ keV and $E_5 = 6.0 - 10.0$ keV. For each AGN and in each energy bin, the mean of the power spectral index, $\bar{\beta}$, and its 1σ error are obtained (a sufficient number of observations are averaged over in each case to provide quasi-Gaussian errors).

Searching across all 38 AGN in the sample, those cases in which values for $\bar{\beta}$ were constrained across a minimum of four energy bins were then the focus of further analysis. Due to diminishing data quality at high energies, $\bar{\beta}$ values approaching 10 keV could not be constrained for the majority of the sample. It is unsurprising that, of the five AGN for which $\bar{\beta}$ values were constrained across a minimum of four energy bins (IRAS 13224-3809, 1H 0707-495, MRK 766, NGC 4051 and ARK 564), all are bright and amongst the most well-studied AGN by *XMM-Newton*.

6.2 Empirical results

Figure 6.2 shows how $\bar{\beta}$ changes with energy across the five AGN of the sample which satisfy the above criteria. For each AGN, the energy dependence of $\bar{\beta}$ follows an approximately linear trend, with less negative $\bar{\beta}$ values, i.e. a *flattening* of the power spectrum, as the observations approach higher energies. This change in index with energy, $\frac{d\bar{\beta}}{dE}$, was modelled with a simple linear trend fitted with a widely available MCMC routine (`emcee`). Note, ordinary linear regression would also be a viable method here, as Gaussian errors are assumed. The high data quality of IRAS 13224-3809 and NGC 4051 allows for constraints on the mean index in the highest energy bin (E_5, $6-10$ keV), but for ARK 564, MRK 766 and 1H 0707-495, a measurement of the index is limited to only a single observation in E_5. These single points are highlighted in Figure 6.2, but are *not* used to constrain the linear model. For the MCMC fitting, uniform priors are assumed, and a routine with 100 walkers over $10,000$ iterations is implemented, with a discarded burn-in time of the first 2000 steps. The median of each parameter's posterior distribution is returned, along with the percentiles required to highlight 68% credible intervals about the MCMC fit, as shown in Figure 6.2. The best-fitting $\frac{d\bar{\beta}}{dE}$ values returned by this method are provided in Table 6.1, and the total number of observations contributing to each energy bin for each AGN is indicated in Figure 6.2.

As can be seen from Figure 6.2 and Table 6.1, IRAS 13224-3809, ARK 564 and MRK 766 all have near identical values of $\frac{d\bar{\beta}}{dE}$ (indistinguishable within errors), between 0.15 keV^{-1} and 0.16 keV^{-1}, which differ compared to NGC 4051 and 1H 0707-495, which have $\frac{d\bar{\beta}}{dE}$ of 0.08 ± 0.04 keV^{-1} and 0.22 ± 0.05 keV^{-1} respectively.

Although there is limited confidence in the values for $\bar{\beta}$ above 6 keV for most of the sample AGN, it is intriguing to note that the single values for $\bar{\beta}$ in those cases appear to lie below the linear model (see Figure 6.2), i.e. at steeper indexes than a linear model would predict. It is unclear if this is real but may be confirmed in future using *NuSTAR*, to probe energies above 10 keV. Also of note is that in all cases, the very softest mean averaged index lies below the linear relation, indicating that the true description of the energy-dependence likely requires a steeper rise before flattening to higher energies, but there are insufficient data at present to move beyond a simple linear model. Finally,

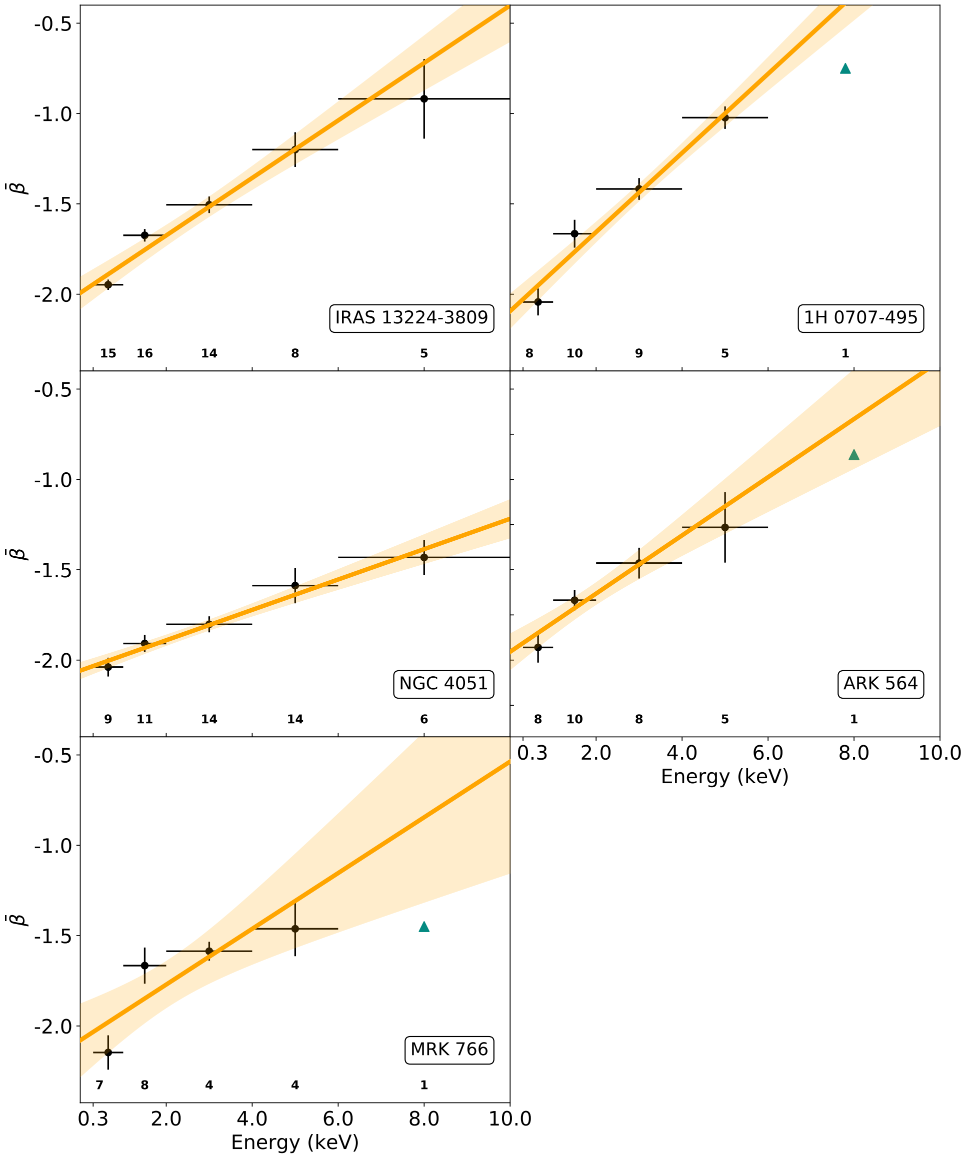

FIGURE 6.2: Energy-dependence of the mean power spectral index, $\bar{\beta}$, when modelled with a PLC across the five AGN for which have constraints in a minimum of four energy bins. The maximum likelihood fit and 68% credible intervals from the MCMC based on a linear model are illustrated. The number of observations that are averaged in order to calculate $\bar{\beta}$ in each energy bin are shown along the bottom of each panel. In those cases limited to a single observation in an energy bin, a single measurement of β is plotted (indicated by the filled triangles) but these values are not used in fitting the linear trend due to insufficient statistics.

TABLE 6.1: Summary of the best fitting $\frac{d\bar{\beta}}{dE}$ values shown in Figure 6.2. Columns indicate: (1) AGN, (2) The gradient of the best-fit linear model, with associated 68% credible interval.

AGN	$\frac{d\bar{\beta}}{dE}$
IRAS 13224-3809	$0.16 \pm^{0.02}_{0.03}$ keV^{-1}
1H 0707-495	$0.22 \pm^{0.02}_{0.02}$ keV^{-1}
NGC 4051	$0.08 \pm^{0.01}_{0.01}$ keV^{-1}
ARK 564	$0.16 \pm^{0.04}_{0.04}$ keV^{-1}
MRK 766	$0.15 \pm^{0.04}_{0.05}$ keV^{-1}

there may exist a bias from red noise leak in the lowest energy bin across each of the AGN in Figure 6.2, as the measured PLC index for each is close to -2 – the shape of the Fèjer kernel – and this effect is most pronounced for steeper red noise profiles, as observed at lower energies.

6.2.1 Excluded AGN

It is important to highlight those AGN where data were *not* available for $\geq$ four bins. In many cases, it was found that the sample AGN power spectra could only be constrained at soft energies, typically $<$ 2 keV, and/or across a small number of observations in total. An example of this is the case of RE J1034+396, which is only well described by a PLC model below 2 keV – likely due to its spectrum being dominated by the soft excess (see e.g. Puchnarewicz et al. 2001; Casebeer et al. 2006; Middleton et al. 2009).

Both PG 1211+143 and RE J1034+396 do show the start of a positive linear trend between index and energy (as in Figure 6.2) but there are only constraints based on multiple observations in E_1 and E_2 for RE J1034+396, and, for PG 1211+143 the constraints are drawn from only a single observation.

PKS 0558-504 is similar in appearing to show a weak positive linear trend across three energy bins ($E_1 - E_3$), but only a single observation contributes to the E_3 bin and none at higher energies for this AGN.

In the case of PG 0003+199, a strong linear trend across four energy bins ($E_1 - E_4$), again comparable to the AGN in Figure 6.2, but in this case the data are limited to a single observation throughout. If considering only this one observation of PG 0003+199, a value of $\frac{d\bar{\beta}}{dE} = 0.35$ keV^{-1} would be inferred, which is notably larger than in the case of 1H 0707-495. However, with only a single observation it is not possible to constrain reliable errors for $\frac{d\bar{\beta}}{dE}$, and so the results for this AGN are simply highlighted as worthy of future investigation.

Lastly, two further cases of statistically limited, apparent negative or non-linear index-energy trends which are observed in PG 1244+026 and PG 1322+659. Both show a flattening in index between E_1 and E_2, before a sudden *decrease* in index in E_3 to power law indices which are even steeper than in the lower energy bins. In both cases however, these trends are from only a single observation.

6.3 Theoretical Framework

The spectra of NLS1s tend to be a complex combination of components (Jin et al. 2012; Done et al. 2013), including a soft excess created by partially ionised reflection (Crummy et al. 2006a, Done and Nayakshin 2007) and/or Compton upscattering of seed disc photons in a cool corona (Middleton et al. 2009; Done et al. 2012), a power law from a hot corona and its reflection from the disc, producing – in addition to a soft excess – a characteristic Fe K_α line and Compton hump (George and Fabian 1991). Imprinted onto this continuum are lines due to photo-ionised absorption by outflows (Tombesi et al. 2010; Tombesi et al. 2011; Pinto et al. 2018). Each component in the spectrum can vary on a range of timescales and are interlinked either through direct propagation (which produces the canonical rms-flux relationship: Uttley and McHardy 2001, and lag to hard energies at low frequencies: Walton et al. 2013), or via irradiation (which can yield a soft lag at high frequencies: Zoghbi et al. 2012; Kara et al. 2016).

I proceed to construct a theoretical framework to model the observed change in power spectral index based on a simplified model of the accretion flow loosely described above. Under the assumption that reflection accounts for some or all of the soft excess, the variability observed is an energy-dependent weighted contribution from the power law and the reflection component. Across any chosen energy band, $E_A \rightarrow E_B$, the total summed lightcurve is defined as $s(E,t) = p(E,t) + r(E,t)$, where $p(E,t)$ represents emission from the propagation (coronal) component, and $r(E,t)$ from reflection. Assuming that $r(E,t)$ is linearly correlated with $p(E,t)$, the two may be related through an impulse response function $\phi(E,t)$:

$$r(E,t) = \phi(E,t) \circledast p(E,t) \tag{6.1}$$

and its Fourier transform (and transfer function $\Phi(\nu)$):

$$R(E,\nu) = \Phi(E,\nu)P(E,\nu) \tag{6.2}$$

These components may be expressed in terms of their complex Fourier amplitudes in the standard way:

$$|P|^2 = P^* P \tag{6.3}$$

$$|R|^2 = R^* R = (\Phi P)^* (\Phi P) = |\Phi|^2 |P|^2 \tag{6.4}$$

The total lightcurve can be then expressed as:

$$s(E,t) = [\phi(E,t) \circledast p(E,t)] + p(E,t) \tag{6.5}$$

and in the Fourier domain:

$$S(E,\nu) = [1 + \Phi(E,\nu)]\, P(E,\nu) \tag{6.6}$$

In this highly simplified case, the observed AGN variability derives from the coronal power law (propagation) and the interaction with the disc (which is determined by the transfer function and therefore geometry). In terms of the Fourier frequency binned power spectrum, the above can be related through weighted contributions in a given band from each component. In rms-squared units, the total amount of power in the power spectrum is directly related to the mean count rate in each component, I, through:

$$\left(\frac{\sigma}{I}\right)^2 = \int_{1/T}^{1/2dt} |S|^2 d\nu \tag{6.7}$$

for an observation $s(E,t)$ of length T and with timebin size dt.

Where the soft excess is dominated not by reflection but by Comptonisation (Middleton et al., 2009; Done et al., 2012), an additional term is added into equation 6.1. This is not considered further however, as the impact of any reprocessing from such emission is limited to considerably narrower energies than by reflection of the coronal emission (which extends over a greater energy range), and – as shown in the Section 6.3.2 – reflection has no impact on the shape of the power spectrum at the frequencies under investigation).

6.3.1 Propagation

The propagation of material inwards through the accretion disc imprints variability across a broad range of radii (and therefore timescales) in the form of local mass accretion rate fluctuations (see Lyubarskii 1997; Kotov et al. 2001). Arévalo and Uttley (2006) explored the effect of the propagation of material acting as a low-pass filter on the shape of the intrinsic power spectrum of the AGN, a process which suppresses high frequency variability. This low-pass filter is described as:

$$\mathrm{PSD_{filtered}} = \mathrm{PSD_{intrinsic}} \left(\frac{\int_{r_{\min}}^{r_\nu} \epsilon(r) 2\pi r dr}{\int_{r_{\min}}^{\infty} \epsilon(r) 2\pi r dr} \right)^2 \tag{6.8}$$

where $\epsilon(r)$ is the radial emissivity profile of the flux (i.e. flux$(r) \propto r^{-\gamma}$) and r_ν the local radius, at which the variability is generated. From Arévalo and Uttley (2006), $\epsilon(r)$ is given by:

$$\epsilon(r) = r^{-\gamma} \left(1 - \sqrt{\frac{r_{\min}}{r}} \right) \tag{6.9}$$

with emissivity index γ, from a minimum radius $r_{\min}$ out to arbitrary radius r. A commonly assumed value for the emissivity index is $\gamma = 3$ (i.e. that of a geometrically thin disc). The value of γ may vary broadly with energy, from a suggested minimum of $\gamma \sim 2$ for low energies up to $\gamma > 5$ at the highest energies in the *XMM-Newton* bandpass (Arévalo and Uttley, 2006).

Assuming the input power spectrum takes the form of a power law allows for the impact of propagation in determining the changing index of the filtered power spectrum (Arévalo and Uttley, 2006) to be explored. The variability is assumed to originate in the inflow (for whichever chosen coronal geometry), with mass accretion rate fluctuations propagating inwards from r_{out} to r_{in}. It is assumed that the variability generated locally at each radius, r_ν, is at the viscous frequency (see Churazov et al. 2001) such that:

$$r_\nu = \left[\frac{2\pi\nu}{\alpha} \left(\frac{H}{R} \right)^{-2} \right]^{-2/3} \tag{6.10}$$

where the frequency is in units of c/R_g (see e.g. Kato et al. 1998; Arévalo and Uttley 2006). In the above, α and $\frac{H}{R}$ are the dimensionless viscosity parameter of Shakura and Sunyaev (1973), and scale height of the accretion disk respectively.

6.3.2 Reflection

Reflection is a well-studied feature of AGN energy spectra (e.g. George and Fabian 1991; Fabian et al. 2004) and in its impact on the shape of the PSD (e.g. Papadakis et al. 2016; Emmanoulopoulos et al. 2016; Chainakun 2019). In assuming that reflection is linearly related to propagation (see equation 6.1), the nature of the variability of the reflection component depends only on propagation and the impulse response function which relates them (see Section 6.4 for where these assumptions break down).

In order to infer the effect of reflection on the shape of the power spectrum, the transfer function in equation 6.2 must be defined, which is both energy-dependent (Campana and Stella, 1995; Poutanen, 2002; Cassatella et al., 2012; Wilkins and Fabian, 2013; Papadakis et al., 2016; Ingram et al., 2019) and dictated by the geometry of the corona. A number of coronal geometries have been considered in the literature including a (point-source) lamppost corona, possibly at the base of a jet (Martocchia and Matt 1996; Reynolds and Begelman 1997; Merloni and Fabian 2002; Taylor and Reynolds 2018a) or in a two-source system (Chainakun, 2019), a sandwich-type corona on top of the disc (Di Matteo et al., 1997), a corona as part of a hot, inner disc (Done and Kubota, 2006; Done et al., 2012) and a spherical corona of uniform density and fixed temperature (Raginski and Laor 2016; Fabian et al. 2017; García et al. 2019; Chainakun et al. 2019).

In the very simplest case, the transfer function which describes the interaction between disc and corona can be considered as a simple top-hat function, centred on $t = 0$, with width a, equal to the light travel time between the corona and disk, and height, A, chosen such that the area of the top-hat is normalised to unity:

$$\phi(t,a) = \begin{cases} A & \frac{-a}{2} \leq t \leq \frac{a}{2} \\ 0 & \text{otherwise} \end{cases} \tag{6.11}$$

It must be emphasised that this is of course a naïve assumption, as this transfer function is discontinuous in time (not realistic for an extended reflector) and is ignorant of any details about the reflector accept distance to the corona. It is, however, the most extreme case of a reflector, where the impact of reflection is most dominant, and is used here to show that this impact on the shape of the power spectrum is negligible, relative to propagation.

To test this I choose to reparameterise a as h/c, where h is the distance between corona and disc and c the speed of light. The Fourier transform of this top-hat function then takes the form:

$$\Phi(\nu) = \frac{Ah}{c} \operatorname{sinc}\left(\frac{h\nu}{c}\right) \tag{6.12}$$

Due to the nature of the sinc function, variability is suppressed on timescales shorter than the light crossing time between disc and corona, or at frequencies greater than $\sim c/h$. For a sandwich-type coronal model (where the reprocessing is assumed to occur directly above the disc), the light travel time is negligible relative to the frequencies under consideration ($10^{-5} - 10^{-3}$ Hz, i.e. $0.01 - 1$ mHz). Clearly the most extreme impact would theoretically occur for the largest separation between corona and disc, i.e. that of a lamppost geometry, where h is the height of the corona above the black hole.

Figure 6.3 shows a range of simulated power spectra, all produced from an intrinsic slope of $\beta = -1$, assuming $(\frac{H}{R})^2\alpha = 0.3$ (following Arévalo and Uttley 2006), and using various parameter combinations for $\gamma(E)$ and coronal height, h. It should be noted that through equation 6.10, the value of $(\frac{H}{R})^2\alpha$ only alters the viscous frequency range and does not affect how the reflection component changes the shape of the PSD (the impact of different values of α and H/R with reference to modelling propagation are discussed Section 6.3.3). Given that the AGN 1H 0707-495 is known to be extremely reflection dominated (Fabian et al., 2002; Kara et al., 2015), the properties of this source are used to explore the impact of the transfer function. A mass of $M_{\rm BH} = 10^{6.3} M_{\odot}$ (Done and Jin, 2016) is assumed as well as maximal spin (Dauser et al., 2012).

The reflection fraction, $f_{\rm refl} = I_{\rm r}/I_{\rm p}$ (see Dauser et al. 2014) for 1H 0707-495, has been estimated at $f_{\rm refl} = 46^{+18}_{-16}$ by Boller et al. (2021) (using the XSPEC model TBNEW $\times$ TBPCF $\times$ RELXILLLP, to account for both a partial coverer and relativistic reflection) in a recent study with *eROSITA*. The highly conservative assumption is made that $f_{\rm refl} = 100$ over all energy bands, to investigate an extreme case where the weighted sum is completely dominated by the reflection component. Each panel of Figure 6.3 shows the power spectrum generated by both reflection and propagation, along with the weighted sum; it is clear that, unless the height of the reflector is large, $\gtrsim 50R_{\rm g}$ (considerably larger than implied via modelling to-date – Wilkins and Fabian 2011; Taylor and Reynolds 2018b; Alston et al. 2020), the impact on the shape of the power spectrum due to reflection is negligible across the investigated $0.01 - 1$ mHz frequency range.

6.3.3 Modelling propagation

In the previous section it is shown that only under the most extreme condition of a lamppost corona at a height $\gtrsim 50R_g$ above the disc will the input power spectrum be distorted in the frequency range of interest. Of note is that some reflection from a

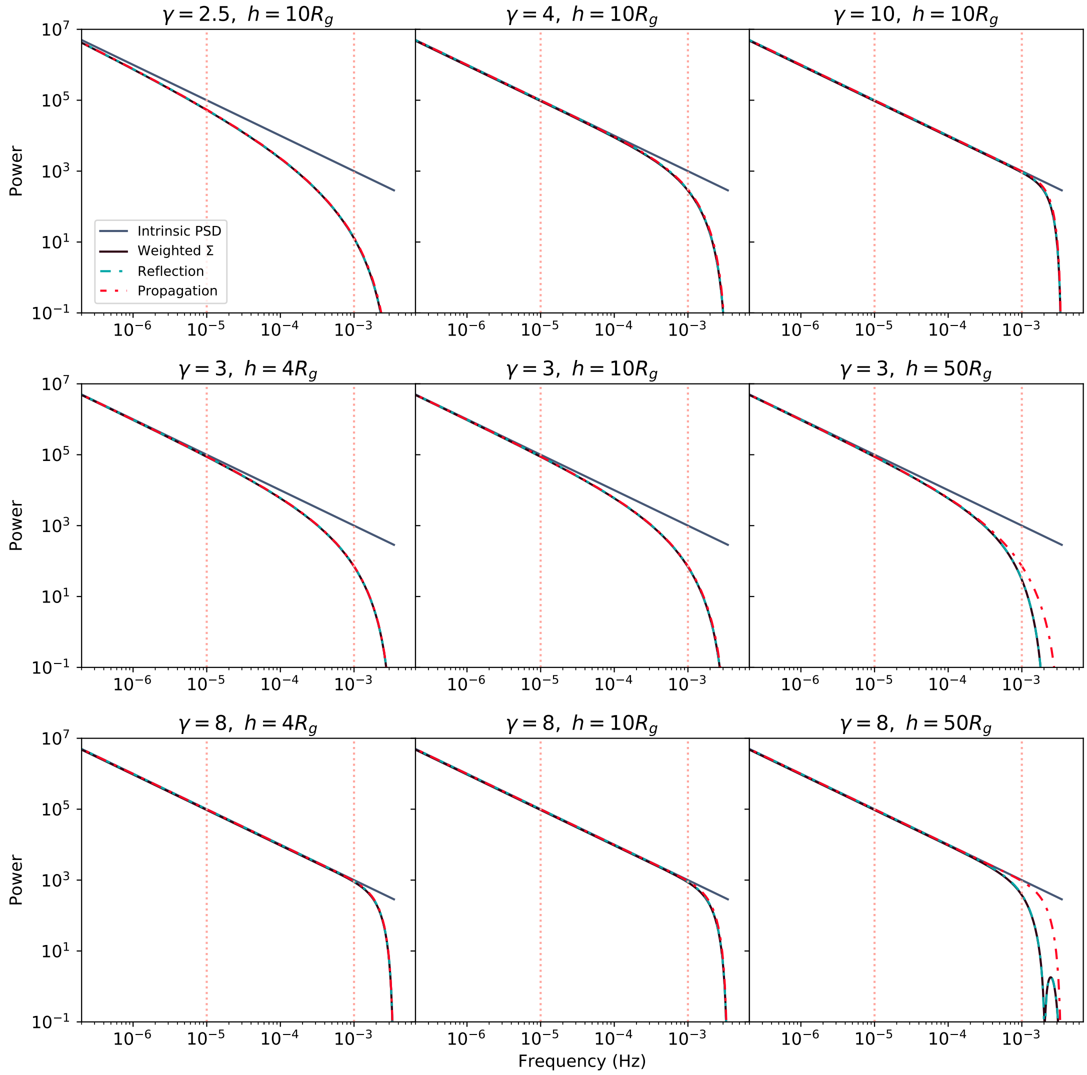

FIGURE 6.3: Simulated power spectra for a set of pre-defined emissivity indices, $\gamma(E)$, for an assumed coronal height h, with an intrinsic power spectral slope of -1. Both propagation and reflection components are shown, as well as the combined weighted power spectrum (and for which only powers between $0.01 - 1$ mHz are considered). For this demonstration I consider 1H 0707-495, with $M_{\rm BH} = 10^{6.3} M_{\odot}$ (Done and Jin, 2016), maximal spin (Dauser et al., 2012) and assume a conservative reflection fraction of $f_{\rm refl} = 100$ (Boller et al., 2021) which is applied equally over all energy bands (which is again an extremely conservative assumption). Assigned energy-dependent emissivity index values are: $\gamma(E_1) = 2.5$, $\gamma(E_2) = 3$; $\gamma(E_3) = 4$, $\gamma(E_4) = 8$ and $\gamma(E_5) = 10$.

vertically extended jet cannot be ruled out, however, emission from closer to the black hole will dominate the spectrum (both due to light bending but also due to Doppler deboosting of emission from an outflowing corona) and it is assumed that any signature of reflection from more distant material (e.g. from the torus) will be considerably weaker than that from the inner regions (as shown to be the case in ARK 564 by Kara et al. 2017).

This simplification allows for the theoretical framework to focus on soley on propagation as the source of energy-dependent changes in the shape of the periodogram (see the propagation component of Figure 6.3). Regardless of the geometry of the corona, it is presumed that the typically large amounts of the variability observed from this component are driven by a changing electron temperature and density, as a result of the mass accretion rate propagations through the disc. Where the corona is the base of a jet (or lamppost) then the changes in the corona (and the power law component) thus contain all of the viscous timescales in the disc down to the ISCO. Should the disc be truncated with a hot flow (as invoked for X-ray binaries: Churazov et al. 2001) then the timescales may be generated in this turbulent component on a potentially shorter timescale (set by the scale-height and viscosity) relative to the disc. Finally in the case of a sandwich geometry then the timescales of variability may well be those of the disc below (Wilkins et al., 2016). In all cases, it can be presumed that the timescales being studied here are limited by those at the ISCO.

Also of note is that variations in the seed photon population may be discounted as the driver for changes in the power spectrum. This is both as the UV emission from the disc is established to be considerably less variable than the corona in NLS1s (Leighly, 1999; Smith and Vaughan, 2007; Ai et al., 2013; Alston et al., 2013b; Done and Jin, 2016), but also because any distortion to the emergent power spectrum due to the transfer function between the disc and corona is approximately the same as that describing reflection, i.e. the maximum impact would occur for a lamppost corona $\gtrsim 50R_g$ above the disc (the travel time through the corona is assumed to be short, as the plasma is optically thin).

Following equation 6.8, the *filtered* power spectrum can be obtained after the filtering of some pre-defined *intrinsic* power spectrum, in a given energy range with a value for the emissivity index $\gamma(E)$. By using equation 6.8 the implicit assumption is made that the corona lies within the disc such that the radial emissivity profile is that of the corona. This cannot be applied to the case where a lamppost geometry is assumed (but see Section 6.4).

It is assumed that the intrinsic power spectrum is well described by a power law with index, $\beta = -1$ which is appropriate for frequencies above the low frequency break but below the high frequency break at the ISCO (Papadakis et al. 2002; Arévalo and Uttley 2006; McHardy et al. 2006). Following Arévalo and Uttley (2006), $r_{\rm in}$ is set to be the position of the ISCO. Given the reported high spin values for these bright AGN (Ogle et al. 2004; Fabian et al. 2013; Done and Jin 2016; Kara et al. 2017; Buisson et al. 2018b), the assumptions are made such that $r_{\text{in}} = 1.25R_g$, and $r_{\text{out}} = 10^4R_g$ (as $r_{\text{out}} > 10^4R_g$ corresponds to frequencies below those which are typically observed). Of note is that for the mass range subtended by the AGN sample (from $10^{6.00} - 10^{6.63}M_\odot$, see Table 6.2), should zero spin ($r_{\text{in}} = 6R_g$) instead be assumed, the viscous frequency at r_{in} would enter the investigated bandpass (depending on the values of α and H/R) – the high reported spins of these AGN implies this is not an issue for this analysis.

The range of viscous frequencies from those radii described above are accessed through equation 6.10 which depends on $(\frac{H}{R})^2\alpha$. Neither $\frac{H}{R}$ nor α are well determined in practice but the impact of ranges in these values and their combination can be explored. Very low scale heights, or low values for the viscosity, combined in such a way that $(\frac{H}{R})^2\alpha \lesssim 0.1$ yields a viscous frequency limit for the ISCO (with r_{in} = 1.25 R_{g}) of $<$ 1mHz, which lies within the observable bandpass. Conversely, for $(\frac{H}{R})^2\alpha \gtrsim 0.1$, the viscous frequency limit is $> 10^{-3}$ Hz. In the following, it is assumed that $(\frac{H}{R})^2\alpha = 0.3$, in order to be consistent with Arévalo and Uttley (2006), and which is appropriate for large scale height inflows (which is quite probable in the inner regions of those high Eddington ratio AGN) and/or large values of α.

The output (filtered) power spectrum is investigated over a frequency range of $0.01 - 1$ mHz, corresponding to the range of frequencies typically accessible in these observations. Finally, a power law is fitted to each simulated power spectrum and a new value of the power law index, β (corresponding to the effect of propagation only) is obtained.

As can be seen from the propagation components in the top panels of Figure 6.3, substantial energy-dependent changes in β are observed, with less negative (flatter) values obtained at higher energies, similar to observation (Figure 6.2). For a given $\gamma(E)$ (and, in the case of Figure 6.3, coronal height, h), expectation values for $\bar{\beta}$ can be produced, or conversely the observed $\bar{\beta}$ can be used to constrain $\gamma(E)$ in this simplified picture. As the exact profile of $\gamma(E)$ is uncertain, it is parameterised in both a linear form:

$$\gamma(E) = \frac{d\gamma}{dE}E + b \tag{6.13}$$

and power law form:

$$\gamma(E) = \gamma_0 E^{\alpha} \tag{6.14}$$

from which values of parameters $(\frac{d\gamma}{dE}, b)$ and (γ_0, α) can be determined which maximise the likelihood function between the observed values of $\bar{\beta}_{\text{obs}}$ and those theoretical values extracted via the above process $\bar{\beta}_{\text{mod}}$. This is equivalent to minimising the negative log-likelihood, $S \equiv -2\ln[\mathcal{L}]$ (Vaughan, 2005), which should be noted is a loss function assumes exponentially distributed data; an assumption which is made here. Assuming emissivity indices $\hat{\gamma}(E_k)$ across energy bands k= $1, 2, ..., n-1$, S may be written as:

$$S = 2\sum_{k=1}^{n-1}\left\{\ln[\bar{\beta}_{\rm mod,k}] + \frac{\bar{\beta}_{\rm obs,k}}{\bar{\beta}_{\rm mod,k}}\right\} \tag{6.15}$$

Similarly satisfactory values are obtained for the negative log likelihood for both models, with a breakdown of the results provided in Table 6.2. Given the small statistical improvement afforded by the linear model ($S_{\rm lin} < S_{\rm PL}$), this model is used for $\gamma(E)$ hereafter. A direct comparison between the data and simulated results for the linear model is plotted in Figure 6.4.

As can be seen from Figure 6.4, the simple linear model for $\gamma(E)$ provides a good description for the changes in power law index across all five AGN, and performs extremely well in the case of ARK 564. Deviations from a good description do occur in the cases of IRAS 13224-3809, 1H 0707-495 and NGC 4051, where systematic offsets are visible as a result of the model not replicating the steep observed linear trend.

The differing nature of the best-fitting emissivity profiles for each AGN is visible from Figure 6.5. The uncertainty on the $\gamma(E)$ values is evaluated through a Monte Carlo routine, whereby x sets of β values are drawn for each AGN, where x is the number of observations in each energy band (see Figure 6.2) to obtain an individual MC value for $\bar{\beta}$. The routine assumes Gaussian errors on the index, exactly as in Figure 6.2. This process is repeated 1000 times and for each set of $\bar{\beta}$ values, for each AGN, a maximum likelihood set of $\gamma(E)$ values is determined which best describe the trend of $\bar{\beta}$ with energy, assuming only a propagation component as before. Figure 6.5 shows both the maximum likelihood set of $\gamma(E)$ values and its 68% confidence intervals, where notably, the emissivity appears considerably flatter with energy in NGC 4051 relative to IRAS 13224-3809 and 1H 0707-495 in particular. The origin of such differences are speculated upon in Section 6.4.

Finally, given the uncertain nature of the input power spectrum (pre-filtering), the impact of having an intrinsic power law index of -0.5 and -1.5 (rather than -1) was explored. In both cases poorer fit statistics between the model and observed values were obtained, justifying the use of an input index of -1, following the assumptions made in this framework.

6.4 On the employed theoretical framework

Modelling this sample of AGN indicates that, in all cases where the data allow for the changing shape of the power spectrum to be explored, there is a positive correlation between power spectral index between $0.01 - 1$ mHz (where the periodogram can be well

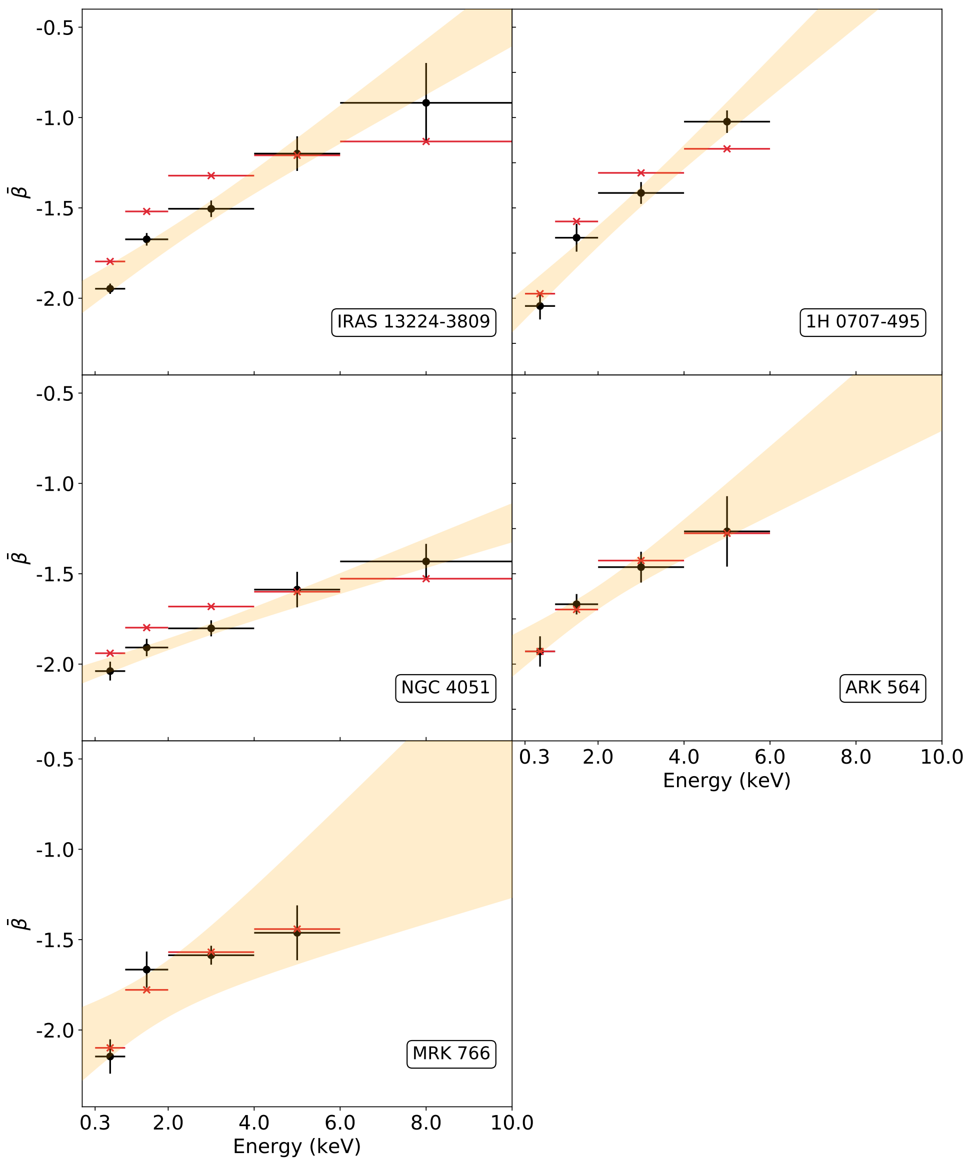

FIGURE 6.4: A comparison of mean power spectral index values, $\bar{\beta}$, as a function of energy between the model (red) and observed values (black), across the five AGN. 68% credible intervals are shown as in Figure 6.2. The best-fitting linear model, $\gamma(E) = \frac{d\gamma}{dE}E + b$, is determined and selects values for $\gamma(E)$ that maximise the likelihood by comparing the theoretical to observed values of $\bar{\beta}$.

TABLE 6.2: AGN properties and results from fitting for $\gamma(E)$, with maximum likelihood determined parameter values $(\frac{d\gamma}{dE}, b)$ and (γ_0, α), and associated negative likelihood values $S_{\rm lin}$ and $S_{\rm PL}$, for linear and power law models respectively, for each AGN in the study meeting the defined data criteria. Black hole masses, $M_{\rm BH}$ and bolometric luminosities, $L_{\rm bol}$, as well as spin, a_*, and inclination angle i, are sourced from the literature: (a) Alston et al. (2019), (b) Buisson et al. (2018a); (c) Fabian et al. (2013); (d) Done and Jin (2016); (e) Dauser et al. (2012); (f) Denney et al. (2010), (g) Woo and Urry (2002); (h) Ogle et al. (2004); (i) Zhang and Wang (2006); (j) Vasudevan and Fabian (2007); (k) Kara et al. (2017); (l) Wang and Lu (2001); (m) Vasudevan et al. (2010); (n) Buisson et al. (2018b).

AGN	$\log_{10}(\frac{M_{\rm BH}}{M_\odot})$	$\log_{10}(\frac{L_{\rm bol}}{L_\odot})$	a_*	i(deg)	$\frac{d\gamma}{dE}$	b	$S_{\rm lin}$	α	γ_0	$S_{\rm PL}$
IRAS 13224-3809	6.0 (a)	11.0 (b)	0.989 ± 0.001 (c)	62.3 ± 1.3 (c)	0.29	1.83	13.41	0.22	2.23	13.45
1H 0707-495	6.3 (d)	10.9 (d)	$0.998^{+0.000}_{-0.002}$ (e)	$52.0^{+1.7}_{-1.8}$ (e)	0.53	1.73	11.21	0.32	2.37	11.22
NGC 4051	6.2 (f)	10.0 (g)	$0.973^{+0.025}_{-0.000}$ (h)	$48.0^{+4.0}_{-3.0}$ (h)	0.11	1.99	15.54	0.11	2.16	15.55
ARK 564	6.4 (i)	10.7 (j)	$0.998^{+0.000}_{-0.000}$ (k)	$22.0^{+7.0}_{-2.0}$ (k)	0.35	2.11	11.57	0.29	2.36	11.57
MRK 766	6.6 (l)	10.9 (m)	$0.92^{+0.078}_{-0.000}$ (n)	$46.0^{+1.0}_{-2.0}$ (n)	0.36	2.31	12.25	0.22	2.75	12.24

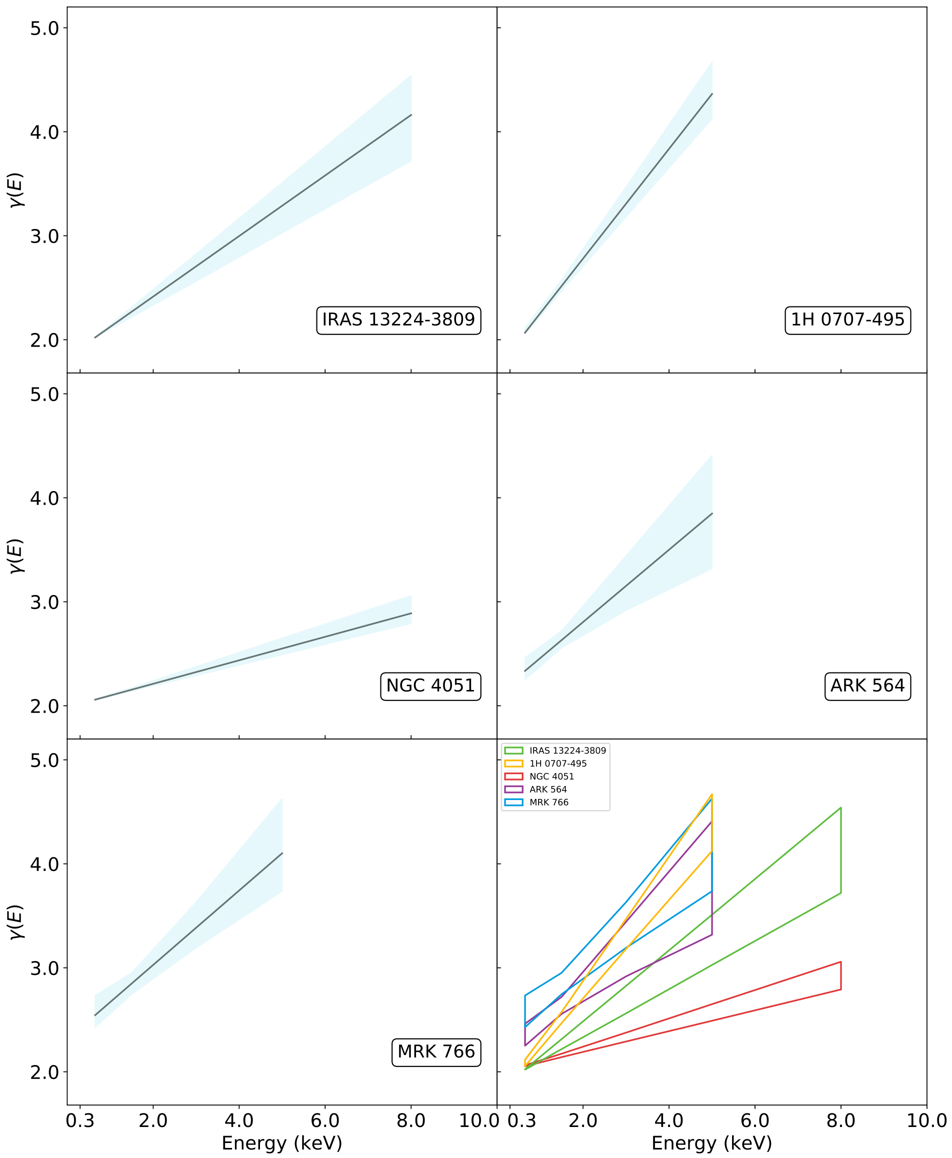

FIGURE 6.5: The maximum-likelihood determined values for the emissivity index function, $\gamma(E)$, and $\sim 68\%$ (1σ) confidence intervals, when applying a linear model, $\gamma(E) = \frac{d\gamma}{dE}E + b$, to the observed $\bar{\beta}$ values across each AGN (as in Figure 6.4). Bottom right panel shows the overlay of the (1σ) confidence intervals in $\gamma(E)$ for all five AGN.

described as a single power law) and energy (across the $0.3 - 10$ keV range), such that the index flattens with increasing energy. Assuming a simple model of propagating fluctuations – which is observationally supported by the presence of hard lags at low frequencies in AGN (Walton et al., 2013), the ubiquitous linear rms-flux relationship (Uttley and McHardy, 2001), and log-normal flux distribution (Gaskell, 2004) – I have been able to obtain corresponding constraints on the emissivity as a function of energy, after accounting for the role of reflection (and assuming a disc-like geometry). To explore the latter, a top-hat transfer function is assumed in order to crudely approximate irradiation of the disc, with the width set by the light-travel time from the corona to the optically thick reflecting material. In the lamppost model this is set by the height of the corona above the black hole and is the geometry where one would naturally expect the biggest impact on the shape of the power spectrum. As reflection only distorts the power spectrum at frequencies higher than 1/the light-travel time (equation 6.10), the distance of corona to reflector needs to be substantial ($\gtrsim 50R_{\rm g}$ – Figure 6.3) for reflection to have a substantial effect on the shape of the power spectrum in the frequency range of interest.

As the impact of reflection can be considered minimal in this study, the theoretical framework focused only on propagation and assumed that the inflow acts a low pass filter, weighted by the radial emissivity profile. This naturally finds an analogy with those models where the coronal emission is created directly in the flow (e.g. Done et al. 2012). It is found that this model requires the emissivity to be around R^{-2} for energies around the soft excess before increasing to a maximum of $\sim R^{-5}$. It is perhaps intriguing to note that radiation pressure or advection dominated flows are expected to have flatter emissivity profiles (with $\gamma < 3$: e.g. Watarai et al. 2000b) which may be consistent with such a component producing some of the soft excess (Middleton et al. 2009; Done et al. 2012) or it may be that such a region has a larger scale-height which pushes the variability to higher frequencies (as the viscous timescale goes as $(H/R)^2$), also potentially flattening the index. With increasing energy it appears the power law index flattens (see Figure 6.2), appearing to saturate and then possibly begins to inflect. At present, there are insufficient statistics to constrain this further, however, future observations using instruments with higher energy coverage e.g. *NuSTAR*, provide the opportunity to investigate this further. Finally, whilst the analysis assumes an input power law index of -1, other values for the shape of the intrinsic noise are excluded by virtue of producing incompatible results, given the initial assumptions of coronal geometry (as in Section 6.3.3).

6.4.1 Relation to black hole macroscopic properties

$\gamma(E)$ is found to vary across the AGN sample (Figure 6.5) through different measurements of $\frac{d\gamma}{dE}$. It is plausible that such differences could be due to geometrical effects (e.g.

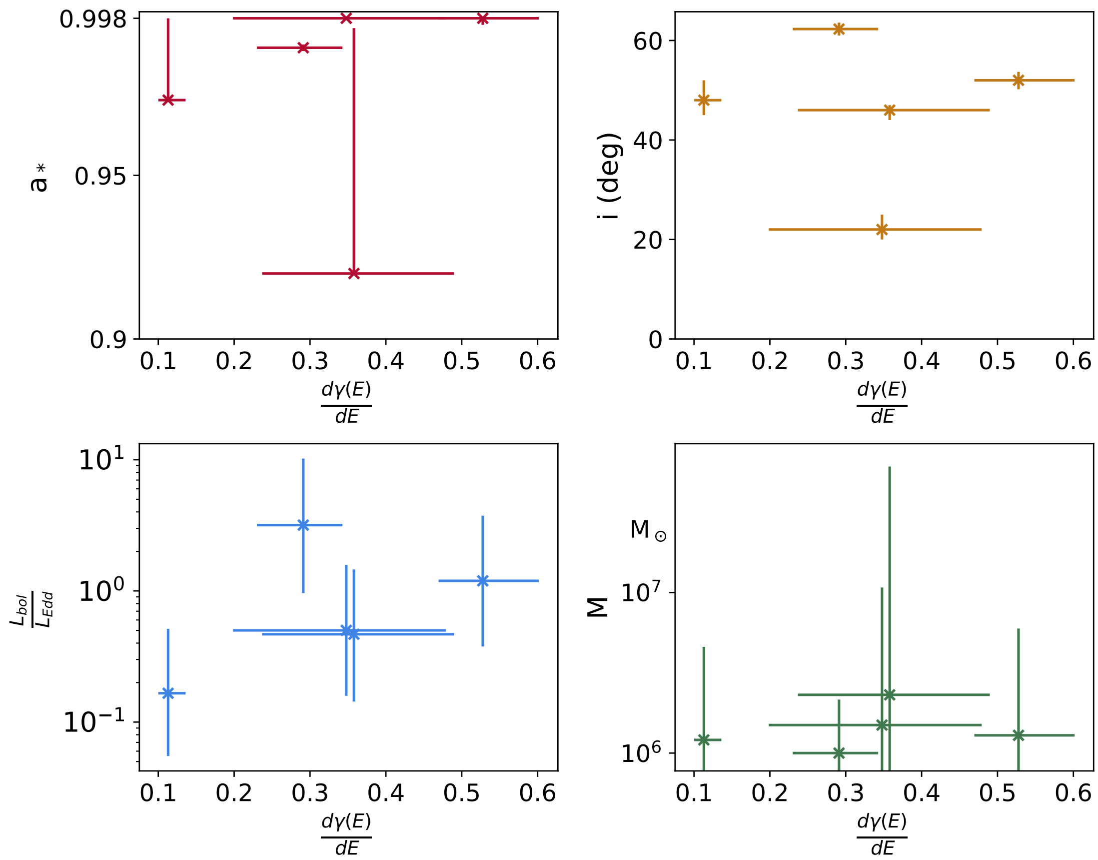

FIGURE 6.6: Key macro-properties for the AGN sample – spin, inclination, Eddington ratio and BH mass plotted against $\frac{d\gamma}{dE}$ (see Table 6.2).

different scale-heights) or some bulk property of the AGN, notably accretion rate, mass and spin. The spins, inclinations, black hole masses and Eddington scaled accretion rates are obtained using $L_{\rm bol}$ from the literature – see Table 6.2. Note however that the determination of both spin and inclination is highly model dependent, with statistical errors on each very likely to be underestimates (e.g. see Reynolds 2014; Middleton et al. 2016). These values should therefore be used with due caution.

Figure 6.6 plots $\frac{d\gamma}{dE}$ versus the AGN parameters of interest and finds a lack of correlation with spin, inclination and BH mass but possible hints of a positive correlation with Eddington ratio. In examining the Eddington ratio, there appears to be slightly stronger evidence of a correlation, with the only outlier being IRAS 13224-3809 with a highly uncertain value for $L_{\rm bol}/L_{\rm Edd}$ (see Buisson et al. 2018a). Of note is that the Eddington ratio is also highly uncertain for 1H 0707-495 (Done and Jin, 2016); clearly both a considerably larger AGN sample and a more accurate handle on the key macro-properties is required before any claim of a correlation can be made.

6.4.2 Geometry limitations

One of the most important assumptions in this analysis is the geometry which dictates how the variability is filtered and modified by an assumed radial emissivity (c.f. Arévalo and Uttley 2006). The assumption here of a continuous disc-like inflow is in contrast to models where the corona sits above the black hole and is probably the base of a jet (Wilkins and Gallo, 2015). Such lamppost geometries lead to increased emissivities in the inner portions of the disc – and therefore the reflected emission – due to light-bending (Wilkins and Fabian 2011; Gonzalez et al. 2017). However, caution may be needed in assuming a disc-like coronal geometry, as the magnitude of the hard lags – set by propagation – may be in conflict with the radial extent of the corona as inferred from micro-lensing studies (Mosquera et al., 2013).

Perhaps more importantly, the corona (regardless of geometry) is subject to other heating/cooling effects besides propagation which are beyond the scope of this work. Such a model may well explain the changing shape of the power spectrum with energy *without* the need to invoke a changing emissivity (e.g. Sun et al. 2020). Finally, in future it will be interesting to compare the changing shape of the power spectrum with energy in the AGN sample to that seen in XRBs, as there have been recent reports of similar coronal behaviours and geometries between both types of accreting objects (see e.g. Kara et al. 2019; Alston et al. 2020).

6.5 Chapter Summary

In this chapter I first identify a key empirical trend in the shape of the energy-dependent periodograms of five bright, highly variable AGN (IRAS 13224-3809, 1H 0707-495, NGC 4051, ARK 564 and MRK 766) across multiple observations using *XMM-Newton*, finding a ubiquitous flattening of the broad-band noise with increasing energy. This is in agreement with several previous studies, most of which focus on a limited number of observations, often for a single source. Utilising the energy resolution of the study presented in Chapter 3, this trend is observed over a minimum of four, and up to five, energy bins in the *XMM-Newton* bandpass for these five AGN.

In an attempt to explain the above relationship, I develop a rudimentary framework incorporating the effects of both propagating fluctuations through the accretion flow, and the reflection component which I assume to be linearly related to propagation via a simple top-hat impulse response function. Upon investigation, it is found that over the frequency bandpass which is typically observed, $0.01 - 1$ mHz, the impact of reflection is essentially negligible, unless invoking a lamppost coronal geometry, with a corona at a height above the disc which is much beyond what is expected from current modelling. Thus for even the most reflection dominated sources (e.g. 1H 0707-495), propagation is the sole effect driving the change in the nature of X-ray variability, within this framework.

By describing the propagation component as a low-pass filter which suppressed high frequency variability and where the flux from the disc is described through a radial emissivity profile, the change in power spectral index with energy can be related to the energy-dependent emissivity index, $\gamma(E)$. I parameterise $\gamma(E)$ into both linear and power law functions and use maximum likelihood statistics to determine the best-fitting values of $\gamma(E)$ to describe the observed trend of flattening power spectral indexes, for each AGN. I find the linear parameterisation of $\gamma(E)$ very slightly statistically preferable, and show the difference in $\gamma(E)$ across each AGN in turn. From this result, it is shown that $\gamma(E)$ goes as $\gamma \underset{\sim}{\propto} R^{-2}$ at low energies, towards $\gamma \underset{\sim}{\propto} R^{-5}$ at the highest energies, across most of the sample – NGC 4051 being the possible exception here, where only $\gamma \underset{\sim}{\propto} R^{-3}$ is reached at the highest investigated energies.

I then attempt to relate the parameters of this linear function to macroscopic properties of the black hole in each AGN (as determined from literature). In each case of black hole spin, inclination and mass, there is no apparent trend, although the sample size is of course highly restricted. There is a faint hint of a trend with Eddington ratio, although the systematic uncertainties on all of these properties are such that drawing any further conclusion is not possible.

Chapter 7

Concluding remarks

The goal of this research was to investigate X-ray variability in AGN observed at a high energy resolution, in order to both search for QPOs, and investigate the energy-dependent nature of the power spectrum. In doing so, this work probes the nature of AGN accretion over a large sample of highly variable AGN and builds upon previous studies of AGN variability which came before it. In this concluding chapter I will summarise the key results of this work, highlighting both its successes and limitations, before discussing the prospects for future exploratory research based on this work.

7.1 Search for AGN QPOs

An open question in accretion physics is whether QPOs in AGN are more widely present than currently known, motivated by the detection of many LFQPOs, and to a less numerous extent, HFQPOs, in XRBs (Remillard and McClintock, 2006; Ingram and Motta, 2020). The search for QPOs in AGN has a chequered history however, with numerous claims being subsequently disregarded for lack of proper statistical testing for periodicities in red noise lightcurves (Vaughan and Uttley, 2005; Vaughan and Uttley, 2006). To-date, this leaves the only repeated detection of a statistically significant AGN QPO in RE J1034+396 (Gierliński et al., 2008; Alston et al., 2014b), alongside a $> 3\sigma$ detection in a single observation of MS 2254.9–3712, in an energy band of $1.2 - 5.0$ keV (Alston et al., 2015).

This work sets out first to conduct a deep search for AGN QPOs using an energy resolved approach across 200 archival *XMM-Newton* observations of 38 bright, variable AGN. The analysis implemented for this search was based on a rigorous null hypothesis test of QPO candidates confined to a single Fourier bin within the red noise dominated periodogram, with both PLC and BKNPLC models used to determine the shape of the underlying broad-band noise. PLC models were found to be statistically preferred in $\sim$ 90% of cases, and the uncertainty on each model was determined through bootstrap and GMM statistical methods. Global significance values for the QPO candidates were determined in each case of a best-fitting PLC model, and the threshold for reporting these candidates of interest was set at $> 3\sigma$. Across the entire sample, a total of 21 QPO candidates are found at $> 3\sigma$, including 4 observations re-detecting the QPO in RE J1034+396, while 3 other QPO candidates are found at borderline $\sim 3\sigma$. No $\gtrsim 3\sigma$ candidates are detected in the remaining 178 observations (N.B. 2 observations of IRAS 13224-3809 find two distinct QPO candidates in different energy bands, see Chapter 4).

This initial study alone is insufficient to claim multiple detections of highly significant QPOs however, as several additional factors may influence the detection significance. Correctly modelling the broad-band noise in AGN itself is a difficult procedure, due to the limitations of data quality which are observed as AGN broad-band noise. Additional tests were conducted to test for the undetected presence of a break in the initial BKNPLC model fit, in case of QPO mis-identification or in case of a comparable BKNPLC model (with a break at, or below the QPO candidate frequency) causing a drop in statistical significance – this check flagged five candidates. Modelling the broad-band noise instead as a 'double Lorentzian' following McHardy et al. (2007) found such a model would not reduce QPO significance over the investigated frequency range.

A study into the uncertainty on the white noise cutoff, which sets the upper bound of the investigated broad-band noise, showed the limitations in setting a fixed cutoff frequency, above which any data are discarded. The method of white noise cutoff determination, and the criteria by which a power spectrum is further investigated (e.g. minimum number of bins), remains an open decision in any new study. Additional biases were also investigated, including the impact of negative count rates (produced from the subtracted, stochastic background) and found this to be within the error expected from the broad-band noise PLC model fits and the effect further suppressed by the implementation of the aforementioned frequency cutoff. An analysis into the role of red noise leak found it could reduce the detection significance of each QPO candidate, causing sixteen candidates to drop to a $< 3\sigma$ significance if following the conservative assumption of an intrinsic power law index of -2. Finally, a revised statistical philosophy, in assuming all observations to be independent trials, found the significance of the QPO candidates diminished, with the exception of those detected across multiple frequencies which are instead found at very high significance ($> 4\sigma$ for ARK 564 and $> 6\sigma$ for 1H 0707-495 and IRAS 13224-3809).

This study concludes with the significant possibility of new AGN QPOs being detected in several NLS1 AGN – including in IRAS 13224-3809, 1H 0707-495 and ARK 564. If this is indeed the case, it represents a remarkable finding, offering a new sample of AGN QPOs to help advance the study of AGN variability.

7.1.1 Future Prospects

There are a multitude of possibilities for further study branching out from this work. A new sample of probable AGN QPOs allows for the study of the QPO state in greater detail than was possible before, where studies relied only on RE J1034+396 (Middleton et al., 2009, 2011; Jin et al., 2020, 2021). An investigation into the energy spectrum of an AGN across observations where a QPO *is*, and *is not*, detected may infer some key parameters or characteristics which underpin the QPO state. In addition, the nature of the QPO variability can be probed with both the rms and/or covariance spectrum (Middleton et al., 2011), especially at the QPO frequency and in energy bands where the QPO significance is highest.

Future deep QPO searches have numerous avenues open to exploration. The timescales of AGN QPOs reported to date likely correspond with those HFQPO in XRBs, assuming mass scale invariance (Middleton and Done, 2010). LFQPOs in XRBs are more commonly observed phenomena, but the expected LFQPO period on AGN timescales corresponds to ∼months. Given the capabilities of all-sky monitors such as *MAXI*, it may be possible in future to concatenate ∼years of X-ray observations of a large number of AGN, possibly allowing AGN LFQPO timescales to be probed.

On a statistical front, it is possible to move beyond the frequentist techniques implemented in this analysis, either through the use of a fully Bayesian framework (Vaughan, 2010), or through more novel continuous time autoregressive moving average (CARMA) methods (Kelly et al., 2014; Moreno et al., 2019). The latter which use Gaussian processes to estimate the power spectrum through a summation of Lorentzian components within a Bayesian framework – an approach implemented by Alston et al. (2019) in the study of IRAS 13224-3809. With the ability to incorporate gaps in observations, this may also be useful in a deep search for LFQPOs in AGN. A Bayesian approach would then allow for the properties of the QPO candidates to be represented as fully probabilistic distributions.

In addition to implementing a Bayesian modelling framework (given sufficient computational power to do so), a future update could plan to effectively remove the white noise cutoff routine to instead model both red noise and Poisson noise across the full frequency bandpass, to ensure no QPO candidate is 'lost' at a frequency higher than the cutoff. This in turn may require a change in information criterion test, if now fitting to Poisson noise. Such a future study could additionally investigate the remaining 'flareless' lightcurve segments for each observation, which were not blindly selected (and in turn, act as additional blind tests for new observations and non-blind tests for those observations already of interest) – in most cases of interest however, these unstudied segments are considerably shorter than the analysed segment. Finally, the detection of statistically significant breaks through the BKNPLC model allows for the possible study of the energy dependence of break features across the investigated sample, which may in turn help set prior distributions for energy dependent breaks in AGN, if conducting a Bayesian analysis.

7.2 Energy-dependent broad-band noise and emissivity profiles

Following from the analysis of 38 bright AGN in Chapter 3, energy-resolved periodograms were modelled in five energy bins, $0.3 - 1.0$, $1.0 - 2.0$, $2.0 - 4.0$, $4.0 - 6.0$ and $6.0 - 10.0$ keV. After applying strict data criteria (both in rejecting observations without sufficient power and sources for which there were too few observations to provide error estimates), leaves a total of five AGN: IRAS 13224-3809, 1H 0707-495, NGC 4051, ARK 548 and MRK 766. In all five cases, the power law index is observed to be steep at low energies and becomes increasingly flat towards higher energies (in all cases, only PLC models, statistically preferred over BKNPLC models are considered). To-date this has only been reported for a very small number of AGN (with only one such AGN within the sample – NGC 4051, see McHardy et al. 2004; Vaughan et al. 2011) and across only a small number of energy bins (Nandra and Papadakis, 2001; Vaughan et al., 2003b; McHardy et al., 2005; Jin et al., 2020). This analysis therefore represents a much broader investigation of the energy dependence observed in AGN power spectra.

Following Arévalo and Uttley (2006), a framework is created combining the impact of both propagation and reflection, before determining that the impact of reflection is negligible, even for the case of extremely reflection dominated sources. The well-accepted propagation model for accretion (Lyubarskii 1997; Kotov et al. 2001; Ingram and Done 2011; Turner and Reynolds 2021) makes a clear prediction that the shape of the observed power spectrum should be modified by the area of the inflow producing the variability, and the radial emissivity profile as a function of energy – the latter implicitly assuming a simple disc-like geometry. Modelling the energy-dependence of the power spectrum should therefore provide an insight into the changing radial emissivity under the conditions of the assumed coronal geometry.

The power-spectra of the AGN sample are modelled in five energy bands assuming changes driven by the propagation model of Arévalo and Uttley (2006) and are used to determine the emissivity index as a function of energy, parameterising it as a linear function. This modelling is remarkably successful in most cases with the index starting at $\gamma < 3$ at low energies (which may well be consistent with an ADAF providing some of the soft excess emission, e.g. Done et al. 2012) and rising to $\gamma > 4$. The best-fitting emissivity function varies between sources; and an attempt is made to correlate $\gamma(E)$ with some of the key macro-properties of the AGN (mass, spin, inclination and Eddington ratio), finding either a lack of a correlation or only a tentative hint (with Eddington ratio).

7.2.1 Future Prospects

It will be interesting to compare these results for a simplified disc-like geometry to a more complex geometry incorporating a more realistic Compton scattering scenario. There is also opportunity to increase the number of sources for this study, to further test this tentative correlation with Eddington ratio, or by using *NuSTAR* to extend the energy range of this study up to $\sim$ 80 keV. The latter would allow for an improved study of the nature of the observed trend of flattening power spectral indices, which was modelled with a linear function in this work, but showed signs of non-linearity at the extremes of the investigated energy range.

Finally, this work opens up the potential for a comparison study investigating the observed energy dependence of the power spectral index for XRBs. Given the broad energy range and shorter variability timescales of XRBs over AGN, *NuSTAR* could again prove an ideal instrument for such a study. It remains an intriguing question as to whether the energy dependent nature of the power spectrum of XRBs follow the observed case of AGN presented here, and if such a framework could similarly apply to the XRB accretion system as a further test of mass scale invariance.

7.3 Final Word

The study of X-ray variability in AGN offers insight into the most extreme physical environments known to exist in the universe. This work has been undertaken with the aim of examining only a few of the plethora of open questions which remain on the topic. In doing so, it both shines some light into the nature of energy dependent AGN variability and forms a basis for future investigations to expand our understanding further.

Appendix A

Observation Table

AGN	Obs ID	Duration (ks)	Flareless Duration (ks)	QPO?
PG 0003+199	0101040101	31.60	23.44	
PG 0003+199	0306870101	132.70	61.24	
PG 0003+199	0510010701	16.70	16.70	
PG 0003+199	0600540501	80.70	34.96	
PG 0003+199	0600540601	130.40	43.78	
PG 0003+199	0741280201	137.40	30.51	
PG 0050+124	0110890301	20.00	9.73	
PG 0050+124	0300470101	82.90	24.00	
PG 0050+124	0743050301	20.40	2.37	
PG 0050+124	0743050801	20.40	7.10	
PG 0157+001	0101640201	11.20	10.19	
PG 0844+349	0103660201	21.20	9.86	
PG 0844+349	0554710101	12.60	12.60	
PG 0947+396	0111290101	18.80	18.79	
PG 0953+414	0111290201	12.30	4.68	
PG 1048+342	0109080701	30.00	17.30	
PG 1115+407	0111290301	16.00	12.10	
PG 1116+215	0111290401	7.00	6.99	
PG 1116+215	0201940101	106.90	78.44	
PG 1116+215	0201940201	7.10	1.94	
PG 1116+215	0554380101	88.00	47.37	
PG 1116+215	0554380201	88.20	70.50	
PG 1116+215	0554380301	88.70	71.24	
PG 1202+281	0109080101	13.80	13.29	
PG 1211+143	0112610101	53.10	41.13	
PG 1211+143	0208020101	57.40	20.54	
PG 1211+143	0502050101	58.90	46.49	

AGN	Obs ID	Duration (ks)	Flareless Duration (ks)	QPO?
PG 1211+143	0502050201	43.40	36.59	
PG 1211+143	0745110101	83.60	42.92	
PG 1211+143	0745110201	100.60	62.67	
PG 1211+143	0745110301	99.10	53.04	
PG 1211+143	0745110401	96.60	92.03	
PG 1211+143	0745110501	54.60	20.34	
PG 1211+143	0745110601	91.90	35.79	
PG 1211+143	0745110701	95.60	33.09	
PG 1244+026	0051760101	8.10	8.10	
PG 1244+026	0675320101	123.40	71.81	✓
PG 1244+026	0744440101	117.90	44.02	
PG 1244+026	0744440201	118.40	83.69	
PG 1244+026	0744440301	120.40	42.78	
PG 1244+026	0744440401	126.90	36.40	
PG 1244+026	0744440501	118.50	27.60	
PG 1307+085	0110950401	12.00	4.75	
PG 1309+355	0109080201	26.90	17.64	
PG 1322+659	0109080301	9.30	4.41	
PG 1322+659	0206180201	66.40	38.28	
PG 1352+183	0109080401	13.40	2.22	
PG 1402+261	0109081001	9.70	9.70	
PG 1402+261	0400200101	36.60	35.81	
PG 1402+261	0400200201	18.40	17.30	
PG 1404+226	0051760201	18.20	10.04	
PG 1404+226	0763480101	99.60	66.15	
PG 1427+480	0109080901	37.70	27.44	
PG 1440+356	0005010101	24.50	19.44	
PG 1440+356	0005010201	28.30	27.47	
PG 1440+356	0005010301	26.00	16.17	
PG 1440+356	0107660201	27.60	14.46	
PG 1440+356	0801510101	133.70	6.55	
PG 1444+407	0109080601	20.00	9.18	
PG 1501+106	0070740101	10.80	10.41	
PG 1501+106	0070740301	13.30	11.53	
PG 1501+106	0112910201	8.40	8.40	
PG 1501+106	0205340201	45.90	19.51	
PG 1501+106	0205340401	29.00	12.09	
PG 1501+106	0763790501	22.30	15.58	
1H 0707-495	0148010301	78.00	65.48	
1H 0707-495	0506200201	38.60	25.37	

AGN	Obs ID	Duration (ks)	Flareless Duration (ks)	QPO?
1H 0707-495	0506200301	38.60	38.60	
1H 0707-495	0506200401	40.60	7.57	
1H 0707-495	0506200501	40.80	29.58	
1H 0707-495	0511580101	121.50	48.67	
1H 0707-495	0511580201	0.20	0.20	
1H 0707-495	0511580301	104.10	24.21	
1H 0707-495	0511580401	101.80	88.99	
1H 0707-495	0554710801	96.00	29.56	
1H 0707-495	0653510301	113.90	95.19	✓
1H 0707-495	0653510401	125.80	94.69	
1H 0707-495	0653510501	117.00	94.72	✓
1H 0707-495	0653510601	119.60	105.85	✓
NGC 4051	0109141401	117.00	25.77	✓
NGC 4051	0157560101	49.90	35.52	
NGC 4051	0606320101	45.20	41.83	
NGC 4051	0606320201	44.30	42.35	
NGC 4051	0606320301	31.30	24.17	
NGC 4051	0606320401	28.70	27.91	
NGC 4051	0606321301	30.10	24.51	
NGC 4051	0606321401	39.20	34.61	
NGC 4051	0606321501	38.80	36.12	
NGC 4051	0606321601	41.40	37.95	
NGC 4051	0606321701	38.30	28.37	
NGC 4051	0606321801	39.90	39.83	✓
NGC 4051	0606321901	6.20	4.30	
NGC 4051	0606322001	36.90	24.05	
NGC 4051	0606322101	37.60	29.51	
NGC 4051	0606322201	41.10	39.16	
NGC 4051	0606322301	42.20	24.27	
NGC 4151	0112310101	29.90	29.90	
NGC 4151	0112830201	56.90	33.63	
NGC 4151	0112830501	19.60	19.60	
NGC 4151	0143500101	18.50	6.87	
NGC 4151	0143500201	18.50	7.83	
NGC 4151	0143500301	18.50	10.31	
NGC 4151	0402660101	39.90	37.64	
NGC 4151	0402660201	48.20	37.75	
NGC 4151	0657840101	11.80	11.80	
NGC 4151	0657840301	10.40	8.87	
NGC 4151	0657840401	9.70	9.70	

AGN	Obs ID	Duration (ks)	Flareless Duration (ks)	QPO?
NGC 4151	0679780101	9.40	6.67	
NGC 4151	0679780201	12.40	11.96	
NGC 4151	0679780301	7.60	7.60	
NGC 4151	0679780401	9.40	9.40	
NGC 4151	0761670101	33.60	14.23	
NGC 4151	0761670201	41.10	17.44	
NGC 4151	0761670301	43.60	17.95	
NGC 4151	0761670401	43.40	18.57	
NGC 4151	0761670501	38.30	34.90	
NGC 4151	0761670601	42.60	39.23	
NGC 4151	0761670701	48.00	38.08	
NGC 4151	0761670801	43.40	25.77	
NGC 4151	0761670901	43.90	25.50	
RE J1034+396	0109070101	12.80	8.70	
RE J1034+396	0506440101	91.30	28.94	✓
RE J1034+396	0561580201	60.80	22.65	
RE J1034+396	0655310101	44.30	28.26	
RE J1034+396	0655310201	53.00	41.60	✓
RE J1034+396	0675440101	36.20	23.92	✓
RE J1034+396	0675440201	29.40	28.82	✓
RE J1034+396	0675440301	32.20	31.30	
ARK 564	0006810101	10.60	4.95	✓
ARK 564	0006810301	11.80	3.96	
ARK 564	0206400101	98.90	21.11	
ARK 564	0670130201	59.00	16.63	
ARK 564	0670130301	55.40	10.90	
ARK 564	0670130401	62.50	21.22	
ARK 564	0670130501	66.80	17.18	✓
ARK 564	0670130601	60.40	33.20	
ARK 564	0670130701	55.20	44.71	✓
ARK 564	0670130801	57.70	51.65	✓
ARK 564	0670130901	55.40	17.58	
IRAS 13349+2438	0096010101	44.50	8.69	
IRAS 13349+2438	0402080201	42.60	38.50	
IRAS 13349+2438	0402080301	68.40	25.52	
IRAS 13349+2438	0402080801	18.40	11.41	
E 1346+266	0109070201	70.10	51.67	
PHL 1092	0110890901	25.50	12.49	
PHL 1092	0505400101	61.90	18.72	
PHL 1092	0610000201	28.10	28.10	

AGN	Obs ID	Duration (ks)	Flareless Duration (ks)	QPO?
PHL 1092	0653840301	25.10	20.21	
PHL 1092	0653840401	29.00	27.37	
TON S180	0110890401	29.40	4.43	
TON S180	0110890701	17.90	5.07	
TON S180	0764170101	135.30	61.31	
TON S180	0790990101	30.40	11.65	
PKS 0558-504	0116700301	5.40	5.39	
PKS 0558-504	0117500201	0.10	0.10	
PKS 0558-504	0117710201	0.10	0.10	
PKS 0558-504	0117710601	16.00	15.99	
PKS 0558-504	0117710701	19.50	13.23	
PKS 0558-504	0125110101	13.50	13.50	
PKS 0558-504	0129360201	10.70	3.27	
PKS 0558-504	0137550201	11.70	7.17	
PKS 0558-504	0137550601	11.40	11.40	
PKS 0558-504	0555170201	121.00	52.18	
PKS 0558-504	0555170301	126.00	73.53	
PKS 0558-504	0555170401	123.30	66.22	
PKS 0558-504	0555170501	124.40	14.44	
PKS 0558-504	0555170601	115.30	37.00	
MRK 359	0112600601	7.30	4.03	
MRK 359	0655590201	29.40	24.44	
MRK 359	0655590501	24.40	12.20	
MRK 766	0096020101	38.90	21.30	
MRK 766	0109141301	128.50	89.38	
MRK 766	0304030101	95.00	77.85	
MRK 766	0304030301	98.40	38.35	✓
MRK 766	0304030401	98.40	22.62	
MRK 766	0304030501	95.00	18.00	
MRK 766	0304030601	98.40	85.38	
MRK 766	0304030701	34.50	31.71	
MRK 766	0763790401	26.30	22.45	
MRK 1044	0112600301	7.90	4.89	
MRK 1044	0824080301	136.30	13.42	
MRK 1044	0824080401	138.40	126.10	
MS 22549-3712	0205390101	70.90	27.84	
MS 22549-3712	0748391001	97.00	32.04	
IRAS 13224-3809	0110890101	60.80	26.74	
IRAS 13224-3809	0673580101	126.10	57.63	
IRAS 13224-3809	0673580201	125.10	76.46	

AGN	Obs ID	Duration (ks)	Flareless Duration (ks)	QPO?
IRAS 13224-3809	0673580401	127.50	85.22	
IRAS 13224-3809	0780560101	52.00	38.42	
IRAS 13224-3809	0780561301	134.40	125.29	✓
IRAS 13224-3809	0780561401	86.20	82.92	✓
IRAS 13224-3809	0780561501	137.40	95.25	
IRAS 13224-3809	0780561601	137.40	83.14	
IRAS 13224-3809	0780561701	137.40	113.20	✓
IRAS 13224-3809	0792180101	137.60	124.58	
IRAS 13224-3809	0792180201	137.10	128.63	✓
IRAS 13224-3809	0792180301	130.60	53.26	✓
IRAS 13224-3809	0792180401	137.40	92.64	
IRAS 13224-3809	0792180501	131.70	93.83	✓
IRAS 13224-3809	0792180601	132.60	105.02	✓

TABLE A.1: Complete table of archived *XMM-Newton* observations used in the search for AGN QPOs, with columns: 1) AGN, 2) Obs ID, 3) Total observation duration, 4) Longest continuous 'flareless' segment (blind selection), 5) QPO candidate of interest, which underwent further investigation in Chapter 4.

References

M. Abramowicz, M. Jaroszynski, and M. Sikora. Relativistic, accreting disks. *A&A*, 63: 221–224, February 1978.

M. A. Abramowicz and W. Kluźniak. A precise determination of black hole spin in GRO J1655-40. *A&A*, 374:L19–L20, August 2001.

M. A. Abramowicz, B. Czerny, J. P. Lasota, and E. Szuszkiewicz. Slim Accretion Disks. *ApJ*, 332:646, September 1988.

Y. L. Ai, W. Yuan, H. Zhou, T. G. Wang, X. B. Dong, J. G. Wang, and H. L. Lu. A Comparative Study of Optical/Ultraviolet Variability of Narrow-line Seyfert 1 and Broad-line Seyfert 1 Active Galactic Nuclei. *AJ*, 145(4):90, April 2013.

H. Akaike. A New Look at the Statistical Model Identification. *IEEE Transactions on Automatic Control*, 19:716–723, January 1974.

W. N. Alston, S. Vaughan, and P. Uttley. The flux-dependent X-ray time lags in NGC 4051. *MNRAS*, 435(2):1511–1519, Oct 2013a.

W. N. Alston, S. Vaughan, and P. Uttley. Ultraviolet and X-ray variability of NGC 4051 over 45 days with XMM-Newton and Swift. *MNRAS*, 429(1):75–84, February 2013b.

W. N. Alston, C. Done, and S. Vaughan. X-ray time delays in the narrow line Seyfert 1 galaxy PG 1244+026. *MNRAS*, 439(2):1548–1555, April 2014a.

W. N. Alston, J. Markevičiūtė, E. Kara, A. C. Fabian, and M. Middleton. Detection of a QPO in five XMM-Newton observations of RE J1034+396. *MNRAS*, 445:L16–L20, November 2014b.

W. N. Alston, M. L. Parker, J. Markevičiūtė, A. C. Fabian, M. Middleton, A. Lohfink, E. Kara, and C. Pinto. Discovery of an
2-h high-frequency X-ray QPO and iron Kα reverberation in the active galaxy MS 2254.9-3712. *MNRAS*, 449:467–476, May 2015.

W. N. Alston, A. C. Fabian, D. J. K. Buisson, E. Kara, M. L. Parker, A. M. Lohfink, P. Uttley, D. R. Wilkins, C. Pinto, B. De Marco, E. M. Cackett, M. J. Middleton, D. J.

Walton, C. S. Reynolds, J. Jiang, L. C. Gallo, A. Zogbhi, G. Miniutti, M. Dovciak, and A. J. Young. The remarkable X-ray variability of IRAS 13224-3809 - I. The variability process. *MNRAS*, 482(2):2088–2106, January 2019.

W. N. Alston, A. C. Fabian, E. Kara, M. L. Parker, M. Dovciak, C. Pinto, J. Jiang, M. J. Middleton, G. Miniutti, D. J. Walton, D. R. Wilkins, D. J. K. Buisson, M. D. Caballero-Garcia, E. M. Cackett, B. De Marco, L. C. Gallo, A. M. Lohfink, C. S. Reynolds, P. Uttley, A. J. Young, and A. Zogbhi. A dynamic black hole corona in an active galaxy through X-ray reverberation mapping. *Nature Astronomy*, page 2, January 2020.

E. R. Anderson, Jr. Duvall, T. L., and S. M. Jefferies. Modeling of Solar Oscillation Power Spectra. *ApJ*, 364:699, December 1990.

R. Antonucci. Unified models for active galactic nuclei and quasars. *ARA&A*, 31:473–521, January 1993.

P. Arévalo and P. Uttley. Investigating a fluctuating-accretion model for the spectral-timing properties of accreting black hole systems. *MNRAS*, 367(2):801–814, April 2006.

K. A. Arnaud. XSPEC: The First Ten Years. In George H. Jacoby and Jeannette Barnes, editors, *Astronomical Data Analysis Software and Systems V*, volume 101 of *Astronomical Society of the Pacific Conference Series*, page 17, January 1996.

K. A. Arnaud, G. Branduardi-Raymont, J. L. Culhane, A. C. Fabian, C. Hazard, T. A. McGlynn, R. A. Shafer, A. F. Tennant, and M. J. Ward. EXOSAT observations of a strong soft X-ray excess in MKN 841. *MNRAS*, 217:105–113, November 1985.

D. I. Ashton and M. J. Middleton. Searching for energy-resolved quasi-periodic oscillations in AGN. *MNRAS*, 501(4):5478–5499, March 2021a.

Dominic I. Ashton and M. J. Middleton. Constraining Energy-dependent emissivity profiles of AGN inflows [Accepted, awaiting publication upon acceptance of revisions]. *MNRAS*, September 2021b.

S. A. Balbus and J. F. Hawley. A Powerful Local Shear Instability in Weakly Magnetized Disks. I. Linear Analysis. *ApJ*, 376:214, July 1991.

S. A. Balbus and J. F. Hawley. A Powerful Local Shear Instability in Weakly Magnetized Disks. IV. Nonaxisymmetric Perturbations. *ApJ*, 400:610–621, December 1992.

J. M. Bardeen, W. H. Press, and S. A. Teukolsky. Rotating Black Holes: Locally Nonrotating Frames, Energy Extraction, and Scalar Synchrotron Radiation. *ApJ*, 178:347–370, December 1972.

J. M. Bardeen, B. Carter, and S. W. Hawking. The four laws of black hole mechanics. *Communications in Mathematical Physics*, 31(2):161–170, June 1973.

R. Barlow. *Fourier Analysis*. John Wiley & Sons Ltd., Chichester, England, 1999.

M. C. Begelman. Black holes in radiation-dominated gas: an analogue of the Bondi accretion problem. *MNRAS*, 184:53–67, July 1978.

M. C. Begelman, C. F. McKee, and G. A. Shields. Compton heated winds and coronae above accretion disks. I. Dynamics. *ApJ*, 271:70–88, August 1983.

M. C. Begelman, M. Volonteri, and M. J. Rees. Formation of supermassive black holes by direct collapse in pre-galactic haloes. *MNRAS*, 370(1):289–298, July 2006.

J. S. Bendat and A. G. Piersol. *Random Data: Analysis and Measurement Procedures*. Wiley, New York, 1986.

N. Bennert, B. Jungwiert, S. Komossa, M. Haas, and R. Chini. Size and properties of the narrow-line region in Seyfert-1 galaxies from spatially-resolved optical spectroscopy. *A&A*, 459(1):55–69, November 2006.

O. Blaes. General Overview of Black Hole Accretion Theory. , 183(1-4):21–41, September 2014.

O. M. Blaes, P. Arras, and P. C. Fragile. Oscillation modes of relativistic slender tori. *MNRAS*, 369(3):1235–1252, July 2006a.

O. M. Blaes, P. Arras, and P. C. Fragile. Oscillation modes of relativistic slender tori. *MNRAS*, 369(3):1235–1252, July 2006b.

R. Blandford, D. Meier, and A. Readhead. Relativistic Jets from Active Galactic Nuclei. *ARA&A*, 57:467–509, August 2019.

R. D. Blandford. Physical processes in active galactic nuclei. In R. D. Blandford, H. Netzer, L. Woltjer, T. J. L. Courvoisier, and M. Mayor, editors, *Active Galactic Nuclei*, pages 161–275, January 1990.

A. J. Blustin, M. J. Page, S. V. Fuerst, G. Branduardi-Raymont, and C. E. Ashton. The nature and origin of Seyfert warm absorbers. *A&A*, 431:111–125, February 2005.

Th. Boller, W. N. Brandt, A. C. Fabian, and H. H. Fink. ROSAT monitoring of persistent giant and rapid variability in the narrow-line Seyfert 1 galaxy IRAS 13224-3809. *MNRAS*, 289(2):393–405, August 1997.

Th. Boller, R. Keil, J. Trümper, P. T. O'Brien, J. Reeves, and M. Page. Detection of an X-ray periodicity in the Narrow-line Seyfert 1 Galaxy Mrk 766 with XMM-Newton. *A&A*, 365:L146–L151, January 2001.

Th. Boller, T. Liu, P. Weber, R. Arcodia, T. Dauser, J. Wilms, K. Nandra, J. Buchner, A. Merloni, M. J. Freyberg, M. Krumpe, and S. G. H. Waddell. Extreme ultra-soft X-ray variability in an eROSITA observation of the narrow-line Seyfert 1 galaxy 1H 0707-495. *A&A*, 647:A6, March 2021.

T. A. Boroson. Black Hole Mass and Eddington Ratio as Drivers for the Observable Properties of Radio-loud and Radio-quiet QSOs. *ApJ*, 565(1):78–85, January 2002.

S. Bowyer, E. T. Byram, T. A. Chubb, and H. Friedman. X-ray Sources in the Galaxy. *Nature*, 201(4926):1307–1308, March 1964.

E. Breedt, I. M. McHardy, P. Arévalo, P. Uttley, S. G. Sergeev, T. Minezaki, Y. Yoshii, Y. Sakata, P. Lira, and N. G. Chesnok. Twelve years of X-ray and optical variability in the Seyfert galaxy NGC 4051. *MNRAS*, 403(2):605–619, April 2010.

A. M. Brown. Locating the γ-ray emission region of the flat spectrum radio quasar PKS 1510-089. *MNRAS*, 431(1):824–835, May 2013.

D. J. K. Buisson, A. M. Lohfink, W. N. Alston, E. M. Cackett, C. Y. Chiang, T. Dauser, B. De Marco, A. C. Fabian, L. C. Gallo, J. A. García, J. Jiang, E. Kara, M. J. Middleton, G. Miniutti, M. L. Parker, C. Pinto, P. Uttley, D. J. Walton, and D. R. Wilkins. Is there a UV/X-ray connection in IRAS 13224-3809? *MNRAS*, 475(2):2306–2313, April 2018a.

D. J. K. Buisson, M. L. Parker, E. Kara, R. V. Vasudevan, A. M. Lohfink, C. Pinto, A. C. Fabian, D. R. Ballantyne, S. E. Boggs, F. E. Christensen, W. W. Craig, D. Farrah, C. J. Hailey, F. A. Harrison, C. Ricci, D. Stern, D. J. Walton, and W. W. Zhang. NuSTAR observations of Mrk 766: distinguishing reflection from absorption. *MNRAS*, 480(3):3689–3701, November 2018b.

D. N. Burrows, J. E. Hill, J. A. Nousek, J. A. Kennea, A. Wells, J. P. Osborne, A. F. Abbey, A. Beardmore, K. Mukerjee, A. D. T. Short, G. Chincarini, S. Campana, O. Citterio, A. Moretti, C. Pagani, G. Tagliaferri, P. Giommi, M. Capalbi, F. Tamburelli, L. Angelini, G. Cusumano, H. W. Bräuninger, W. Burkert, and G. D. Hartner. The Swift X-Ray Telescope. , 120(3-4):165–195, October 2005.

S. Campana and L. Stella. Reverberation by a relativistic accretion disc. *MNRAS*, 272(3):585–598, February 1995.

B. W Carroll and D. A. Ostlie. *An Introduction to Modern Astrophysics*. Addison-Wesley Publishing Company, Inc, 1996.

D. A. Casebeer, K. M. Leighly, and E. Baron. FUSE Observation of the Narrow-Line Seyfert 1 Galaxy RE 1034+39: Dependence of Broad Emission Line Strengths on the Shape of the Photoionizing Spectrum. *ApJ*, 637(1):157–182, January 2006.

P. Cassatella, P. Uttley, J. Wilms, and J. Poutanen. Joint spectral-timing modelling of the hard lags in GX 339-4: constraints on reflection models. *MNRAS*, 422(3):2407–2416, May 2012.

P. M. Chadwick, K. Lyons, T. J. L. McComb, K. J. Orford, J. L. Osborne, S. M. Rayner, S. E. Shaw, K. E. Turver, and G. J. Wieczorek. Very High Energy Gamma Rays from PKS 2155-304. *ApJ*, 513(1):161–167, March 1999.

P. Chainakun. Modeling the X-Ray Power Spectra of AGN by Using Reprocessing Echoes from an Extended Corona. *ApJ*, 878(1):20, June 2019.

P. Chainakun, A. Watcharangkool, A. J. Young, and S. Hancock. X-ray time lags in AGN: inverse-Compton scattering and spherical corona model. *MNRAS*, 487(1):667–680, July 2019.

L. Chevallier, S. Collin, A. M. Dumont, B. Czerny, M. Mouchet, A. C. Gonçalves, and R. Goosmann. The role of absorption and reflection in the soft X-ray excess of Active Galactic Nuclei. I. Preliminary results. *A&A*, 449(2):493–508, April 2006.

E. Churazov, M. Gilfanov, and M. Revnivtsev. Soft state of Cygnus X-1: stable disc and unstable corona. *MNRAS*, 321(4):759–766, March 2001.

D. Coe. Fisher matrices and confidence ellipses: A quick-start guide and software, 2009.

NuSTAR Observatory Collaboration. The Nuclear Spectroscopic Telescope Array (NuSTAR) High-energy X-Ray Mission. *ApJ*, 770(2):103, June 2013.

A. Comastri. *Compton-Thick AGN: The Dark Side of the X-Ray Background*, volume 308, page 245. Springer Netherlands, 2004.

A. H. Compton. A Quantum Theory of the Scattering of X-rays by Light Elements. *Physical Review*, 21(5):483–502, May 1923.

J. W Cooley and J. W Tukey. An algorithm for the machine calculation of complex Fourier series. *"Math. Comp."*, 19(90):297–301, April 1965.

J. M. Corral-Santana, J. Casares, T. Muñoz-Darias, F. E. Bauer, I. G. Martínez-Pais, and D. M. Russell. BlackCAT: A catalogue of stellar-mass black holes in X-ray transients. *A&A*, 587:A61, March 2016.

J. Crummy, A. C. Fabian, L. Gallo, and R. R. Ross. An explanation for the soft X-ray excess in active galactic nuclei. *MNRAS*, 365(4):1067–1081, Feb 2006a.

J. Crummy, A. C. Fabian, L. Gallo, and R. R. Ross. An explanation for the soft X-ray excess in active galactic nuclei. *MNRAS*, 365(4):1067–1081, February 2006b.

B. Czerny and K. Hryniewicz. The origin of the broad line region in active galactic nuclei. *A&A*, 525:L8, January 2011.

B. Czerny and P. T. Zycki. Weak Soft X-Ray Excesses Need Not Result from the High-Frequency Tail of the Optical/Ultraviolet Bump in Active Galactic Nuclei. *ApJ*, 431: L5, August 1994.

B. Czerny, M. Nikołajuk, Agata Różańska, A. M. Dumont, Z. Loska, and P. T. Zycki. Universal spectral shape of high accretion rate AGN. *A&A*, 412:317–329, December 2003.

T. Dauser, J. Wilms, C. S. Reynolds, and L. W. Brenneman. Broad emission lines for a negatively spinning black hole. *MNRAS*, 409(4):1534–1540, December 2010.

T. Dauser, J. Svoboda, N. Schartel, J. Wilms, M. Dovčiak, M. Ehle, V. Karas, M. Santos-Lleó, and H. L. Marshall. Spectral analysis of 1H 0707-495 with XMM-Newton. *MNRAS*, 422(3):1914–1921, May 2012.

T. Dauser, J. Garcia, J. Wilms, M. Böck, L. W. Brenneman, M. Falanga, K. Fukumura, and C. S. Reynolds. Irradiation of an accretion disc by a jet: general properties and implications for spin measurements of black holes. *MNRAS*, 430(3):1694–1708, April 2013.

T. Dauser, J. Garcia, M. L. Parker, A. C. Fabian, and J. Wilms. The role of the reflection fraction in constraining black hole spin. *MNRAS*, 444:L100–L104, October 2014.

T. Dauser, J. García, D. J. Walton, W. Eikmann, T. Kallman, J. McClintock, and J. Wilms. Normalizing a relativistic model of X-ray reflection. Definition of the reflection fraction and its implementation in relxill. *A&A*, 590:A76, May 2016.

S. W. Davis, C. Done, and O. M. Blaes. Testing Accretion Disk Theory in Black Hole X-Ray Binaries. *ApJ*, 647(1):525–538, August 2006.

J. E. Deeter and P. E. Boynton. Techniques for the estimation of red power spectra. I - Context and methodology. *ApJ*, 261:337–350, October 1982.

J. W. den Herder, A. C. Brinkman, S. M. Kahn, G. Branduardi-Raymont, K. Thomsen, H. Aarts, M. Audard, J. V. Bixler, A. J. den Boggende, J. Cottam, T. Decker, L. Dubbeldam, C. Erd, H. Goulooze, M. Güdel, P. Guttridge, C. J. Hailey, K. Al Janabi, J. S. Kaastra, P. A. J. de Korte, B. J. van Leeuwen, C. Mauche, A. J. McCalden, R. Mewe, A. Naber, F. B. Paerels, J. R. Peterson, A. P. Rasmussen, K. Rees, I. Sakelliou, M. Sako, J. Spodek, M. Stern, T. Tamura, J. Tandy, C. P. de Vries, S. Welch, and A. Zehnder. The Reflection Grating Spectrometer on board XMM-Newton. *A&A*, 365:L7–L17, January 2001.

K. D. Denney, B. M. Peterson, R. W. Pogge, A. Adair, D. W. Atlee, K. Au-Yong, M. C. Bentz, J. C. Bird, D. J. Brokofsky, E. Chisholm, M. L. Comins, M. Dietrich, V. T. Doroshenko, J. D. Eastman, Y. S. Efimov, S. Ewald, S. Ferbey, C. M. Gaskell, C. H. Hedrick, K. Jackson, S. A. Klimanov, E. S. Klimek, A. K. Kruse, A. Ladéroute, J. B. Lamb, K. Leighly, T. Minezaki, S. V. Nazarov, C. A. Onken, E. A. Petersen, P. Peterson, S. Poindexter, Y. Sakata, K. J. Schlesinger, S. G. Sergeev, N. Skolski, L. Stieglitz, J. J. Tobin, C. Unterborn, M. Vestergaard, A. E. Watkins, L. C. Watson, and Y. Yoshii. Reverberation Mapping Measurements of Black Hole Masses in Six Local Seyfert Galaxies. *ApJ*, 721(1):715–737, Sep 2010.

G. C. Dewangan, Th. Boller, K. P. Singh, and K. M. Leighly. A 10-day ASCA observation of the narrow-line Seyfert 1 galaxy IRAS 13224-3809. *A&A*, 390:65–80, July 2002.

T. Di Matteo, E. G. Blackman, and A. C. Fabian. Two-temperature coronae in active galactic nuclei. *MNRAS*, 291(1):L23–L27, October 1997.

C. Done. The Origin of the Soft Excess in High L/L_{Edd} AGN. *Progress of Theoretical Physics Supplement*, 169:248–251, January 2007.

C. Done. Observational characteristics of accretion onto black holes. *arXiv e-prints*, August 2010.

C. Done and C. Jin. The mass and spin of the extreme Narrow Line Seyfert 1 Galaxy 1H 0707-495 and its implications for the trigger for relativistic jets. *MNRAS*, 460(2): 1716–1724, August 2016.

C. Done and A. Kubota. Disc-corona energetics in the very high state of Galactic black holes. *MNRAS*, 371(3):1216–1230, September 2006.

C. Done and S. Nayakshin. Can the soft excess in AGN originate from disc reflection? *MNRAS*, 377(1):L59–L63, May 2007.

C. Done, M. Gierliński, and A. Kubota. Modelling the behaviour of accretion flows in X-ray binaries. Everything you always wanted to know about accretion but were afraid to ask. *A&A Rev.*, 15(1):1–66, December 2007a.

C. Done, M. Gierliński, M. Sobolewska, and N. Schurch. The Origin of the Soft Excess in AGN. In L. C. Ho and J. W. Wang, editors, *The Central Engine of Active Galactic Nuclei*, volume 373 of *Astronomical Society of the Pacific Conference Series*, page 121, October 2007b.

C. Done, S. W. Davis, C. Jin, O. Blaes, and M. Ward. Intrinsic disc emission and the soft X-ray excess in active galactic nuclei. *MNRAS*, 420(3):1848–1860, March 2012.

C. Done, S. W. Davis, C. Jin, O. Blaes, and M. Ward. Intrinsic disc emission and the soft X-ray excess in active galactic nuclei. *Monthly Notices of the Royal Astronomical Society*, 420(3):1848–1860, 02 2012. ISSN 0035-8711.

C. Done, C. Jin, M. Middleton, and M. Ward. A new way to measure supermassive black hole spin in accretion disc-dominated active galaxies. *MNRAS*, 434(3):1955–1963, September 2013.

Jr. Duvall, T. L. and J. W. Harvey. Solar Doppler shifts: sources of continuous spectra. In Douglas O. Gough, editor, *Seismology of the Sun and the Distant Stars*, volume 169 of *NATO Advanced Study Institute (ASI) Series C*, pages 105–116, January 1986.

A. Eckart, R. Genzel, T. Ott, and R. Schödel. Stellar orbits near Sagittarius A*. *MNRAS*, 331(4):917–934, April 2002.

R. Edelson and K. Nandra. A Cutoff in the X-Ray Fluctuation Power Density Spectrum of the Seyfert 1 Galaxy NGC 3516. NASA STI/Recon Technical Report N, May 1999.

R. Edelson, T. J. Turner, K. Pounds, S. Vaughan, A. Markowitz, H. Marshall, P. Dobbie, and R. Warwick. X-Ray Spectral Variability and Rapid Variability of the Soft X-Ray Spectrum Seyfert 1 Galaxies Arakelian 564 and Ton S180. *ApJ*, 568(2):610–626, April 2002.

R. A. Edelson, J. H. Krolik, and G. F. Pike. Broad-Band Properties of the CfA Seyfert Galaxies. III. Ultraviolet Variability. *ApJ*, 359:86, August 1990.

D. Emmanoulopoulos, I. E. Papadakis, A. Epitropakis, T. Pecháček, M. Dovčiak, and I. M. McHardy. A search for X-ray reprocessing echoes in the power spectral density functions of AGN. *MNRAS*, 461(2):1642–1655, September 2016.

Event Horizon Telescope Collaboration. First M87 Event Horizon Telescope Results. I. The Shadow of the Supermassive Black Hole. *ApJ*, 875(1):L1, April 2019a.

Event Horizon Telescope Collaboration. First M87 Event Horizon Telescope Results. II. Array and Instrumentation. *ApJ*, 875(1):L2, April 2019b.

A. C. Fabian. A short introduction to broad and variable iron lines around black holes. *Astronomische Nachrichten*, 327(10):943, December 2006.

A. C. Fabian, M. J. Rees, L. Stella, and N. E. White. X-ray fluorescence from the inner disc in Cygnus X-1. *MNRAS*, 238:729–736, May 1989.

A. C. Fabian, K. Iwasawa, C. S. Reynolds, and A. J. Young. Broad Iron Lines in Active Galactic Nuclei. *PASP*, 112(775):1145–1161, September 2000.

A. C. Fabian, D. R. Ballantyne, A. Merloni, S. Vaughan, K. Iwasawa, and Th. Boller. How the X-ray spectrum of a narrow-line Seyfert 1 galaxy may be reflection-dominated. *MNRAS*, 331(3):L35–L39, April 2002.

A. C. Fabian, G. Miniutti, L. Gallo, Th. Boller, Y. Tanaka, S. Vaughan, and R. R. Ross. X-ray reflection in the narrow-line Seyfert 1 galaxy 1H 0707-495. *MNRAS*, 353(4): 1071–1077, October 2004.

A. C. Fabian, A. Zoghbi, R. R. Ross, P. Uttley, L. C. Gallo, W. N. Brandt, A. J. Blustin, T. Boller, M. D. Caballero-Garcia, J. Larsson, J. M. Miller, G. Miniutti, G. Ponti, R. C. Reis, C. S. Reynolds, Y. Tanaka, and A. J. Young. Broad line emission from iron K- and L-shell transitions in the active galaxy 1H0707-495. *Nature*, 459(7246):540–542, May 2009.

A. C. Fabian, E. Kara, D. J. Walton, D. R. Wilkins, R. R. Ross, K. Lozanov, P. Uttley, L. C. Gallo, A. Zoghbi, G. Miniutti, T. Boller, W. N. Brandt, E. M. Cackett, C. Y. Chiang, T. Dwelly, J. Malzac, J. M. Miller, E. Nardini, G. Ponti, R. C. Reis, C. S. Reynolds, J. F. Steiner, Y. Tanaka, and A. J. Young. Long XMM observation of the narrow-line Seyfert 1 galaxy IRAS 13224-3809: rapid variability, high spin and a soft lag. *MNRAS*, 429(4):2917–2923, March 2013.

A. C. Fabian, A. Lohfink, E. Kara, M. L. Parker, R. Vasudevan, and C. S. Reynolds. Properties of AGN coronae in the NuSTAR era. *MNRAS*, 451(4):4375–4383, August 2015.

A. C. Fabian, A. Lohfink, R. Belmont, J. Malzac, and P. Coppi. Properties of AGN coronae in the NuSTAR era - II. Hybrid plasma. *MNRAS*, 467(3):2566–2570, May 2017.

B. L. Fanaroff and J. M. Riley. The morphology of extragalactic radio sources of high and low luminosity. *MNRAS*, 167:31P–36P, May 1974.

C. Fanti, R. Fanti, C. Lari, L. Padrielli, H. van der Laan, and H. de Ruiter. A search for radio emission from a sample of optically selected quasars. *A&A*, 61(4):487–491, November 1977.

L. G. Fishbone and V. Moncrief. Relativistic fluid disks in orbit around Kerr black holes. *ApJ*, 207:962–976, August 1976.

Roger Fletcher. *Practical methods of optimization*. John Wiley & Sons, 1987.

J. BJ Fourier. *Théorie analytique de la chaleur*. Dudot, Paris, 1822.

P. C. Fragile, Warner A. Miller, and Eric Vandernoot. Iron-Line Emission as a Probe of Bardeen-Petterson Accretion Disks. *ApJ*, 635(1):157–166, December 2005.

J. Frank, A. King, and D. Raine. *AccretioninAstro*. Cambridge Univ. Press. (Cambridge), 2002.

H. Friedman and E. T. Byram. X-rays from Sources 3C 273 and M 87. *Science*, 158(3798): 257–259, October 1967.

K. Fukumura, D. Kazanas, I. Contopoulos, and E. Behar. Magnetohydrodynamic Accretion Disk Winds as X-ray Absorbers in Active Galactic Nuclei. *ApJ*, 715(1):636–650, May 2010.

J. García and T. R. Kallman. X-ray Reflected Spectra from Accretion Disk Models. I. Constant Density Atmospheres. *ApJ*, 718(2):695–706, August 2010.

J. García, T. R. Kallman, and R. F. Mushotzky. X-ray Reflected Spectra from Accretion Disk Models. II. Diagnostic Tools for X-ray Observations. *ApJ*, 731(2):131, April 2011.

J. García, T. Dauser, C. S. Reynolds, T. R. Kallman, J. E. McClintock, J. Wilms, and W. Eikmann. X-Ray Reflected Spectra from Accretion Disk Models. III. A Complete Grid of Ionized Reflection Calculations. *ApJ*, 768(2):146, May 2013.

J. García, T. Dauser, A. Lohfink, T. R. Kallman, J. F. Steiner, J. E. McClintock, L. Brenneman, J. Wilms, W. Eikmann, C. S. Reynolds, and F. Tombesi. Improved Reflection Models of Black Hole Accretion Disks: Treating the Angular Distribution of X-Rays. *ApJ*, 782(2):76, February 2014.

J. A. García, E. Kara, D. Walton, T. Beuchert, T. Dauser, E. Gatuzz, M. Balokovic, J. F. Steiner, F. Tombesi, R. M. T. Connors, T. R. Kallman, F. A. Harrison, A. Fabian, J. Wilms, D. Stern, L. Lanz, C. Ricci, and D. R. Ballantyne. Implications of the Warm Corona and Relativistic Reflection Models for the Soft Excess in Mrk 509. *ApJ*, 871(1): 88, January 2019.

J. A. García, E. Sokolova-Lapa, T. Dauser, J. Madej, A. Różańska, A. Majczyna, F. A. Harrison, and J. Wilms. Accurate Treatment of Comptonization in X-Ray Illuminated Accretion Disks. *ApJ*, 897(1):67, July 2020.

E. Gardner and C. Done. A physical model for the X-ray time lags of narrow-line Seyfert type 1 active galactic nuclei. *MNRAS*, 442(3):2456–2473, August 2014.

C. M. Gaskell. Lognormal X-Ray Flux Variations in an Extreme Narrow-Line Seyfert 1 Galaxy. *ApJ*, 612(1):L21–L24, September 2004.

N. Gehrels. Confidence Limits for Small Numbers of Events in Astrophysical Data. *ApJ*, 303:336, April 1986.

I. M. George and A. C. Fabian. X-ray reflection from cold matter in Active Galactic Nuclei and X-ray binaries. *MNRAS*, 249:352, March 1991.

I. M. George, T. J. Turner, Hagai Netzer, K. Nandra, R. F. Mushotzky, and T. Yaqoob. ASCA Observations of Seyfert 1 Galaxies. III. The Evidence for Absorption and Emission Due to Photoionized Gas. *ApJS*, 114(1):73–120, January 1998.

S. Giacché, R. Gilli, and L. Titarchuk. Analysis of x-ray spectral variability and black hole mass determination of the nls1 galaxy mrk 766. *Astronomy & Astrophysics*, 562: A44, Feb 2014. ISSN 1432-0746. .

R. Giacconi, H. Gursky, F. R. Paolini, and B. B. Rossi. Evidence for x Rays From Sources Outside the Solar System. *Phys. Rev. Lett.*, 9(11):439–443, December 1962.

R. Giacconi, E. Kellogg, P. Gorenstein, H. Gursky, and H. Tananbaum. An X-Ray Scan of the Galactic Plane from UHURU. *ApJ*, 165:L27, April 1971.

M. Gierliński and C. Done. Black hole accretion discs: reality confronts theory. *MNRAS*, 347(3):885–894, Jan 2004.

M. Gierliński, M. Middleton, M. Ward, and C. Done. A periodicity of ~1hour in X-ray emission from the active galaxy RE J1034+396. *Nature*, 455(7211):369–371, September 2008.

A. G. Gonzalez, D. R. Wilkins, and L. C. Gallo. Probing the geometry and motion of AGN coronae through accretion disc emissivity profiles. *MNRAS*, 472(2):1932–1945, December 2017.

O. González-Martín and S. Vaughan. X-ray variability of 104 active galactic nuclei. XMM-Newton power-spectrum density profiles. *A&A*, 544:A80, August 2012.

R. W. Goodrich. Spectropolarimetry of "Narrow-Line" Seyfert 1 Galaxies. *ApJ*, 342:224, July 1989.

M. J. Graham, S. G. Djorgovski, D. Stern, A. J. Drake, A. A. Mahabal, C. Donalek, E. Glikman, S. Larson, and E. Christensen. A systematic search for close supermassive black hole binaries in the Catalina Real-time Transient Survey. *MNRAS*, 453(2): 1562–1576, October 2015a.

M. J. Graham, S. G. Djorgovski, Daniel Stern, E. Glikman, A. J. Drake, A. A. Mahabal, C. Donalek, S. Larson, and E. Christensen. A possible close supermassive black-hole binary in a quasar with optical periodicity. *Nature*, 518(7537):74–76, February 2015b.

A. R. Green, I. M. McHardy, and H. J. Lehto. On the nature of rapid X-ray variability in active galactic nuclei. *MNRAS*, 265:664–680, December 1993.

A. R. Green, I. M. McHardy, and C. Done. The discovery of non-linear X-ray variability in NGC 4051. *MNRAS*, 305(2):309–318, April 1999.

J. L. Greenstein. Red-Shift of the Unusual Radio Source: 3C 48. *Nature*, 197(4872): 1041–1042, March 1963.

B. Groves. The Narrow-line Region: Current Models and Future Questions. In L. C. Ho and J. W. Wang, editors, *The Central Engine of Active Galactic Nuclei*, volume 373 of *Astronomical Society of the Pacific Conference Series*, page 511, October 2007.

P. W. Guilbert and M. J. Rees. 'Cold' material in non-thermal sources. *MNRAS*, 233: 475–484, July 1988.

A. C. Gupta, A. Tripathi, P. J. Wiita, P. Kushwaha, Z. Zhang, and C. Bambi. Detection of a quasi-periodic oscillation in γ-ray light curve of the high-redshift blazar B2 1520+31. *MNRAS*, 484(4):5785–5790, April 2019.

H. Gursky, E. Kellogg, S. Murray, C. Leong, H. Tananbaum, and R. Giacconi. A Strong X-Ray Source in the Coma Cluster Observed by UHURU. *ApJ*, 167:L81, August 1971.

F. Haardt and L. Maraschi. A Two-Phase Model for the X-Ray Emission from Seyfert Galaxies. *ApJ*, 380:L51, October 1991.

F. Haardt and L. Maraschi. X-Ray Spectra from Two-Phase Accretion Disks. *ApJ*, 413: 507, August 1993.

J. P. Halpern. Variable X-ray absorption in the QSO MR 2251-178. *ApJ*, 281:90–94, June 1984.

J. P. Halpern and H. L. Marshall. A Long EUVE Observation of the Seyfert Galaxy RX J0437.4-4711. *ApJ*, 464:760, June 1996.

S. W. Hawking. Black hole explosions? *Nature*, 248(5443):30–31, March 1974.

S. W. Hawking. Particle creation by black holes. *Communications in Mathematical Physics*, 43(3):199–220, August 1975.

S. F. Hönig. Redefining the Torus: A Unifying View of AGNs in the Infrared and Submillimeter. *ApJ*, 884(2):171, October 2019.

S. F. Hönig and T. Beckert. Active galactic nuclei dust tori at low and high luminosities. *MNRAS*, 380(3):1172–1176, September 2007.

X-M. Hua and L. Titarchuk. Comptonization Models and Spectroscopy of X-Ray and Gamma-Ray Sources: A Combined Study by Monte Carlo and Analytical Methods. *ApJ*, 449:188, August 1995.

I. G Hughes and P. A. Hase. *Measurements and their Uncertainties*. Oxford Univ. Press. (Oxford), 2010.

A. Ingram and C. Done. A physical model for the continuum variability and quasi-periodic oscillation in accreting black holes. *MNRAS*, 415(3):2323–2335, Aug 2011.

A. Ingram and S. Motta. Solutions to the relativistic precession model. *MNRAS*, 444(3): 2065–2070, November 2014.

A. Ingram and Sara Motta. A review of quasi-periodic oscillations from black hole X-ray binaries: observation and theory. *arXiv e-prints*, art. arXiv:2001.08758, January 2020.

A. Ingram, M. van der Klis, M. Middleton, C. Done, D. Altamirano, L. Heil, P. Uttley, and M. Axelsson. A quasi-periodic modulation of the iron line centroid energy in the black hole binary H1743-322. *MNRAS*, 461(2):1967–1980, September 2016.

A. Ingram, G. Mastroserio, T. Dauser, P. Hovenkamp, M. van der Klis, and J. A. García. A public relativistic transfer function model for X-ray reverberation mapping of accreting black holes. *MNRAS*, 488(1):324–347, September 2019.

A. R. Ingram. Modelling aperiodic X-ray variability in black hole binaries as propagating mass accretion rate fluctuations: A short review. *Astronomische Nachrichten*, 337 (4-5):385, May 2016.

W. Ishibashi and T. J. L. Courvoisier. X-ray power law spectra in active galactic nuclei. *A&A*, 512:A58, March 2010.

K. Iwasawa, A. C. Fabian, W. N. Brandt, H. Kunieda, K. Misaki, Y. Terashima, and C. S. Reynolds. Detection of an X-ray periodicity in the Seyfert galaxy IRAS 18325-5926. *MNRAS*, 295:L20–L24, March 1998.

K. Jahoda, C. B. Markwardt, Y. Radeva, A. H. Rots, M. J. Stark, J. H. Swank, T. E. Strohmayer, and W. Zhang. Calibration of the Rossi X-Ray Timing Explorer Proportional Counter Array. *ApJS*, 163(2):401–423, April 2006.

F. Jansen, D. Lumb, B. Altieri, J. Clavel, M. Ehle, C. Erd, C. Gabriel, M. Guainazzi, P. Gondoin, R. Much, R. Munoz, M. Santos, N. Schartel, D. Texier, and G. Vacanti. XMM-Newton observatory. I. The spacecraft and operations. *A&A*, 365:L1–L6, January 2001.

G. HM. Jenkins and D. G. Watts. *Spectral Analysis and Its Applications*. Holden-Day. San Francisco, 1968.

Y-F. Jiang, S. W. Davis, and J. M. Stone. Iron Opacity Bump Changes the Stability and Structure of Accretion Disks in Active Galactic Nuclei. *ApJ*, 827(1):10, August 2016.

C. Jin, C. Done, M. Ward, M. Gierliński, and J. Mullaney. The Seyfert AGN RX J0136.9-3510 and the spectral state of super Eddington accretion flows. *MNRAS*, 398(1):L16–L20, September 2009a.

C. Jin, C. Done, M. Ward, M. Gierliński, and J. Mullaney. The Seyfert AGN RX J0136.9-3510 and the spectral state of super Eddington accretion flows. *MNRAS*, 398(1):L16–L20, September 2009b.

C. Jin, M. Ward, and C. Done. A combined optical and X-ray study of unobscured type 1 active galactic nuclei - III. Broad-band SED properties. *MNRAS*, 425(2):907–929, September 2012.

C. Jin, C. Done, M. Middleton, and M. Ward. A long XMM-Newton observation of an extreme narrow-line Seyfert 1: PG 1244+026. *MNRAS*, 436(4):3173–3185, December 2013.

C. Jin, C. Done, and M. Ward. Re-observing the NLS1 Galaxy RE J1034+396. I. the Long-term, Recurrent X-ray QPO with a High Significance. *arXiv e-prints*, art. arXiv:2005.05857, May 2020.

C. Jin, C. Done, and M. Ward. Re-observing the NLS1 galaxy RE J1034+396 - II. New insights on the soft X-ray excess, QPO, and the analogy with GRS 1915+105. *MNRAS*, 500(2):2475–2495, January 2021.

J. S. Kaastra, R. Mewe, D. A. Liedahl, S. Komossa, and A. C. Brinkman. X-ray absorption lines in the Seyfert 1 galaxy NGC 5548 discovered with Chandra-LETGS. *A&A*, 354: L83–L86, February 2000.

E. Kara, E. M. Cackett, A. C. Fabian, C. Reynolds, and P. Uttley. The curious time lags of pg 1244+026: discovery of the iron k reverberation lag. *Monthly Notices of the Royal Astronomical Society: Letters*, 439(1):L26–L30, Dec 2013. ISSN 1745-3925. .

E. Kara, A. C. Fabian, E. M. Cackett, J. F. Steiner, P. Uttley, D. R. Wilkins, and A. Zoghbi. The closest look at 1H0707-495: X-ray reverberation lags with 1.3 Ms of data. *MNRAS*, 428(4):2795–2804, Feb 2013.

E. Kara, A. C. Fabian, A. M. Lohfink, M. L. Parker, D. J. Walton, S. E. Boggs, F. E. Christensen, C. J. Hailey, F. A. Harrison, G. Matt, C. S. Reynolds, D. Stern, and W. W. Zhang. The Compton hump and variable blue wing in the extreme low-flux NuSTAR observations of 1H0707-495. *MNRAS*, 449(1):234–242, May 2015.

E. Kara, W. N. Alston, A. C. Fabian, E. M. Cackett, P. Uttley, C. S. Reynolds, and A. Zoghbi. A global look at X-ray time lags in Seyfert galaxies. *MNRAS*, 462(1): 511–531, October 2016.

E. Kara, J. A. García, A. Lohfink, A. C. Fabian, C. S. Reynolds, F. Tombesi, and D. R. Wilkins. The high-eddington nls1 ark 564 has the coolest corona. *Monthly Notices of the Royal Astronomical Society*, 468(3):3489–3498, Mar 2017. ISSN 1365-2966. .

E. Kara, J. F. Steiner, A. C. Fabian, E. M. Cackett, P. Uttley, R. A. Remillard, K. C. Gendreau, Z. Arzoumanian, D. Altamirano, S. Eikenberry, T. Enoto, J. Homan, J. Neilsen, and A. L. Stevens. The corona contracts in a black-hole transient. *Nature*, 565(7738): 198–201, January 2019.

E. Kara, J. F. Steiner, A. C. Fabian, E. M. Cackett, P. Uttley, R. A. Remillard, K. C. Gendreau, Z. Arzoumanian, D. Altamirano, S. Eikenberry, and et al. The corona contracts in a black-hole transient. *Nature*, 565(7738):198–201, Jan 2019. ISSN 1476-4687. .

S. Kaspi, W. N. Brandt, H. Netzer, R. Sambruna, G. Chartas, G. P. Garmire, and J. A. Nousek. Discovery of Narrow X-Ray Absorption Lines from NGC 3783 with the Chandra High Energy Transmission Grating Spectrometer. *ApJ*, 535(1):L17–L20, May 2000.

P. Katgert, J. K. Katgert-Merkelijn, R. S. Le Poole, and H. van der Laan. A first 1415 MHz survey with the Westerbork Synthesis Radio Telescope: An attempt to detect radio emission from quasi-stellar objects. *A&A*, 23:171–194, March 1973.

S. Kato, J. Fukue, and S. Mineshige. Black-hole accretion disks. In *Black-hole accretion disks. Edited by Shoji Kato*, January 1998.

K. I. Kellermann, R. Sramek, M. Schmidt, D. B. Shaffer, and R. Green. VLA Observations of Objects in the Palomar Bright Quasar Survey. *AJ*, 98:1195, October 1989.

B. C. Kelly, A. C. Becker, M. Sobolewska, A. Siemiginowska, and P. Uttley. Flexible and Scalable Methods for Quantifying Stochastic Variability in the Era of Massive Time-domain Astronomical Data Sets. *ApJ*, 788(1):33, June 2014.

Roy P. Kerr. Gravitational Field of a Spinning Mass as an Example of Algebraically Special Metrics. *Phys. Rev. Lett.*, 11(5):237–238, September 1963.

A. R. King and K. A. Pounds. Black hole winds. *MNRAS*, 345(2):657–659, October 2003.

O. G. King, T. Hovatta, W. Max-Moerbeck, D. L. Meier, T. J. Pearson, A. C. S. Readhead, R. Reeves, J. L. Richards, and M. C. Shepherd. A quasi-periodic oscillation in the blazar J1359+4011. *MNRAS*, 436:L114–L117, November 2013.

O. Klein and T. Nishina. Über die Streuung von Strahlung durch freie Elektronen nach der neuen relativistischen Quantendynamik von Dirac. *Zeitschrift fur Physik*, 52(11-12):853–868, November 1929.

A. N. Kolmogorov. A refinement of previous hypotheses concerning the local structure of turbulence in a viscous incompressible fluid at high Reynolds number. *Journal of Fluid Mechanics*, 13:82–85, January 1962.

A. Nikolaevich Kolmogorov. Dissipation of Energy in Locally Isotropic Turbulence. *Akademiia Nauk SSSR Doklady*, 32:16, April 1941.

O. Kotov, E. Churazov, and M. Gilfanov. On the X-ray time-lags in the black hole candidates. *MNRAS*, 327(3):799–807, November 2001.

M. Kozlowski, M. Jaroszynski, and M. A. Abramowicz. The analytic theory of fluid disks orbiting the Kerr black hole. *A&A*, 63(1-2):209–220, February 1978.

J. H Krolik. *Active Galactic Nuclei*. Princeton University Press, NJ, 1999.

B Lambert. *A Student's Guide to Bayesian Statistics*. Sage Publications Ltd, London, 2018.

A. Laor. Line Profiles from a Disk around a Rotating Black Hole. *ApJ*, 376:90, July 1991.

A. Lawrence and I. Papadakis. X-Ray Variability of Active Galactic Nuclei: A Universal Power Spectrum with Luminosity-dependent Amplitude. *ApJ*, 414:L85, September 1993.

A. Lawrence, M. G. Watson, K. A. Pounds, and M. Elvis. Low-frequency divergent X-ray variability in the Seyfert galaxy NGC4051. *Nature*, 325(6106):694–696, February 1987.

J. C. Lee, A. C. Fabian, C. S. Reynolds, W. N. Brandt, and K. Iwasawa. The X-ray variability of the Seyfert 1 galaxy MCG-6-30-15 from long ASCA and RXTE observations. *MNRAS*, 318(3):857–874, November 2000.

K. M. Leighly. A Comprehensive Spectral and Variability Study of Narrow-Line Seyfert 1 Galaxies Observed by ASCA. I. Observations and Time Series Analysis. *ApJS*, 125 (2):297–316, December 1999.

A. R. Liddle. Information criteria for astrophysical model selection. *Monthly Notices of the Royal Astronomical Society: Letters*, 377(1):L74–L78, May 2007. ISSN 1745-3933. .

LIGO Scientific Collaboration and Virgo Collaboration. Observation of Gravitational Waves from a Binary Black Hole Merger. *Phys. Rev. Lett.*, 116(6):061102, February 2016.

D. Lynden-Bell. Galactic Nuclei as Collapsed Old Quasars. *Nature*, 223(5207):690–694, August 1969.

Yu. E. Lyubarskii. Flicker noise in accretion discs. *MNRAS*, 292(3):679–685, December 1997.

X. Ma, L. Tao, S-N. Zhang, L. Zhang, Q-C. Bu, M-Y. Ge, Y-P. Chen, J-L. Qu, S. Zhang, F-J. Lu, L-M. Song, Y-J. Yang, F. Yuan, C. Cai, Xue-Lei Cao, Z. Chang, G. Chen, L. Chen, T-X. Chen, Y-B. Chen, Y. Chen, W. Cui, W-W. Cui, J-K. Deng, Y-W. Dong, Y-Y. Du, M-X. Fu, G-H. Gao, H. Gao, M. Gao, Y-D. Gu, J. Guan, C-C. Guo, D-W. Han, Y. Huang, J. Huo, L. Ji, S-M. Jia, L-H. Jiang, W-C. Jiang, J. Jin, Y-J. Jin, L-D. Kong, B. Li, C-K. Li, G. Li, M-S. Li, T-P. Li, W. Li, X. Li, X-B. Li, X-F. Li, Y-G. Li, Z-W. Li, X-H. Liang, J-Y. Liao, B-S. Liu, C-Z. Liu, G-Q. Liu, H-W. Liu, X-J. Liu, Y-N. Liu, B. Lu, X-F. Lu, Q. Luo, T. Luo, B. Meng, Y. Nang, J-Y. Nie, G. Ou, N. Sai, R-C. Shang, X-Y. Song, L. Sun, Y. Tan, Y-L. Tuo, C. Wang, G-F. Wang, J. Wang, L-J. Wang, W-S. Wang, Y-S. Wang, X-Y. Wen, B-Y. Wu, B-B. Wu, M. Wu, G-C. Xiao, S. Xiao, F-G. Xie, S-L. Xiong, H. Xu, Y-P. Xu, J-W. Yang, S. Yang, Y-J. Yang, Q-B. Yi, Q-Q. Yin, Y. You, A-M. Zhang, C-M. Zhang, F. Zhang, H.-M. Zhang, J. Zhang, T. Zhang, W-C. Zhang, W. Zhang, W-Z. Zhang, Y. Zhang, Y-F. Zhang, Y-J. Zhang, Y. Zhang, Z. Zhang, Z. Zhang, Z-L. Zhang, H-S. Zhao, X-F. Zhao, S-J. Zheng, D-K. Zhou, J-F. Zhou, Y-X. Zhu, Y. Zhu, and R-L. Zhuang. Discovery of oscillations above 200 keV in a black hole X-ray binary with Insight-HXMT. *Nature Astronomy*, 5:94–102, January 2021.

K. Makishima, Y. Maejima, K. Mitsuda, H. V. Bradt, R. A. Remillard, I. R. Tuohy, R. Hoshi, and M. Nakagawa. Simultaneous X-Ray and Optical Observations of GX 339-4 in an X-Ray High State. *ApJ*, 308:635, September 1986.

A. Markowitz, R. Edelson, S. Vaughan, P. Uttley, I. M. George, R. E. Griffiths, S. Kaspi, A. Lawrence, I. McHardy, K. Nandra, K. Pounds, J. Reeves, N. Schurch, and R. Warwick. X-Ray Fluctuation Power Spectral Densities of Seyfert 1 Galaxies. *ApJ*, 593(1): 96–114, August 2003.

A. Markowitz, I. Papadakis, P. Arévalo, T. J. Turner, L. Miller, and J. N. Reeves. The Energy-dependent X-Ray Timing Characteristics of the Narrow-Line Seyfert 1 Mrk 766. *ApJ*, 656(1):116–128, February 2007.

N. Marshall, R. S. Warwick, and K. A. Pounds. The variability of X-ray emission from active galaxies. *MNRAS*, 194:987–1002, March 1981.

A. Martocchia and G. Matt. Iron Kalpha line intensity from accretion discs around rotating black holes. *MNRAS*, 282(4):L53–L57, October 1996.

N. Mashian and A. Loeb. Hunting black holes with Gaia. *MNRAS*, 470(3):2611–2616, September 2017.

S. Mathur. Narrow-line Seyfert 1 galaxies and the evolution of galaxies and active galaxies. *MNRAS*, 314(4):L17–L20, June 2000.

G. Matt. Obscured active galactic nuclei: the hidden side of the X-ray Universe. *Philosophical Transactions of the Royal Society of London Series A*, 360(1798):2045, September 2002.

G. Matt, G. C. Perola, and L. Piro. The iron line and high energy bump as X-ray signatures of cold matter in Seyfert 1 galaxies. *A&A*, 247:25, July 1991.

G. Matt, A. C. Fabian, and R. R. Ross. Iron K-alpha lines from X-ray photoionized accretion discs. *MNRAS*, 262:179–186, May 1993a.

G. Matt, A. C. Fabian, and R. R. Ross. X-ray photoionized accretion discs : UV and X-ray continuum spectra and polarization. *MNRAS*, 264:839–852, October 1993b.

G. Matt, A. C. Fabian, and R. R. Ross. Iron K fluorescent lines from relativistic, ionized discs. *MNRAS*, 278(4):1111–1120, February 1996.

I. M. McHardy. X-ray variability of active galactic nuclei. In J. Hunt and B. Battrick, editors, *Two Topics in X-Ray Astronomy, Volume 1: X Ray Binaries. Volume 2: AGN and the X Ray Background*, volume 296 of *ESA Special Publication*, pages 1111–1124, November 1989.

I. M. McHardy, I. E. Papadakis, P. Uttley, M. J. Page, and K. O. Mason. Combined long and short time-scale X-ray variability of NGC 4051 with RXTE and XMM-Newton. *MNRAS*, 348(3):783–801, March 2004.

I. M. McHardy, K. F. Gunn, P. Uttley, and M. R. Goad. MCG-6-30-15: long time-scale X-ray variability, black hole mass and active galactic nuclei high states. *MNRAS*, 359 (4):1469–1480, June 2005.

I. M. McHardy, E. Koerding, C. Knigge, P. Uttley, and R. P. Fender. Active galactic nuclei as scaled-up Galactic black holes. *Nature*, 444(7120):730–732, December 2006.

I. M. McHardy, P. Arévalo, P. Uttley, I. E. Papadakis, D. P. Summons, W. Brinkmann, and M. J. Page. Discovery of multiple Lorentzian components in the X-ray timing properties of the Narrow Line Seyfert 1 Ark 564. *MNRAS*, 382(3):985–994, December 2007.

A. Merloni and A. C. Fabian. Accretion disc coronae as magnetic reservoirs. *MNRAS*, 321(3):549–552, March 2001.

A. Merloni and A. C. Fabian. Coronal outflow dominated accretion discs: a new possibility for low-luminosity black holes? *MNRAS*, 332(1):165–175, May 2002.

M. Middleton. Black Hole Spin: Theory and Observation. In C. Bambi, editor, *Astrophysics of Black Holes: From Fundamental Aspects to Latest Developments*, volume 440 of *Astrophysics and Space Science Library*, page 99, 2016.

M. Middleton and C. Done. The X-ray binary analogy to the first AGN quasi-periodic oscillation. *MNRAS*, 403:9–16, March 2010.

M. Middleton, C. Done, and M. Gierliński. An absorption origin for the soft excess in Seyfert 1 active galactic nuclei. *MNRAS*, 381(4):1426–1436, Nov 2007.

M. Middleton, C. Done, M. Ward, M. Gierliński, and N. Schurch. RE J1034+396: the origin of the soft X-ray excess and quasi-periodic oscillation. *MNRAS*, 394:250–260, March 2009.

M. Middleton, P. Uttley, and C. Done. Searching for the trigger of the active galactic nucleus quasi-periodic oscillation: 8 years of RE J1034+396. *MNRAS*, 417:250–260, October 2011.

M. J. Middleton, M. L. Parker, C. S. Reynolds, A. C. Fabian, and A. M. Lohfink. The view of AGN-host alignment via reflection spectroscopy. *MNRAS*, 457(2):1568–1576, April 2016.

G. Miniutti, R. D. Saxton, M. Giustini, K. D. Alexander, R. P. Fender, I. Heywood, I. Monageng, M. Coriat, A. K. Tzioumis, A. M. Read, C. Knigge, P. Gandhi, M. L. Pretorius, and B. Agís-González. Nine-hour X-ray quasi-periodic eruptions from a low-mass black hole galactic nucleus. *Nature*, 573(7774):381–384, September 2019.

K. Mitsuda, H. Inoue, K. Koyama, K. Makishima, M. Matsuoka, Y. Ogawara, N. Shibazaki, K. Suzuki, Y. Tanaka, and T. Hirano. Energy spectra of low-mass binary X-ray sources observed from Tenma. *PASJ*, 36:741–759, January 1984.

J. Moreno, M. S. Vogeley, G. T. Richards, and W. Yu. Stochastic Modeling Handbook for Optical AGN Variability. *PASP*, 131(1000):063001, March 2019.

E. H. Morgan, R. A. Remillard, and J. Greiner. RXTE Observations of QPOs in the Black Hole Candidate GRS 1915+105. *ApJ*, 482(2):993–1010, June 1997.

A. M. Mosquera, C. S. Kochanek, B. Chen, X. Dai, J. A. Blackburne, and G. Chartas. The Structure of the X-Ray and Optical Emitting Regions of the Lensed Quasar Q 2237+0305. *ApJ*, 769(1):53, May 2013.

C. Motch, M. J. Ricketts, C. G. Page, S. A. Ilovaisky, and C. Chevalier. Simultaneous X-ray/optical observations of GX 339-4 during the May 1981 optically bright state. *A&A*, 119:171–176, March 1983.

S. E. Motta, T. Muñoz-Darias, A. Sanna, R. Fender, T. Belloni, and L. Stella. Black hole spin measurements through the relativistic precession model: XTE J1550-564. *MNRAS*, 439:L65–L69, March 2014.

N. Murray and J. Chiang. Disk Winds and Disk Emission Lines. *ApJ*, 474(1):91–103, January 1997.

N. Murray, J. Chiang, S. A. Grossman, and G. M. Voit. Accretion Disk Winds from Active Galactic Nuclei. *ApJ*, 451:498, October 1995.

K. Nandra and I. E. Papadakis. Temporal Characteristics of the X-Ray Emission of NGC 7469. *ApJ*, 554(2):710–724, June 2001.

K. Nandra and K. A. Pounds. GINGA observations of the X-ray spectra of Seyfert galaxies. *MNRAS*, 268:405–429, May 1994.

K. Nandra, I. M. George, R. F. Mushotzky, T. J. Turner, and T. Yaqoob. ASCA Observations of Seyfert 1 Galaxies. I. Data Analysis, Imaging, and Timing. *ApJ*, 476(1):70–82, February 1997.

R. Narayan and I. Yi. Advection-dominated Accretion: A Self-similar Solution. *ApJ*, 428:L13, June 1994.

R. Narayan and I. Yi. Advection-dominated Accretion: Underfed Black Holes and Neutron Stars. *ApJ*, 452:710, October 1995.

R. Narayan, R. Mahadevan, and E. Quataert. Advection-dominated accretion around black holes. In M. A. Abramowicz, G. Björnsson, and J. E. Pringle, editors, *Theory of Black Hole Accretion Disks*, pages 148–182, January 1998.

M. A. Nowak. Toward a Unified View of Black-Hole High-Energy States. *PASP*, 107: 1207, Dec 1995.

P. M. Ogle, K. O. Mason, M. J. Page, N. J. Salvi, F. A. Cordova, I. M. McHardy, and W. C. Priedhorsky. Relativistic O VIII Emission and Ionized Outflow in NGC 4051 Measured with XMM-Newton. *ApJ*, 606(1):151–167, May 2004.

D. E. Osterbrock. *Astrophysics of gaseous nebulae and active galactic nuclei*. University Science Books, 1989.

B. Paczynski and G. Bisnovatyi-Kogan. A Model of a Thin Accretion Disk around a Black Hole. , 31:283, January 1981.

D. N. Page and K. S. Thorne. Disk-Accretion onto a Black Hole. Time-Averaged Structure of Accretion Disk. *ApJ*, 191:499–506, July 1974.

K. L. Page, J. N. Reeves, P. T. O'Brien, and M. J. L. Turner. XMM-Newton spectroscopy of high-redshift quasars. *MNRAS*, 364(1):195–207, November 2005.

H-W. Pan, W. Yuan, S. Yao, X-L. Zhou, B. Liu, H. Zhou, and S-N. Zhang. Detection of a Possible X-Ray Quasi-periodic Oscillation in the Active Galactic Nucleus 1H 0707-495. *ApJ*, 819(2):L19, March 2016.

I. Papadakis, T. Pecháček, M. Dovčiak, A. Epitropakis, D. Emmanoulopoulos, and V. Karas. Signatures of X-ray reverberation in the power spectra of AGN. *A&A*, 588:A13, April 2016.

I. E. Papadakis. The scaling of the X-ray variability with black hole mass in active galactic nuclei. *MNRAS*, 348(1):207–213, February 2004.

I. E. Papadakis and A. Lawrence. A detailed X-ray variability study of the Seyfert galaxy NGC 4051. *MNRAS*, 272(1):161–183, January 1995.

I. E. Papadakis, W. Brinkmann, H. Negoro, and M. Gliozzi. Detection of a high frequency break in the X-ray power spectrum of Ark 564. *A&A*, 382:L1–L4, January 2002.

D. R. Pasham, R. A. Remillard, P. C. Fragile, A. Franchini, N. C. Stone, G. Lodato, J. Homan, D. Chakrabarty, F. K. Baganoff, J. F. Steiner, E. R. Coughlin, and N. R. Pasham. A loud quasi-periodic oscillation after a star is disrupted by a massive black hole. *Science*, 363(6426):531–534, February 2019.

F. Pedregosa, G. Varoquaux, A. Gramfort, V. Michel, B. Thirion, O. Grisel, M. Blondel, P. Prettenhofer, R. Weiss, V. Dubourg, J. Vanderplas, A. Passos, D. Cournapeau, M. Brucher, M. Perrot, and E. Duchesnay. Scikit-learn: Machine learning in Python. *Journal of Machine Learning Research*, 12:2825–2830, 2011.

B. M. Peterson. *The Broad-Line Region in Active Galactic Nuclei*, volume 693, page 77. Lecture Notes in Physics, Vol. 693, 2006.

B. M. Peterson, I. M. McHardy, B. J. Wilkes, P. Berlind, R. Bertram, M. Calkins, S. J. Collier, J. P. Huchra, S. Mathur, I. Papadakis, J. Peters, R. W. Pogge, P. Romano, S. Tokarz, P. Uttley, M. Vestergaard, and R. M. Wagner. X-Ray and Optical Variability in NGC 4051 and the Nature of Narrow-Line Seyfert 1 Galaxies. *ApJ*, 542(1):161–174, October 2000.

P. O. Petrucci, A. Merloni, A. Fabian, F. Haardt, and E. Gallo. The effects of a Comptonizing corona on the appearance of the reflection components in accreting black hole spectra. *MNRAS*, 328(2):501–510, December 2001.

F. Pfefferkorn, Th. Boller, V. Burwitz, and P. Predehl. CHANDRA observation of the narrow-line Seyfert 1 galaxy IRAS 13224-3809. *arXiv e-prints*, art. astro-ph/0106203, June 2001.

E. Piconcelli, E. Jimenez-Bailón, M. Guainazzi, N. Schartel, P. M. Rodríguez-Pascual, and M. Santos-Lleó. The XMM-Newton view of PG quasars. I. X-ray continuum and absorption. *A&A*, 432(1):15–30, March 2005.

C. Pinto, W. Alston, M. L. Parker, A. C. Fabian, L. C. Gallo, D. J. K. Buisson, D. J. Walton, E. Kara, J. Jiang, A. Lohfink, and C. S. Reynolds. Ultrafast outflows disappear in high-radiation fields. *MNRAS*, 476(1):1021–1035, May 2018.

J. Poutanen. Impact of reverberation in flared accretion discs on temporal characteristics of X-ray binaries. *MNRAS*, 332(2):257–270, May 2002.

J. Poutanen, G. Lipunova, S. Fabrika, A. G. Butkevich, and P. Abolmasov. Supercritically accreting stellar mass black holes as ultraluminous X-ray sources. *MNRAS*, 377 (3):1187–1194, May 2007.

W. H. Press and G. B. Rybicki. Desperately Seeking Non-Gaussianity: The Light Curve of 0957+561. In D. Maoz, A. Sternberg, and E. M. Leibowitz, editors, *Astronomical Time Series*, volume 218 of *Astrophysics and Space Science Library*, page 61, January 1997.

W. H. Press, S. A. Teukolsky, W. T. Vetterling, and B. P. Flannery. *Numerical Recipes*. Cambridge Univ. Press. (Cambridge), 1996.

J. E. Pringle. Accretion discs in astrophysics. *ARA&A*, 19:137–162, January 1981.

D. Proga and T. R. Kallman. On the Role of the Ultraviolet and X-Ray Radiation in Driving a Disk Wind in X-Ray Binaries. *ApJ*, 565(1):455–470, January 2002.

D. Proga and T. R. Kallman. Dynamics of Line-driven Disk Winds in Active Galactic Nuclei. II. Effects of Disk Radiation. *ApJ*, 616(2):688–695, December 2004.

D. Proga, J. M. Stone, and J. E. Drew. Radiation-driven winds from luminous accretion discs. *MNRAS*, 295(3):595–617, April 1998.

D. Proga, J. M. Stone, and T. R. Kallman. Dynamics of Line-driven Disk Winds in Active Galactic Nuclei. *ApJ*, 543(2):686–696, November 2000.

E. M. Puchnarewicz and R. Soria. Do NLS1s and ultrasoft AGN have irradiated, warped accretion disks? *arXiv e-prints*, art. astro-ph/0202030, February 2002.

E. M. Puchnarewicz, K. O. Mason, A. Siemiginowska, and K. A. Pounds. The high-temperature big blue bump in the Seyfert galaxy RE J1034+396. *MNRAS*, 276(1): 20–32, September 1995.

E. M. Puchnarewicz, K. O. Mason, A. Siemiginowska, A. Fruscione, A. Comastri, F. Fiore, and I. Cagnoni. Constraining the Black Hole Mass and Accretion Rate in the Narrow-Line Seyfert 1 Galaxy RE J1034+396. *ApJ*, 550(2):644–654, April 2001.

I. Raginski and Ari Laor. AGN coronal emission models - I. The predicted radio emission. *MNRAS*, 459(2):2082–2096, June 2016.

M. J. Rees. Black Hole Models for Active Galactic Nuclei. *ARA&A*, 22:471–506, January 1984.

J. N. Reeves and M. J. L. Turner. X-ray spectra of a large sample of quasars with ASCA. *MNRAS*, 316(2):234–248, August 2000.

J. N. Reeves, K. Nandra, I. M. George, K. A. Pounds, T. J. Turner, and T. Yaqoob. The XMM-Newton Iron Line Profile of NGC 3783. *ApJ*, 602(2):648–658, February 2004.

R. C. Reis and J. M. Miller. On the Size and Location of the X-Ray Emitting Coronae around Black Holes. *ApJ*, 769(1):L7, May 2013.

R. C. Reis, J. M. Miller, M. T. Reynolds, K. Gültekin, D. Maitra, A. L. King, and T. E. Strohmayer. A 200-Second Quasi-Periodicity After the Tidal Disruption of a Star by a Dormant Black Hole. *Science*, 337(6097):949, August 2012.

R. A. Remillard and J. E. McClintock. X-ray properties of black-hole binaries. *Annual Review of Astronomy and Astrophysics*, 44(1):49–92, Sep 2006. ISSN 1545-4282. .

C. S. Reynolds. *X-Ray Emission and Absorption in Active Galaxies*. PhD thesis, University of Cambridge, 1996.

C. S. Reynolds. An X-ray spectral study of 24 type 1 active galactic nuclei. *MNRAS*, 286 (3):513–537, April 1997.

C. S. Reynolds. Measuring Black Hole Spin Using X-Ray Reflection Spectroscopy. , 183 (1-4):277–294, September 2014.

C. S. Reynolds and M. C. Begelman. Iron Fluorescence from within the Innermost Stable Orbit of Black Hole Accretion Disks. *ApJ*, 488(1):109–118, October 1997.

P. M. Rodríguez-Pascual, D. Alloin, J. Clavel, D. M. Crenshaw, K. Horne, G. A. Kriss, J. H. Krolik, M. A. Malkan, H. Netzer, P. T. O'Brien, B. M. Peterson, G. A. Reichert, W. Wamsteker, T. Alexander, P. Barr, R. D. Blandford, J. N. Bregman, T. E. Carone, S. Clements, T. J. Courvoisier, M. M. De R.is, M. Dietrich, H. Dottori, R. A. Edelson, A. V. Filippenko, C. M. Gaskell, J. P. Huchra, J. B. Hutchings, W. Kollatschny, A. P. Koratkar, K. T. Korista, A. Laor, G. M. MacAlpine, P. G. Martin, D. Maoz, B. McCollum, S. L. Morris, G. C. Perola, R. W. Pogge, R. L. Ptak, M. C. Recondo-González, J. M. Rodríguez-Espinoza, E. L. Rokaki, M. Santos-Lleó, K. Sekiguchi, J. M. Shull, M. A. J. Snijders, L. S. Sparke, G. M. Stirpe, R. E. Stoner, W. H. Sun, S. J. Wagner, I. Wanders, J. Wilkes, C. Winge, and W. Zheng. Steps toward Determination of the Size and Structure of the Broad-Line Region in Active Galactic Nuclei. IX. Ultraviolet Observations of Fairall 9. *ApJS*, 110(1):9–20, May 1997.

R. R. Ross and A. C. Fabian. The effects of photoionization on X-ray reflection spectra in active galactic nuclei. *MNRAS*, 261:74–82, March 1993.

R. R. Ross and A. C. Fabian. A comprehensive range of X-ray ionized-reflection models. *MNRAS*, 358(1):211–216, March 2005.

R. R. Ross, A. C. Fabian, and A. J. Young. X-ray reflection spectra from ionized slabs. *MNRAS*, 306(2):461–466, June 1999.

R. E. Rothschild, P. R. Blanco, D. E. Gruber, W. A. Heindl, D. R. MacDonald, D. C. Marsden, M. R. Pelling, L. R. Wayne, and P. L. Hink. In-Flight Performance of the High-Energy X-Ray Timing Experiment on the Rossi X-Ray Timing Explorer. *ApJ*, 496(1):538–549, March 1998.

J. L. Ryan, A. Siemiginowska, M. A. Sobolewska, and J. Grindlay. Characteristic Variability Timescales in the Gamma-Ray Power Spectra of Blazars. *ApJ*, 885(1):12, November 2019.

G. B. Rybicki and A. P. Lightman. *Radiative processes in astrophysics*. John Wiley & Sons, 1979.

M. Sako, S. M. Kahn, E. Behar, J. S. Kaastra, A. C. Brinkman, Th. Boller, E. M. Puchnarewicz, R. Starling, D. A. Liedahl, J. Clavel, and M. Santos-Lleo. Complex resonance absorption structure in the X-ray spectrum of IRAS 13349+2438. *A&A*, 365:L168–L173, January 2001.

J. D. Scargle. Wavelet and Other Multi-resolution Methods for Time Series Analysis. In G. Jogesh Babu and Eric D. Feigelson, editors, *Statistical Challenges in Modern Astronomy II*, page 333, January 1997.

M. Schmidt. 3C 273: A Star-like Object with Large Red-Shift. In Ivor Robinson, Alfred Schild, and E. L. Schucking, editors, *Quasi-Stellar Sources and Gravitational Collapse*, page 455, January 1963.

K. Schwarzschild. On the Gravitational Field of a Mass Point According to Einstein's Theory. *Abh. Konigl. Preuss. Akad. Wissenschaften Jahre 1906,92, Berlin,1907*, 1916:189–196, January 1916.

F. D. Seward and P. A. Charles. *Exploring the X-ray Universe, 2nd edition*. Cambridge Univ. Press. (Cambridge), 2010.

N. I. Shakura and R. A. Sunyaev. Black holes in binary systems. Observational appearance. *A&A*, 24:337–355, 1973.

G. A. Shields. A Brief History of Active Galactic Nuclei. *PASP*, 111(760):661–678, June 1999.

S. A. Sim, D. Proga, L. Miller, K. S. Long, and T. J. Turner. Multidimensional modelling of X-ray spectra for AGN accretion disc outflows - III. Application to a hydrodynamical simulation. *MNRAS*, 408(3):1396–1408, November 2010.

K. L. Smith, R. F. Mushotzky, P. T. Boyd, and R. V. Wagoner. Evidence for an Optical Low-frequency Quasi-periodic Oscillation in the Kepler Light Curve of an Active Galaxy. *ApJ*, 860(1):L10, June 2018.

M. G. Smith and A. E. Wright. A radio study of optically selected QSOs. *MNRAS*, 191: 871–886, June 1980.

R. Smith and S. Vaughan. X-ray and optical variability of Seyfert 1 galaxies as observed with XMM-Newton. *MNRAS*, 375(4):1479–1487, March 2007.

M. A. Sobolewska and C. Done. What is the origin of the soft excess in active galactic nuclei? *MNRAS*, 374(1):150–158, January 2007.

L. Stella. Measuring black hole mass through variable line profiles from accretion disks. *Nature*, 344(6268):747–749, April 1990.

L. Stella and M. Vietri. Lense-Thirring Precession and Quasi-periodic Oscillations in Low-Mass X-Ray Binaries. *ApJ*, 492(1):L59–L62, January 1998.

L. Stella, E. Arlandi, G. Tagliaferri, and G. L. Israel. Continuum Power Spectrum Components in X-Ray Sources: Detailed Modelling and Search for Coherent Periodicities. *arXiv e-prints*, art. astro-ph/9411050, November 1994.

L. Stella, M. Vietri, and S. M. Morsink. Correlations in the quasi-periodic oscillation frequencies of low-mass x-ray binaries and the relativistic precession model. *The Astrophysical Journal*, 524(1):L63–L66, Oct 1999. ISSN 0004-637X.

L. Strüder, U. Briel, K. Dennerl, R. Hartmann, E. Kendziorra, N. Meidinger, E. Pfeffermann, C. Reppin, B. Aschenbach, W. Bornemann, H. Bräuninger, W. Burkert, M. Elender, M. Freyberg, F. Haberl, G. Hartner, F. Heuschmann, H. Hippmann, E. Kastelic, S. Kemmer, G. Kettenring, W. Kink, N. Krause, S. Müller, A. Oppitz, W. Pietsch, M. Popp, P. Predehl, A. Read, K. H. Stephan, D. Stötter, J. Trümper, P. Holl, J. Kemmer, H. Soltau, R. Stötter, U. Weber, U. Weichert, C. von Zanthier, D. Carathanassis, G. Lutz, R. H. Richter, P. Solc, H. Böttcher, M. Kuster, R. Staubert, A. Abbey, A. Holland, M. Turner, M. Balasini, G. F. Bignami, N. La Palombara, G. Villa, W. Buttler, F. Gianini, R. Lainé, D. Lumb, and P. Dhez. The European Photon Imaging Camera on XMM-Newton: The pn-CCD camera. *A&A*, 365:L18–L26, January 2001.

M. Sun, Y. Xue, W. N. Brandt, W-M. Gu, J. R. Trump, Z. Cai, Z. He, D-b. Lin, T. Liu, and J. Wang. Corona-heated Accretion-disk Reprocessing: A Physical Model to Decipher the Melody of AGN UV/Optical Twinkling. *ApJ*, 891(2):178, March 2020.

R. A. Sunyaev and L. G. Titarchuk. Comptonization of X-rays in plasma clouds. Typical radiation spectra. *A&A*, 500:167–184, June 1980.

M. Tagger and R. Pellat. An accretion-ejection instability in magnetized disks. *A&A*, 349:1003–1016, September 1999.

C. Bruce Tarter, Wallace H. Tucker, and Edwin E. Salpeter. The Interaction of X-Ray Sources with Optically Thin Environments. *ApJ*, 156:943, June 1969.

B. G. Taylor, R. D. Andresen, A. Peacock, and R. Zobl. The EXOSAT Mission. , 30(1-4): 479–494, March 1981.

C. Taylor and C. S. Reynolds. X-Ray Reverberation from Black Hole Accretion Disks with Realistic Geometric Thickness. *ApJ*, 868(2):109, December 2018a.

C. Taylor and C. S. Reynolds. Exploring the Effects of Disk Thickness on the Black Hole Reflection Spectrum. *ApJ*, 855(2):120, March 2018b.

H. Thirring. Über die Wirkung rotierender ferner Massen in der Einsteinschen Gravitationstheorie. *Physikalische Zeitschrift*, 19:33, January 1918.

K. S. Thorne. Disk-Accretion onto a Black Hole. II. Evolution of the Hole. *ApJ*, 191: 507–520, July 1974.

J. Timmer and M. Koenig. On generating power law noise. *A&A*, 300:707, August 1995.

L. Titarchuk and V. Osherovich. Correlations between Kilohertz Quasi-periodic Oscillations and Low-Frequency Features Attributed to Radial Oscillations and Diffusive Propagation in the Viscous Boundary Layer around a Neutron Star. *ApJ*, 518(2):L95–L98, June 1999.

F. Tombesi, M. Cappi, J. N. Reeves, G. G. C. Palumbo, T. Yaqoob, V. Braito, and M. Dadina. Evidence for ultra-fast outflows in radio-quiet AGNs. I. Detection and statistical incidence of Fe K-shell absorption lines. *A&A*, 521:A57, October 2010.

F. Tombesi, M. Cappi, J. N. Reeves, G. G. C. Palumbo, V. Braito, and M. Dadina. Evidence for Ultra-fast Outflows in Radio-quiet Active Galactic Nuclei. II. Detailed Photoionization Modeling of Fe K-shell Absorption Lines. *ApJ*, 742(1):44, November 2011.

F. Tombesi, M. Cappi, J. N. Reeves, R. S. Nemmen, V. Braito, M. Gaspari, and C. S. Reynolds. Unification of X-ray winds in Seyfert galaxies: from ultra-fast outflows to warm absorbers. *MNRAS*, 430(2):1102–1117, April 2013.

M. J. L. Turner, A. Abbey, M. Arnaud, M. Balasini, M. Barbera, E. Belsole, P. J. Bennie, J. P. Bernard, G. F. Bignami, M. Boer, U. Briel, I. Butler, C. Cara, C. Chabaud, R. Cole, A. Collura, M. Conte, A. Cros, M. Denby, P. Dhez, G. Di Coco, J. Dowson, P. Ferrando, S. Ghizzardi, F. Gianotti, C. V. Goodall, L. Gretton, R. G. Griffiths, O. Hainaut, J. F. Hochedez, A. D. Holland, E. Jourdain, E. Kendziorra, A. Lagostina, R. Laine, N. La Palombara, M. Lortholary, D. Lumb, P. Marty, S. Molendi, C. Pigot, E. Poindron, K. A. Pounds, J. N. Reeves, C. Reppin, R. Rothenflug, P. Salvetat, J. L. Sauvageot, D. Schmitt, S. Sembay, A. D. T. Short, J. Spragg, J. Stephen, L. Strüder, A. Tiengo, M. Trifoglio, J. Trümper, S. Vercellone, L. Vigroux, G. Villa, M. J. Ward, S. Whitehead, and E. Zonca. The European Photon Imaging Camera on XMM-Newton: The MOS cameras. *A&A*, 365:L27–L35, January 2001.

S. G. D. Turner and C. S. Reynolds. Investigating the Theory of Propagating Fluctuations with Numerical Models of Stochastic Accretion Discs. *MNRAS*, March 2021.

Y. Ueda, K. Yamaoka, and R. Remillard. GRS 1915+105 in “Soft State”: Nature of Accretion Disk Wind and Origin of X-ray Emission. *ApJ*, 695(2):888–899, April 2009.

P. Uttley. Astrophysics: Heartbeat of an active galaxy. *Nature*, 455(7211):294–295, September 2008.

P. Uttley and I. M. McHardy. The flux-dependent amplitude of broadband noise variability in X-ray binaries and active galaxies. *MNRAS*, 323(2):L26–L30, May 2001.

P. Uttley, I. M. McHardy, and I. E. Papadakis. Measuring the broad-band power spectra of active galactic nuclei with RXTE. *MNRAS*, 332(1):231–250, May 2002.

P. Uttley, I. M. McHardy, and S. Vaughan. Non-linear X-ray variability in X-ray binaries and active galaxies. *MNRAS*, 359(1):345–362, May 2005.

P. Uttley, E. M. Cackett, A. C. Fabian, E. Kara, and D. R. Wilkins. X-ray reverberation around accreting black holes. *A&A Rev.*, 22:72, August 2014a.

P. Uttley, E. M. Cackett, A. C. Fabian, E. Kara, and D. R. Wilkins. X-ray reverberation around accreting black holes. *A&A Rev.*, 22:72, August 2014b.

P. Uttley, I. M. McHardy, and S. Vaughan. The rms-flux relation in accreting objects: not a simple “volume control”. A response to Koen 2016. *A&A*, 601:L1, May 2017.

M. van der Klis. Fourier Techniques in X-ray Timing. In *Timing Neutron Stars, eds. H. Ogelman and E.P.J. van den Heuvel. NATO ASI Series C, Vol. 262, p. 27-70. Dordrecht: Kluwer, 1988.*, volume 262, pages 27–70, 1988.

R. V. Vasudevan and A. C. Fabian. Piecing together the X-ray background: bolometric corrections for active galactic nuclei. *MNRAS*, 381(3):1235–1251, November 2007.

R. V. Vasudevan, A. C. Fabian, P. Gandhi, L. M. Winter, and R. F. Mushotzky. The power output of local obscured and unobscured AGN: crossing the absorption barrier with Swift/BAT and IRAS. *MNRAS*, 402(2):1081–1098, February 2010.

S. Vaughan. A simple test for periodic signals in red noise. *A&A*, 431:391–403, February 2005.

S. Vaughan. A Bayesian test for periodic signals in red noise. *MNRAS*, 402:307–320, February 2010.

S. Vaughan and A. C. Fabian. The high frequency power spectrum of Markarian 766. *MNRAS*, 341(2):496–500, May 2003.

S. Vaughan and P. Uttley. Where are the x-ray quasi-periodic oscillations in active galaxies? *Monthly Notices of the Royal Astronomical Society*, 362(1):235–244, Sep 2005. ISSN 1365-2966. .

S. Vaughan and P. Uttley. Detecting X-ray QPOs in active galaxies. *Advances in Space Research*, 38(7):1405–1408, January 2006.

S. Vaughan, R. Edelson, R. S. Warwick, and P. Uttley. On characterizing the variability properties of X-ray light curves from active galaxies. *MNRAS*, 345:1271–1284, November 2003a.

S. Vaughan, A. C. Fabian, and K. Nandra. X-ray continuum variability of MCG-6-30-15. *MNRAS*, 339(4):1237–1255, March 2003b.

S. Vaughan, P. Uttley, K.A. Pounds, K. Nandra, and T. E. Strohmayer. The rapid x-ray variability of ngc 4051. *MNRAS*, 413(4):2489–2499, June 2011.

S. Vaughan, P. Uttley, A. G. Markowitz, D. Huppenkothen, M. J. Middleton, W. N. Alston, J. D. Scargle, and W. M. Farr. False periodicities in quasar time-domain surveys. *MNRAS*, 461:3145–3152, September 2016.

M. P. Veron-Cetty and P. Veron. VizieR Online Data Catalog: Quasars and Active Galactic Nuclei (13th Ed.) (Veron+ 2010). *VizieR Online Data Catalog*, art. VII/258, Feb 2010.

M. Volonteri, M. Sikora, J. P. Lasota, and A. Merloni. The Evolution of Active Galactic Nuclei and their Spins. *ApJ*, 775(2):94, October 2013.

R. V. Wagoner, Alexander S. Silbergleit, and Manuel Ortega-Rodríguez. "Stable" Quasi-periodic Oscillations and Black Hole Properties from Diskoseismology. *ApJ*, 559(1): L25–L28, September 2001.

R. Walter and H. H. Fink. The ultraviolet to soft X-ray bump of Seyfert 1 type active galactic nuclei. *A&A*, 274:105, July 1993.

D. J. Walton, A. Zoghbi, E. M. Cackett, P. Uttley, F. A. Harrison, A. C. Fabian, E. Kara, J. M. Miller, R. C. Reis, and C. S. Reynolds. Hard X-Ray Lags in Active Galactic Nuclei: Testing the Distant Reverberation Hypothesis with NGC 6814. *ApJ*, 777(2): L23, November 2013.

J-M. Wang. A Limit Relation between Black Hole Mass and Hβ Width: Testing Super-Eddington Accretion in Active Galactic Nuclei. *AJ*, 125(6):2859–2864, June 2003.

T. Wang and Y. Lu. Black hole mass and velocity dispersion of narrow line region in active galactic nuclei and narrow line seyfert 1 galaxies. *A&A*, 377(1):52–59, 2001. .

K. Watarai and J. Fukue. Radiative Disk Winds from a Self-Similar Slim Disk. *PASJ*, 51: 725, October 1999.

K. Watarai, J. Fukue, M. Takeuchi, and S. Mineshige. Galactic Black-Hole Candidates Shining at the Eddington Luminosity. *PASJ*, 52:133, February 2000a.

K. Watarai, J. Fukue, M. Takeuchi, and S. Mineshige. Galactic Black-Hole Candidates Shining at the Eddington Luminosity. *PASJ*, 52:133, February 2000b.

P. Whittle. Estimation and information in stationary time series. *Arkiv for Matematik*, 2 (5):423–434, August 1953.

D. R. Wilkins and A. C. Fabian. Determination of the X-ray reflection emissivity profile of 1H 0707-495. *MNRAS*, 414(2):1269–1277, June 2011.

D. R. Wilkins and A. C. Fabian. The origin of the lag spectra observed in agn: Reverberation and the propagation of x-ray source fluctuations. *Monthly Notices of the Royal Astronomical Society*, 430(1):247–258, Jan 2013. ISSN 0035-8711. .

D. R. Wilkins and L. C. Gallo. Driving extreme variability: the evolving corona and evidence for jet launching in Markarian 335. *MNRAS*, 449(1):129–146, May 2015.

D. R. Wilkins, E. M. Cackett, A. C. Fabian, and C. S. Reynolds. Towards modelling X-ray reverberation in AGN: piecing together the extended corona. *MNRAS*, 458(1): 200–225, May 2016.

J-H. Woo and C. M. Urry. Active Galactic Nucleus Black Hole Masses and Bolometric Luminosities. *ApJ*, 579(2):530–544, November 2002.

E-P. Zhang and J-M. Wang. The Unified Model of Active Galactic Nuclei. I. Non-Hidden Broad-Line Region Seyfert 2 and Narrow-Line Seyfert 1 Galaxies. *ApJ*, 653(1):137–151, December 2006.

P. Zhang and Z. Wang. A Radio Quasi-periodic Oscillation of 176 day in the Radio-loud Narrow-line Seyfert 1 Galaxy J0849+5108. *arXiv e-prints*, art. arXiv:2104.04124, April 2021.

P. Zhang, P-f. Zhang, J-z. Yan, Y-z. Fan, and Q-z. Liu. An x-ray periodicity of 1.8 hr in narrow-line seyfert 1 galaxy mrk 766. *The Astrophysical Journal*, 849(1):9, Oct 2017. ISSN 1538-4357. .

P-f. Zhang, P. Zhang, N-h. Liao, J-z. Yan, Y-z. Fan, and Q-z. Liu. Two Transient X-Ray Quasi-periodic Oscillations Separated by an Intermediate State in 1H 0707-495. *ApJ*, 853(2):193, Feb 2018.

J. Zhou, Z. Wang, L. Chen, P. J. Wiita, J. Vadakkumthani, N. Morrell, P. Zhang, and J. Zhang. A 34.5 day quasi-periodic oscillation in γ-ray emission from the blazar PKS 2247-131. *Nature Communications*, 9:4599, November 2018.

A. Zoghbi and A. C. Fabian. X-ray reverberation close to the black hole in RE J1034+396. *MNRAS*, 418(4):2642–2647, December 2011.

A. Zoghbi, A. C. Fabian, C. S. Reynolds, and E. M. Cackett. Relativistic iron K X-ray reverberation in NGC 4151. *MNRAS*, 422(1):129–134, May 2012.